

2018

Nanostructured Interfaces for Single Molecule Sensing and Molecular Fingerprinting

Buddini I. Karawdeniya
University of Rhode Island, buddinironb@yahoo.com

Follow this and additional works at: https://digitalcommons.uri.edu/oa_diss

Terms of Use

All rights reserved under copyright.

Recommended Citation

Karawdeniya, Buddini I., "Nanostructured Interfaces for Single Molecule Sensing and Molecular Fingerprinting" (2018). *Open Access Dissertations*. Paper 736.
https://digitalcommons.uri.edu/oa_diss/736

This Dissertation is brought to you by the University of Rhode Island. It has been accepted for inclusion in Open Access Dissertations by an authorized administrator of DigitalCommons@URI. For more information, please contact digitalcommons-group@uri.edu. For permission to reuse copyrighted content, contact the author directly.

NANOSTRUCTURED INTERFACES
FOR
SINGLE MOLECULE SENSING AND MOLECULAR FINGERPRINTING

BY
BUDDINI IROSHIKA KARAWDENIYA

A DISSERTATION SUBMITTED IN PARTIAL FULFILLMENT OF THE
REQUIREMENTS FOR THE DEGREE OF
DOCTOR OF PHILOSOPHY
IN
CHEMISTRY

UNIVERSITY OF RHODE ISLAND
2018

DOCTOR OF PHILOSOPHY DISSERTATION

OF

BUDDINI IROSHIKA KARAWDENIYA

APPROVED:

Dissertation Committee:

Major Professor Jason R. Dwyer

Dugan Hayes

Geoffrey Bothun

Jiyeon Kim

Nasser H. Zawia

DEAN OF THE GRADUATE SCHOOL

UNIVERSITY OF RHODE ISLAND

2018

ABSTRACT

Nanoscale interfaces can have a profound influence on sensor performance, arising from the increased surface-area-to-volume ratio on length scales <100 nm, and often on the emergence of new phenomena on this length scale and even enhancement of existing phenomena. These interfaces can be used to form sensing devices capable of molecular sensing and fingerprinting. Attaining rapid and reliable molecular information with low analyte concentrations and minimal instrument overhead is crucial for many fields including the pharmaceutical industry, food quality analysis, biomedicine, water quality analysis, etc., to meet the current demands of sample analysis. Nanoscale elements in these nanosensors, in amalgam with other physical and chemical driving forces are useful for attaining low limits of detection with the ultimate goal of observing one molecule-at-a-time. This proposal contains two approaches to develop nanostructured sensors—one optical and one non-optical—to reach this goal. The first study is designed to develop a non-optical sensor—a solid state nanopore—for carbohydrate biopolymers—a class of abundant biomolecules that nevertheless have not been extensively characterized like other biomolecules (DNA or proteins), due to inadequate sensing capabilities to easily tackle the molecular complexity by classical methods alone. Additionally, methods to enhance and control the pore surface chemistry are investigated. Second, a series of accessible and low-cost surface enhanced Raman substrates are fabricated on a range of supports using electroless gold plating, to create optical sensors with vibrational selectivity and multifunctional capabilities.

ACKNOWLEDGMENTS

I would like to extend my sincerest thanks to my parents for their unconditional support and encouragement throughout this journey. Without their hard work, patience and perseverance, I never could have reached here. Thank you for believing in me and being there for me always and in return only expecting to hear my success story. Best thing ever happened to me is having them as my parents! Thank you to my little sister, who keeps me happy and motivated, just by her smiles and texts.

Thank you to my husband's family for all their love and support, especially my mother-in-law and father-in-law, for always wishing me the best.

Thank you to all other extended family that believed in me, specially my aunt and uncle (Loku Amma and Loku Thaththa) for all those long math and chemistry tutoring lessons on weekends when I was in middle school, (which I was not allowed to skip!) that kept me on my toes and fueled my enthusiasm in science.

To all our friends—back at home and RI for all the support—especially all the close friends at RI, for all the superb Friday night board games, road trips, cookouts and never-ending debates over the most [in]significant things that made these few years extremely interesting.

Randal and Bethany Curtis and their five beautiful children for making us feel at home all this time. Time spent with them is precious and memorable. They are one major reason I love Rhode Island!

Thank you to my school Samudradevi Balika Vidyalaya, my Alma Mata University of Colombo and Institute of Chemistry Ceylon for laying the foundation

of chemistry for me. I would like to acknowledge all the teachers and lecturers that have encouraged me to choose a career in science.

All my colleagues in Dwyer group, Julie, Elaine, Dan and Lucas, Jon, Rob and James for their support and input throughout the years and making my life full of very interesting discussions and memorable moments. Wish you all the best!

Special thank you to my dearest husband, love of my life, for all those million times he said, “you can do this”. Being a superb and dedicated researcher himself, I am very grateful, for his enormous support, superb research ideas, debates over science theories and encouragement in and out of the lab. Also, for simply being the fun loving, easy going, caring and funny person he is throughout these eleven years we have known each other, and for being my best friend. I would not have done this without him!

Thank you to all my committee members, Prof. Dugan Hayes, Prof. Geoffrey Bothun, Prof. J. Kim and Prof. Stephen Kennedy and early committee member Prof. Mindy Levine for all the input and much valued discussions provided and instrument facilities provided. All the research groups in the department of chemistry, for instrument facilities provided from time to time. Thank you to Dr. William Euler for his support throughout the years. I would like to thank Dr. Al Bach for NMR training and assistance in exploring other analytical instruments.

Entire teaching faculty at URI Chemistry (especially Dr.Susan Geldart) for the assistance and guidance provided when working as a teaching assistant. Entire staff at URI, Department of Chemistry and Sally Beauman in RI NSF EPSCoR office for their immense support all these years.

This research has been supported by NSF CAREER award CBET-1150085, in part by NSF EPSCoR Cooperative Agreement #IIA-1330406 and by the University of Rhode Island, including URI graduate fellowship in 2016.

Finally, very special thank you to my supervisor Prof. Jason R. Dwyer for being a great mentor from the start and guiding me through tough research terrains and encouraging me every single step of the way. He always recognized my hard work and always guided me to develop skills a researcher needs. His kind, professional and diligent nature is noteworthy. I appreciate his support and attentive work ethics that paved the way for me to reach here today and I am glad to work with him all these years!

DEDICATION

To

my mother, Kumuduni Kahaduwa

for inspiring me

with her invincible courage, diligent personality and self-motivation to reach the goals

but most of all, for teaching me that a good scientist is the one who preserves humanity above all.

And

my father, Daya Karawdeniya

for convincing me

education is wealth, integrity is strength and for being such a wonderful and respected human being.

above all, for your collective nature and perseverance.

And

my grandmother, Ms. Asilin Kahaduwa

who is not with us anymore, to whom I had to say good-bye from thousands of miles away

for her caring personality and unconditional love.

PREFACE

This dissertation is in manuscript format.

All supporting information appears in appendices.

- Chapter 1: Introduction to Nanostructured Interfaces for Single Molecule Sensing and Molecular Fingerprinting.
- Chapter 2: manuscript submitted and under review in *Nature Communications* journal.
- Chapter 3: published in *ACS Applied Materials and Interfaces* 2014, 6, pp. 10952-10957. 50.
- Chapter 4: published in *ACS Applied Materials and Interfaces*, 2016, 8, pp 34964–34969.
- Chapter 5: published in *ACS Appl. Mater. Interfaces*, 2016, 8 (44), pp 30583–30589.
- Chapter 6: published in *Electrophoresis*, 2018, 39, pp 626-634.
- Chapter 7: published in *ACS Appl. Nano Mater.*, 2018, 1 (2), pp 960–968.

TABLE OF CONTENTS

ABSTRACT	ii
ACKNOWLEDGMENTS	iii
DEDICATION.....	vi
PREFACE.....	vii
TABLE OF CONTENTS	viii
LIST OF FIGURES	xii
LIST OF TABLES.....	xxx
CHAPTER 1: PREFACE	1
INTRODUCTION TO NANOSTRUCTURED INTERFACES FOR	1
SINGLE MOLECULE SENSING AND MOLECULAR FINGERPRINTING	1
NON-OPTICAL SENSOR: NANOPORE FOR SENSING POLYSACCHARIDES.....	2
OPTICAL SENSOR: SURFACE ENHANCED RAMAN SUBSTRATES	8
ABBREVIATION	12
LITERATURE CITED.....	13
CHAPTER 2: PREFACE	15
CHAPTER 2	16
TASTY, THERAPEUTIC, OR TOXIC? GAUGING THIN-FILM SOLID-STATE NANOPORES FOR POLYSACCHARIDE SENSING	16
ABSTRACT	16
RESULTS.....	20
DISCUSSION.....	28
METHODS.....	33
AUTHOR INFORMATION.....	34
Corresponding Author	34
Author Contributions	34
Acknowledgements	34
REFERENCES	35
CHAPTER 3: PREFACE	39
Published: ACS Applied Materials and Interfaces 2014, 6, pp. 10952-10957	39
CHAPTER 3	41
ELECTROLESS PLATING OF THIN GOLD FILMS DIRECTLY ONTO SILICON NITRIDE THIN FILMS AND INTO MICROPORES.	41
ABSTRACT	41
INTRODUCTION	41
MATERIALS AND METHODS	44
DISCUSSION.....	45

AUTHOR INFORMATION.....	53
AUTHOR CONTRIBUTIONS	54
FUNDING SOURCES	54
ACKNOWLEDGEMENTS.....	54
ASSOCIATED CONTENT.....	54
ABBREVIATIONS	54
REFERENCES	55
CHAPTED 4: PREFACE	58
Published: ACS Applied Materials and Interfaces, 2016, 8, 34964–34969	58
CHAPTER 4.....	59
SOLUTION-BASED PHOTO-PATTERNED GOLD FILM FORMATION ON SILICON NITRIDE	59
ABSTRACT	59
INTRODUCTION	60
AUTHOR INFORMATION.....	69
ACKNOWLEDGMENT	70
ABBREVIATIONS	70
REFERENCES	71
CHAPTED 5: PREFACE	74
Published: ACS Appl. Mater. Interfaces, 2016, 8 (44), pp 30583–30589	74
CHAPTER 5.....	75
REAL-TIME PROFILING OF SOLID-STATE NANOPORES DURING SOLUTION-PHASE NANOFABRICATION.	75
ABSTRACT	75
THEORY	81
RESULTS AND DISCUSSION.....	84
REFERENCES	93
CHAPTER 6: PREFACE	96
Published: <i>Electrophoresis</i>, 2018, 39, 626-634	96
CHAPTER 6.....	97
CONDUCTANCE-BASED PROFILING OF NANOPORES: ACCOMMODATING FABRICATION IRREGULARITIES	97
ABSTRACT	97
INTRODUCTION	98
METHODS.....	102
RESULTS AND DISCUSSION.....	105
CONCLUDING REMARKS	113
REFERENCES	116

CHAPTER 7: PREFACE	123
Published: ACS Appl. Nano Mater., 2018, 1 (2), pp 960–968.....	123
CHAPTER 7.....	124
A GENERAL STRATEGY TO MAKE AN ON-DEMAND LIBRARY OF STRUCTURALLY AND FUNCTIONALLY DIVERSE SERS SUBSTRATES.....	124
ABSTRACT	124
INTRODUCTION	125
EXPERIMENTAL.....	129
RESULTS AND DISCUSSION.....	131
CONCLUSIONS	142
REFERENCES	145
APPENDIX 1: CHAPTER 2 SUPPORTING INFORMATION.....	151
REAGENTS AND MATERIALS.....	151
INSTRUMENTAL DETAILS	152
GENERAL NANOPORE SENSING PROCEDURE	153
POLYSACCHARIDE VISCOSITY MEASUREMENTS.....	154
ACID AND ENZYMATIC DIGESTION PROCEDURES	156
PREPARATION OF HEAT MAPS BY HISTOGRAMMING INDIVIDUAL EVENTS	158
RECOGNITION FLAG GENERATION.....	163
REFERENCES	165
APPENDIX 2: CHAPTER 3 SUPPORTING INFORMATION.....	166
MATERIALS	166
ELECTROLESS PLATING.....	167
CHARACTERIZATION.....	169
REFERENCES	175
APPENDIX 3: CHAPTER 4 SUPPORTING INFORMATION.....	176
MATERIALS AND EQUIPMENT.....	176
PRECAUTIONS FOR WORKING WITH HYDROFLUORIC ACID	177
PREPARATION OF REAGENTS.....	178
PALLADIUM SOLUTIONS ³	178
AMMONIACAL SILVER NITRATE ⁴	179
SODIUM GOLD (I) SULFITE ⁶⁻⁷	179
METALLIZATION.....	180
PD (II) / AG (I) / AU (I).....	181
AG (I) / AU (I).....	181
CHARACTERIZATION.....	182
GRID RECOGNITION	182

THICKNESS OF DEPOSITED GOLD	182
WIDTH OF GOLD AND COPPER (TEM) GRID LINES	183
SURFACE AREA COVERAGE.....	183
SELECTIVITY	184
INSTALLATION AND REMOVAL OF 1-ALKENE-DERIVED MONOLAYER ...	185
REFERENCES	187
APPENDIX 4: CHAPTER 5 SUPPORTING INFORMATION	188
METHOD OF CALCULATING VOLUME (A) AND SURFACE (B) INTEGRALS	191
TUTORIAL: Stepwise Construction of Figure 5.4	192
REFERENCES	197
APPENDIX 5: CHAPTER 6 SUPPORTING INFORMATION.....	198
REFERENCES	204
APPENDIX 6: CHAPTED 7 SUPPORTING INFORMATION.....	205
MATERIALS	205
ELECTROLESS PLATING.....	207
MATERIAL-SPECIFIC SURFACE PREPARATION.....	207
POLYMER-GRAFTED SILICON NITRIDE.....	208
SILICON NANOPILLAR ARRAY (GOLD-ETCHED SILMECO).....	209
CELLULOSE	209
SILICON- AND SILICON NITRIDE SURFACES.....	209
ELECTROLESS PLATING SCHEME.....	210
SURFACE CHARACTERIZATION OF ELECTROLESSLY PLATED FILMS	211
SURFACE ENHANCED RAMAN SPECTROSCOPY	214
SPECTRAL ACQUISITION.....	214
SPECTRAL ACQUISITION FOR DRIED SAMPLES.....	215
SPECTRAL ANALYSIS	215
REFERENCES	219

LIST OF FIGURES

Chapter 1

Figure number	Page
Figure 1.1: Example of different monomers, linkages and branched polysaccharides.....	3
Figure 1.2: Solid-state nanopore experimental setup. Nanopore is mounted in a PTFE cell and connects two electrolyte reservoirs. Ag/AgCl electrodes are immersed in each well to apply a voltage that results in a current corresponding to the pore size.	5
Figure 1.3: Molecular information can be extracted by the characteristic current blockages. In each pore, current blockage magnitude (I_0-I_b) corresponds to the molecule size, dwell time (τ) corresponds to the length of the molecule and frequency of blockages corresponds to concentration of the analyte molecule.	6
Figure 1.4: Energy level diagram of Raman scattering.....	10
Figure 1.5: Illustration of a coinage metal film on a support as a SERS substrate.	11

Chapter 2

Figure number	Page
Figure 2.1: Schematic of the nanopore setup. Analyte was added to the headstage side (“cis-” side, according to nanopore convention) unless otherwise noted, and applied voltages were referenced to the ground electrode (“trans-” side) on the other side.....	20
Figure 2.2: Representative nanopore current trace and events from sodium alginate samples from two different sources. a) A representative segment of an <i>AI</i> -induced current trace using a ~22 nm-diameter pore; the solid blue line marks	

the most frequent event level, $\langle i_b \rangle$, and the blue dashed line is its mean across all events. The magnified current event is from the same trace. b) *A2*- and c) enzyme-digested-*A2*-associated single events through a ~ 22 nm-diameter pore. All currents were measured in response to a 200 mV applied voltage...23

Figure 2.3: Combination heat map-scatter plots of alginate-induced events. Event counts (plotted as \log_{10} on the colour axis) of a) 4 μL 0.2% (w/v) *A1* using a ~ 19 nm diameter pore (~ 0.321 events/s), b) 20 μL of 3% (w/v) *A2* using a ~ 22 nm (~ 0.046 events/s) and c) 20 μL of 10-minute enzyme digested 3% (w/v) *A2* using a ~ 23 nm diameter pore (~ 0.112 events/s), all in pH ~ 7 buffered 1 M KCl. The experiment in (a) was repeated d) using a ~ 5 nm nanopore (~ 0.403 events/s), and e) an ~ 18 nm-diameter pore, but in 0.1 M KCl (vs. 1M KCl in (a)) electrolyte buffered at pH ~ 7 (~ 0.0527 events/s)....25

Figure 2.4: Heparin calibration curve. Three trials were performed, with at least 500 events per run extracted from 900 s-long measurements in a ~ 9 nm pore at -200 mV applied voltage after consecutive addition of 1 μL aliquots to the head-stage side of the same nanopore. Error bars are the standard deviation for the three trials.....27

Figure 2.5: Nanopore resistive-pulse analysis of heparin, OSCS, and their mixture. a) Superimposed scatter plots of 4 μL heparin, OSCS and OSCS-contaminated heparin added to 4 M potassium chloride at -200 mV and measured using a ~ 14 nm pore. The colours in the legend correspond to the listed sample and are blended (using transparency) in the plot where events from different samples overlap. b) Recognition flags of heparin, OSCS and their mixture from four independent trials accurately identify the presence of the OSCS aliquot in the mixture.....28

Chapter 3

Figure number	Page
Figure 3.1: (a) Photograph array of plating results at 3°C. Top row, left-to-right – HF etch omitted, 1 h plating after HNO ₃ preparation, HNO ₃ step replicate, plasma-cleaned only (subsequent steps omitted). Bottom row, left-to-right, Scheme 3.1 followed for plating times of 30 minutes, 1 hour, 2 hours, and 3 hours. The scratches in the film arose during handling of the chips. (b) Adhesive tape could lift most of the gold film to give an edge for (c) AFM measurements of electroless gold deposition film thickness as a function of time and temperature.	47
Figure 3.2. SEM images of a film after 2h of gold plating at 3°C. The inset is of the same film at lower magnification.	49
Figure 3.3. Measured spectra from 1cm ² silicon nitride substrates soaked in 0.01M NBT for 5 minutes: from a substrate electrolessly gold-plated at 3°C for 3 hours (red), from the same chip plasma cleaned, annealed at 280°C for 20 minutes, and plasma cleaned again before NBT exposure (blue), and from a sputtered (30s) gold film (black).	50
Figure 3.4. Gold coating can be seen to cover (a) the planar membrane and curved inner pore surface of the free-standing membrane area, with its uncoated equivalent shown in (c). A purposefully fractured membrane in (b) shows the gold coating on the micropore surface and the silicon nitride membrane (dark line) with intact gold coating. In image (d), plating also occurred on the bottom of the 200nm-deep well where it intersects with the silicon substrate.	53

Chapter 4

Figure number

Page

Figure 4.1: (a) 50 and 100 mesh copper TEM grids on a SiN_x-coated silicon chip; (b) 50 mesh 1-octene replica during the evaporation of a dichloromethane drop from a photopatterned chip, with image contrast, gamma, and brightness adjusted for image clarity; (c) gold replicas after Sn (II) surface sensitization followed by 5 minutes of Ag (I) and 30 minutes of Au (I) at ~3°C, with corresponding (d) FE-SEM image of a 100 mesh pattern; (e) gold replica after Pd (II) surface treatment followed 5 minutes of Ag (I) and 30 minutes of Au (I) at ~3°C, with corresponding (f) FE-SEM, (g) DHM (5× magnification) images of a 100 mesh pattern, with color intensity legend denoting film thickness (nm), and (h) histogram giving the film thickness distribution measured inside the bars of the micrograph in (g).....65

Figure 4.2: FESEM image of a subsection of a 100 mesh pattern on a SiN_x chip processed with Pd (II), Ag (I), and then Au (I) baths, as detailed in the SI. Vertical and horizontal bars composed of lighter pixels correspond to gold-replicated grid lines on the chip. Zooming into regions outside the bars (b) reveals very little presence of gold grains, confirming the visually observed spatial selectivity as seen in Figure 4.1d. Zooming into these bars at the same magnification (c) reveals the clear grain structure, and high infilling after only 30 minutes of gold plating.67

Figure 4.3: (a) A composite of an electron image (top) and three EDS maps (descending from nitrogen to silicon to gold). (b) FESEM image of a patterned

SiN_x chip (left) and pixel intensity (right) taken from the micrograph along the green line. (c) Electron image of a subsection of a 100 mesh pattern on a SiN_x chip. (d) Pixel intensity along each colored line in (c), along with line profiles of spatially-registered EDS maps corresponding to (e) silicon and (f) gold channels (Boltzmann fit is shown in green, with corresponding edge slopes, $dx = 0.81, 0.59, \text{ and } 0.87 \mu\text{m}$ from top to bottom).....68

Chapter 5

Figure number	Page
Figure 5.1: (a) Cylindrical, (b) double-conical, (c) conical-cylindrical, and (d) hyperbolic nanopore half-profile cross-sections cylindrically symmetric about the vertical z -axis (dotted line) of the pore. Profiles are shown before (black line) and after (blue line) material deposition to decrease the limiting nanopore radius, r_0 , by an amount Δr_i determined by the deposition time and material transfer rate.	84
Figure 5.2: The plotted lines denote the pairings of limiting nanopore radius, r_0 , and nanopore length, L , for each nanopore profile, that will produce a 200 nS conductance.	85
Figure 5.3: Nanopores with an initial 200 nS conductance ($L(t_0) = 10 \text{ nm}$, $r_0(t_0)$ from Figure 5.2) show a shape-dependent decrease in conductance due to material deposition at a constant rate, v_{mt} . The inset plots the rate of conductance change, calculated using nearest-neighbor differences, $\frac{dG}{dt} \cong \frac{G(t_{i+1}) - G(t_i)}{t_{i+1} - t_i}$	86
Figure 5.4: The conductance of initially 200 nS (a) cylindrical, (b) double-conical, (c) conical-cylindrical, and (d) hyperbolic nanopores can be satisfied by a	

range of radii (dotted vertical lines). Fixed decreases of each possible radius (in time) generate characteristic conductance progressions that depend on the nanopore shape and initial size (conductance curves labelled with their particular Δr_i). Simulated experimental conductance data versus time for $G_{\text{shape}}^{\text{expt}}(t_0) = 200 \text{ nS}$, $r_{0,\text{shape}}(t_0) = 3.5 \text{ nm}$ pores of each shape were compared to the plots in (a-d) to reveal the (e) cylindrical (red), (f) double-conical (blue), (g) conical-cylindrical (black), and (h) hyperbolic (magenta) experimental nanopore size and shapes by the constancy of the fitting $r_{0,\text{shape}}(t_0)$. The relevant experimental profiles for each column are inset in the top row.89

Chapter 6

Figure number

Page

Figure 6.1. a) Top view of $Lt_0 = 10 \text{ nm}$ cylindrical nanopores that yield a 200 nS conductance with the radii of the two inward-pointing defects given in the legend. b) Top view of the initially 1 nm-radius defect nanopore from (a), closing at $v_{\text{mt}} = 0.6 \text{ nm/h}$ with deposition time indicated. c) Progression of conductance (and r_0^{pinch} in inset) with time for the cylindrical nanopores from (a).119

Figure 6.2 (a) Experimental post-fabrication measurements of nanopore conductance and their corresponding TEM-based mean $r_{0,\text{TEM}}^{\text{expt}}$ (green stars)[43] were plotted versus several models: Equation 1 (solid markers) – cylindrical (red circles), double-conical (blue triangles), conical-cylindrical with an inner cylinder length of $0.6L$ (black squares), and hyperbolic (magenta diamonds); and with an added access resistance term, by Equation

S1 (hollow markers) – cylindrical with length L (small circles) and cylindrical with a $0.37L$ effective length [43] (large circles). To not bias further analysis with an explicit choice of nanopore profile, the $r_{0,TEM}^{expt}$ were fit to Equation S1 with G_{bulk} and $G_{surface}$ from the cylindrical model weighted by fit parameters: αG_{bulk} and $\beta G_{surface}$ (orange triangles— $r_{0,TEM}^{\alpha,\beta}(G)$). (b) Time-dependent conductance measurements were taken from the experimental work of Yanagi *et al.*[43] and were used with $r_{0,TEM}^{\alpha,\beta}(G)$ to determine $r_{0,TEM}^{\alpha,\beta}(t_i)$ (c) Candidate profiles matching those in (a) were used at each discrete value of $G(t_i)$ to calculate an $r_{0,candidate}(t_i)$. The figure compares the fit and experimentally-derived radii where the correct candidate size should result in a straight line at a ratio of 1. Selected data markers are shown for clarity..... 119

Figure 6.3. Conductances during simulated material deposition onto nanopores with initial conductances of 200 nS, and $r_0^{pinch}(t_0) = 4$ nm, were fit with candidate cylindrical nanopores: a defect-free pore, and pores with 0.1 and 1.0 nm-radius defects. Dotted and solid lines denote the pinch and outline radii, respectively. a) 0.1 nm defect pore and b) 1.0 nm defect pore profiles were used to furnish the simulated conductance data. The correct candidate profile in each case was indicated by the horizontal slope of the fit data; the defect-free $r_0(t_0)$ nearly completely overlaps with $r_0^{pinch}(t_0)$ for the 0.1 nm defect pores. Selected data markers are shown for clarity..... 120

Figure 6.4: a) Conductances and (inset) radii as a function of profile and time when simulating deposition onto surfaces of initially 200 nS, $L(t_0) = 10$ nm nanopores. Dotted curves in the conductance plots belong to the cylindrical pores with defects, and denote the corresponding r_0^{pinch} in the inset (solid line-

r_0^{outline}) and in (b)-(c). Conductance versus time for b) 0.1 nm-defect and c) 1.0 nm-defect cylindrical pores were fit with each candidate profile in the legend; horizontal fit lines for each case indicated the correct simulated profile. Selected data markers are shown for clarity. 121

Figure 6.5: Single (solid lines) and double (dotted lines)—left to right matching the half-profile sketches—cylindrical (red circles), double-conical (blue triangles), conical-cylindrical (black squares), and hyperbolic (magenta diamonds) profiles were used to simulate nanopore conductance values versus time. Eight candidate profiles (4 shapes, single and double) were used to fit (a-d) single pore simulated data and (e-h) double pore data from the 4 shapes. All experimental pores were initially 200 nS conductance. The correct nanopore shape was indicated by the constancy of the fit to $r_0(t_0)$ in time, and is labelled with the corresponding shape and number of pores. Selected data markers are shown for clarity. 121

Chapter 7

Figure number	Page
Figure 7.1: a) Representative substrates before (supports, top row) and after (bottom row) electroless gold plating. Left to right: Silicon nitride, polymer-grafted silicon nitride, paper, nanocellulose paper, nanopillar silicon (Silmeco etched of its as-supplied gold coating), silicon nanoporous substrates. b) Laser-induced damage at 250 mW sets an excitation power limit for paper (top, showing a through-hole) and nanocellulose paper (bottom, showing a hollow in the thicker substrate).	131

Figure 7.2: Representative baseline-corrected spectra of each substrate at 10^{-5} M NBT in ethanol (~57 mW for cellulose and as-supplied Silmeco; ~250 mW for all others). The dotted spectrum in the bottom panel shows the signal (scaled $20\times$) at 250 mW from 5 μ L of 1.6×10^{-5} M NBT in acetonitrile drop-cast onto the electrolessly-replated Silmeco. The vertical dotted lines denote the integration range for the NBT peak of interest. 136

Figure 7.3: SEM images of, from left-to-right by column, gold-plated silicon nitride, polymer-grafted silicon nitride, and nanoporous silicon nitride. The top two rows show top-down images while the bottom row shows an angled view of gold film cross-sections. The inset in the center micrograph more clearly shows a representative highly-structured flake. 138

Figure 7.4: SEM images of gold-plated paper substrates (top row) and gold-plated nanocellulose paper substrates (bottom row)..... 140

Figure 7.5: SEM image of a nanopillar substrate after gold etch (left), and with an electrolessly plated gold film peeled off of the underlying nanopillar support (right). 141

Appendix 1

Figure number	Page
Supplementary Figure 2.1: Calibration curve of sodium alginate event frequency versus concentration of <i>AI</i> . Three trials were performed, with each data point including at least 1000 events extracted from at least 1 h long measurements at 200 mV applied voltage after consecutive additions of 4 μ L aliquots to the headstage side of the same nanopore. Error bars represent the standard deviation across the trials.....	155

Supplementary Figure 2.2: A special nanopore configuration in which the electrolyte wells proximal to the electrodes and to the nanopore were physically separated. The purpose of this configuration was to determine if the current blockages arose from analyte interaction with the electrodes, or with the nanopore, itself. The electrolyte wells in the lower PTFE cell held the electrodes and were separated by an intact SiN_x membrane that did not allow ionic flow. These wells were connected through electrolyte-filled silicone tubing and an electrolyte-filled beaker (acting as a diffusion trap), to a second electrolyte-filled PTFE cell in which the wells were separated by a SiN_x nanopore. With analyte injected into the bottom cell, the only possible mechanism of current blockage was either by direct interaction with the electrodes, or by the passage of analyte through the tubing and beaker of solution until it could interact with the nanopore. When a 4 μL aliquot of the alginate was added to the head stage side of the lower cell, only 18 appreciable current transients were detected in a 1 hour measuring period, contrasted with 561 events in 1 hour when the alginate was directly injected adjacent to the head stage side of the nanopore. The additional electrolyte between electrodes and nanopore reduces the cross-pore applied potential compared to the usual single-cell sensing configuration. 156

Supplementary Figure 2.3: UV/Vis spectra of acid and enzymatic digestion products. a) Stock *A1* subjected to 16 h of sulphuric acid digestion generated a ~270 nm absorption band characteristic of the digested polysaccharide^{10, 11} that was replicated in the samples taken from the headstage and from the groundstage sample wells after 4 days of a translocation experiment (200 μL aliquot). The dashed lines denote the UV/Vis spectra of the sample before

digestion, and the solid lines denote the spectra after digestion. b) Alginate lyase digestion of alginate is expected to introduce chromophores with a peak absorption at ~232 nm, consistent with observations here.¹² 157

Supplementary Figure 2.4: Histograms of (top row) $\langle i_b \rangle / \langle i_0 \rangle$ (bottom row) duration in \log_{10} of *A1* alginate in (a) ~5 nm and (b) ~19 nm pore, *A2* in (c) ~22 nm, (d) 10-min enzyme digested *A2* in ~23 nm pore, (e) heparin and (f) OSCS in the same ~14 nm pore with the bin size set automatically by the measurement statistics as described above. 159

Supplementary Figure 2.5: Plots of \log_{10} of event duration (τ) versus area under each event for alginate *A1* in a) ~5 nm and b) ~19 nm diameter pores and c) for alginate *A2* in a ~22 nm diameter pore recorded for 1 hour in 1 M KCl at pH ~7. Two distinct event distribution tails are visible corresponding to short-lived spike-like pulses and longer-lived rectangular blockages. The longer-lived tail for *A2* is more prominent as a percentage of total events than for *A1*, consistent with the appearance of the combined heat and scatter plots in Figure 2.3. The shorter events could be attributed to either “bumps” or fast translocations, and longer-lived events could be attributed to slower translocations or longer-lived interactions with the pore (in both cases, complementary measurements independently confirmed alginate translocation). The low molecular weight and high M/G ratio (more G is attributed to stiffness) of *A2* meant, it has a greater probability of translocating through a given pore hence tails seen in the figure above are not surprising. Area under each event was calculated by integrating the interpolation function (interpolation order of 1) of each event in Mathematica. 160

Supplementary Figure 2.6: Representative current events of *A1* alginate at pH 3,5 and 7 at negative and positive 200 mV applied on the head stage side for 1-hour each in the same ~8 nm diameter pore at 1M KCl. 161

Supplementary Figure 2.7: Infrared spectra of alginate samples. The intensity of the peaks near 1400 and 1600 cm^{-1} , relative to the remainder of the spectrum, are consistent with a lesser proportion of carboxylic acid salt residues in (a) *A1* than in (b) *A2*. Comparison of the intensity of the guluronic (G) unit absorption at ~1025 cm^{-1} to the mannuronic (M) unit absorption at ~1100 cm^{-1} allows calculation of the M/G ratio that varies with particular alginate source.¹⁴ Using this approach, alginate *A1* was determined to be ~63%G/37%M, and alginate *A2* was ~57%G/43%M. These relative proportions were supported by additional analysis: in Supplementary Figure 3b, the particular alginate lyase was a mannuronic lyase, so that the greater absorption from the digestion of *A2* than *A1* was consistent with a greater proportion of *M* in *A2*. 162

Supplementary Figure 2.8: Heparin and OSCS events. A representative a) i) segment of a heparin induced-current trace using a ~10 nm-diameter pore with a magnified current event from the same trace, and from ii) OSCS through the same pore in response to a -200 mV applied voltage in 4 M KCl at pH ~7. b) Contour+scatter plots of i) heparin, ii) OSCS and iii) heparin contaminated with OSCS through a ~14 nm diameter pore..... 163

Supplementary Figure 2.9: Hue plots of show the outcomes of recognition flag generation (and measurement statistics—see procedure detailed above) after steps 3 (top) and 7 (bottom), based on **fb = ibi0** and **log10 τ** of the individual events. The identification threshold, determined by the measurement statistics

of each run, is given by the blue line. The corresponding final recognition flags, showing successful detection of the toxic OSCS impurity across four independent trials in ~8.6, 9.8, 9.9, and 13.6 nm (left to right), are shown in Figure 2.5..... 164

Appendix 2

Figure number	Page
Supporting Information Figure S3.1: Elemental analysis of gold films. At left, XPS scans comparing a sputtered gold film with an electrolessly plated gold film. The curves are vertically offset for clarity. At right, EDS profiling confirms the gold composition of one of the larger surface particles.	172
Supporting Information Figure S3.2: XPS spectra at key steps in the application of Scheme 1, and after selected control experiments. The label given to each spectrum indicates the terminal steps of Scheme 1 (or control experiment variation) that were performed on the substrate. The control data center on the effect of HF etching (performed or omitted) and tin sensitization (with standard solution or tin-free control). The scattered points are experimental data, and solid lines are used for the fit to the data (individual components and their sum). Each plot includes the center value and (width) of each component used to fit the experimental spectrum.	172

Appendix 3

Figure number	Page
Figure S-4. 1: (a) Use of the standard Pd (II) surface treatment solution produced excellent spatial selectivity and pattern quality for the process flow Pd (II)/Ag (I)/Au (I). The pattern quality was sensitive to the solution preparation, as shown by the example in (b) for which we omitted phosphoric acid from the Pd (II) solution. (c) Metallization begun with the Ag (I) solution, as a Ag (I)/Au (I) process flow, produced marginal pattern quality, (d) as did replacing 1-octene with an air layer during the patterning step.....	185
Figure S-4.2: XPS peaks corresponding to Br 3d region. (a) Photo-attachment of 11-bromo-1-undecene to the surface (black spectra) was followed by (b) removal of the alkane monolayer through prolonged exposure (18 hours) to UV in air (red spectra).	186

Appendix 4

Figure number	Page
Figure S-5.1: 2D cross-sections of pristine (black lines) (a) cylindrical, (b) double conical, (c) conical-cylindrical and (d) hyperbolic nanopore profiles modified uniformly across their surfaces by a thickness of Δr_i (blue lines).	189
Figure S-5.2: As 10 nm-long nanopores of different shapes, all with initial conductances of 200 nS are progressively reduced in size due to material deposition, the profile-dependent decreases in the conductances are caused by profile-dependent changes in the underlying geometry integrals, A and B . ..	192

Appendix 5

Figure number	Page
Figure S6.1: (a) Cylindrical, (b) double-conical, (c) conical-cylindrical, and (d) hyperbolic nanopore half-profile cross-sections cylindrically symmetric about the vertical z -axis (dotted vertical line) of the pore. Profiles are shown before (black line) and after (blue line) material deposition to decrease the limiting nanopore radius, r_0 , by an amount Δr_i determined by the deposition time and material transfer rate. Reprinted with permission from [1]. Copyright 2016 American Chemical Society.	198
Figure S6.2: Simulations of conductance versus time for initially 200 nS pores with Lt_0/r_0t_0 ratios of 0.5 (blue), 1.0 (magenta), and 1.5 (red) for (a) single and (c) double pores, with (dotted lines) and without (solid-lines) the access resistance term in Equation S1. In (b) and (d), we fit candidate pore models with and without access resistance using the conductance data in (a) and (c) that included the access resistance. There are three correct fits in (b) and (d)—one for each Lt_0/r_0t_0 —that are indicated by the horizontal slope of the fit r_0t_0 versus t data. Neglecting the access resistance when fitting the conductance-versus-time simulations results in a ~ 2 nm overestimate of the nanopore dimensions and a nonzero slope that indicates the incorrect fit. The simulations used step sizes in the nanopore radius of 0.01 nm to calculate G versus t , and 0.05 nm to determine r_0t_0	200
Figure S6.3: Plots of nanopore ($L=10$ nm, $r_0=6.45$ nm) conductance in time at pH 4 (red), 7 (black), and 10 (blue), showing the effect of pH on initial conductance (200 nS at pH 7) and on the time-evolution of the nanopore conductance, (a) with and (e) without access resistance. The influence of the solution pH is through the nanopore surface charge density, σ (equation (1)), and so pores of	

identical shape and size immersed in solutions of different pH may have different conductances. The inset shows the difference between the curves at all pH values, relative to the curve at pH 7. Geometry determinations (b-d) with and (f-h) without access resistance included in the candidate cylindrical profile were performed using the data in (a) and (e), using values of 4, 7, and 10 for the solution pH, respectively.....202

Figure S6.4: a) Pairings of r_0 and L for a given nanopore shape and number (solid line-single pore; dotted line-double pore) giving a nanopore with 200 nS conductance. b) Change in conductance with time for 10 nm-long profiles with single and double pore configurations. The simulations used step sizes in the nanopore radius of 0.01 nm to calculate G versus t203

Appendix 6

Figure number	Page
Figure S7.1: Au4f peaks of X-ray photoelectron spectroscopy data confirm gold deposition on the surface of each substrate. Photographs of gold-coated substrates are shown as insets.....	212
Figure S7.2: As-acquired spectra of support materials, substrates, and analyte. Spectra are displayed at full vertical range at left, and scaled at right to more clearly reveal the details of the baseline. (a) 1.67×10^{-4} M NBT in acetonitrile was added to each element (drop-casting followed by 5 minutes of air-drying: 20 μ L aliquots for silicon- and silicon-nitride-containing elements; 5 μ L aliquots for commercial silicon nanopillar and nanoporous silicon nitride; and by soaking for 5 minutes followed by 5 minutes of vacuum drying: 1 mL for paper and 10 mL for nanocellulose paper), with the solvent allowed to dry before spectral acquisition. (b) Elements were immersed in 10^{-4} M solutions of	

NBT in ethanol and spectra were recorded after signal level saturation in time.
.....213

Figure S7.3: Peak area ratio as a function of concentration for a) SERS and b) normal Raman measurements, with solid lines to aid the eye. Spectra were acquired using 250 mW excitation, except as noted: for cellulose substrates and commercial substrate, excitation was limited to 57 mW. Limits of detection ($LOD = 3s_{blank}/sensitivity$) were estimated by fitting the first 3–4 data points of each response curve to a straight line. The sensitivity was equated to the linear slope and the standard deviation of the blank, s_{blank} , was calculated from experimental measurements. The LOD, in matching order to the substrates, were 2.58×10^{-10} , 2.7×10^{-10} , 2.13×10^{-10} , 1.08×10^{-9} , 1.16×10^{-8} and 3.62×10^{-11} M, but these should be understood, along with the data below, as providing a benchmark for optimizing the *application-specific* substrate preparation.217

Figure S7.4: We constructed a crude paper-based assembly to demonstrate the prospects of using electrolessly gold-plated supports as multifunction SERS substrates. This assembly incorporated physical filtration of a heterogeneous sample, chromatographic separation of a multicomponent mixture, and SERS readout. The sample was constructed from NBT in acetonitrile and 4-aminothiophenol (ATP) in ethanol, with dirt added to the mixture. The mixture was spotted onto chromatography paper (7.5 cm×2.5 cm), which physically filtered the dirt (a view of the back shows the dirt did not fully penetrate through the paper). A separation was run in 4% (v/v) ethyl acetate in hexane. Iodine staining allowed visual determination of the ATP retention time (photograph shown as an inset), but SERS was needed to localize the

NBT spot. After sampling then separation, squares of electrolessly gold-coated paper were placed on a glass slide underneath the two individual analyte spots. Transfer of the separated analytes was achieved using 10–40 μL drops of ethanol and SER spectra were then recorded from each piece of electrolessly gold-plated readout paper.218

LIST OF TABLES

Table S-5.1: Definitions of notation used in describing the nanopore profiles. ...	188
Table S-5.2: Geometric profiles and equations describing nanopore shapes before (black line) and after (blue line) a uniform surface modification of thickness of Δr_i over the entire pore surface. We provide the equations that determine the nanopore profile, r_z , for the piecewise integration, between points labelled with undercase letters, of volume (A) and surface (B) integrals.	191

CHAPTER 1: PREFACE

INTRODUCTION TO NANOSTRUCTURED INTERFACES FOR SINGLE MOLECULE SENSING AND MOLECULAR FINGERPRINTING

CHAPTER 1

INTRODUCTION TO NANOSTRUCTURED INTERFACES FOR SINGLE MOLECULE SENSING AND MOLECULAR FINGERPRINTING

NON-OPTICAL SENSOR: NANOPORE FOR SENSING

POLYSACCHARIDES

Molecular structure determines the function of biomolecules, and exploring this biological context requires the ability to determine structure, often structural dynamics underpinning intermolecular interactions, and to detect subtle chemical differences including sample heterogeneity at low molecular concentrations. While conventional techniques such as nuclear magnetic resonance (NMR) and mass spectrometry (MS) yield extensive chemical insights, there remains a pressing need for chemical analysis tools that have low capital and operating costs, don't require highly skilled operators, and can deliver reliable information in a short analysis time. Some samples can be especially challenging. The field of biomolecular sensing has devoted tremendous effort to the study of DNA (genomics) and proteins (proteomics). While conventional methods are powerful for such analyses, there has nevertheless been consistent effort to develop new, higher-performance tools such as nanopore single-molecule sensors.^{1,2,3} The structure determination of polysaccharides, however, remains challenging for conventional methods. The field has lacked the attention it deserves mainly due to the complications associated with tackling the complexities in sample heterogeneity, limited available sample quantities, monomer composition, crosslinking, polymerization, isomeric forms and branching as depicted by Figure 1.1. Nevertheless, amidst all

the biopolymers, carbohydrates are a vital class associated with mediating many biological functions, including cell-cell interactions, cell proliferation, apoptosis and microbial interaction with the body and thus are vital for disease detection and as drug targets.^{4,5,6} Given that difficulties have severely hindered the use of conventional chemical analysis tools and methods, it is essential to develop new tools that may be better able to address key issues in glycomics— the comprehensive study of structure and function of carbohydrates.

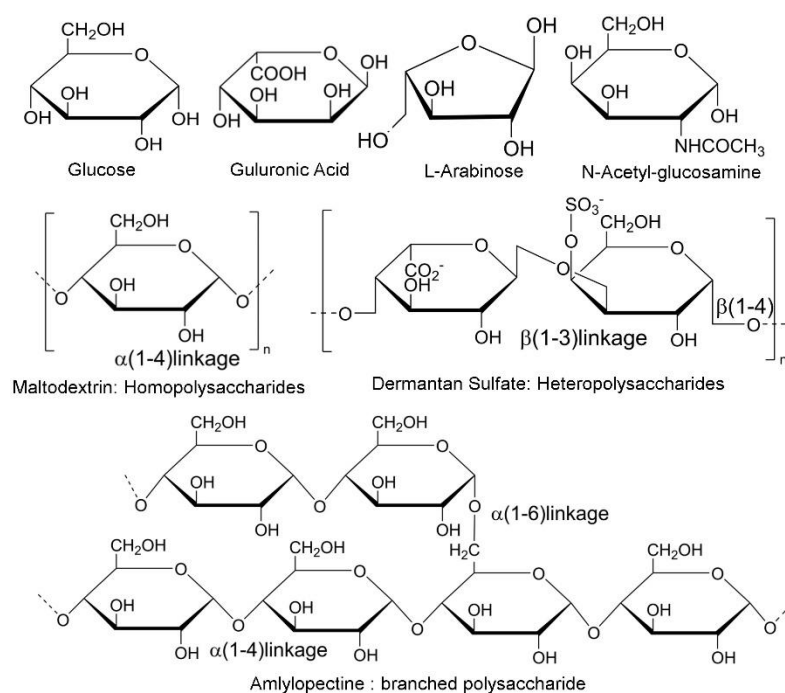


Figure 1.1: Example of different monomers, linkages and branched polysaccharides.

We proposed to use a nanopore—an effective and robust non-optical single-molecule sensing device—operated on an ostensibly simple principle. Nanopore is a nanometer scale channel that connect two electrolyte compartments. A typical nanopore setup is shown in Figure 1.2. When a voltage bias is applied across an open pore it results in an open pore current (i_0). When an analyte molecule is added to one compartment it can eventually get driven to the other side through the pore due to one or many phenomena like diffusion, electrophoresis, electroosmosis etc. When the analyte molecule enters the pore, it disrupts the ion movement causing the open pore current and results in a new current (i_b), often of a lower magnitude than the open pore current. Once the molecule exits the pore, the current returns to the open pore current as shown in Figure 1.3.⁷ The current blockage relative to the open pore current (i_b/i_0) in a given pore at a specified condition provides information about the molecule. This current blockage is characteristic of the molecular structure at a particular pH, salt concentration, temperature, pore shape, etc.⁸ and by analyzing the current events using a given pore, indications of the molecular size, length, charge and concentration can be determined. Two of the most compelling advantages of nanopore sensors are the requirement of small sample volume and less complicated sample preparation that avoids molecular labelling, chemical modification or surface immobilization of the molecules so that its structure and properties are preserved. By providing a very small volume for the ions to pass through, nanopore sensors ensure that a single molecule interrupts a significant fraction of ions as it passes through the pore. This large signal eliminates the complication associated with enzyme amplification and attachment of identification groups, such as fluorophores.⁷ This is vitally important because

while DNA studies benefit from amplification techniques such as polymerase chain reaction (PCR), there is no equivalent for glycan analysis.

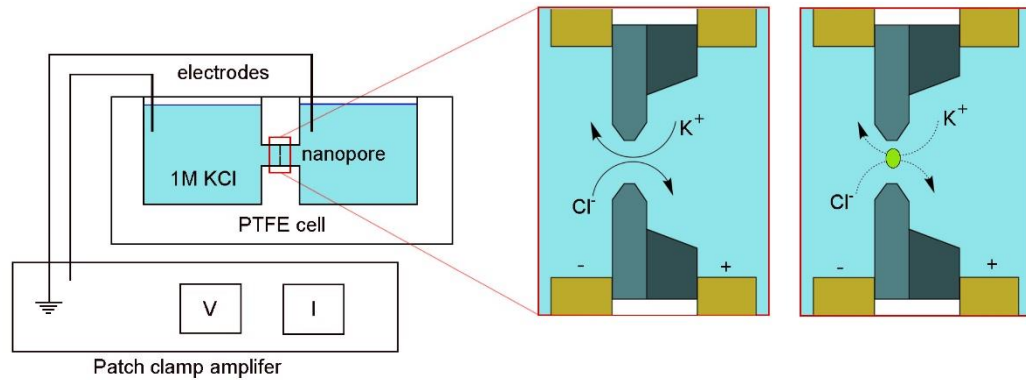


Figure 1.2: Solid-state nanopore experimental setup. Nanopore is mounted in a PTFE cell and connects two electrolyte reservoirs. Ag/AgCl electrodes are immersed in each well to apply a voltage that results in a current corresponding to the pore size.

The first nanopore-based sensors used naturally-occurring nanopores—nanoscale devices mainly secreted by bacteria as exotoxins. They spontaneously insert into lipid bilayers and act as nano-gates for selected molecules to pass through.⁷ While these biological nanopores have atomically highly reproducible composition and structure, the supporting lipid bilayer is not stable for use over an extended time period and the fixed pore size means they have a limited set of molecules they can sense in simple translocation-based schemes. To overcome these difficulties synthetic pores were introduced which are more durable, robust and size tunable.⁸ Synthetic pores are stable over a vast range of pH and temperature conditions, compatible with methods to create pores of tunable sizes to match the analyte properties, amenable to surface chemical modification (with appropriate care) to manipulate the surface chemistry as required.⁹ The need for minimal sample preparation and sample volume furthermore supports the prospect of a commercial sensor.¹⁰ Silicon nitride is a material that had gained lot of attention due to its

immanent robustness, nanofabrication compatibility, mechanical strength, chemical resistance, and dielectric strength.^{11,12} With the intention of extending the sensing capabilities of these novel sensors for sugar structure and property determinations, we proposed to use silicon nitride nanopore sensors, that could enable the detection of as little as one molecule of sugar at a time.⁷ While silicon nitride synthetic pores are size tunable by transmission electron, scanning electron, or He-ion microscopes we fabricated nanopores of desired size in-house by a recently discovered simple process called dielectric break down¹³ and size-analyzed them by a conductance-based method based on a recently developed theoretical framework.¹⁴

DNA translocation through synthetic nanopores has been widely explored and being a charged molecule, its transport via electrophoretic movement is widely studied.¹ In addition to electrophoretic movement, electroosmotic transport also plays a role in nanopore experiments if the nanopore wall is charged.¹⁵

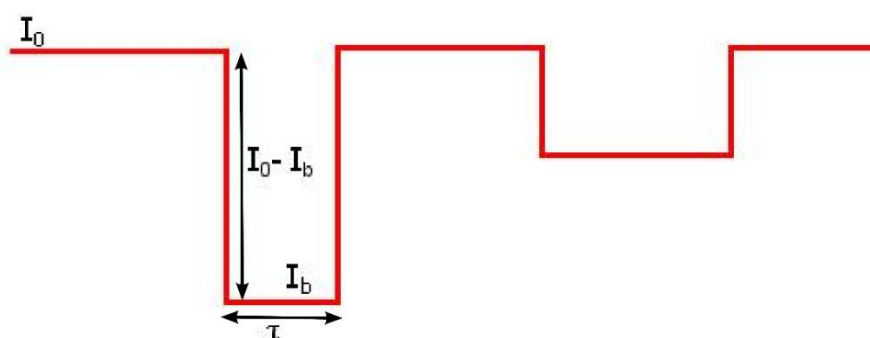


Figure 1.3: Molecular information can be extracted by the characteristic current blockages. In each pore, current blockage magnitude ($I_0 - I_b$) corresponds to the molecule size, dwell time (τ) corresponds to the length of the molecule and frequency of blockages corresponds to concentration of the analyte molecule.

Kasianowicz *et al.* demonstrated polymer translocation through nanopores using polyethylene glycol (PEG) as the test molecule that indicated uncharged molecules

could still be profiled by ion-adsorbed electrophoretic nanopore sensing.¹⁶ Carbohydrates are polymers in biological systems and in theory should act similarly to DNA if charged and similar to PEG if uncharged. We intended establish the fundamentals of using nanopore sensors for single molecule sugar characterization. While no literature exists on using nanopore sensors for polysaccharide structure determination so far, there have been promising initial attempts to use oligosaccharides with nanopores, albeit with protein nanopores and not the solid-state nanopores of interest to us and the nanopore community.^{18,19,20} We explored the possibility of extending the sensing ability of solid-state nanopores to polysaccharides as shown in chapter 2. Further, different strategies to enhance the nanopore sensing platform were studied and described in later chapters as well as adventitious nanostructured platforms discovered during these studies. Enhancing nanopore sensing by surface coating the pore interiors with metal thin films are investigated in chapter 3. Chapter 4 describes a procedure developed for micro/nano patterning, inspired by work in chapter 3. To include a complete study of these nanochannels, chapter 5 and 6 provide a theoretical model to answer complications associated with nanopore size and shape determination.

OPTICAL SENSOR: SURFACE ENHANCED RAMAN SUBSTRATES

Raman spectroscopy is a vibrational spectroscopy technique for sample chemical analysis and vibrational fingerprinting. An energy level diagram for Raman scattering is shown in Figure 1.4. It provides a scope of information on functional groups of a molecule and allows vibrational fingerprinting. With no interference from water vapor, Raman spectroscopy can be used to analyze water-based samples in contrast to its counterpart—IR spectroscopy. Despite this advantage, the Raman scattering process produces generally weak signals, and this reality limited widespread adoption and routine use of the technique. Later, it was discovered that coinage metals (e.g.: gold, silver, copper) could enhance the molecular Raman signal. Based on this concept, surface enhanced Raman spectroscopic (SERS) substrates as shown in Figure 1.5—suitably coinage metal coated devices—were introduced that enhance the molecular Raman signal.²¹ These consist of nanoscale metal structures that can provide higher surface area-to-volume ratio. Moreover, an incident beam of appropriate frequency could generate localized surface plasmon resonance of the metal that enhances the Raman signal of the analytes in the vicinity. Metal nanoparticles in the vicinity to each other could create hot spots that further enhance the Raman signal. Furthermore, nanoparticles of different shapes have been tested to create hot spots, e.g. pillars etc. and to provide higher surface area-to-volume ratio for the analyte binding as well as to provide sharp edges (as in nano-stars, pyramids and cubes) to enhance signal.^{22,23,24,25} There is still some debate over the mechanism of enhancement, and out of the proposed mechanisms, electromagnetic and chemical enhancement mechanisms are widely accepted.²⁶ Electromagnetic enhancement states that excitation of localized surface plasmon resonance (LSPR) occurs when the

collective oscillation of valence electrons of a coinage metal is in resonance with the incident light. This LSPR enhances the electromagnetic field of the analyte molecule, which in theory can reach an enhancement factor of $\sim 10^4 - 10^8$.²⁶ Chemical enhancement occurs when the molecule has lone pairs that can bind to the metal surface. Charge transfer between the bound analyte and the metal enhances the Raman signal in addition to the electromagnetic enhancement. Total SERS enhancement is the product of electromagnetic and chemical enhancement factors and could reach $\sim 10^{10} - 10^{11}$ values.²¹

Over time, many types of SERS substrates have been designed, out of which some have been put in use as effective sensing devices. Yet, analytical performance, manufacturing cost, both personnel and material, and handling difficulties have limited these SERS sensors from being widely used in routine domestic and industrial applications. Here, we proposed to develop and test a general method to create at-will SERS substrates from a variety of base materials exhibiting their own unique material and structural properties and functions. In addition to the metal film being structured, the support substrates themselves were structured, thus introducing additional possibility for enhancement. Furthermore, we are interested in a wide variety of support substrates with the goal of fabrication of substrates with effective and multifunctional capabilities, such as filtration, separation by chromatography, etc. We need robust and flexible SERS substrates suitable for water quality analysis, biofluid analysis for disease detection, contaminant analysis, food analysis, or explosives detection. Our goal was to create SERS substrates that are compatible with low-cost SERS sensing approaches, and that are not as susceptible to damage as some highly specialized substrates can be. Thus, we proposed to target many of the ease-of-operation benefits outlined for nanopore

sensing, but in an optical sensing context. To prepare the substrates we proposed to leverage an electroless plating technique that we developed to gold plate silicon nitride surfaces.

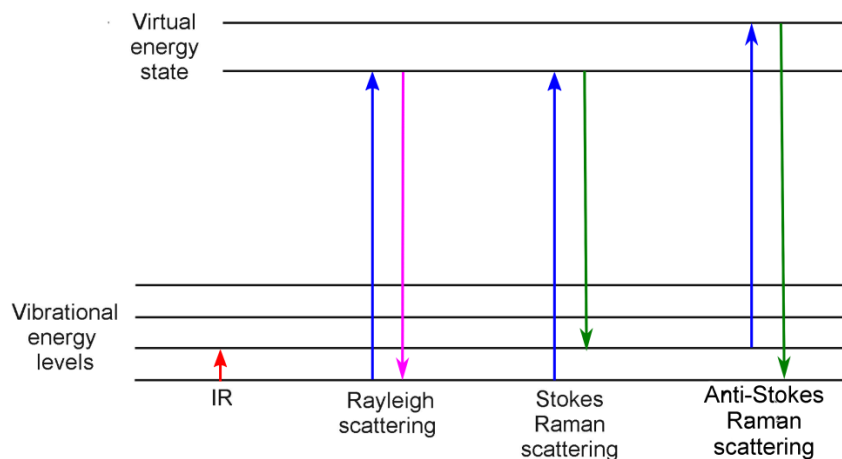


Figure 1.4: Energy level diagram of Raman scattering with an IR absorption transition shown for scaling and context.

The gold plating procedure we developed was tried out on a set of support materials from silicon nitride to paper and nanocellulose judiciously chosen to obtain low cost and disposable SERS sensors with a variety of properties.²⁷ This plating process does not require any voltage application and can be done on insulating material, thus on silicon nitride, silicon, glass or even on paper. It takes only about 3-4 hours to fabricate each substrate using the electroless plating process we developed, and shown in Scheme 1 in appendix 6 (chapter 7 supporting information). This strategy has been first demonstrated using silicon nitride supports and yields enhanced Raman spectra as shown in chapter 4.²⁷

Depending on the support substrate the resultant metal film nano-structure may be different and will provide the opportunity to chemically tune the metal film structure to obtain higher Raman enhancement factors. Paper based SERS devices have the additional advantages of ease of handling with respect to damage to the

substrate and ease of transport allowing on-site use even in resource-limited settings. Disposal can be done simply through burning. Such inexpensive SERS substrates thus have the potential to be used as low cost but reliable sensors for applications from water quality analysis to biomedical analysis. Fabrication and evaluation of a series of Raman substrates are demonstrated in detail under chapter 7. Metal film structure and composition of all the substrates were analyzed by scanning electron microscopy (SEM) and X-ray photoelectron spectroscopy (XPS), respectively. Obtained raw SERS spectra will be processed by custom-written Mathematica programs to baseline-correct the spectra. The relative performance of each substrate will be evaluated using calibration curves, and limit of detection (LOD) and enhancement factor (EF) calculations. For demonstration purposes, we would use 4-nitrobenzenethiol (NBT, also known as 4-nitrothiophenol) as the analyte to study the enhancing of its SERS signal by our series of SERS substrates.

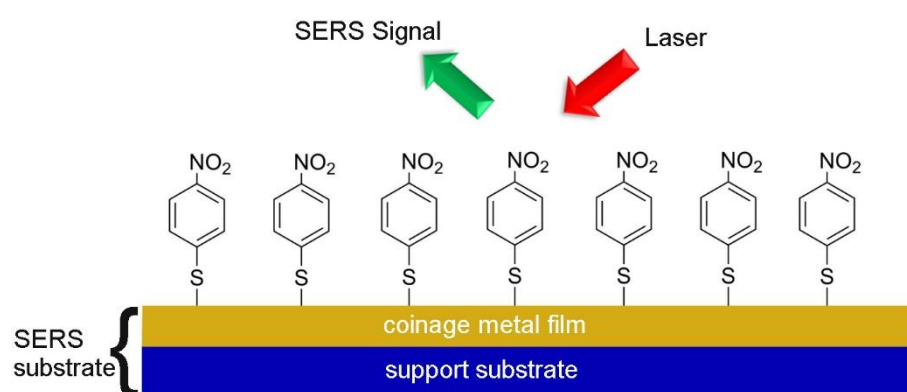


Figure 1.5: Illustration of a coinage metal film on a support as a SERS substrate.

ABBREVIATION

SERS: surface enhanced Raman spectroscopy

LSPR: localized surface plasmon resonance

PEG: polyethylene glycol

NMR: Nuclear Magnetic Resonance

IR: Infrared Spectroscopy

MALDI-MS: Matrix Assisted Laser Desorption Ionization- Mass Spectroscopy

ESI-MS: Electron Spray Ionization Mass Spectroscopy

UV-Vis: Ultraviolet-Visible Spectroscopy

PTFE: Polytetrafluoroethylene

LPCVD: Low Pressure Chemical Vapor Deposition

SEM: Scanning Electron Microscopy

XPS: X-ray Photoelectron Spectroscopy

LITERATURE CITED

1. Single, P., Molecule, D. N. A., Using, T. & Nanopores, F. Probing Single Dna Molecule Transport Using. **4**, 2293–2298 (2014).
2. Oukhaled, A., Bacri, L., Pastoriza-Gallego, M., Betton, J. M. & Pelta, J. Sensing proteins through nanopores: Fundamental to applications. *ACS Chem. Biol.* **7**, 1935–1949 (2012).
3. Howorka, S. & Siwy, Z. Nanopore analytics: sensing of single molecules. *Chem. Soc. Rev.* **38**, 2360–2384 (2009).
4. Bishop, J. R., Schuksz, M. & Esko, J. D. Heparan sulphate proteoglycans fine-tune mammalian physiology. *Nature* **446**, 1030–1037 (2007).
5. Dube, D. H. & Bertozzi, C. R. Glycans in cancer and inflammation--potential for therapeutics and diagnostics. *Nat. Rev. Drug Discov.* **4**, 477–488 (2005).
6. Williams, S. J. & Davies, G. J. Protein-carbohydrate interactions: Learning lessons from nature. *Trends Biotechnol.* **19**, 356–362 (2001).
7. Branton, D. *et al.* The potential and challenges of nanopore sequencing. *Nat. Biotechnol.* **26**, 1146–53 (2008).
8. Wanunu, M., Sutin, J., McNally, B., Chow, A. & Meller, A. DNA translocation governed by interactions with solid-state nanopores. *Biophys. J.* **95**, 4716–25 (2008).
9. Bandara, Y. M. N. D. Y., Karawdeniya, B. I., Whelan, J. C., Ginsberg, L. D. S. & Dwyer, J. R. Solution-Based Photo-Patterned Gold Film Formation on Silicon Nitride. 6–11 (2016). doi:10.1021/acsami.6b12720
10. Bayley, H. & Martin, C. R. Resistive-pulse sensing - from microbes to molecules. *Chem. Rev.* **100**, 2575–2594 (2000).
11. Ciarlo, D. R. Silicon nitride thin windows for biomedical microdevices. *Biomed. Microdevices* **4**, 63–68 (2002).
12. Fallis, a. . Etch Rates for Micromachining Processing. *J. Chem. Inf. Model.* **53**, 1689–1699 (2013).
13. Kwok, H., Briggs, K. & Tabard-Cossa, V. Nanopore fabrication by controlled dielectric breakdown. *PLoS One* **9**, (2014).
14. Bandara, Y. M. N. D. Y., Karawdeniya, B. I. & Dwyer, J. R. Real-Time Profiling of Solid-State Nanopores during Solution-Phase Nanofabrication. *ACS Appl. Mater. Interfaces* **8**, 30583–30589 (2016).
15. Mathwig, K., Albrecht, T., Goluch, E. D. & Rassaei, L. Challenges of biomolecular detection at the nanoscale: Nanopores and microelectrodes. *Anal. Chem.* **87**, 5470–5475 (2015).
16. Reiner, J. E., Kasianowicz, J. J., Nablo, B. J. & Robertson, J. W. F. Theory for polymer analysis using nanopore-based single-molecule mass spectrometry. **107**, 6–11 (2010).

17. Fertah, M., Belfkira, A., Dahmane, E. montassir, Taourirte, M. & Brouillette, F. Extraction and characterization of sodium alginate from Moroccan *Laminaria digitata* brown seaweed. *Arab. J. Chem.* (2014). doi:10.1016/j.arabjc.2014.05.003
18. Bacri, L. *et al.* Discrimination of neutral oligosaccharides through a nanopore. *Biochem. Biophys. Res. Commun.* **412**, 561–564 (2011).
19. Fennouri, A. *et al.* Single molecule detection of glycosaminoglycan hyaluronic acid oligosaccharides and depolymerization enzyme activity using a protein nanopore. *ACS Nano* **6**, 9672–9678 (2012).
20. A. Fennouri M. Pastoriza-Gallego, L. Auvray, J. Pelta, L. Bacri, R. D. Kinetics of Enzymatic Degradation of High Molecular Weight Polysaccharides through a Nanopore: Experiments and Data-Modeling. *Anal. Chem.* **85**, 8488–8492 (2013).
21. Sharma, B., Frontiera, R. R., Henry, A.-I., Ringe, E. & Van Duyne, R. P. SERS: Materials, applications, and the future. *Mater. Today* **15**, 16–25 (2012).
22. Wu, K. *et al.* Wafer-Scale Leaning Silver Nanopillars for Molecular Detection at Ultra-Low Concentrations. *J. Phys. Chem. C* **119**, 2053–2062 (2015).
23. Schmidt, M. S., Hübner, J. & Boisen, A. Large area fabrication of leaning silicon nanopillars for Surface Enhanced Raman Spectroscopy. *Adv. Mater.* **24**, 11–18 (2012).
24. Rotz, M. W. *et al.* High Relaxivity Gd (III) À DNA Gold Nanostars : Investigation of Shape Effects on Proton Relaxation. 3385–3396 (2015). doi:10.1021/nn5070953
25. Lee, S. Y. *et al.* Dispersion in the SERS enhancement with silver nanocube dimers. *ACS Nano* **4**, 5763–5772 (2010).
26. Stiles, P. L., Dieringer, J. a, Shah, N. C. & Van Duyne, R. P. Surface-enhanced Raman spectroscopy. *Annu. Rev. Anal. Chem. (Palo Alto. Calif).* **1**, 601–26 (2008).
27. Whelan, J. C. *et al.* Electroless plating of thin gold films directly onto silicon nitride thin films and into micropores. *ACS Appl. Mater. Interfaces* **6**, 10952–10957 (2014).

CHAPTER 2: PREFACE

TASTY, THERAPEUTIC, OR TOXIC? GAUGING THIN-FILM SOLID- STATE NANOPORES FOR POLYSACCHARIDE SENSING

Buddini Iroshika Karawdeniya, Y.M. Nuwan D.Y. Bandara, Jonathan W. Nichols,
Robert B. Chevalier, and Jason R. Dwyer*

Department of Chemistry, University of Rhode Island, 140 Flagg Road, Kingston,
02881, USA

This manuscript is formatted for publication according to Nature Communications
standards and currently under review.

CHAPTER 2

TASTY, THERAPEUTIC, OR TOXIC? GAUGING THIN-FILM SOLID-STATE NANOPORES FOR POLYSACCHARIDE SENSING

Buddini Iroshika Karawdeniya, Y.M. Nuwan D.Y. Bandara, Jonathan W. Nichols, Robert B. Chevalier, and Jason R. Dwyer*

Department of Chemistry, University of Rhode Island, 140 Flagg Road, Kingston, 02881, USA.

*jason_dwyer@uri.edu

ABSTRACT

Polysaccharides have key roles in a multitude of biological functions, and they can be harnessed for therapeutic roles, with the clinically ubiquitous anticoagulant heparin being a standout example. Their complexity—*e.g.* >100 naturally occurring monosaccharides with variety in linkage and branching structure—significantly complicates their analysis in comparison to other biopolymers such as DNA and proteins. More, and improved, analysis tools have been called for, and we demonstrate that solid-state silicon nitride nanopore sensors and tuned sensing conditions can be used to reliably detect native polysaccharides and enzymatic digestion products, to differentiate between different polysaccharides in straightforward assays, to provide new experimental insights into nanopore electrokinetics, and to uncover polysaccharide properties. Nanopore sensing allowed us to easily differentiate between a clinical heparin sample and one spiked with the contaminant that caused deaths in 2008 when its presence went undetected by conventional assays. The work reported here lays the foundation to further

explore polysaccharide characterization and develop assays using thin-film solid-state nanopore sensors.

Oligo- and polysaccharides are ubiquitous in nature, with a broad spectrum of roles that includes energy-storage and provision (including as a foodstuff), structural building block (e.g. cellulose), therapeutic function (e.g. the anticoagulant heparin), and a vital part in biological recognition processes.¹⁻¹¹ Conventional chemical analysis tools are frequently challenged by the daunting complexity of polysaccharide analysis:^{12, 13} identification of monomer composition (~120 naturally occurring monomers!) and sequence, monomer linkage types, stereochemistry, polymer length, and degree of polymer branching.¹³ These challenges were tragically driven home in 2008 when undetected contamination of the common anticoagulant heparin by a structurally similar adulterant, oversulfated chondroitin sulfate (OSCS), resulted in profoundly adverse clinical consequences in the United States, including ~100 deaths.¹⁴⁻¹⁹ Glycan samples can be challenged by heterogeneity and low abundance in addition to chemical and structural diversity, so while new analysis tools have been broadly called for,^{12, 13, 20} single-molecule-sensitive methods are a particularly compelling goal for glycomics—more so given the absence of sample amplification techniques analogous to PCR for DNA sequencing²¹. Nanopore single-molecule methods have emerged as a powerful tool for characterizing DNA and proteins including aspects of sequence, structure, and interactions.²²⁻²⁸ Monomer-resolved length determinations of more prosaic polyethylene glycol samples further buttress the potential of suitably configured nanopore assays for the analysis of polymers with biological utility.²⁹ The simplest implementation for nanopore measurements places the nanopore—a <100 nm-long nanofluidic channel through an insulating membrane—between two

electrolyte solutions (Figure 2.1). Ion passage through the nanopore in response to a voltage applied across the pore gives the baseline “open pore” current, i_0 ; passage of a molecule into, across, or through the nanopore disrupts this ion flow to give a blocked-pore current, i_b . A discernible current perturbation reveals the presence of an analyte, and the sign, magnitude, and temporal structure of i_b depend strongly on size and shape of the analyte—and of the nanopore—and on the applied voltage and bulk and interfacial charge distributions. It thus provides insight into analyte presence, identity, and properties, including interactions between the analyte and pore interior or surface.²⁹⁻³² Analysis of the resistive-pulse characteristics of a sample offers the potential to glean molecular-level insights, but the i_b characteristics can also be used more simply as benchmarks in quality assurance assays where atypical i_b signal sample impurities.

Much groundwork must be laid, including proof-of-principle experiments, if nanopore methods are to emerge as a tool for glycan profiling—and by extension as a tool for –omics writ-large (spanning genomics, proteomics, and glycomics). Protein nanopores, polymer, and glass-supported nanopores have been used to detect sugar-pore binding, polysaccharides, and enzyme-digested oligosaccharides.³³⁻⁴² While solid-state nanopores in thin (~10 nm) membranes have been often portrayed as the preeminent nanopore platform, their use to profile classes of molecules beyond DNA and proteins is in its infancy. These nanopores can be size-tuned⁴³ to match analyte dimensions (especially relevant for branched polysaccharides), and when fabricated from conventional nanofabrication materials such as silicon nitride (SiN_x),^{44, 45} offer resistance to chemical and mechanical insult alongside low barriers to large-scale manufacturing and device integration. The potential for integration of additional instrumentation components, such as

control and readout electrodes, around the thin-film nanopore core, is especially compelling.^{28, 44, 45} Recent (nanopore-free) work on recognition electron tunneling measurements on polysaccharides, for example, has reaffirmed the importance of a nanopore development path that values augmented nanopore sensing capabilities.⁴⁶ A key question concerning the use of SiN_x nanopores for polysaccharide sensing is whether this fabrication material is compatible with sensing glycans. The often challenging surface chemistry of SiN_x (giving rise to a complex surface charge distribution)^{44, 45, 47} may lead to analyte-pore interactions that hinder or prevent its use. Variability in polysaccharide electrokinetic mobility arising from differences in molecular structures may exacerbate the effect of these interactions. These issues become particularly important when analyte translocation through a constricted pore is required, such as in transverse electron tunneling measurements.^{28, 46}

The aims of the present work were threefold: (1) to introduce and test the feasibility of SiN_x nanopores for sensing polysaccharides; (2) to explore the preliminary performance of this class of nanopores in this implementation; and (3) to gauge the prospects of a clinically relevant assay to detect a toxic impurity in the anticoagulant heparin. The broader implications of the successful use of SiN_x—a readily nanofabrication-compatible material—to form the nanopores would be to conceivably smooth the path to large-scale production and to provide a platform amenable to modification for nanopore sensing configurations beyond resistive pulse sensing. We chose a set of polysaccharides with varied compositions to both gauge performance and challenge the SiN_x nanopores. Naturally occurring sodium alginate, with applications in biomedical and food industries, presents an overall negative, but unexceptional, formal charge in neutral pH aqueous solutions. We

used samples from two different suppliers—*A1* (Alfa Aesar; $M_n \sim 74$ kDa based on viscosity measurements) and *A2* (FMC Corporation; $M_n \sim 18$ kDa based on viscosity measurements)—to explore the sourcing variability for a sample extracted from seaweed.⁴⁸ This variability can be as prosaic as molecular weight to more enticing changes in the relative abundances of alginate’s constituent mannuronate (M) and guluronate (G) residues.⁴⁸ In contrast to alginate, heparin, the prevalent anticoagulant drug, is the most highly negative charge-dense biological molecule known.⁴⁹ This exceptional charge density couples with the demonstrated difficulty, by other methods, of detecting the negatively charged oversulfated chondroitin sulfate (OSCS; contaminant molecular weight ~ 17 kDa⁵⁰) in a heparin sample¹⁴⁻¹⁷ to make the analysis of heparin (~ 16 kDa) and OSCS by nanopore a compelling experimental test with clinical relevance.

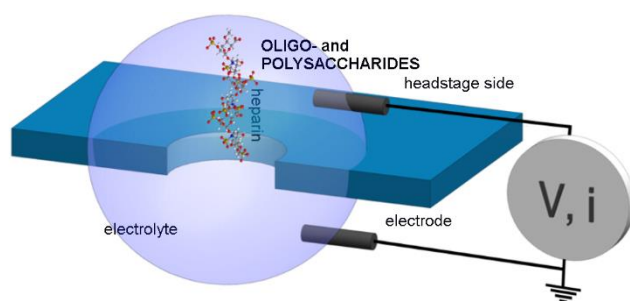


Figure 2.1: Schematic of the nanopore setup. Analyte was added to the headstage side (“cis-” side, according to nanopore convention) unless otherwise noted, and applied voltages were referenced to the ground electrode (“trans-” side) on the other side.

RESULTS

Introduction of anionic alginate *A1* ($M_n \sim 74$ kDa) into the headstage sample well failed to generate detectable transient current changes when a negative headstage voltage (the polarity consistent with purely electrophoretic motion for an anionic analyte) was applied with the analyte in the same well (Figure 2.1). Application of

a positive potential, instead, generated transient current changes (here denoted “events”) that could be readily differentiated from the open current noise with ~60:1 event-to-noise frequency compared to analyte-free scans. Figure 2.2 shows a representative time trace of *AI*-induced events, with a characteristic event magnified. The frequency of discrete current blockages associated with the addition of *AI* showed a linear increase with analyte concentration (Supplementary Figure 2.1), so that regardless of mechanism, with appropriate measurement conditions, the event frequency can be used to determine the analyte concentration. The mechanism of *AI*-induced signal generation was investigated in a series of experiments. Using a setup (Supplementary Figure 2.2) that physically separated electrodes and nanopore, events were only detected when *AI* was injected into the well proximal to the nanopore, thus supporting a signal generation mechanism involving interaction with the nanopore and not with the electrodes. This result did not, however, distinguish between passage-free collision with the nanopore opening (“bumping” or “blocking”) or translocation through the pore.³² Either mechanism (including extending the idea of “bumping” or “blocking” to allow for transient interactions of the analyte with the pore mouth), though, has the potential to deliver analytically useful sensing performance. Low analyte concentrations challenge the direct investigation of polysaccharide translocation through small, single nanopores. In one experiment to investigate this, a solution of *AI* was added to the headstage side of a ~22 nm-diameter nanopore and was left overnight with a +200 mV applied voltage. The initially analyte-free contents of the ground-stage side were then transferred to the headstage side of a fresh ~17 nm-diameter pore, and an appreciable number of *AI*-characteristic events (182 in 1 h) were detected again at +200 mV. Acid digestion was used as a signal generation and

amplification technique (complete details in the Supplementary Information) to convert *AI* polymers to many smaller fragment-derived species absorbing at ~ 270 nm.^{51, 52} This spectrophotometric assay (Supplementary Figure 2.3) was used to confirm translocation of polysaccharide through a ~ 9 nm SiN_x nanopore.

The analyte-induced translocation blockage current, i_b , is expected to be determined by the properties of the analyte and its size relative to the nanopore, among other experimental factors (including interfacial phenomena).^{30, 32} For each individual current blockage, we calculated the blockage duration, τ , and the fractional blockage current magnitude, $f_b = \langle i_b \rangle / \langle i_0 \rangle$, where $\langle \dots \rangle$ denotes a time-average, and i_0 is the current through the pore when unobstructed by analyte. Plots of number of events as a function of τ and f_b (Figure 2.3) provide an overarching summary of the total current trace. Given detectable differences as a function of analyte, such plots and other representations have the potential to function as analyte fingerprints in quality assurance assays. Fingerprints for *AI* are shown in Figure 2.3, acquired in 1 M KCl, pH ~ 7 solutions using a +200 mV applied voltage. Supplementary Figures 2.4 and 5 provide alternative presentations of the experimental measurements. The (most frequent) f_b increased in magnitude with increasing nanopore radius, r_{pore} (that is, the relative magnitude of the current perturbations due to the analyte were reduced). This parallels the behavior observed in studies of DNA translocation that could be described using a simple volume-exclusion framework: $r_{\text{analyte}}^2 / r_{\text{pore}}^2 = 1 - f_b$.

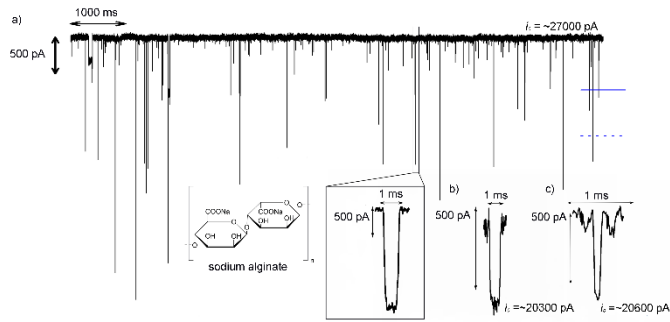


Figure 2.2: Representative nanopore current trace and events from sodium alginate samples from two different sources. a) A representative segment of an *A1*-induced current trace using a ~ 22 nm-diameter pore; the solid blue line marks the most frequent event level, $\langle i_b \rangle$, and the blue dashed line is its mean across all events. The magnified current event is from the same trace. b) *A2*- and c) enzyme-digested-*A2*-associated single events through a ~ 22 nm-diameter pore. All currents were measured in response to a 200 mV applied voltage.

. For example, reducing the ion concentration from 1 to 0.1 M KCl increases the Debye layer thickness changing the electrostatic size of the pore with consequences for electrokinetic phenomena, and electroosmosis especially. Comparing Figures 2.3a and 3e, this change of concentration did not affect the voltage polarity needed to generate events, but decreased the f_b for the same experimental configuration, and appreciably lengthened the (most frequent) blockage duration. More profoundly, the 10-fold salt concentration decrease reduced the frequency of events 6-fold in the same size ~ 18 nm-diameter pore. We found, and exploited in a more general context for the sensing of heparin and OSCS (below), that such a simple change of electrolyte concentration is a powerful parameter for tuning our ability to sense polysaccharides. Changing the electrolyte pH offers a similar parameter for tuning the sensing performance of nanopores with ionizable surface groups. The surface charge of SiN_x nanopores can be tuned from negative through its isoelectric point ($\sim 4.3 \pm 0.3$) to positive,^{44, 53} and the consequence of this pH change is seen in Supplementary Figure 2.6: the voltage polarity for signal generation is opposite at pH 3 and 5 (and opposite to the

electrophoretic direction for all pH values), and the event frequency is at its minimum nearest the isoelectric point and increases with increase and decrease in pH from this point.

After the initial exploratory and proof-of-principle experiments using *A1*, we turned to the second sodium alginate sample, *A2*, obtained from a separate supplier. In general, the interplay between analyte charge density, monomer chemical nature and polymer linkages, and electrolyte composition, is expected to influence nanopore sensing. Experiments showing the polarity-dependence of event occurrence, and its frequency, as a function of pH showed the same qualitative behavior as for *A1* in Supplementary Figure 2.6, but with lower event frequencies overall. Both alginate samples were readily digested by alginate lyase (Supplementary Figure 2.3),⁵⁴ but infrared spectroscopy showed that *A2* contained a dramatically greater proportion of carboxylate groups than *A1* (Supplementary Figure 2.7), so that the overall charge density of this molecule was expected to be higher than *A1*. Further analysis was consistent with alginate *A1* having a ratio of guluronic (G) to mannuronic (M) residues exceeding that of *A2*, with values from IR spectroscopy of ~63%G/37%M and ~57%G/43%M, respectively.⁴⁸ Nanopore profiling of *A2* showed differences compared to *A1*. Using the same electrolyte for *A2* as for *A1*, measurements generated a ~7-fold lower event frequency with longer durations for *A2* compared to *A1*, in spite of at the 75-fold higher *A2* concentrations required for reasonable measurement times. Enzymatic digestion of *A2* produced events at a higher frequency than for undigested *A2*, but still at lower frequency than for *A1*. The events for the digested sample of *A2* were ten-fold shorter-lived than for the *A2* polymer, but not appreciably different in terms of blockage depth (Figure 2.3).

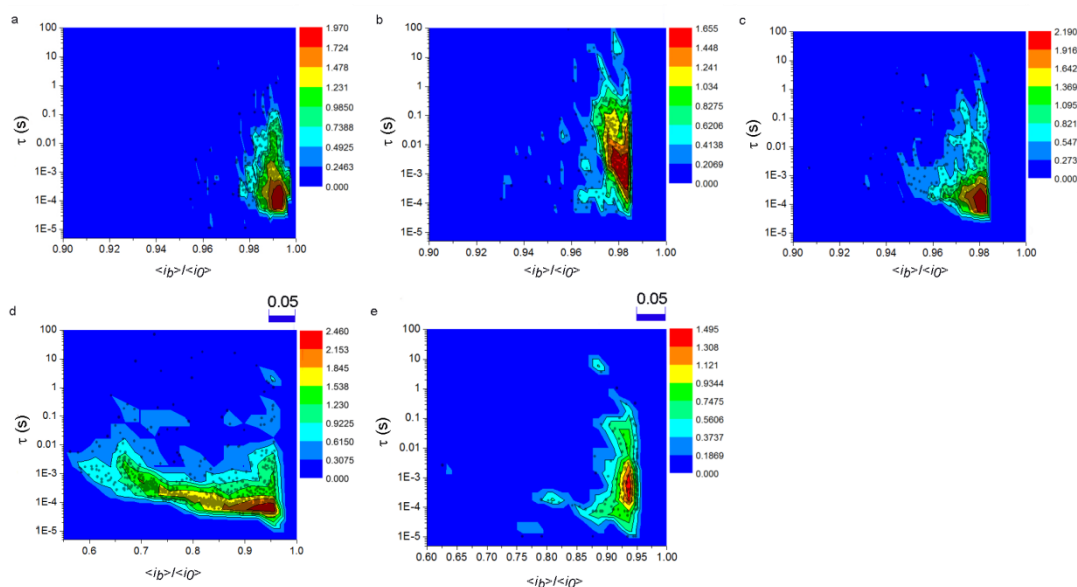


Figure 2.3: Combination heat map-scatter plots of alginate-induced events. Event counts (plotted as \log_{10} on the colour axis) of a) 4 μL 0.2% (w/v) *AI* using a ~ 19 nm diameter pore (~ 0.321 events/s), b) 20 μL of 3% (w/v) *A2* using a ~ 22 nm (~ 0.046 events/s) and c) 20 μL of 10-minute enzyme digested 3% (w/v) *A2* using a ~ 23 nm diameter pore (~ 0.112 events/s), all in pH ~ 7 buffered 1 M KCl. The experiment in (a) was repeated d) using a ~ 5 nm nanopore (~ 0.403 events/s), and e) an ~ 18 nm-diameter pore, but in 0.1 M KCl (vs. 1M KCl in (a)) electrolyte buffered at pH ~ 7 (~ 0.0527 events/s).

These initial survey experiments showed measurement outcomes with strong sensitivity to analyte identity, with the number of anionic carboxylate moieties being a compelling differentiator between *AI* and *A2*. We then turned to the pressing specific challenge of (anionic) heparin sensing and (anionic) OSCS impurity detection. The first change, from the earlier work, was that the signal generation voltage polarity now corresponded with the conventional electrophoretic direction for an anionic species. Acid digestion experiments akin to those in Supplementary Figure 2.3 confirmed that heparin could translocate through the pore in response to an applied voltage. As with *AI*, heparin could be detected in 1 M KCl electrolyte, but the heparin event blockage magnitude and event frequency were both greater in 4 M KCl, and so measurements were performed at this higher salt concentration (see Supplementary Figure 2.8 for

representative events and a heat map). Plots of event frequency versus heparin concentration were linear (Figure 2.4), with a limit of detection of 0.379 USP heparin units/mL (in a 500 μ L well). In comparison, clinical dosage levels of $\sim 10^4$ units/day using $\sim 10^3$ units/mL stock solutions are not uncommon. Heparin and alginate fingerprints differed in appearance from each other, but also through the profoundly different measurement configuration—opposite applied voltage polarity and fourfold higher electrolyte concentration for heparin—used to acquire them. We were more keenly interested, though, in whether an OSCS impurity in heparin could be detected. We performed measurements on unadulterated USP samples of either heparin or OSCS under identical experimental conditions. On the level of individual events, heparin and OSCS differed in their apparent interaction with the nanopore, with OSCS having a greater propensity to permanently block the pore unless a ~ 1.3 V (“zap”) pulse—a common approach leveraging the electrokinetic basis of analyte motion—was quickly applied manually when indications suggesting an impending permanent blockage arose. In addition, events associated with the heparin and OSCS samples differed appreciably in the current fluctuations during individual current blockages: OSCS current blockages exhibited $\sim 2\text{--}3\times$ greater current noise, $\sigma(f_b)$, than heparin-induced events. Overall, in spite of considerable overlap in the most frequent event f_b and τ , the distribution of event characteristics revealed a key difference between heparin and OSCS samples (Figure 2.5 and Supplementary Figure 2.9). Namely, events measured using heparin samples exhibited a longer duration tail in the total event duration distribution, while events measured using OSCS samples exhibited a longer tail in f_b . Measurements of mixtures of heparin and OSCS (16 ppm each) yielded event distributions showing both tails, consistent with the presence of both the heparin

therapeutic and its contaminant. We developed an automatic thresholding procedure based on event distribution statistics in f_b and τ (details in the Supplementary Information) to collapse the event distribution fingerprints into recognition flags denoting the presence or absence of each component. In brief, OSCS was declared present when events occurred with $f_{b,\text{sample}} \lesssim \text{mode}(f_{b,\text{USP heparin}}^{\text{binned}}) - 3\sigma(f_{b,\text{USP heparin}}^{\text{binned}})$, and heparin was declared present when events occurred with $\tau_{\text{sample}} \gtrsim \text{mode}((\log_{10} \tau_{\text{USP OSCS}})^{\text{binned}}) - 3\sigma((\log_{10} \tau_{\text{USP OSCS}})^{\text{binned}})$. Figure 2.5 shows the correct recognition of USP heparin, USP OSCS, and a mixture of both, across four trials using nanopores of slightly different sizes. The OSCS contaminant levels detected here were fourfold lower (without efforts to explore a lower bound) than the OSCS detection limit reported in the work that examined and quantified the contaminant in suspect heparin lots.¹⁸

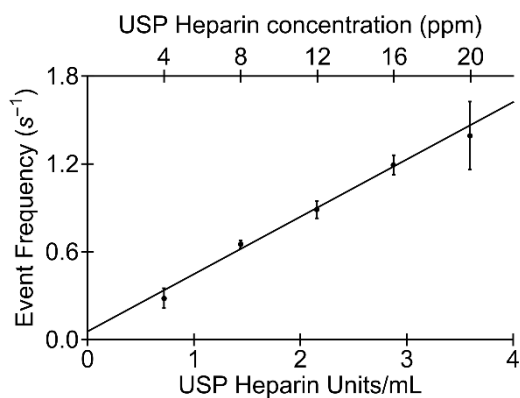


Figure 2.4: Heparin calibration curve. Three trials were performed, with at least 500 events per run extracted from 900 s-long measurements in a ~ 9 nm pore at -200 mV applied voltage after consecutive addition of $1 \mu\text{L}$ aliquots to the head-stage side of the same nanopore. Error bars are the standard deviation for the three trials.

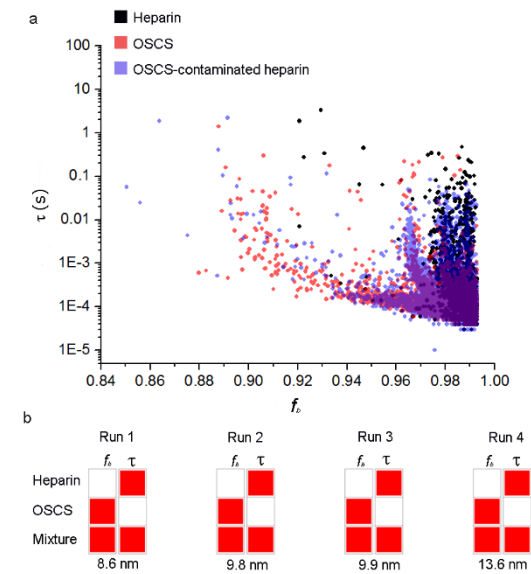


Figure 2.5: Nanopore resistive-pulse analysis of heparin, OSCS, and their mixture. a) Superimposed scatter plots of 4 μ L heparin, OSCS and OSCS-contaminated heparin added to 4 M potassium chloride at -200 mV and measured using a \sim 14 nm pore. The colours in the legend correspond to the listed sample and are blended (using transparency) in the plot where events from different samples overlap. b) Recognition flags of heparin, OSCS and their mixture from four independent trials accurately identify the presence of the OSCS aliquot in the mixture.

DISCUSSION

We demonstrated the feasibility of using SiN_x nanopores to characterize glycans exhibiting a variety of chemical compositions, including a prevalent therapeutic, heparin. The extremely high charge density carried by heparin poses a particular challenge to a nanoscale sensor element that can, itself, be charged. More generally, unwanted interactions between analyte and nanopore—and the ease and feasibility of ameliorative steps—can imperil nanopore-based experiments: that none of the diverse polysaccharides considered here catastrophically clogged the nanopore—even when subjected to the stringent test of translocation through the pore—was salutary.⁴⁷ Indeed, nanopore sensing was successful over a number of electrolyte concentration ranges, from 0.1 to 4 M KCl, for which shielding of the charged nanopore surface would be quite different in degree. With translocation

possible through SiN_x nanopores, even with their charged surface, a rich set of nanopore-based sensing configurations should be within reach. In this work, we used a straightforward resistive-pulse sensing paradigm to readily detect and differentiate between different polysaccharides, including enzymatic digestion products and two separate alginate samples differing in relative monomer composition. We used voltage polarity and electrolyte composition alongside the distribution of events as a function of f_b and τ to construct fingerprints and recognition flags characteristic of each sample. Linear calibration curves show that these measurements easily support concentration determinations in addition to analyte recognition.

From a fundamental perspective, nanopores can be a powerful tool for exploring molecular, interfacial, and intermolecular phenomena, often arising from only simple changes of experimental conditions. Electrolyte-dependent interfacial interactions—at nanopore and molecule surfaces—are complex, and treatments of widely varying levels of sophistication have emerged from decades of experimental and theoretical studies of the canonical nanopore-DNA system, in particular.³² For example, changes of electrolyte concentration have been observed to reverse the sign of the current perturbation in DNA translocations through solid-state nanopores, and to decrease dextran sulfate blockage frequencies while increasing their durations using ~1.3 nm-diameter pores where the Debye length was comparable to the pore dimensions.^{42, 55} With the larger pores used here, overlapping Debye layers would not be expected in 0.1 M KCl solutions, leaving three expected principal effects of lowering the electrolyte concentration from 1 M KCl: a lowering of the potential across the pore and thus of the overall electrophoretic force on an analyte near the pore; a reduction in the available

number of bulk ions displaced by the analyte volume; and a change in the ion distribution around charged interfaces—the nanopore and analyte surfaces—that influences the nanopore signal through a complex overall mechanism within a given experimental configuration. Blockage magnitudes measured here in the more conventional 1 M KCl would be consistent with, in a simple volume exclusion sense ($r_{\text{analyte}}^2 / r_{\text{pore}}^2 = 1 - f_b$), translocation of linearized polysaccharides. Deeper blockages would be expected from the polysaccharides here with hydrodynamic radii on par with the nanopore diameters. Polysaccharide translocation was independently confirmed and signals were generated only when the analytes had access to the nanopores, so these events either arose from analyte interactions with the pore mouth rather than from complete translocation, or the blockage magnitude analysis must include additional factors such as charge density carried by the analyte, itself, and mobile charge at the analyte-solution and solution-nanopore interfaces.^{55, 56} The effects of these and more complex interfacial phenomena emerged in one of the more startling observations in this work: that the voltage polarity for signal generation with both alginate samples was opposite to that expected for electrophoretic motion of an anionic polymer, whereas for heparin the voltage polarity was consistent with electrophoresis.

In addition, when comparing the two alginates, the more charge-rich *A2* was detected at a lower event frequency than *A1*. Nanopore-based studies with polyethylene glycol polymers point to a change of effective analyte charge by sorption of electrolyte ions (K^+ for those studies) with the resultant analyte motion then being electrophoretic for the voltage polarity and the sign of the sorbed charge.²⁹ The results of Supplementary Figure 2.6, however, point to pH-dependent changes in the voltage polarity required for sensing alginates, with the polarity

having opposite signs on either side of the isoelectric point of SiN_x . Mirroring this change in the voltage polarity is the SiN_x surface charge that is positive at lower pH and negative at higher pH. This change in surface charge sign causes a reversal in the direction of electroosmotic motion for a fixed voltage polarity (and thus fixed electrophoretic direction).^{44, 45} The apparent mobility of an analyte in response to electrolyte flow through the surface-charged nanochannel is the sum of its electrophoretic and electroosmotic mobilities. Changes of solution pH can then tune the apparent analyte mobility and even overall direction of analyte motion. Changes of solution pH can also affect the charge density and sign of analytes (and thus the voltage polarity required for electrophoresis in a given direction) containing at least one acidic or basic functional group as determined by the balance of acid-base equilibria (determined by functional group abundance and pK_a). Given the acidic functional groups in the analytes here, the changes in nanopore surface chemistry should dominate the effective mobility and its voltage polarity dependence. The event frequency and voltage polarity behaviors are consistent with the distinct physicochemical properties of each analyte in a signal generation method in which both electrophoresis and electroosmosis occur simultaneously. Alginate *A1* has the lowest charge density, and thus its electrophoretic response is dominated by electroosmosis with the electrophoretic and electroosmotic driving forces being in opposition in the negatively charged SiN_x pores at pH ~ 7 . Alginate *A2* is more negatively charged and so one would anticipate a stronger electrophoretic driving force; the direction of signal generation is still consistent with electroosmosis. The lower event frequency compared to *A1* can be understood as arising from opposing electrophoretic and electroosmotic driving forces, but with the electrophoretic force on *A2* being

greater than on *A1*. More detailed exploration of the differences between *A1* and *A2* must also contend with their different molecular weights and their different chain flexibilities arising from their different M/G ratios. In the case of heparin, the charge density is sufficiently high so that events are detected using a voltage polarity that would drive the anionic polymer towards the nanopore. Experimental investigations including and beyond the ones presented here, exploring the underpinnings of the nanopore-generated signal using (polysaccharide) biopolymers with greater chemical and structural complexity than the canonical nanopore test molecule, DNA, or than homopolymers such as polyethylene glycol, should also provide fertile ground for high-level simulations. Interfacial effects will require additional study in the context of polysaccharides, but hold possibilities for tuning sensing selectivity and sensitivity. Indeed, explicit consideration of sensing conditions—including nanopore size, electrolyte composition, and voltage polarity—already augments the ability to compare nanopore molecular fingerprints as shown in Figure 2.3.

The failure in 2008 to detect an OSCS contaminant in clinical heparin samples had previously led to patient morbidity and mortality,¹⁴⁻¹⁸ so that our ability to use a simple nanopore-based assay to quantify heparin levels and detect OSCS at clinically meaningful contamination levels, is itself significant. In a broader sense, we expect that these initial results exploring polysaccharide structure can, by analogy with earlier nanopore DNA and protein sensing supporting genomics and proteomics, spotlight the potential of using nanopores as a tool for glycomics. The demonstration of polysaccharide translocation through nanofabrication-compatible SiN_x nanopores portends the development of more sophisticated sensing schemes as seen in the use of nanopores for genomics.

Similarly, the successful use of chemical tuning—of electrolyte composition and by enzyme addition—to alter the nanopore signal generated by diverse polysaccharides suggests that nanopore glycomics might borrow from and extend upon similar approaches developed for nanopore genomics. There is an ongoing need in glycomics for new tools to cope with the analytical challenges caused by the structural and physicochemical complexity of polysaccharides, and by the often inherently heterogeneous nature of naturally derived carbohydrates. The demonstrations of nanopore sensing here provide a beachhead for ongoing efforts to develop solid-state nanopores as a promising platform technology for glycomics.

METHODS

A full listing of the experimental details is available in the Supplementary Information. Nanopores were formed via dielectric breakdown⁴³ in nominally 10 nm-thick silicon nitride (SiN_x) membranes. Nanopore sizes were inferred from their conductance, G , determined from Ohmic current-voltage data. Nanopores used for measurements produced stable open-pore (analyte-free) currents in the electrolyte solutions used. Polysaccharides were commercially obtained: sodium alginate samples from two different sources - *A1* (Alfa Aesar, Ward Hill, MA) and *A2* (FMC Corporation Health and Nutrition, PA, USA); USP heparin sodium salt; and USP OSCS. For routine measurements, sample aliquots were added to the headstage side (Figure 2.1), leaving the ground side free of initially added analyte. Current blockages were extracted using a current-threshold analysis. All applied voltages are stated with the polarity of the electrode on the headstage side relative to ground on the ground side of the sample cell.

Code Availability. Labview source code to view the current event files can be supplied upon request.

Data Availability. The datasets generated during the current study are available from the corresponding author on reasonable request.

AUTHOR INFORMATION

Corresponding Author

Email: jason_dwyer@uri.edu

Author Contributions

All authors have contributed to, and approve, the manuscript.

Acknowledgements

This research has been supported by NSF CAREER award CBET-1150085, and by the University of Rhode Island, including URI graduate fellowships for Y. M. Nuwan D. Y. Bandara and Buddini Iroshika Karawdeniya. We thank Travis Leffert for preliminary polysaccharide measurements. We thank the Lucht Group (URI Dept. of Chemistry) for access to their IR spectrometer, and K.W.D. Kaveendi Chandrasiri and Bharathy S. Parimalam for acquiring IR spectra. We thank the group of Prof. Stephen Kennedy (URI Depts. Of Electrical, Computer and Biomedical Engineering, & Chemical Engineering) for samples of alginate *A2*.

REFERENCES

1. Imberty, A. & Pérez, S. Structure, Conformation, and Dynamics of Bioactive Oligosaccharides: Theoretical Approaches and Experimental Validations. *Chem. Rev.* **100**, 4567-4588 (2000).
2. DeMarco, M.L. & Woods, R.J. Structural glycobiology: A game of snakes and ladders. *Glycobiology* **18**, 426-440 (2008).
3. Dove, A. The bittersweet promise of glycobiology. *Nature Biotechnology* **19**, 913-917 (2001).
4. Ernst, B. & Magnani, J.L. From carbohydrate leads to glycomimetic drugs. *Nat Rev Drug Discov* **8**, 661-677 (2009).
5. Pinho, S.S. & Reis, C.A. Glycosylation in cancer: mechanisms and clinical implications. *Nat Rev Cancer* **15**, 540-555 (2015).
6. Seeberger, P.H. Chemical glycobiology: why now? *Nat Chem Biol* **5**, 368-372 (2009).
7. Lichtenstein, R.G. & Rabinovich, G.A. Glycobiology of cell death: when glycans and lectins govern cell fate. *Cell Death Differ* **20**, 976-986 (2013).
8. Dalziel, M., Crispin, M., Scanlan, C.N., Zitzmann, N. & Dwek, R.A. Emerging Principles for the Therapeutic Exploitation of Glycosylation. *Science* **343** (2014).
9. Essentials of Glycobiology, Edn. 2. (Cold Spring Harbor Laboratory Press, 2009).
10. Linhardt, R.J. & Toida, T. Role of Glycosaminoglycans in Cellular Communication. *Acc. Chem. Res.* **37**, 431-438 (2004).
11. Kovalenko, I. et al. A Major Constituent of Brown Algae for Use in High-Capacity Li-Ion Batteries. *Science* **334**, 75-79 (2011).
12. National Research Council Transforming Glycoscience: A Roadmap for the Future. (The National Academies Press, Washington, DC; 2012).
13. Czjzek, M. Biochemistry: A wine-induced breakdown. *Nature* **544**, 45-46 (2017).
14. Lester, J., Chandler, T. & Gemene, K.L. Reversible Electrochemical Sensor for Detection of High-Charge Density Polyanion Contaminants in Heparin. *Anal. Chem.* **87**, 11537-11543 (2015).
15. Kim, D.-H., Park, Y.J., Jung, K.H. & Lee, K.-H. Ratiometric Detection of Nanomolar Concentrations of Heparin in Serum and Plasma Samples Using a Fluorescent Chemosensor Based on Peptides. *Anal. Chem.* **86**, 6580-6586 (2014).
16. Liu, H., Zhang, Z. & Linhardt, R.J. Lessons learned from the contamination of heparin. *Natural Product Reports* **26**, 313-321 (2009).
17. Korir, A. & Larive, C. Advances in the separation, sensitive detection, and characterization of heparin and heparan sulfate. *Analytical & Bioanalytical Chemistry* **393**, 155-169 (2009).
18. Kishimoto, T.K. et al. Contaminated Heparin Associated with Adverse Clinical Events and Activation of the Contact System. *New England Journal of Medicine* **358**, 2457-2467 (2008).
19. Guerrini, M. et al. Oversulfated chondroitin sulfate is a contaminant in heparin associated with adverse clinical events. *Nat Biotech* **26**, 669-675 (2008).

20. Kailemia, M.J., Ruhaak, L.R., Lebrilla, C.B. & Amster, I.J. Oligosaccharide Analysis by Mass Spectrometry: A Review of Recent Developments. *Anal. Chem.* **86**, 196-212 (2014).
21. Kasianowicz, J.J., Brandin, E., Branton, D. & Deamer, D.W. Characterization of individual polynucleotide molecules using a membrane channel. *Proceedings of the National Academy of Sciences* **93**, 13770-13773 (1996).
22. Haywood, D.G., Saha-Shah, A., Baker, L.A. & Jacobson, S.C. Fundamental Studies of Nanofluidics: Nanopores, Nanochannels, and Nanopipets. *Anal. Chem.* **87**, 172-187 (2015).
23. Taniguchi, M. Selective Multidetector Using Nanopores. *Anal. Chem.* **87**, 188-199 (2015).
24. Reiner, J.E. et al. Disease Detection and Management via Single Nanopore-Based Sensors. *Chem. Rev.* **112**, 6431-6451 (2012).
25. Howorka, S. & Siwy, Z. Nanopore analytics: sensing of single molecules. *Chem. Soc. Rev.* **38**, 2360-2384 (2009).
26. Miles, B.N. et al. Single Molecule Sensing with Solid-State Nanopores: Novel Materials, Methods, and Applications. *Chem. Soc. Rev.* **42**, 15-28 (2013).
27. Oukhaled, A., Bacri, L., Pastoriza-Gallego, M., Betton, J.-M. & Pelta, J. Sensing Proteins through Nanopores: Fundamental to Applications. *ACS Chemical Biology* **7**, 1935-1949 (2012).
28. Branton, D. et al. The potential and challenges of nanopore sequencing. *Nat. Biotechnol.* **26**, 1146-1153 (2008).
29. Reiner, J.E., Kasianowicz, J.J., Nablo, B.J. & Robertson, J.W.F. Theory for polymer analysis using nanopore-based single-molecule mass spectrometry. *Proceedings of the National Academy of Sciences* **107**, 12080-12085 (2010).
30. Wanunu, M., Sutin, J., McNally, B., Chow, A. & Meller, A. DNA Translocation Governed by Interactions with Solid-State Nanopores. *Biophys. J.* **95**, 4716-4725 (2008).
31. Carbonaro, A. & Sohn, L.L. A resistive-pulse sensor chip for multianalyte immunoassays. *Lab on a Chip* **5** (2005).
32. Aksimentiev, A. Deciphering ionic current signatures of DNA transport through a nanopore. *Nanoscale* **2**, 468-483 (2010).
33. Bacri, L. et al. Discrimination of neutral oligosaccharides through a nanopore. *Biochem. Biophys. Res. Commun.* **412**, 561-564 (2011).
34. Fennouri, A. et al. Single Molecule Detection of Glycosaminoglycan Hyaluronic Acid Oligosaccharides and Depolymerization Enzyme Activity Using a Protein Nanopore. *ACS Nano* **6**, 9672-9678 (2012).
35. Fennouri, A. et al. Kinetics of Enzymatic Degradation of High Molecular Weight Polysaccharides through a Nanopore: Experiments and Data-Modeling. *Anal. Chem.* **85**, 8488-8492 (2013).
36. Kullman, L., Winterhalter, M. & Bezrukov, S.M. Transport of Maltodextrins through Maltoporin: A Single-Channel Study. *Biophys. J.* **82**, 803-812 (2002).
37. Zhao, S. et al. Sugar-stimulated robust nanodevice: 4-Carboxyphenylboronic acid modified single glass conical nanopores. *Electrochem. Commun.* **36**, 71-74 (2013).

38. Zheng, Y.-B. et al. A temperature, pH and sugar triple-stimuli-responsive nanofluidic diode. *Nanoscale* **9**, 433-439 (2017).
39. Nguyen, Q.H., Ali, M., Neumann, R. & Ensinger, W. Saccharide/glycoprotein recognition inside synthetic ion channels modified with boronic acid. *Sensors and Actuators B: Chemical* **162**, 216-222 (2012).
40. Viložny, B. et al. Carbohydrate-actuated nanofluidic diode: switchable current rectification in a nanopipette. *Nanoscale* **5**, 9214-9221 (2013).
41. Sun, Z. et al. pH gated glucose responsive biomimetic single nanochannels. *Chem. Commun.* **48**, 3282-3284 (2012).
42. Oukhaled, G., Bacri, L., Mathé, J., Pelta, J. & Auvray, L. Effect of screening on the transport of polyelectrolytes through nanopores. *EPL (Europhysics Letters)* **82**, 48003 (2008).
43. Kwok, H., Briggs, K. & Tabard-Cossa, V. Nanopore Fabrication by Controlled Dielectric Breakdown. *PLoS ONE* **9**, e92880 (2014).
44. Dwyer, J.R., Bandara, Y.M.N.D.Y., Whelan, J.C., Karawdeniya, B.I. & Nichols, J.W. in *Nanofluidics*, 2nd Edition, Edn. 2. (eds. J. Edel, A. Ivanov & M. Kim) (Royal Society for Chemistry, 2016).
45. Dwyer, J.R. & Harb, M. Through a Window, Brightly: A Review of Selected Nanofabricated Thin-Film Platforms for Spectroscopy, Imaging, and Detection. *Appl. Spectrosc.* **71**, 2051-2075 (2017).
46. Im, J. et al. Electronic single-molecule identification of carbohydrate isomers by recognition tunnelling. *Nature Communications* **7**, 13868 (2016).
47. Yusko, E.C. et al. Controlling protein translocation through nanopores with bio-inspired fluid walls. *Nature Nanotechnology* **6**, 253-260 (2011).
48. Pereira, L., Sousa, A., Coelho, H., Amado, A.M. & Ribeiro-Claro, P.J.A. Use of FTIR, FT-Raman and ¹³C-NMR spectroscopy for identification of some seaweed phycocolloids. *Biomol. Eng* **20**, 223-228 (2003).
49. Linhardt, R.J. 2003 Claude S. Hudson Award Address in Carbohydrate Chemistry. Heparin: Structure and Activity. *J. Med. Chem.* **46**, 2551-2564 (2003).
50. Viskov, C. et al. Isolation and Characterization of Contaminants in Recalled Unfractionated Heparin and Low-Molecular-Weight Heparin. *Clinical and Applied Thrombosis/Hemostasis* **15**, 395-401 (2009).
51. Foulger, J.H. THE USE OF THE MOLISCH (α -NAPHTHOL) REACTIONS IN THE STUDY OF SUGARS IN BIOLOGICAL FLUIDS. *J. Biol. Chem* **92**, 345-353 (1931).
52. Hallal, J.L.J., Lucho, A.M.S. & Gonçalves, R.S. Electrochemical polymerization of furfural on a platinum electrode in aqueous solutions of potassium biphthalate. *Materials Research* **8**, 23-29 (2005).
53. Hoogerheide, D.P., Garaj, S. & Golovchenko, J.A. Probing Surface Charge Fluctuations with Solid-State Nanopores. *Phys. Rev. Lett.* **102**, 256804 (2009).
54. Skidmore, M.A., Guimond, S.E., Dumax-Vorzet, A.F., Yates, E.A. & Turnbull, J.E. Disaccharide compositional analysis of heparan sulfate and heparin polysaccharides using UV or high-sensitivity fluorescence (BODIPY) detection. *Nat. Protocols* **5**, 1983-1992 (2010).
55. Smeets, R.M.M. et al. Salt Dependence of Ion Transport and DNA Translocation through Solid-State Nanopores. *Nano Lett.* **6**, 89-95 (2006).

56. Binqun, L. & Aleksei, A. Control and reversal of the electrophoretic force on DNA in a charged nanopore. *J. Phys.: Condens. Matter* **22**, 454123 (2010).

CHAPTER 3: PREFACE

Published: ACS Applied Materials and Interfaces 2014, 6, pp. 10952-10957.

ELECTROLESS PLATING OF THIN GOLD FILMS DIRECTLY ONTO

SILICON NITRIDE THIN FILMS AND INTO MICROPORES

Julie C. Whelan, Buddini Iroshika Karawdeniya, Y.M. Nuwan D.Y. Bandara,
Brian D. Velleco, Caitlin M. Masterson, Jason R. Dwyer

Department of Chemistry, University of Rhode Island, Kingston, RI, USA

Reprinted with permission from:

Electroless Plating of Thin Gold Films Directly onto Silicon Nitride Thin Films
and into Micropores. Julie C. Whelan, Buddini Iroshika Karawdeniya, Y.M.
Nuwan D.Y. Bandara Brian D. Velleco, Caitlin M. Masterson, and Jason R. Dwyer.
ACS ACS Appl. Mater. Interfaces, 2014, 6 (14), pp 10952–10957.

Copyright 2014 American Chemical Society.

A subsequent correction was issued, and the corresponding changes have been
made

within the text of this thesis. Correction to Electroless Plating of Thin Gold Films
Directly onto Silicon Nitride Thin Films and into Micropores. Julie C. Whelan,

Buddini Iroshika Karawdeniya†, Y.M. Nuwan D.Y. Bandara†, Brian D. Velleco,
Caitlin M. Masterson and Jason R. Dwyer*.

CHAPTER 3

ELECTROLESS PLATING OF THIN GOLD FILMS DIRECTLY ONTO SILICON NITRIDE THIN FILMS AND INTO MICROPORES.

Julie C. Whelan, Buddini Iroshika Karawdeniya‡, Y.M. Nuwan D.Y. Bandara‡, Brian D. Velleco, Caitlin M. Masterson and Jason R. Dwyer*.

Department of Chemistry, University of Rhode Island, 51 Lower College Road, Kingston, RI, 02881, United States.

ABSTRACT

A method to directly electrolessly plate silicon-rich silicon nitride with thin gold films was developed and characterized. Films with thicknesses less than 100nm were grown at 3 and 10°C between 0.5 and 3 hours, with mean grain sizes between ~20-30nm. The method is compatible with plating free-standing ultrathin silicon nitride membranes, and we successfully plated the interior walls of micropore arrays in 200nm-thick silicon nitride membranes. The method is thus amenable to coating planar, curved, and line-of-sight-obscured silicon nitride surfaces.

KEYWORDS: Electroless plating; thin gold films; silicon nitride; micropores; surface enhanced Raman spectroscopy (SERS); tin sensitization.

INTRODUCTION

Thin gold films have widespread technological utility, from forming conductive elements and overlayers, to serving as a platform for chemical surface modification by molecular self-assembly¹. For gold films incorporated into

conventional micro- and nanofabricated devices, silicon nitride is an appealing choice for a substrate. It is a standard nanofabrication material, offering, in addition, favorable inherent properties such as mechanical strength²⁻³, chemical resistance, and dielectric strength⁴⁻⁵. Silicon nitride is thus ubiquitous as a structural and functional element in nanofabricated devices where it plays a variety of roles^{2, 5-8}. Its surface chemistry, however, presents especial challenges given the complex mixture of silicon-, oxygen-, and nitrogen-bearing surface species⁵. The nominal surface modification of silicon nitride is frequently carried out in practice using silane-based modification of a silica layer that may itself not be well-defined⁹. Thus, there remains both a need and opportunity to expand the suite of approaches useful for surface functionalizing silicon nitride directly. Electroless deposition is a particularly compelling approach to film formation: deposition proceeds from solution allowing the coating of three-dimensional surfaces, including surfaces hidden from line-of-sight deposition methods; no electrochemical instrumentation is required; no electrical power must be supplied nor must the substrate be conductive; there is no need for expensive vacuum deposition equipment; and a variety of classical physicochemical parameters such as reagent composition, solution properties such as pH and viscosity, and temperature, are available to tune the film properties¹⁰⁻¹¹. There is a wealth of familiar approaches for the electroless plating of substrates such as polymers, for example, but no established prior art for the direct metal-cation-mediated electroless plating of gold onto silicon nitride¹²⁻¹³. A particularly compelling sequence exists for the electroless gold plating of poly(vinylpyrrolidone)-coated polycarbonate substrates (Au/PVP)¹³: direct sensitization of the PVP surface with Sn^{2+} , activation by immersion in ammoniacal silver nitrate to oxidize the surface

Sn^{2+} to Sn^{4+} by reducing Ag^+ to elemental silver (producing, also, a small amount of silver oxide), and finally gold plating by galvanic displacement of the silver with reduction of Au(I) to Au(0) accompanied by the oxidation of formaldehyde. Amine and carbonyl groups in the PVP layer were proposed to complex the tin cation during sensitization¹³. Extending this approach, Sn^{2+} has been reported to complex effectively with oxygen-rich polymer surfaces¹² and with quartz and silica substrates^{10, 14-16}. Tin(II) sensitization has also been reported on NaOH-roughened surfaces¹⁷, suggesting that a specific chemical interaction may not be essential¹⁸, and underscoring the utility of electroless plating for rough and high-surface-area surfaces where physical deposition is challenged¹⁹. In principle, though, a smooth silicon nitride substrate with a well-defined silica surface layer should be amenable to direct tin sensitization. Yet, electroless deposition of gold on planar silicon nitride has been limited to routes requiring the use of a silica layer with organic linkers and metal layers between the silicon nitride and gold overlayer¹⁸. In the first case, covalent attachment of an organic monolayer using silane chemistry can be beneficial for film adhesion, but adds operational complexity¹⁸ and can constrain downstream processing conditions. In the second case, the intervening layers may lend beneficial properties, or may similarly introduce compositional constraints on applications, or morphological constraints on the final gold film nanostructure. Regardless of the ability to carry out a silica-based modification, it does not eliminate the benefits of a direct functionalization of silicon nitride. We present a dramatically simplified electroless gold deposition method in which we eliminate the initial covalent attachment of an organic monolayer to the substrate, and in which we do not need to initially mask the silicon nitride surface chemistry with a silica overlayer. Our method directly sensitizes the silicon nitride substrate

with a Sn^{2+} solution, followed by a series of metal ion treatments in which we exert control over the gold film thickness using process time and temperature. Film thicknesses ranged from 30 to 100nm for deposition times from 0.5-3h, and temperatures of 3 and 10°C.

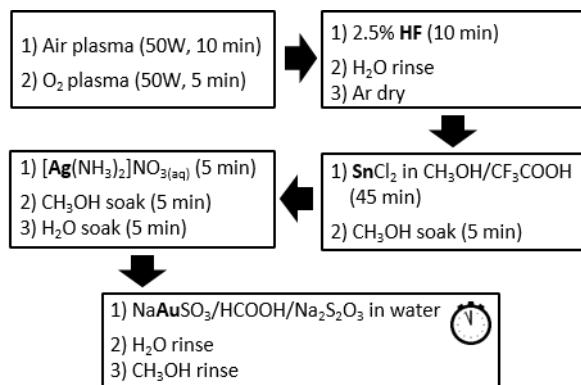
MATERIALS AND METHODS

Full details of materials and preparation are provided in the Supporting Information. In brief, polished silicon-rich low-pressure chemical vapor deposited (LPCVD) silicon nitride-coated silicon wafers were cleaved into $\sim 1\text{cm}^2$ chips. The chips were then electrolessly plated with gold deposited from solution as outlined in Scheme 3.1. Ultrasonic cleaning of the substrate²⁰ was strictly avoided so that straightforward extension of the scheme to ultrathin silicon nitride windows would not cause window fracture²⁻³. Each chip was plasma-cleaned and then briefly etched in a dilute hydrofluoric acid (HF) solution to remove unwanted native silicon oxide and expose the silicon nitride surface^{4, 20}. The prepared chips were immersed in a tin(II) chloride sensitizing solution, followed by a soak in ammoniacal silver nitrate solution^{10, 13}. The chips were carefully rinsed between each step of the process. Electroless gold plating was carried out by immersing chips in $\sim 1.5\text{-}3\text{mL}$ (0.75mL for micropores) of sodium gold sulfite plating solution²¹, with gentle rocking, in a refrigerator (3°C plating) or thermoelectric cooler (10°C plating). After plating for the desired time at the desired temperature, the chips were carefully rinsed, dried and then characterized. Gold film thicknesses were obtained by atomic force microscopy (AFM) measurements across an edge from the film to the substrate. Film morphology was examined by field-emission scanning electron microscopy (FE-SEM) and analyzed using a watershed analysis. Elemental analysis of the gold film was carried out by energy-dispersive x-ray

spectroscopy (EDS) and by x-ray photoelectron spectroscopy (XPS).

Characterization details are provided in the Supporting Information.

Scheme 3.1. Electroless plating of silicon nitride. The silicon nitride-coated substrates are plasma-cleaned of organics and HF-etched before the surface is exposed to Sn^{2+} ions which are oxidized during the redox-driven deposition of an elemental silver layer. Gold plating begins with galvanic displacement of the elemental silver.



DISCUSSION

Figure 3.1 shows photographs of an array of silicon nitride-coated substrates subjected either strictly to the steps in Scheme 3.1, or to control experiment variations. Adherence to Scheme 3.1 produced gold films, evaluated by visual inspection, with good quality and excellent macroscopic surface coverage, and delivered these results reliably over many months of repeated trials. More detailed characterization of these films is provided below. Departures from the scheme, however, yielded generally poor or inconsistent results. We focused our attention on varying the surface preparation steps, specifically testing surface preparations that did not involve HF etching designed to remove the oxygen-containing overlayer. Tin(II) sensitization after sodium hydroxide surface roughening had been reported on silicon nitride powders of unknown stoichiometry^{5, 17}. Indeed, surface roughening to improve film adhesion is a familiar preliminary process in electroless plating¹¹. Substituting 1, 4.5, or 9M NaOH treatments for the HF

etching of Scheme 3.1, however, generated only gold smudges after 3 hours of plating at 3°C. The silicon-rich nature of our LPCVD films is a possible contributing factor to the poor plating quality after NaOH treatment in comparison to the published results¹⁷, given the general challenge that silicon nitride stoichiometry and available surface species—and thus functionalization opportunities²⁰—depend on the details of the silicon nitride synthesis⁵. Our use of large-area, planar substrates introduces another likely explanation: it provides a stringent test of film deposition quality, and easily reveals defects that may be more difficult to discern on a film coating a powder. Traditional silicon nitride surface modification schemes rely frequently on modification of a silica layer on the silicon nitride surface²²⁻²³ rather than of the silicon nitride, itself. Careful attention to the quality of the oxygen-containing surface layer can circumvent difficulties that stem from a lack of definition of this silica layer²². Holtzman and Richter used nitric acid to enrich the number of surface hydroxyl groups on silicon nitride so that they could use silane chemistry to provide an organic monolayer foundation for an overlying electrolessly deposited gold film¹⁸. While successful, the approach must contend with the acknowledged challenges of silane chemistry¹⁸ and with the persistence of the organic linker layer. Given the affinity of Sn²⁺ for such an oxygen-enriched silicon nitride surface, and given prior demonstrations of electroless gold plating on silica surfaces¹⁰, we replaced the HF etch in Scheme 3.1 with a 20 minute treatment in 10% (v/v) nitric acid at 80°C. The results, shown in Figure 3.1, were promising, with repeated, although not consistent, deposition of (visually inspected) high-quality gold films. It is likely feasible to optimize this route to routinely deposit high-quality, uniform gold films, but our goal was to develop a simple route to electrolessly plate gold directly onto silicon nitride.

Treatment of silicon-rich LPCVD silicon nitride surfaces with dilute hydrofluoric acid eliminates the native oxide^{4, 23} and leaves a H-terminated surface with Si-H, NH and NH₂ moieties²². Given the appeal of this surface for surface functionalizations^{20, 22}, we tested its compatibility with tin(II)-based sensitization. Scheme 3.1 thus follows the plasma-based cleaning steps with an HF etch step that removes oxide and H-terminates the surface²², and ends with the gold plating treatments¹³. We note that in the absence of the HF-etching step, chips would sporadically be coated with patchy gold layers, but no uniform high-quality gold films were observed on these chips even after 3 hours in the gold plating solution.

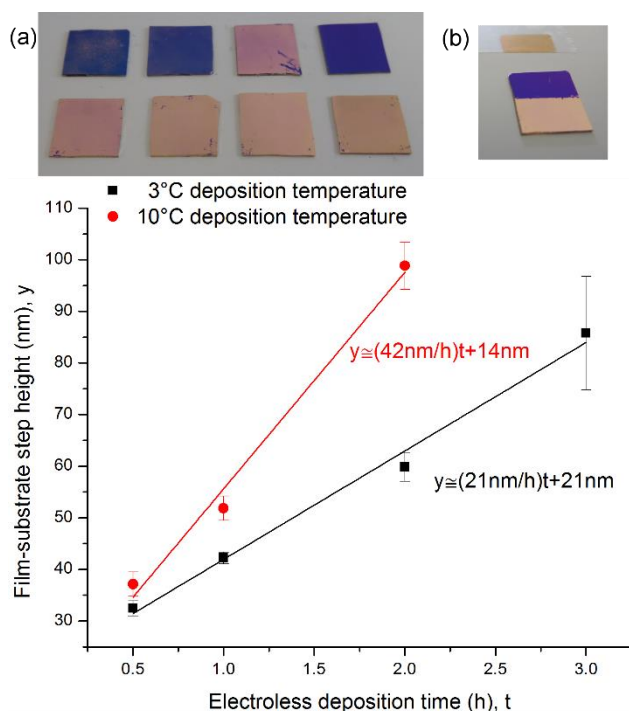


Figure 3.1: (a) Photograph array of plating results at 3°C. Top row, left-to-right – HF etch omitted, 1 h plating after HNO₃ preparation, HNO₃ step replicate, plasma-cleaned only (subsequent steps omitted). Bottom row, left-to-right, Scheme 3.1 followed for plating times of 30 minutes, 1 hour, 2 hours, and 3 hours. The scratches in the film arose during handling of the chips. (b) Adhesive tape could lift most of the gold film to give an edge for (c) AFM measurements of electroless gold deposition film thickness as a function of time and temperature.

The row of visually high quality, high coverage gold films shown in Figure 3.1 were electrolessly plated at 3°C for increasing lengths of time, with strict

adherence to Scheme 3.1. The gold films survived extensive handling including prolonged immersion in liquids interspersed with repeated rinsing and pressurized argon-drying steps, and moreover adhered well to free-standing films that we broke deliberately for imaging (Figure 3.4b). Certainly, in applications using gold-coated, freestanding silicon nitride membranes, consideration of membrane robustness will supersede gold adhesion in importance. The films could, however, be scratched with tweezers and mostly removed with adhesive tape (Figure 3.1b), and this afforded us the ability to perform AFM film thickness measurements. A swath of the gold film was removed and the mean difference in height between the film and the bare substrate was averaged across several representative line profiles and several independently plated chips for each plating time and temperature (see Supporting Information for details). Figure 3.1 plots the step height from plated film to bare substrate as a function of time: at 3°C a step height of ~30nm after 30 minutes with a linear fit yielding a ~20nm/h deposition rate thereafter, and at 10°C a step height of ~35nm after 30 minutes with a linear fit yielding a deposition rate of ~40nm/h thereafter. The intercept likely arises from residual silver nanoislands scattered across the substrate. Shorter plating times than those shown in Figure 3.1 typically produced chips with a purple-blue hue. Four-point film resistivities were measured for the films plated at 3°C for all the time points listed, and were in the range $\sim 3\text{-}5 \times 10^{-6} \Omega\cdot\text{cm}$; thin film resistivities higher than the known bulk gold resistivity ($2.2 \times 10^{-6} \Omega\cdot\text{cm}$)¹¹ are not surprising¹⁸. SEM micrographs afford a further detailed view of the film structure (Figure 3.2). Microscopic substrate coverage was high, but not complete, after 30 minutes of plating at 3°C, but was on par, after 30 minutes at 10°C and 1 hour at 3°C, with the coverage shown in the SEM micrograph shown in Figure 3.2. Micrographs for both temperatures and all

plating times were subjected to watershed analysis (see Supporting Information for details) and yielded area-equivalent mean grain radii from 20-30nm. It is clear from the SEM images, however, that the film structure is more complex than can be represented in a single equivalent grain size. There were large agglomerates on the film surface, seen also in AFM line profiles, with radii of several hundred nanometers. EDS analysis of these larger features showed them to be gold (see Supporting Information, Figure S3.1). Many of these outcroppings had quite convoluted shapes; there is the potential for quite compelling applications arising from both the regular and irregular film grain structures²⁴⁻²⁵. Indeed, the films are useful as a platform for surface-enhanced Raman spectroscopy (SERS). Figure 3.3 shows a demonstration spectrum of 4-nitrothiophenol (NBT) taken from an electrolessly gold-coated silicon nitride substrate. Annealing of these films caused an attendant decrease in the SERS signal, and after annealing for 24 hours at 280°C, the mean grain size had increased to nearly 50nm.

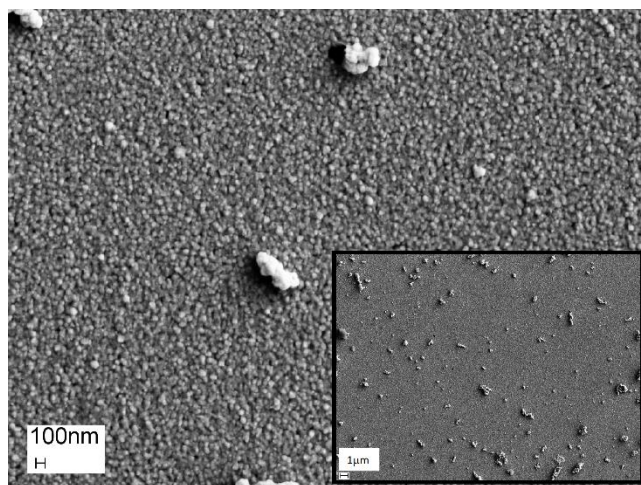


Figure 3.2. SEM images of a film after 2h of gold plating at 3°C. The inset is of the same film at lower magnification.

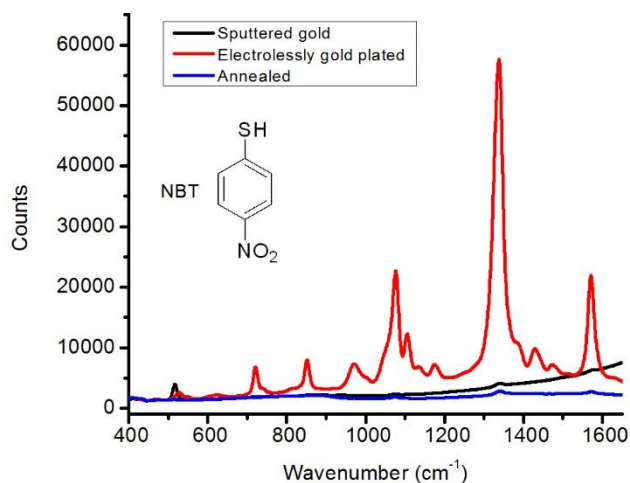


Figure 3.3. Measured spectra from 1cm² silicon nitride substrates soaked in 0.01M NBT for 5 minutes: from a substrate electrolessly gold-plated at 3°C for 3 hours (red), from the same chip plasma cleaned, annealed at 280°C for 20 minutes, and plasma cleaned again before NBT exposure (blue), and from a sputtered (30s) gold film (black).

While the electroless gold plating was strongly sensitive to the surface preparation of the silicon nitride, we note, for completeness, that the exposed silicon at the edges of the chips was consistently gold-plated, regardless of whether the wafer was treated with HF, HNO₃ or NaOH. Polished ~1cm² silicon chips treated according to Scheme 3.1 developed uniform, high-quality gold films across the surface. This result suggests that the silicon-rich nature of our silicon nitride films may contribute to the electroless plating process in Scheme 3.1. Candidate mechanisms for tin-sensitizing silicon nitride thus extend beyond those involving nitrogen-containing surface species¹³. The prospect of definitive elucidation of the mechanism, however, must be weighed in the context of clear precedent in the literature that the complexity of silicon nitride surface chemistry makes it difficult to unravel surface attachment mechanisms²⁰. The chemical complexity of the reagents and supporting media involved in electroless plating further compounds the challenges, compared to physical deposition in vacuum or covalent attachment chemistry in solution. Nevertheless, the steps of various electroless plating

approaches have a sound electrochemical basis and the method has a demonstrable outcome¹¹. XPS spectra were recorded from silicon nitride chips after each major step of Scheme 3.1. Selected spectra and details of the analysis are provided in the Supporting Information (Figure S3.2). XPS spectra were also recorded from silicon chips for use as a guide to unravelling the overlapping contributions to the Si2p region of the silicon nitride spectra, especially. HF treatment of the oxygen-plasma-cleaned silicon and silicon nitride caused a significant diminution of oxygen-related peaks at ~104eV (Si2p) and ~533eV (O1s), with the first component no longer evident. These spectral features—including the residual O1s peak that could indicate surface reoxidation generating a small number of surface hydroxyl groups, but has been principally attributed to presumably surface-inaccessible bulk oxygen—are consonant with those recorded from silicon nitride substrates prepared for direct covalent chemical modification^{9, 20, 22}. The tin(II) treatment steps caused an appreciable widening of the residual, post-HF-etch O1s peaks of silicon and silicon nitride. We subjected silicon and silicon nitride substrates to two control treatments at this stage of Scheme 3.1: in the first, we omitted the hydrofluoric acid step prior to the introduction of the tin solution, and in the second, we prepared the tin sensitizing solution without adding tin. In none of the cases was the appreciable widening of the O1s peak observed. The broad, low-amplitude 102.5eV Si2p peak that appeared after Scheme 3.1 tin-sensitization of silicon also appeared after tin-free control processing, and it suggests submonolayer oxygen coverage that can arise from aqueous processing^{23, 26}. The analogous formation of silicon oxynitride²⁷⁻²⁸ on the silicon nitride substrate would be more difficult to discern from the main Si2p peak due to spectral overlap. Tin oxidation states can be difficult to definitively identify by XPS measurement^{16, 29},

but the shifts of the best-fit $\sim 487\text{eV}$ $\text{Sn}3d_{5/2}$ peak to lower binding energy after the addition of silver(I) ions to both substrates (by $\sim 0.5\text{eV}$ for SiN_x and $\sim 0.15\text{eV}$ for Si), would be consistent in direction with the oxidation of tin(II). The $\text{Sn}3d_{5/2}$ peaks were affected by the substrate preparation, with $\sim 0.2\text{eV}$ greater width on silicon and silicon nitride substrates that had not been treated with hydrofluoric acid, with an accompanying $\sim 0.4\text{eV}$ shift to higher binding energy on the silicon substrate. Overall, the XPS spectra suggest complex roles for oxygen and tin in the surface sensitization steps and, while the detailed mechanism of sensitization remains unresolved, adherence to Scheme 3.1 exposed the silicon-rich LPCVD silicon nitride surface for direct surface modification and yielded high-quality gold films.

In fact, in spite of complex and challenging surface chemistry, the choice of silicon nitride as a substrate opens a panoply of possible applications for consideration, and the use of a solution-based gold plating method allows us to coat surfaces that are difficult or impossible to reach by line-of-sight metal coating methods. We paid special attention in our development to be able to coat free-standing thin silicon nitride membranes. As a final demonstration of the capabilities of this method, we electrolessly gold plated micropore arrays fabricated in thin (200nm) silicon nitride membranes. Figure 3.4 shows two representative gold-coated $2\mu\text{m}$ micropores, with the first plated into a free-standing portion of the membrane, and the second plated in a region of the silicon nitride pores overlapped with the underlying silicon support frame. Gold plating of the pore walls allows for the straightforward subsequent use of thiol chemistry for surface chemical functionalization. By choosing complementary pore dimensions and gold film thickness, either by fabricating pores with smaller initial sizes, or by increasing the plating time, this electroless plating process can also be used to

physically tune the pore dimensions. This method thus provides access to surfaces that may not be accessible to line-of-sight methods, and it moreover provides control over both surface physicochemical properties and physical dimensions of surface and internal pores⁷. In addition, the method is well-suited for tuning and enhancing the properties and performance of thin film and pore-based devices.

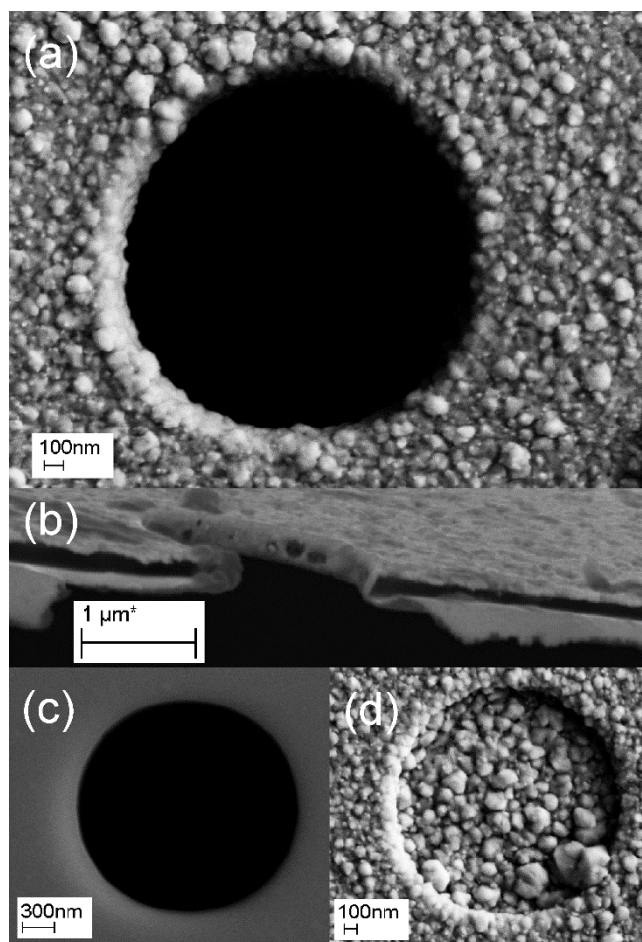


Figure 3.4. Gold coating can be seen to cover (a) the planar membrane and curved inner pore surface of the free-standing membrane area, with its uncoated equivalent shown in (c). A purposefully fractured membrane in (b) shows the gold coating on the micropore surface and the silicon nitride membrane (dark line) with intact gold coating. In image (d), plating also occurred on the bottom of the 200nm-deep well where it intersects with the silicon substrate.

AUTHOR INFORMATION

Corresponding Author:

* E-mail: jdwyer@chm.uri.edu.

AUTHOR CONTRIBUTIONS

All authors have given approval to the final version of the manuscript. / ‡These authors contributed equally.

FUNDING SOURCES

NSF CAREER award CBET-1150085, in part by NSF EPSCoR Cooperative Agreement #IIA-1330406, and by the University of Rhode Island.

ACKNOWLEDGEMENTS

We thank Sarah Golden for custom software used in data analysis. This research has been supported by NSF CAREER award CBET-1150085, in part by NSF EPSCoR Cooperative Agreement #IIA-1330406, and by the University of Rhode Island.

ASSOCIATED CONTENT

Supporting Information Available: Experimental details, methods and sample characterizations. This material is available free of charge via the Internet at <http://pubs.acs.org>.

ABBREVIATIONS

AFM, Atomic Force Microscopy; SEM, Scanning Electron Microscopy; FE-SEM, field-emission SEM; EDS, energy-dispersive X-ray spectroscopy; LPCVD, low-pressure chemical vapor deposition; XPS, x-ray photoelectron spectroscopy; PVP, poly(vinylpyrrolidone); SERS; surface-enhanced Raman spectroscopy.

REFERENCES

1. Love, J. C.; Estroff, L. A.; Kriebel, J. K.; Nuzzo, R. G.; Whitesides, G. M., Self-Assembled Monolayers of Thiolates on Metals as a Form of Nanotechnology. *Chem. Rev.* 2005, *105*, 1103-1170.
2. Mueller, C.; Harb, M.; Dwyer, J. R.; Miller, R. J. D., Nanofluidic Cells with Controlled Pathlength and Liquid Flow for Rapid, High-Resolution In Situ Imaging with Electrons. *J. Phys. Chem. Lett.* 2013, *4*, 2339-2347.
3. Ciarlo, D. R., Silicon Nitride Thin Windows for Biomedical Microdevices. *Biomed. Microdevices* 2002, *4*, 63-68.
4. Williams, K. R.; Muller, R. S., Etch rates for micromachining processing. *J. Microelectromech. Syst.* 1996, *5*, 256-269.
5. Habraken, F. H. P. M.; Kuiper, A. E. T., Silicon Nitride and Oxynitride Films. *Mater. Sci. Eng., R* 1994, *12*, 123-175.
6. Miles, B. N.; Ivanov, A. P.; Wilson, K. A.; Dogan, F.; Japrun, D.; Edel, J. B., Single Molecule Sensing with Solid-State Nanopores: Novel Materials, Methods, and Applications. *Chem. Soc. Rev.* 2013, *42*, 15-28.
7. Frament, C. M.; Bandara, N.; Dwyer, J. R., Nanopore Surface Coating Delivers Nanopore Size and Shape through Conductance-Based Sizing. *ACS Appl. Mater. Interfaces* 2013, *5*, 9330-9337.
8. Fine, D.; Grattoni, A.; Goodall, R.; Bansal, S. S.; Chiappini, C.; Hosali, S.; van de Ven, A. L.; Srinivasan, S.; Liu, X.; Godin, B.; Brousseau, L.; Yazdi, I. K.; Fernandez-Moure, J.; Tasciotti, E.; Wu, H.-J.; Hu, Y.; Klemm, S.; Ferrari, M., Silicon Micro- and Nanofabrication for Medicine. *Adv. Healthcare Mater.* 2013, *2*, 632-666.
9. Arafat, A.; Giesbers, M.; Rosso, M.; Sudhölter, E. J. R.; Schroën, K.; White, R. G.; Yang, L.; Linford, M. R.; Zuilhof, H., Covalent Biofunctionalization of Silicon Nitride Surfaces. *Langmuir* 2007, *23*, 6233-6244.
10. Ahn, W.; Taylor, B.; Dall'Asen, A. G.; Roper, D. K., Electroless Gold Island Thin Films: Photoluminescence and Thermal Transformation to Nanoparticle Ensembles. *Langmuir* 2008, *24*, 4174-4184.
11. Møller, P.; Nielsen, L. P., *Advanced Surface Technology*. Møller & Nielsen APS: Denmark, 2013; Vol. 1, p 594.
12. Charbonnier, M.; Romand, M., Polymer Pretreatments for Enhanced Adhesion of Metals Deposited by the Electroless Process. *Int. J. Adhes. Adhes.* 2003, *23*, 277-285.
13. Menon, V. P.; Martin, C. R., Fabrication and Evaluation of Nanoelectrode Ensembles. *Anal. Chem.* 1995, *67*, 1920-1928.
14. Kobayashi, Y.; Tadaki, Y.; Nagao, D.; Konno, M., Deposition of Gold Nanoparticles on Silica Spheres by Electroless Metal Plating Technique. *J. Colloid Interface Sci.* 2005, *283*, 601-604.

15. Miller, T. C.; Holcombe, J. A., Evaluation of Electroless Gold Deposited on Porous Silica for Ligand Attachment for Metal Ion-Exchange. *Anal. Chim. Acta* 2002, *454*, 37-44.
16. Kobayashi, Y.; Salgueiriño-Maceira, V.; Liz-Marzán, L. M., Deposition of Silver Nanoparticles on Silica Spheres by Pretreatment Steps in Electroless Plating. *Chem. Mater.* 2001, *13*, 1630-1633.
17. Wanbao, H.; Baolin, Z.; Hanrui, Z.; Wenlan, L., Preparation and Sintering of Ni-Coated Si₃N₄ Composite Powders. *Ceram. Int.* 2005, *31*, 811-815.
18. Holtzman, A.; Richter, S., Electroless Plating of Silicon Nitride Using (3-Aminopropyl) Triethoxysilane. *J. Electrochem. Soc.* 2008, *155*, D196-D202.
19. Díaz, D. J.; Williamson, T. L.; Guo, X.; Sood, A.; Bohn, P. W., Electroless Deposition of Gold and Platinum for Metallization of the Intrapore Space in Porous Gallium Nitride. *Thin Solid Films* 2006, *514*, 120-126.
20. Rosso, M.; Giesbers, M.; Arafat, A.; Schroën, K.; Zuilhof, H., Covalently Attached Organic Monolayers on SiC and Si_xN₄ Surfaces: Formation Using UV Light at Room Temperature. *Langmuir* 2009, *25*, 2172-2180.
21. Ko, J. W.; Koo, H. C.; Kim, D. W.; Seo, S. M.; Kang, T. J.; Kwon, Y.; Yoon, J. L.; Cheon, J. H.; Kim, Y. H.; Kim, J. J.; Park, Y. J., Electroless Gold Plating on Aluminum Patterned Chips for CMOS-Based Sensor Applications. *J. Electrochem. Soc.* 2010, *157*, D46-D49.
22. Arafat, A.; Schroën, K.; de Smet, L. C. P. M.; Sudhölter, E. J. R.; Zuilhof, H., Tailor-Made Functionalization of Silicon Nitride Surfaces. *J. Am. Chem. Soc.* 2004, *126*, 8600-8601.
23. Bermudez, V. M., Wet-Chemical Treatment of Si₃N₄ Surfaces Studied Using Infrared Attenuated Total Reflection Spectroscopy. *J. Electrochem. Soc.* 2005, *152*, F31-F36.
24. Soleymani, L.; Fang, Z.; Lam, B.; Bin, X.; Vasilyeva, E.; Ross, A. J.; Sargent, E. H.; Kelley, S. O., Hierarchical Nanotextured Microelectrodes Overcome the Molecular Transport Barrier To Achieve Rapid, Direct Bacterial Detection. *ACS Nano* 2011, *5*, 3360-3366.
25. Stiles, P. L.; Dieringer, J. A.; Shah, N. C.; Van Duyne, R. P., Surface-Enhanced Raman Spectroscopy. *Annu. Rev. Anal. Chem.* 2008, *1*, 601-626.
26. Chen, M.; Batra, I. P.; Brundle, C. R., Theoretical and Experimental Investigations of the Electronic Structure of Oxygen on Silicon. *J. Vac.Sci. Technol.* 1979, *16*, 1216-1220.
27. Du, H.; Tressler, R. E.; Spear, K. E.; Pantano, C. G., Oxidation Studies of Crystalline CVD Silicon Nitride. *J. Electrochem. Soc.* 1989, *136*, 1527-1536.
28. Vasquez, R. P.; Hecht, M. H.; Grunthaler, F. J.; Naiman, M. L., X-ray Photoelectron Spectroscopy Study of the Chemical Structure of Thermally Nitrided SiO₂. *Appl. Phys. Lett.* 1984, *44*, 969-971.

29. Themlin, J.-M.; Chtaïb, M.; Henrard, L.; Lambin, P.; Darville, J.; Gilles, J.-M., Characterization of Tin Oxides by X-Ray-Photoemission Spectroscopy. *Phys. Rev. B: Condens. Matter Mater. Phys.* 1992, *46*, 2460-2466.

CHAPTER 4: PREFACE

Published: ACS Applied Materials and Interfaces, 2016, 8, 34964–34969

SOLUTION-BASED PHOTO-PATTERNED GOLD FILM FORMATION ON SILICON NITRIDE.

Y.M. Nuwan D.Y. Bandara, Buddini Iroshika Karawdeniya, Julie C. Whelan,
Lucas D.S. Ginsberg§, and Jason R. Dwyer*.

Department of Chemistry, University of Rhode Island, 140 Flagg Road, Kingston,
RI, 02881, United States.

Reprinted with permission from:

Solution-Based Photo-Patterned Gold Film Formation On Silicon Nitride. Y.M.
Nuwan D.Y. Bandara, Buddini Iroshika Karawdeniya, Julie C. Whelan, Lucas D.S.
Ginsberg§, and Jason R. Dwyer*. ACS Appl. Mater. Interfaces, 2016, 8 (51), pp
34964–34969

Copyright 2016 American Chemical Society.

CHAPTER 4
SOLUTION-BASED PHOTO-PATTERNED GOLD FILM FORMATION
ON SILICON NITRIDE

Y.M. Nuwan D.Y. Bandara, Buddini Iroshika Karawdeniya, Julie C. Whelan,
Lucas D.S. Ginsberg[§], and Jason R. Dwyer*.

Department of Chemistry, University of Rhode Island, 140 Flagg Road, Kingston,
RI, 02881, United States.

ABSTRACT

Silicon nitride fabricated by low-pressure chemical vapor deposition (LPCVD) to be silicon-rich (SiN_x), is a ubiquitous insulating thin film in the microelectronics industry, and an exceptional structural material for nanofabrication. Free-standing <100 nm-thick SiN_x membranes are especially compelling, particularly when used to deliver forefront molecular sensing capabilities in nanofluidic devices. We developed an accessible, gentle, and solution-based photo-directed surface metallization approach well-suited to forming patterned metal films as integral structural and functional features in thin-membrane-based SiN_x devices—for use as electrodes or surface chemical functionalization platforms, for example—augmenting existing device capabilities and properties for a wide range of applications.

KEYWORDS: Patterned metallization; Photocontrolled metallization; Silicon nitride covalent photomasking; Silicon nitride surface functionalization; Silicon nitride membrane; Thin gold films; Electroless plating; Hydrosilylation.

INTRODUCTION

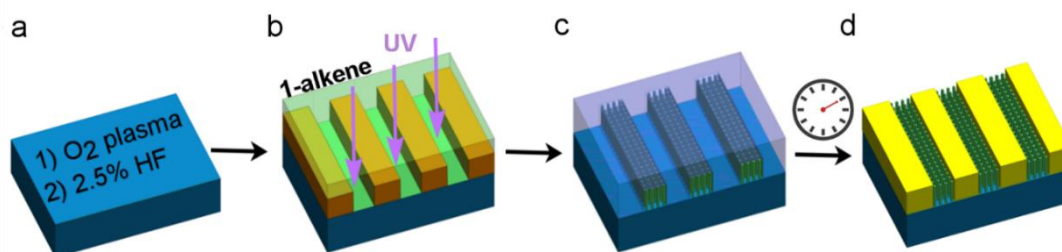
Thin, silicon-rich silicon nitride films prepared by low pressure chemical vapor deposition (LPCVD SiN_x) are a prevalent element of micro- and nanofabricated devices and they can be used to confer mechanical and chemical robustness, diffusion inhibition, and dielectric strength.¹⁻³ Devices and applications exploiting these beneficial native features can be augmented and improved using designer metal overlayers that fulfill structural roles, serve as electrodes, and provide alternative surface chemistry options, including as a platform for subsequent thiol monolayer self-assembly. The field of nanopore single-molecule sensing offers compelling examples of the prospects of merging SiN_x thin films and designer metal layers into devices, and does this within a nanofluidic context where the need for versatile metallizing approaches is clear.³⁻⁷ The most common solid-state nanopores are <100 nm-diameter nanofluidic channels formed through <100 nm-thick, free-standing SiN_x films, and nanopore-integrated metal films can enhance sensing capabilities by serving as optical elements such as light shields and plasmonic films, as electrodes for tunneling and other molecular control and sensing functions, and as a means to tune nanopore size and surface chemistry.³⁻⁸ The nanoscale dimensions of the SiN_x film and pore can be significant barriers to efforts to incorporate such functional metal films, particularly when the interior of the pore must be metallized. Solution-based metallization routes offer an appealing route with natural compatibility with nanofluidic devices. Surface capture of nanoparticles—by specific and nonspecific attachment mechanisms—is a possible

solution-based route to surface metallization.⁹⁻¹² Electroless plating is a compelling alternative: a solution-based process useful for metallizing a wide variety of materials, including nonconductive and irregularly shaped materials.^{7, 13-14} Solution access, rather than line-of-sight as in physical vapor deposition, dictates where surface plating will occur, so that electroless plating is an appealing choice for fashioning nanofluidic devices where even irregular and concealed surfaces may require metallization. To fully exploit solution-based metallization as a tool for micro- and nanofabrication, however, requires control not just over the plated film composition, thickness, and grain size, but also over its spatial disposition, which must be at least partly independent of underlying substrate patterning.¹⁵ We wanted a patterning approach that did not need mechanical access to target surfaces, both to improve the generality of the approach, and to minimize the risk of damage that can accompany repeated handling of thin films—especially of free-standing thin-films. We sought to develop a gentle, solution-based patterned metallization approach¹⁶⁻¹⁷ capable of plating a range of even structured substrates, including inside existing (nano)fluidic channels.^{3, 7, 14-15, 18} The horizons of single-molecule science have recently been dramatically expanded by the development of simple methods for fabricating nanopores: entirely solution-based processes requiring only uncomplicated instrumentation are removing barriers to the widespread use of nanopore methods.¹⁹ To conserve the benefits of simple pore formation methods, our focus also included developing similarly widely-accessible, straightforward solution-based approaches to patterned metallization. We therefore wanted to avoid the instrumentation and processing overhead associated with traditional photoresist-based approaches and more exotic analogues and alternatives.^{11, 20-23} Instead, we chose to photo-pattern the covalent attachment of an organic

monolayer to SiN_x,²⁴ and to investigate its ability to then template the substrate metallization. By only attaching the protective layer where it was desired, rather than removing portions of a patterned photoresist film, for example, we sought to simplify the processing compared to conventional approaches. With the use of an initially liquid patterning precursor (here, 1-octene), we sought to gain greater tolerance to irregularities—including the presence of engineered structures such as nanofluidic channels—of the SiN_x surface. For metallization, we initially adopted an electroless plating approach that had been specifically developed for gold-plating SiN_x.^{7, 25}

The approach is outlined in Scheme 4.1, and full details of materials, instrumentation, and safety precautions are provided in the Supporting Information (SI). We had previously developed a gold electroless plating approach for SiN_x that required a hydrofluoric acid (HF) etching step prior to surface metallization^{7, 25}. The HF etching step offered a natural point to incorporate patterned monolayer formation in an effort to guide the spatial extent of the substrate metallization. An alkane monolayer could be covalently linked to HF-etched SiN_x through the photochemically-driven hydrosilylation of a 1-alkene.²⁴ Tremendous care must be exercised in the use of HF, and we detail the precautions—including additional protective equipment and monitored work—in the SI. The UV (254 nm) photoirradiation was through copper transmission electron microscopy (TEM) grid masks, with different bar sizes and spacings (see SI for specifications), that had been placed directly on the wafer (without securing them or preventing liquid access underneath), with both wafer and mask then immersed in the 1-alkene. Plating selectivity depended on rigid adherence to the rinsing steps detailed in the

SI, and, as in prior work, we ensured compatibility of the process with free-standing ultrathin SiN_x membranes by avoiding ultrasonic cleaning steps.²⁰



Scheme 4.1: A SiN_x substrate is (a) plasma treated and hydrofluoric-acid etched, then (b) immersed in 1-octene for photopatterning (254 nm) through a TEM grid. The patterned substrate is then (c) immersed in a series of metallizing solutions to yield (d) a patterned gold film. A detailed description of solution compositions and process flow is provided in the SI.

We proposed to spatially pattern LPCVD SiN_x metallization by forming a physical barrier on the surface to control where the metal plating could take place. The first step of patterned plating thus involved the formation of this patterned protective layer. In our prior work to develop an electroless gold plating procedure for SiN_x , we found it was essential to first etch the SiN_x surface with dilute HF.⁷ This same initial etching step forms the starting point for the covalent attachment of 1-alkenes (or 1-alkynes) by photochemical (or thermal) hydrosilylation on silicon-rich SiN_x ^{2, 24} to form alkane monolayers that could potentially function as a barriers for electroless plating. Photoirradiation using a UV lamp (254 nm) proved convenient in transferring the spatial patterning offered by a selection of copper transmission electron microscopy (TEM) grids (Figure 4.1a) to the SiN_x surface. Figure 4.1b is a photograph of a representative substrate after patterned irradiation through a thin (<2 mm) layer of neat 1-octene held under a quartz plate in a specially constructed holder. This optical micrograph taken during the evaporation of a dichloromethane drop placed on the surface reveals the transfer of the TEM grid pattern to the surface-functionalized substrate. Such patterned substrates were

then electrolessly gold-plated, using the three-solution—Sn (II)/Ag (I)/Au (I)—process beginning with Sn (II) sensitization that had been proven successful for HF-etched SiN_x (see SI for complete details of metallization solutions and process flow).^{7, 25} While gold replicas of the TEM grid masks can be seen in Figure 4.1c, it is also apparent that the plating spatial selectivity was quite poor compared to its Pd (II)-initiated counterpart, Pd (II)/Ag (I)/Au (I) (*vide infra*, and calculation details in SI). Substrate tolerance of electroless plating, via substrate tolerance of the Sn (II) sensitization step, is one of the benefits of electroless plating:^{13, 23} it is clearly—in this instance, at least—detrimental to patterned metallization. Figure 4.1d provides a magnified view, by field emission scanning electron microscopy (FE-SEM), of a Sn (II)/Ag (I)/Au (I)-metallized substrate. We did not explore using ultrasonic cleaning steps to improve the plating selectivity,^{20, 26} because we wanted to remain compatible with plating free-standing SiN_x films that are a compelling structural element, especially for nanofluidic devices.³⁻⁷

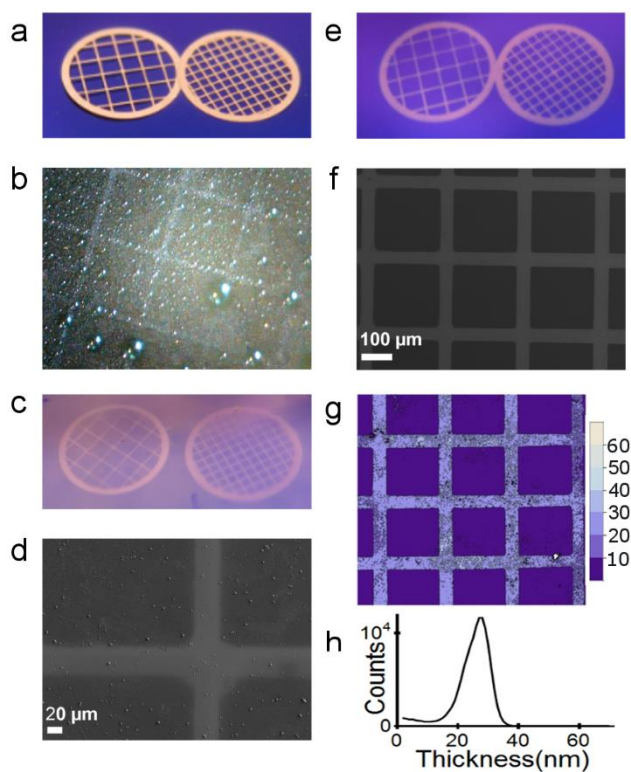


Figure 4.1: (a) 50 and 100 mesh copper TEM grids on a SiN_x-coated silicon chip; (b) 50 mesh 1-octene replica during the evaporation of a dichloromethane drop from a photopatterned chip, with image contrast, gamma, and brightness adjusted for image clarity; (c) gold replicas after Sn (II) surface sensitization followed by 5 minutes of Ag (I) and 30 minutes of Au (I) at ~3°C, with corresponding (d) FE-SEM image of a 100 mesh pattern; (e) gold replica after Pd (II) surface treatment followed 5 minutes of Ag (I) and 30 minutes of Au (I) at ~3°C, with corresponding (f) FE-SEM, (g) DHM (5× magnification) images of a 100 mesh pattern, with color intensity legend denoting film thickness (nm), and (h) histogram giving the film thickness distribution measured inside the bars of the micrograph in (g).

We abandoned Sn (II)-sensitized electroless plating when efforts to improve the spatial selectivity by using different rinsing steps, for example, proved ineffective. We tested, instead, a palladium-based treatment²⁷ in place of the Sn (II) sensitization step to give an overall process flow of Pd (II)/Ag (I)/Au (I). The use of this Pd (II) surface treatment solution delivered extremely high pattern fidelity, as seen in Figures 4.1e and 1f. The rich chemistry of the native SiN_x surface, and of the palladium species, complicates the determination of the mechanism, and indeed may allow for multiple mechanisms to be simultaneously operational.^{3, 13, 23,}

²⁸ Figure S-4.1 shows the results of several process chemistry variations, all displaying lower metallized pattern quality than seen in Figures 4.1e and 4.1f. For example, substrate photopatterning through an air layer—likely through a photochemical oxidation route similar to that seen on silicon²⁹—instead of 1-octene (Figure S-4.1) yielded spatial selectivity degraded by smudges of gold across the surface. The patterned monolayer-templated route offers benefits beyond preserving pattern quality. Photohydrosilylation offers lower process overhead and better compatibility with fluidic channels than conventional photoresist-based approaches, and a suitable hydrosilylated monolayer confers some resistance to any subsequent HF etching, but can be readily removed if necessary (Figure S-4.2).^{2, 18, 24} The metal plating selectivity when using 1-octene with Pd (II) surface treatment as the first step was easily reproducible across scores

of patterned gold depositions when scrupulous adherence to the rinsing steps was maintained. The results shown in Figures 4.1e and 1f are thus representative and reproducible.

We focus in this work on characterizing the spatial selectivity and the physical structure of the gold layers resulting from this successful initial Pd (II) surface treatment. We present analyses of gold replicas produced after ~30 minute immersions in the Au (I) bath. This duration provides a balanced perspective of film nascence and degree of spatial selectivity. Examination of gold replicas using digital holographic microscopy (DHM; Figure 4.1g) allowed us to determine that the gold films were $\sim 23 \pm 1.5$ nm thick. Higher magnification scanning electron micrographs in Figure 4.2 upheld the quality of selectivity demonstrated in Figures 4.1e and f. There was only sparse gold coverage where the photoirradiation had installed the protective layer, between the mask grid lines. The gold grid lines, themselves, could be resolved into gold features with 28 ± 5 nm mean diameters providing ~83% surface area coverage (across 15 different grids, with a 13% standard deviation) after the 30 minutes of immersion in the gold plating bath at $\sim 3^\circ\text{C}$. This degree of infilling is high in the context of low-process-overhead patterned metallization steps,³⁰ and particularly when targeting suitability for use with structured surfaces incompatible with more involved conventional patterning, such as in enclosed nanofluidic channels.

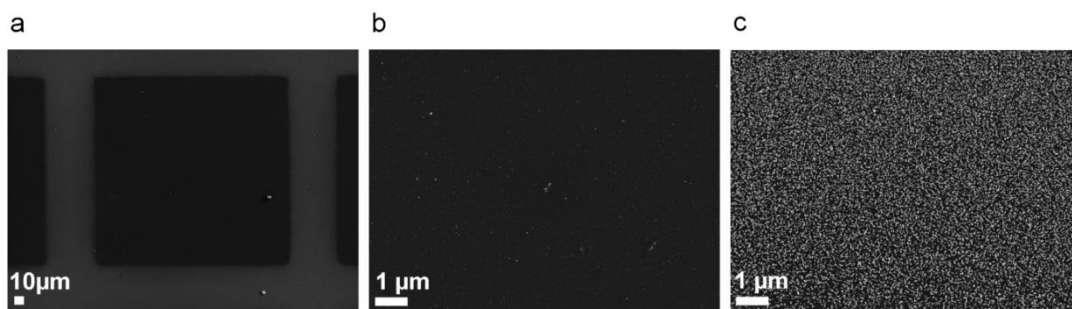


Figure 4.2: FESEM image of a subsection of a 100 mesh pattern on a SiN_x chip processed with Pd (II), Ag (I), and then Au (I) baths, as detailed in the SI. Vertical and horizontal bars composed of lighter pixels correspond to gold-replicated grid lines on the chip. Zooming into regions outside the bars (b) reveals very little presence of gold grains, confirming the visually observed spatial selectivity as seen in Figure 4.1d. Zooming into these bars at the same magnification (c) reveals the clear grain structure, and high infilling after only 30 minutes of gold plating.

To explore the spatial patterning in further detail, we focus on gold replicas of 100 mesh copper grids. The copper bars of these grid masks were $54.4 \pm 1.3 \mu\text{m}$ wide (measured by FE-SEM with analysis details in the SI), and they were placed on the SiN_x surfaces under 1-octene without securing them or attempting to prevent liquid access underneath. The spatial selectivity, defined in a classical signal-to-noise sense (details in the SI), was ~ 10.1 for the 1-octene-patterned Pd (II)/Ag (I)/Au (I) route that we focus on here, in contrast to ~ 2.7 for the 1-octene-patterned, Sn (II)-sensitized route, and ~ 3.2 for the former solution steps with air-patterning in place of 1-octene. In addition to FE-SEM micrographs, we collected elemental maps from representative gold replicas using energy-dispersive x-ray spectroscopy (EDS; also commonly abbreviated EDX). The maps and electron micrographs in Figure 4.3a,b are consistent with a thin gold overlayer on SiN_x that possesses a high degree of infilling and spatial selectivity. We used FE-SEM and EDS line profiles across the open spaces and grid lines to characterize the gold replica lines and the edge resolution, with procedural details provided in the SI. The mean line widths of the gold bars in the FE-SEM images of the gold replicas was $44.8 \pm 3.3 \mu\text{m}$, measured from more than 300 lines from each of 9 chips.

To extract the edge resolution, we fit the Au-channel EDS intensity versus linear position to Boltzmann functions and recovered sub-micrometer ($0.92 \pm 0.24 \mu\text{m}$; 15 EDS line profiles) transition widths from metal-free to metallized segments.

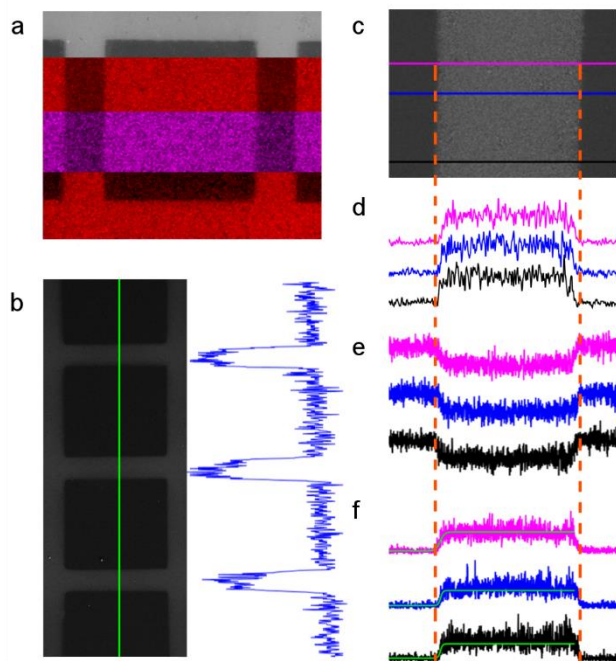


Figure 4.3: (a) A composite of an electron image (top) and three EDS maps (descending from nitrogen to silicon to gold). (b) FESEM image of a patterned SiN_x chip (left) and pixel intensity (right) taken from the micrograph along the green line. (c) Electron image of a subsection of a 100 mesh pattern on a SiN_x chip. (d) Pixel intensity along each colored line in (c), along with line profiles of spatially-registered EDS maps corresponding to (e) silicon and (f) gold channels (Boltzmann fit is shown in green, with corresponding edge slopes, $dx = 0.81, 0.59,$ and $0.87 \mu\text{m}$ from top to bottom).

We developed a solution-based method to form spatially patterned metal features on silicon-rich SiN_x thin films. This approach leverages the benefits of electroless plating and establishes a low-overhead surface-patterning approach suitable for SiN_x thin films. We ensured that spatial selectivity could be achieved without using ultrasonic excitation or other mechanically disruptive manipulations so that the patterning approach would be compatible with free-standing thin SiN_x membranes useful in a host of other applications, particularly for nanofluidics.

Photochemical hydrosilylation linkage of organic monolayers to SiN_x is a flexible and appealing route to surface-functionalize SiN_x, especially in conjunction with spatial patterning. The templating monolayer may serve as a permanent or removable coating, protecting the underlying SiN_x or being removed to expose it after metallization. The ability to readily modify the surface functional groups of these high quality monolayers using standard chemical transformations² dramatically widens the prospects of this simple patterned metallization approach. The already-excellent metallization selectivity could conceivably be further improved and prolonged by tuning the monolayer electrostatics and hydrophobicity, for example. Similarly, the monolayer surface chemistry could be tuned to promote metal layer adhesion if application needs permit the metal layer to rest on the monolayer, itself.^{9-12, 23} More tantalizingly, a base monolayer may be used as a platform for further chemical tuning of the surface, in which demonstrated properties and function² can be installed around the patterned gold layer. Thus, we contend that the patterned metallization strategy introduced here is promising and useful not only for delivering a spatially-selective solution-derived metal film, but one primed for further development.

ASSOCIATED CONTENT

Supporting Information.: Experimental details, method, and sample characterizations. This material is available free of charge via the Internet at <http://pubs.acs.org>.

AUTHOR INFORMATION

Corresponding Author:

* E-mail: jdwyer@chm.uri.edu.

[§]Present address: Chemistry, D62 Hildebrand Hall, UC Berkeley, Berkeley, CA,
USA 94720

AUTHOR CONTRIBUTIONS

All authors have given approval to the final version of the manuscript.

FUNDING SOURCES

NSF CAREER award CBET-1150085, in part by NSF EPSCoR Cooperative Agreement #IIA-1330406, and by the University of Rhode Island.

ACKNOWLEDGMENT

This research has been supported by NSF CAREER award CBET-1150085, in part by NSF EPSCoR Cooperative Agreement #IIA-1330406 and by the University of Rhode Island. YMNB received support from a 2015 University of Rhode Island Graduate School Fellowship. We are grateful to Lyncée Tec SA (Lausanne, Switzerland) for graciously providing DHM analyses of our patterned gold films.

ABBREVIATIONS

SEM, Scanning Electron Microscopy; FE-SEM, Field-Emission SEM; EDS, Energy-Dispersive X-Ray Spectroscopy; LPCVD, Low-Pressure Chemical Vapor Deposition; SiN_x, (Silicon-rich) Silicon Nitride; XPS, X-Ray Photoelectron Spectroscopy; DHM, Digital Holographic Microscopy.

REFERENCES

1. Mueller, C.; Harb, M.; Dwyer, J. R.; Miller, R. J. D., Nanofluidic Cells with Controlled Pathlength and Liquid Flow for Rapid, High-Resolution in Situ Imaging with Electrons. *J. Phys. Chem. Lett.* 2013, *4*, 2339-2347.
2. Arafat, A.; Giesbers, M.; Rosso, M.; Sudhölter, E. J. R.; Schroën, K.; White, R. G.; Yang, L.; Linford, M. R.; Zuilhof, H., Covalent Biofunctionalization of Silicon Nitride Surfaces. *Langmuir* 2007, *23*, 6233-6244.
3. Dwyer, J. R.; Bandara, Y. M. N. D. Y.; Whelan, J. C.; Karawdeniya, B. I.; Nichols, J. W., Silicon Nitride Thin Films for Nanofluidic Device Fabrication. In *Nanofluidics, 2nd Edition*, 2 ed.; Edel, J.; Ivanov, A.; Kim, M., Eds. Royal Society for Chemistry: 2017; Chapter 7.
4. Haywood, D. G.; Saha-Shah, A.; Baker, L. A.; Jacobson, S. C., Fundamental Studies of Nanofluidics: Nanopores, Nanochannels, and Nanopipets. *Anal. Chem.* 2015, *87*, 172-187.
5. Taniguchi, M., Selective Multidetector Using Nanopores. *Anal. Chem.* 2015, *87*, 188-199.
6. Kudr, J.; Skalickova, S.; Nejd, L.; Moulick, A.; Ruttkay-Nedecky, B.; Adam, V.; Kizek, R., Fabrication of Solid-State Nanopores and Its Perspectives. *ELECTROPHORESIS* 2015, *36*, 2367-2379.
7. Whelan, J. C.; Karawdeniya, B. I.; Bandara, Y. M. N. D. Y.; Velleco, B. D.; Masterson, C. M.; Dwyer, J. R., Electroless Plating of Thin Gold Films Directly onto Silicon Nitride Thin Films and into Micropores. *ACS Appl. Mater. Interfaces* 2014, *6*, 10952-10957.
8. Dahlin, A. B., Sensing Applications Based on Plasmonic Nanopores: The Hole Story. *Analyst* 2015, *140*, 4748-4759.
9. Jin, Y.; Kang, X.; Song, Y.; Zhang, B.; Cheng, G.; Dong, S., Controlled Nucleation and Growth of Surface-Confined Gold Nanoparticles on a (3-Aminopropyl)Trimethoxysilane-Modified Glass Slide: A Strategy for SPR Substrates. *Anal. Chem.* 2001, *73*, 2843-2849.
10. Asher, T.; Inberg, A.; Glickman, E.; Fishelson, N.; Shacham-Diamand, Y., Formation and Characterization of Low Resistivity Sub-100 nm Copper Films Deposited by Electroless on SAM. *Electrochim. Acta* 2009, *54*, 6053-6057.
11. Flavel, B. S.; Yu, J.; Ellis, A. V.; Quinton, J. S.; Shapter, J. G., Solution Chemistry Approach to Fabricate Vertically Aligned Carbon Nanotubes on Gold Wires: Towards Vertically Integrated Electronics. *Nanotechnology* 2008, *19*, 445301.
12. Vossmeier, T.; DeIonno, E.; Heath, J. R., Light-Directed Assembly of Nanoparticles. *Angew. Chem., Int. Ed. Engl.* 1997, *36*, 1080-1083.
13. Møller, P.; Nielsen, L. P., *Advanced Surface Technology*. Møller & Nielsen APS: Denmark, 2013; Vol. 1, p 594.

14. Menon, V. P.; Martin, C. R., Fabrication and Evaluation of Nanoelectrode Ensembles. *Anal. Chem.* 1995, *67*, 1920-1928.
15. Hulteen, J. C.; Martin, C. R., A General Template-Based Method for the Preparation of Nanomaterials. *J. Mater. Chem.* 1997, *7*, 1075-1087.
16. McCarley, R. L.; Vaidya, B.; Wei, S.; Smith, A. F.; Patel, A. B.; Feng, J.; Murphy, M. C.; Soper, S. A., Resist-Free Patterning of Surface Architectures in Polymer-Based Microanalytical Devices. *J. Am. Chem. Soc.* 2005, *127*, 842-843.
17. Henry, A. C.; McCarley, R. L., Selective Deposition of Metals on Plastics Used in the Construction of Microanalytical Devices: Photo-Directed Formation of Metal Features on PMMA†. *J. Phys. Chem. B* 2001, *105*, 8755-8761.
18. Carvalho, R. R.; Pujari, S. P.; Lange, S. C.; Sen, R.; Vrouwe, E. X.; Zuilhof, H., Local Light-Induced Modification of the inside of Microfluidic Glass Chips. *Langmuir* 2016, *32*, 2389-2398.
19. Kwok, H.; Briggs, K.; Tabard-Cossa, V., Nanopore Fabrication by Controlled Dielectric Breakdown. *PLoS ONE* 2014, *9*, e92880.
20. Han, A.; Kuan, A.; Golovchenko, J.; Branton, D., Nanopatterning on Nonplanar and Fragile Substrates with Ice Resists. *Nano Lett.* 2012, *12*, 1018-1021.
21. Santinacci, L.; Djenizian, T.; Hildebrand, H.; Ecoffey, S.; Mokdad, H.; Campanella, T.; Schmuki, P., Selective Palladium Electrochemical Deposition onto AFM-Scratched Silicon Surfaces. *Electrochim. Acta* 2003, *48*, 3123-3130.
22. Guan, F.; Chen, M.; Yang, W.; Wang, J.; Yong, S.; Xue, Q., Fabrication of Patterned Gold Microstructure by Selective Electroless Plating. *Appl. Surf. Sci.* 2005, *240*, 24-27.
23. Zabetakis, D.; Dressick, W. J., Selective Electroless Metallization of Patterned Polymeric Films for Lithography Applications. *ACS Appl. Mater. Interfaces* 2009, *1*, 4-25.
24. Rosso, M.; Giesbers, M.; Arafat, A.; Schroën, K.; Zuilhof, H., Covalently Attached Organic Monolayers on SiC and Si_xN₄ Surfaces: Formation Using UV Light at Room Temperature. *Langmuir* 2009, *25*, 2172-2180.
25. Whelan, J. C.; Karawdeniya, B. I.; Bandara, Y. M. N. D. Y.; Velleco, B. D.; Masterson, C. M.; Dwyer, J. R., Correction to Electroless Plating of Thin Gold Films Directly onto Silicon Nitride Thin Films and into Micropores. *ACS Appl. Mater. Interfaces* 2015, *7*, 26004-26004.
26. Kong, Y.; Chen, H.; Wang, Y.; Soper, S. A., Fabrication of a Gold Microelectrode for Amperometric Detection on a Polycarbonate Electrophoresis Chip by Photodirected Electroless Plating. *ELECTROPHORESIS* 2006, *27*, 2940-2950.
27. Ko, J. W.; Koo, H. C.; Kim, D. W.; Seo, S. M.; Kang, T. J.; Kwon, Y.; Yoon, J. L.; Cheon, J. H.; Kim, Y. H.; Kim, J. J.; Park, Y. J., Electroless Gold Plating on Aluminum Patterned Chips for CMOS-Based Sensor Applications. *J. Electrochem. Soc.* 2010, *157*, D46-D49.

28. Porter, L. A.; Choi, H. C.; Ribbe, A. E.; Buriak, J. M., Controlled Electroless Deposition of Noble Metal Nanoparticle Films on Germanium Surfaces. *Nano Lett.* 2002, 2, 1067-1071.
29. Fabre, B.; Hennous, L.; Ababou-Girard, S.; Meriadec, C., Electroless Patterned Assembly of Metal Nanoparticles on Hydrogen-Terminated Silicon Surfaces for Applications in Photoelectrocatalysis. *ACS Appl. Mater. Interfaces* 2013, 5, 338-343.
30. Chen, S.-T.; Chen, G.-S., Nanoseeding Via Dual Surface Modification of Alkyl Monolayer for Site-Controlled Electroless Metallization. *Langmuir* 2011, 27, 12143-12148.

CHAPTER 5: PREFACE

Published: ACS Appl. Mater. Interfaces, 2016, 8 (44), pp 30583–30589

REAL-TIME PROFILING OF SOLID-STATE NANOPORES DURING SOLUTION-PHASE NANOFABRICATION.

Y.M. Nuwan D.Y. Bandara, Buddini Iroshika Karawdeniya, and Jason R. Dwyer*.

Department of Chemistry, University of Rhode Island, 140 Flagg Road, Kingston,
RI, 02881, United States.

Reprinted with permission from:

Real-Time Profiling Of Solid-State Nanopores During Solution-Phase
Nanofabrication. Y.M. Nuwan D.Y. Bandara, Buddini Iroshika Karawdeniya, and
Jason R. Dwyer*. ACS Appl. Mater. Interfaces, 2016, 8 (44), pp 30583–30589

Copyright 2016 American Chemical Society.

CHAPTER 5

REAL-TIME PROFILING OF SOLID-STATE NANOPORES DURING SOLUTION-PHASE NANOFABRICATION.

Y.M. Nuwan D.Y. Bandara, Buddini Iroshika Karawdeniya, and Jason R. Dwyer*.

Department of Chemistry, University of Rhode Island, 140 Flagg Road, Kingston,
RI, 02881, United States.

KEYWORDS: Nanopore; dielectric breakdown; electroless plating; nanopore conductance; silicon nitride nanopore; nanopore size; nanopore radius.

ABSTRACT

We describe a method for simply characterizing the size and shape of a nanopore during solution-based fabrication and surface modification, using only low-overhead approaches native to conventional nanopore measurements. Solution-based nanopore fabrication methods are democratizing nanopore science by supplanting the traditional use of charged-particle microscopes for fabrication, but nanopore profiling has customarily depended on microscopic examination. Our approach exploits the dependence of nanopore conductance in solution on nanopore size, shape, and surface chemistry in order to characterize nanopores. Measurements of the changing nanopore conductance during formation by etching or deposition can be analyzed using our method to characterize the nascent nanopore size and shape—beyond the typical cylindrical approximation—in real-time. Our approach thus accords with ongoing efforts to broaden the accessibility of nanopore science from fabrication through use: it is compatible with

conventional instrumentation and offers straightforward nanoscale characterization of the core tool of the field.

INTRODUCTION

A nanopore is a nanofluidic channel, with dimensions in all directions generally less than 100 nm, that can be used to deliver a host of capabilities for single-molecule sensing.¹⁻¹⁰ High-profile nanopore sensing efforts have targeted sequencing single strands of DNA and RNA; protein conformational analysis; and characterization of other biomolecules, molecular complexes, and nanoparticles. In the most straightforward implementation of nanopore sensing, the nanopore is the sole path connecting two reservoirs containing electrolyte solutions. Electrodes in each reservoir establish a potential difference across the nanopore that drives ions through the nanopore: passage of a target molecule, nanoparticle, or complex through the nanopore perturbs that ionic current and provides molecular-level information. That information naturally depends on the target's dimensions and physicochemical properties and the ionic solution composition, but it is also profoundly affected by the size, shape, and surface chemistry of the nanopore. In the case of a (cylinder-like) double-stranded DNA polymer that fills the entire length of a cylindrical nanopore as it transits through, a simple geometric treatment considering only the displacement of bulk ions by the polymer gives a straightforward expression for the macromolecule-induced conductance change¹¹

$$\chi_B \equiv \frac{\langle G \rangle - \langle G_b \rangle}{\langle G \rangle} \cong \left(\frac{r_{DNA}}{r_0} \right)^2 \quad (1)$$

with $\langle G \rangle$ and $\langle G_b \rangle$ the time-averaged conductance through an unobstructed and DNA-containing nanopore, respectively, and r_{DNA} and r_0 the cross-sectional radii of the molecule and nanopore. The expression does not capture the panoply of

complex phenomena giving rise to conductance perturbations in nanopore sensing,¹²⁻¹³ but does, in convenient closed form, appropriately underscore the importance of nanopore dimension. This geometric basis of the conductance change has been used to infer biopolymer conformation, for example: a folded-over polymer presents a larger effective cross-section than a linear one.¹⁴ The more elusive dependence of current change on single-stranded DNA base sequence, for example, underpins efforts to sequence single strands of DNA using nanopores.^{2, 8} In a powerful implementation of nanopore force spectroscopy, details of interaction energetics can be revealed if, and only if, a nanopore size is properly engineered to sterically force the linearization of a folded moiety during passage, or rupture of an intermolecular complex by barring passage of one of the partners.¹⁵⁻¹⁷

The ionic conductance (G), alone, of a nanopore with a charged surface can be expressed as the sum of a bulk and surface conductance term¹⁸⁻²¹

$$G = G_{\text{bulk}} + G_{\text{surface}} = K \cdot A + \mu|\sigma| \cdot B \quad (2)$$

when access resistance is negligible.²² Overlapping Debye layers require a more sophisticated treatment, but need not be considered over a broad useful range of nanopore sizes and solution ionic strengths.²³⁻²⁴ This simple formulation for G has been supported by experimental measurements in which nanopore conductance was measured for nanopores that had size and shape interrogated by combinations of transmission electron microscopy and electron energy loss spectroscopy.^{13, 18}

The bulk conductance is determined by the solution conductivity, K , and a volume integral, A , over the unique nanopore shape: $G_{\text{bulk}} = K \left(\int \frac{dz}{\pi(r(z))^2} \right)^{-1} = K \cdot A$ (with z -axis along the length of the pore). The surface conductance is determined by the

mobility of counterions proximal to the pore surface, μ , the density of surface chargeable groups, σ , and an integral, B , over the surface of the nanopore:

$G_{\text{surface}} = \mu|\sigma| \left(\int \frac{dz}{2\pi r(z)} \right)^{-1} = \mu|\sigma| \cdot B$. The two defined quantities A and B therefore contain information about the size and shape of the nanopore, determined by the collection of geometric parameters, q_j , relevant for a particular shape: $A = A(\{q_j(t)\})$ and $B = B(\{q_j(t)\})$. Nanopore materials are usually chosen with mechanical and physicochemical properties to minimize the change in size and shape in time, t , absent deliberate action. Commonly reported parameter values, which may be only a subset of those needed to fully characterize a given nanopore profile, include the limiting radius (the minimum radius along the profile), r_0 , and total nanopore length, L , that can in some cases be equated with the supporting membrane thickness. The experimentally-supported^{13, 18} treatment of the nanopore conductance here assumes axially and cylindrically symmetric nanopores in a size regime where access resistance is negligible,²² and that any surface charge emerges from a singly ionizable surface species described by a characteristic pK_a



Native or engineered nanopore surface chemistry is an important element in nanopore performance, and contributor to nanopore conductance. The conductance can be naturally exploited for nanopore characterizations in conjunction with solution-based nanopore fabrication methods, and is especially useful when more complex methods present barriers to use. Charged-particle milling is an established, but challenging and burdensome, approach for formation of the smallest, <10 nm nanopores in thin membranes.²⁵⁻²⁸ The use of (scanning) transmission electron microscopes ((S)TEM), helium ion microscopes, and

scanning electron microscopes (SEM) for fabrication imposes time and instrumentation costs; can expose the nanopore to possible surface contamination within the instrument and to risk of damage during handling, transfer, and charged particle beam exposure; and reveals little of the nanopore surface chemistry. In a purely imaging capacity, these microscopes are limited in their ability to characterize organic surface coatings, and without more involved measurements or image analysis,^{18, 29-34} yield only a nanopore limiting radius—not a fully characterized size and shape. Beyond the greater ease and technical benefits of a low-overhead, solution-based nanopore characterization, such an approach can more directly probe nanopore surface chemistry. The capabilities of solution-based nanopore fabrication make a strong case alone, however, for complementary solution-based characterization methods. The benefits and prospects of solution-based nanopore fabrication were demonstrated early-on in the field through the development and use of track-etched polymer nanopores.⁹ Formation of the etchant-susceptible ion-track requires a large-scale heavy ion accelerator facility which naturally imposes a barrier to widespread use of the fabrication method, although accessibility is improved by the ability to perform the solution-based chemical etching step in a standard chemistry lab well after the ion-track formation. Conformal metal coating of these often tortuous polymer nanopores by (solution-based) electroless plating was a vital development in the use of these polymer nanopores: the material deposition allows the nanopore dimensions to be fine-tuned after chemical etching, and the metal film provides a platform for subsequent chemical modification of the nanopore interior surface. Both etching and deposition steps developed for polymer membrane nanopores have been extended to silicon nitride membranes which offer benefits such as the fabrication

of smooth nanopores with lengths <100 nm.^{32, 35} More recently, dielectric breakdown (followed by voltage-assisted etching) of an impervious, insulating membrane, has emerged as a powerful new technique for nanopore fabrication.³⁶ It is an entirely solution-based approach, using essentially the same equipment required for conductance-based nanopore measurements, and quite readily produces nanopores in a wide range of sizes, including in the coveted <5 nm diameter range. The nanopore conductance can be measured during fabrication, providing an indication of the nanopore size at a given point in time. The dielectric breakdown approach allows nanopores to be fabricated in their native environment, in the same holder where they will be used for experiments, and without the contamination and damage risks associated with charged particle techniques. A conductance-based characterization will not damage a molecular surface coating suitable for conductance-based sensing, and can harness the natural and direct connection to the nanopore surface chemistry that makes it a valuable method for characterizing chemically-tailored nanopores.^{9, 23, 34, 37} The conductance model is equally useful when a pore is formed and enlarged, and when an initially large pore is resized by solution-based deposition, including film growth.^{9, 19, 35, 38} Etching and deposition may be used in concert, with a pore being initially etched larger than desired to accommodate an electroless gold film, for example, that may ease nanopore surface chemical modification. In this work we wanted to understand how the measured conductance during nanopore fabrication—by deliberate expansion, closure, or both in consort—could be used to profile the nascent nanochannel. Simulations will focus, for expediency, on nanopores fabricated via deposition of surface coatings: the principles, however, are general.

THEORY

The algebraic structure of $G = K \cdot A + \mu|\sigma| \cdot B$, and its underlying dependencies, means that a single-point conductance measurement can provide enough information to size a nanopore only when the shape is known and the fitting involves only a single geometric degree of freedom. Measurement of G versus K —by changing the electrolyte solution conductivity—for a given nanopore can provide greater insight into the nanopore size, shape, and surface chemistry.^{18, 21-23} The conductance change after adding a monolayer of known thickness, for example, can provide similar information to what is provided after a solution conductivity change, and measuring G versus K for the nanopore before and after monolayer formation provides the richest description of the nanopore within this framework.²³ Changes of electrolyte solution are tedious, however, and disruptive to a solution-based nanopore fabrication approach. A simple ongoing measurement of the nanopore conductance during nanopore formation, however, can be done as part of the fabrication process, and is in fact performed routinely on a single-point measurement basis. Each fixed-time conductance is of course connected through Equation (2) to the instantaneous nanopore size and shape, where the applicability of the conductance model has been independently verified by electron-based imaging and spectroscopy.^{13, 18} A single conductance value, however, offers a limited ability to characterize a nanopore described by more than one free geometric parameter. Measurement and use of a series of conductance values at times t_i : $G(t_0, \{q_j(t_0)\})$, $G(t_1, \{q_j(t_1)\})$, ... $G(t_n, \{q_j(t_n)\})$, can provide more information than the conductance at a single time-point since the changes in conductance are caused by underlying changes in the initial nanopore dimensions, $\{q_j(t_0)\}$, in time. We perform simulations consistent with the following conditions

to demonstrate how to extract this information content. Nanometer-scale deposition or etching should not appreciably change the electrolyte solution conductivity, nor should the nanopore surface chemistry change (except through deliberate action) throughout either type of fabrication process. We make the reasonable assumption that material transfer will be uniform across the surface, so that the nanopore shape will remain unchanged. Silicon nitride, the most common membrane material in which to form nanopores, is amorphous, and so will not inherently be prone to anisotropic etching.³⁹ Electroless plating, a surface deposition method that has been used with great success in resizing nanopores,⁹ conformally coats even rough surfaces,⁴⁰ and film growth by polymer chain extension, for example, should be another effective route to reliably tune nanopore size.⁴¹ We can then write

$$\frac{dG}{dt} = K \frac{dA(\{q_j(t)\})}{dt} + \mu|\sigma| \frac{dB(\{q_j(t)\})}{dt} = K \sum_j \left(\frac{\partial A}{\partial q_j} \right) \frac{dq_j}{dt} + \mu|\sigma| \sum_j \left(\frac{\partial B}{\partial q_j} \right) \frac{dq_j}{dt} = K \sum_j f(\{q_j\}, v_{mt}, t) + \mu|\sigma| \sum_j g(\{q_j\}, v_{mt}, t) \quad (4)$$

where the $\left(\frac{\partial A}{\partial q_j} \right)$ and $\left(\frac{\partial B}{\partial q_j} \right)$ depend on the nanopore profile, and the $\frac{dq_j}{dt}$ depend on the profile and the material transfer rate, v_{mt} , whether by nanopore etching or coating by deposition. The material transfer rate is conveniently measured as the change in nanopore radius over time. While two nanopores with different shapes and sizes may have the same initial conductance, $G(t_0, \{q_j(t_0)\}) = G(t_0, \{q'_j(t_0)\})$, the rates of change of the conductances will be different, and determined by the individual nanopore sizes and shapes (and identical material transfer rates). Measurement of several values of the experimental $G(t_i, \{q_j(t_i)\})$ can use this dependence to enhance real-time conductance-based nanopore characterization

during fabrication. To present concrete examples of the general framework, we selected four representative nanopore profiles: cylindrical, double-conical, conical-cylindrical, and hyperbolic (Figure 5.1).^{18, 21-22, 29, 32} For all profiles, we limited the $\{q_j\}$ to two free parameters per shape: (r_0, L) —the limiting (minimum) radius and total nanopore length (see Tables S-1 and S-2 for notation and equations). Independent experimental studies of nanopore profiles^{18, 22} were used to guide the constraints and to make reasonable parameter value assignments to allow for numerical examples; the nanopore characterization method is general, however, and does not depend upon these particular numerical values.^{21, 23} We restricted the initial outer radius to be 10 nm greater than the initial limiting radius (not applicable to the cylindrical profile),²¹⁻²² and fixed the initial cylinder length of the conical-cylindrical pore to be 0.6 times its initial total length. The deposited coating was piecewise curved to maintain a uniform coating thickness across the entire nanopore surface (Figure 5.1 and Table S-2). Equation (4) then becomes

$$\frac{dG}{dt} = K \left(\left(\frac{\partial A}{\partial r_0} \right) \frac{dr_0}{dt} + \left(\frac{\partial A}{\partial L} \right) \frac{dL}{dt} \right) + \mu |\sigma| \left(\left(\frac{\partial B}{\partial r_0} \right) \frac{dr_0}{dt} + \left(\frac{\partial B}{\partial L} \right) \frac{dL}{dt} \right) = v_{mt} \left[K \left(\frac{\partial A}{\partial r_0} \right) + 2 \left(\frac{\partial A}{\partial L} \right) + \mu |\sigma| \left(\left(\frac{\partial B}{\partial r_0} \right) + 2 \left(\frac{\partial B}{\partial L} \right) \right) \right] \quad (5)$$

Parameter values used in calculations were typical of experiments and consistent with those in prior work with silicon nitride nanopores:²¹ for example, 1 M potassium chloride electrolyte solution in water, $K=14.95 \text{ S}\cdot\text{m}^{-1}$ (calculated using ion mobilities), $\text{pH}=7.0$, and surface $\text{pK}_a=7.9$. The material transfer rate was kept constant, $v_{mt} = dr_0/dt = 0.6 \text{ nm/h}$. More important than the particular parameter values, though, it is the form of equation (2) and its functional dependencies that are significant in this work.

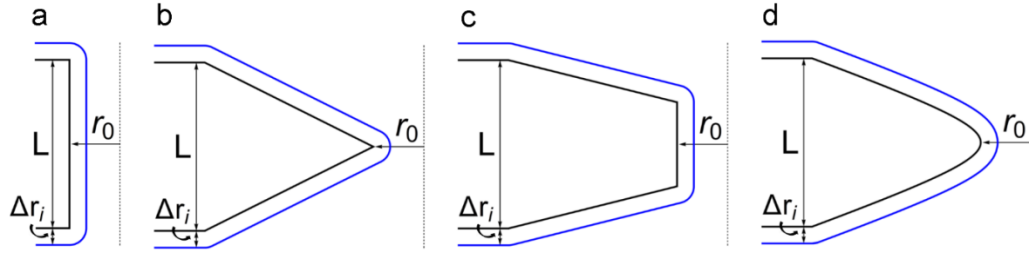


Figure 5.1: (a) Cylindrical, (b) double-conical, (c) conical-cylindrical, and (d) hyperbolic nanopore half-profile cross-sections cylindrically symmetric about the vertical z -axis (dotted line) of the pore. Profiles are shown before (black line) and after (blue line) material deposition to decrease the limiting nanopore radius, r_0 , by an amount Δr_i determined by the deposition time and material transfer rate.

RESULTS AND DISCUSSION

The ability to characterize a nanopore in real-time, during its formation, using only its conductance, is an incredibly compelling goal. Its pursuit relies on the connection between the conductance of a nanopore and its size, shape, and surface chemistry, and its attainment hinges on properly exploiting the functional form of that connection. We will focus on nanopores fabricated by deposition of a coating onto the outer membrane surface and inner surface of an existing, larger pore, but similar arguments hold for a nanopore formed by etching of a smaller pore to create a larger pore. Figure 5.2 highlights a primary challenge of nanopore conductance-based characterizations. The curves show the set of nanopore limiting radii and length, for each chosen nanopore shape, $\{r_{0,\text{shape}}, L_{\text{shape}}\}$, that generate a 200 nS conductance: there is not a unique solution. To use a single-point conductance value to characterize a nanopore by more than a broad range of possible shapes and sizes, or to provide better than an approximate size given an assumed profile, additional information is required.^{21, 23} Most commonly, knowledge of the particular fabrication method and conditions is used to choose an expected nanopore profile, and can often be used to constrain the nanopore length

to an experimental parameter such as the thickness of the membrane in which it is formed. Measurement of the conductance of a nanopore in time, in an essentially single-point sense, has demonstrated utility as a monitor of nanopore evolution even if it cannot provide an unambiguous characterization. Yet the time-dependence provides a set of experimental data points that we seek to mine to more fully characterize the nanopore than is possible using a single-point measurement of the conductance.

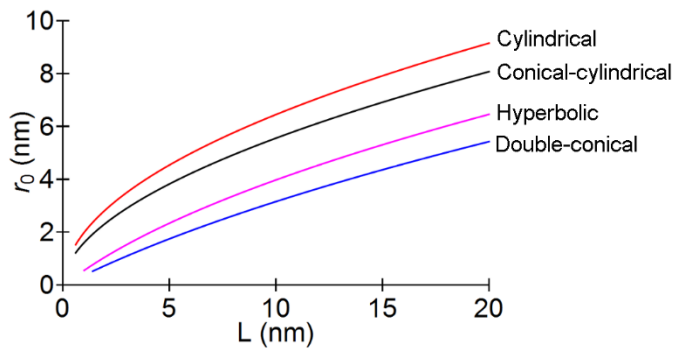


Figure 5.2: The plotted lines denote the pairings of limiting nanopore radius, r_0 , and nanopore length, L , for each nanopore profile, that will produce a 200 nS conductance.

The most immediately striking consequence of a real-time measurement of the conductance is that, as shown in Figure 5.3, it reveals a clear distinction between different nanopore profiles. When different candidate profiles are used to fit experimental nanopore conductance data, the conductance versus time provides a means to determine nanopore shape and size. To produce the data plotted in Figure 5.3, we used the four representative nanopore profiles all with an initial 200 nS conductance and 10 nm total nanopore length. The initial nanopore limiting radii were ~ 6.4 , 3.1, 5.5, and 4.0 nm, respectively, for the cylindrical, double-conical, conical-cylindrical, and hyperbolic nanopore profiles. We calculated the conductance for each profile as the radii were reduced at the same rate, $v_{mt} =$

0.6 nm/h, during a simulated, deposition-based fabrication process. As shown below, the radius change after a given time must be known, but the method does not require a constant material transfer rate. We chose a constant rate, commonly observed in micromachining processing,³⁹ however, because it affords straightforward insights into the functional dependencies beyond what is revealed by the numerical results. Given the form of equation (5), it is perhaps unsurprising that even with constant v_{mt} (and therefore identical absolute rates of change of the radii across profile type), $\frac{dG}{dt}$ is not linear and depends on profile type (inset of Figure 5.3). The quantitative details of this behavior provide a means of extracting nanopore size and shape information from the measured conductance changes. Figure S-5.2 reinforces the geometrical underpinnings of this profiling method, in plots of the geometry integrals, A and B , versus time.

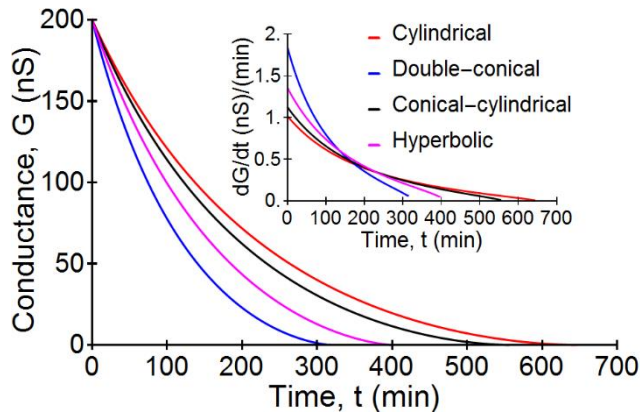


Figure 5.3: Nanopores with an initial 200 nS conductance ($L(t_0) = 10$ nm, $r_0(t_0)$ from Figure 5.2) show a shape-dependent decrease in conductance due to material deposition at a constant rate, v_{mt} . The inset plots the rate of conductance change, calculated using nearest-neighbor differences, $\frac{dG}{dt} \cong \frac{G(t_{i+1}) - G(t_i)}{t_{i+1} - t_i}$.

Figure 5.4 illustrates the general approach we have adopted for extracting quantitative nanopore geometric parameters from $G(t)$ —an approach allowing for a nanopore characterization with the full geometric parameter flexibility outlined

in Figure 5.2, and that emphasizes the minimal number of conductance values required. We chose to simulate the deposition-based fabrication of nanopores with an initial conductance, $G_{\text{shape}}^{\text{expt}}(t_0) = 200 \text{ nS}$, and initial radius, $r_{0,\text{shape}}^{\text{expt}}(t_0) = 3.5 \text{ nm}$ (both values the same for all simulated experimental shapes); Figure 5.2 gives the corresponding initial nanopore lengths, $L_{\text{shape}}^{\text{expt}}(t_0)$, for each nanopore profile. For each nanopore profile, we set the initial nanopore size, $(r_{0,\text{shape}}^{\text{expt}}(t_0), L_{\text{shape}}^{\text{expt}}(t_0))$, and used the progression of dimensions, $(r_{0,\text{shape}}^{\text{expt}}(t_0) - \Delta r_i(t_0, t_i), L_{\text{shape}}^{\text{expt}}(t_0) + 2\Delta r_i(t_0, t_i))$, to simulate the post-deposition conductances $G_{\text{shape}}^{\text{expt}}(t_1)$ and $G_{\text{shape}}^{\text{expt}}(t_2)$. For a constant material transfer rate, v_{mt} , $\Delta r_i = (t_i - t_0)v_{\text{mt}}$. While more generally $\Delta r_i = \Delta r_i(t_i, t_0, v_{\text{mt}}(t))$, the procedure implemented here relies on knowledge of this radius change only, not whether the material transfer rate is constant in time or not. We outline the conceptual framework for the characterization and provide a detailed step-by-step tutorial in the SI. The initial conductance, $G_{\text{shape}}^{\text{expt}}(t_0)$, was used in conjunction with Figure 5.5.2 to establish the set of candidate $\{(r_{0,\text{shape}}(t_0), L_{\text{shape}}(t_0))\}$, for each nanopore profile, whose members all have the initial conductance $G_{\text{shape}}(t_0) = G_{\text{shape}}^{\text{expt}}(t_0)$. The range of candidate sizes, for each candidate shape, is represented by the dotted lines in Figure 5.4a-d. Given $G_{\text{shape}}^{\text{expt}}(t_0)$, alone, neither size nor shape can yet be determined. Each of these possible candidate geometries (size and shape) was then modified by the deposition of material to provide sets of nanopore dimensions given by $\{(r_{0,\text{shape}}(t_0) - \Delta r_i, L_{\text{shape}}(t_0) + 2\Delta r_i)\}$ for times t_1 , t_2 , and t_3 , with corresponding sets of conductances $\{G_{\text{shape}}(t_1)\}$, $\{G_{\text{shape}}(t_2)\}$, and $\{G_{\text{shape}}(t_3)\}$.

(solid curves in Figure 5.4a-d). We then used the post-deposition $G_{\text{shape}}^{\text{expt}}(t_i)$ to determine the nanopore size and shape. We found the initial limiting radius, $r_{0,\text{shape}}(t_0)$, for each nanopore shape, that gave a conductance $G_{\text{shape}}(t_1) = G_{\text{shape}}^{\text{expt}}(t_1)$. That is, when the experimental nanopore was cylindrical, we found the $r_{0,\text{shape}}(t_0)$ for cylindrical, double-conical, conical-cylindrical, and hyperbolic profiles that allowed the candidate pore conductance to match the experimental value, and plotted the radii in Figure 5.4e. Figure 5.4f-h are plots of the $r_{0,\text{shape}}(t_0)$ when the conductances of double-conical, conical-cylindrical, and hyperbolic experimental nanopores were equated to the conductances of the same four candidate shapes. No matter the experimental profile, after two conductance values, all four candidate shapes—with different sizes—were equally viable conductance-based matches. By repeating this process by finding $r_{0,\text{shape}}(t_0)$ to satisfy $G_{\text{shape}}(t_2) = G_{\text{shape}}^{\text{expt}}(t_2)$, the experimental nanopore size and shape both emerge. When the candidate nanopore profile matches the simulated experimental profile, all extracted $r_{0,\text{shape}}(t_0)$ have the same value for all t_i , which essentially delivers a simultaneous solution of $G_{\text{shape}}(t_i, \{q_j(t_i)\}) = G_{\text{shape}}^{\text{expt}}(t_i, \{q_j(t_i)\})$ for all time-points. The curves in Figure 5.4e-h illustrate this successful characterization; the agreement is shown in terms of $r_{0,\text{shape}}(t_0)$, but $L_{\text{shape}}(t_0)$ has the same behavior. Figure 5.4e plots the $r_{0,\text{shape}}(t_0)$ when the simulated $G_{\text{cylindrical}}^{\text{expt}}(t_i)$ values were fit using cylindrical, double-conical, conical-cylindrical, and hyperbolic profiles: only the cylindrical candidate nanopore returns the same $r_{0,\text{shape}}(t_0)$ for different t_i . Figures 5.4f-h show, by the constancy of the correct $r_{0,\text{shape}}(t_0)$, the same successful capture of size and shape of double-conical, conical-cylindrical, and hyperbolic simulated experimental nanopores, respectively. Measurement of

more conductance points does not provide more information, given the framework presented here, but can add numerical robustness to this approach. Alternatively, the formal need for only three conductance values allows one to piecewise repeat the shape-and size-profiling on independent sets of three conductance values throughout the duration of the fabrication, allowing for the possibility to extend this method to anisotropically-etching or -depositing materials. An extreme departure from the usual progression of conductance in time may signal the need for a more involved steady-state solution-based characterization of a pore after fabrication,²¹ although even in this case the present time-dependent method should provide bounds on the evolving nanopore size. We note again, for generality, that while we used a constant v_{mt} , the plating rate must be known, but need not be constant. Fitting conductance values in time leverages the form of equation (2) to reveal the nanopore shape and extract dimensions from a solution-based nanopore fabrication method.

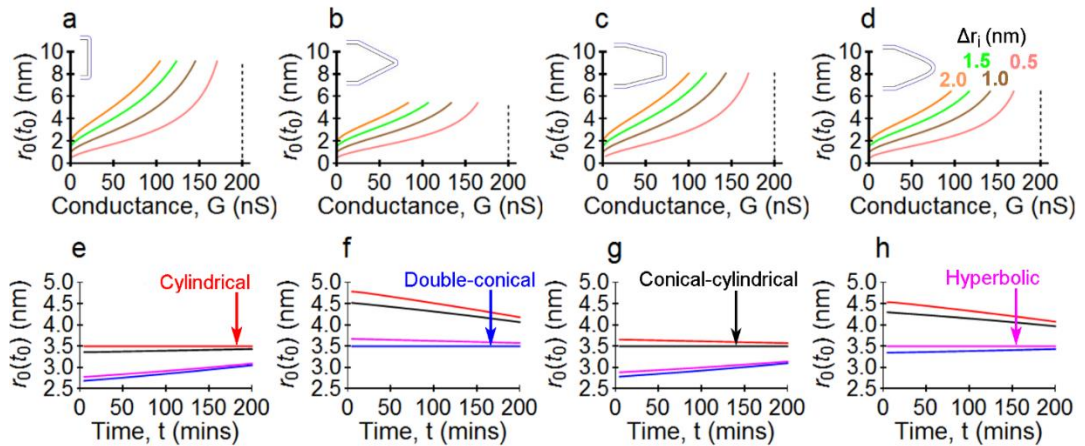


Figure 5.4: The conductance of initially 200 nS (a) cylindrical, (b) double-conical, (c) conical-cylindrical, and (d) hyperbolic nanopores can be satisfied by a range of radii (dotted vertical lines). Fixed decreases of each possible radius (in time) generate characteristic conductance progressions that depend on the nanopore shape and initial size (conductance curves labelled with their particular Δr_i). Simulated experimental conductance data versus time for $G_{\text{shape}}^{\text{expt}}(t_0) = 200$ nS, $r_{0,\text{shape}}(t_0) = 3.5$ nm pores of each shape were compared to the plots in (a-d) to

reveal the (e) cylindrical (red), (f) double-conical (blue), (g) conical-cylindrical (black), and (h) hyperbolic (magenta) experimental nanopore size and shapes by the constancy of the fitting $r_{0,\text{shape}}(t_0)$. The relevant experimental profiles for each column are inset in the top row.

CONCLUSIONS

The charged-particle, complex instrumentation approaches that dominated early nanopore fabrication methods allowed, in principle, for high-resolution nanopore characterizations, although such capability was rarely employed beyond determining a limiting radius. These instrumental approaches face limitations such as high likelihood of surface contamination and inability to probe soft (e.g. organic) nanopore coatings, and they add workflow steps that could be costly in time and instrumentation. Even so, since the nanopores were formed in these instruments, it was expedient to follow fabrication with the chosen degree of characterization in the same instrument. The ongoing development of completely solution-based methods—including the advent of new techniques—to fabricate nanopores has ushered in an exciting new area for nanofluidics, generally, and nanopore science in particular. Nanopores can now be formed in their native liquid environment, and without the instrument and workflow cost of charged-particle methods. We have modelled the nanopore conductance with a simple framework that nevertheless includes an explicit surface chemistry term and has demonstrated concordance with independent experimental characterizations of nanopore sizes and shapes of most importance for routine use in single molecule science.^{13, 18} We have presented theoretical examples that describe the creation of small nanopores by coating larger nanopores, so that fabrication involves a decrease in the nanopore radius and conductance. The results, however, are equally applicable to nanopore

fabrication methods such as dielectric breakdown followed by voltage-assisted etching, or the chemical etching of ion-tracked membranes. The nanopore conductance is routinely measured during dielectric breakdown as a diagnostic, and such a measurement can be readily implemented during nanopore fabrication by material deposition. We have shown here that by analyzing a series of conductance measurements in time, rather than only an instantaneous measurement, we are able to extract information on nanopore size and shape, and thereby enrich the execution and interpretation of nanopore experiments without increasing the experimental burden.

ASSOCIATED CONTENT

Supporting Information. Detailed descriptions of nanopore profiles and a step-by-step tutorial detailing the numerical nanopore characterization. This material is available free of charge via the Internet at <http://pubs.acs.org>.

AUTHOR INFORMATION

Corresponding Author

*E-mail: jdwyer@chm.uri.edu

AUTHOR CONTRIBUTIONS

The manuscript was written through contributions of all authors. All authors have given approval to the final version of the manuscript.

FUNDING SOURCES

This research has been supported by NSF CAREER award CBET-1150085, and by the University of Rhode Island, including 2015 University of Rhode Island Graduate School Fellowships for YMNB and BIK.

ABBREVIATIONS

min., minutes; h, hours.

REFERENCES

1. Haywood, D. G.; Saha-Shah, A.; Baker, L. A.; Jacobson, S. C., Fundamental Studies of Nanofluidics: Nanopores, Nanochannels, and Nanopipets. *Anal. Chem.* 2015, *87*, 172-187.
2. Taniguchi, M., Selective Multidetector Using Nanopores. *Anal. Chem.* 2015, *87*, 188-199.
3. Reiner, J. E.; Balijepalli, A.; Robertson, J. W. F.; Campbell, J.; Suehle, J.; Kasianowicz, J. J., Disease Detection and Management Via Single Nanopore-Based Sensors. *Chem. Rev.* 2012, *112*, 6431-6451.
4. Howorka, S.; Siwy, Z., Nanopore Analytics: Sensing of Single Molecules. *Chem. Soc. Rev.* 2009, *38*, 2360-2384.
5. Miles, B. N.; Ivanov, A. P.; Wilson, K. A.; Dogan, F.; Japrun, D.; Edel, J. B., Single Molecule Sensing with Solid-State Nanopores: Novel Materials, Methods, and Applications. *Chem. Soc. Rev.* 2013, *42*, 15-28.
6. Kudr, J.; Skalickova, S.; Nejd, L.; Moulick, A.; Ruttkay-Nedecky, B.; Adam, V.; Kizek, R., Fabrication of Solid-State Nanopores and Its Perspectives. *ELECTROPHORESIS* 2015, *36*, 2367-2379.
7. Oukhaled, A.; Bacri, L.; Pastoriza-Gallego, M.; Betton, J.-M.; Pelta, J., Sensing Proteins through Nanopores: Fundamental to Applications. *ACS Chemical Biology* 2012, *7*, 1935-1949.
8. Branton, D.; Deamer, D. W.; Marziali, A.; Bayley, H.; Benner, S. A.; Butler, T.; Di Ventra, M.; Garaj, S.; Hibbs, A.; Huang, X. H.; Jovanovich, S. B.; Krstic, P. S.; Lindsay, S.; Ling, X. S. S.; Mastrangelo, C. H.; Meller, A.; Oliver, J. S.; Pershin, Y. V.; Ramsey, J. M.; Riehn, R.; Soni, G. V.; Tabard-Cossa, V.; Wanunu, M.; Wiggin, M.; Schloss, J. A., The Potential and Challenges of Nanopore Sequencing. *Nat. Biotechnol.* 2008, *26*, 1146-1153.
9. Sexton, L. T.; Horne, L. P.; Martin, C. R., Developing Synthetic Conical Nanopores for Biosensing Applications. *Molecular BioSystems* 2007, *3*, 667-685.
10. Bayley, H.; Martin, C. R., Resistive-Pulse Sensing-from Microbes to Molecules. *Chem. Rev.* 2000, *100*, 2575-2594.
11. Wanunu, M.; Sutin, J.; McNally, B.; Chow, A.; Meller, A., DNA Translocation Governed by Interactions with Solid-State Nanopores. *Biophys. J.* 2008, *95*, 4716-4725.
12. Aksimentiev, A., Deciphering Ionic Current Signatures of DNA Transport through a Nanopore. *Nanoscale* 2010, *2*, 468-483.
13. Smeets, R. M. M.; Keyser, U. F.; Krapf, D.; Wu, M.-Y.; Dekker, N. H.; Dekker, C., Salt Dependence of Ion Transport and DNA Translocation through Solid-State Nanopores. *Nano Lett.* 2006, *6*, 89-95.
14. Tabard-Cossa, V.; Trivedi, D.; Wiggin, M.; Jetha, N. N.; Marziali, A., Noise Analysis and Reduction in Solid-State Nanopores. *Nanotechnology* 2007, *18*.

15. Tabard-Cossa, V.; Wiggin, M.; Trivedi, D.; Jetha, N. N.; Dwyer, J. R.; Marziali, A., Single-Molecule Bonds Characterized by Solid-State Nanopore Force Spectroscopy. *ACS Nano* 2009, 3, 3009-3014.
16. McNally, B.; Wanunu, M.; Meller, A., Electromechanical Unzipping of Individual DNA Molecules Using Synthetic Sub-2 Nm Pores. *Nano Lett.* 2008, 8, 3418-3422.
17. Zhao, Q.; Sigalov, G.; Dimitrov, V.; Dorvel, B.; Mirsaidov, U.; Sligar, S.; Aksimentiev, A.; Timp, G., Detecting SnpS Using a Synthetic Nanopore. *Nano Lett.* 2007, 7, 1680-1685.
18. Liebes, Y.; Drozdov, M.; Avital, Y. Y.; Kauffmann, Y.; Rapaport, H.; Kaplan, W. D.; Ashkenasy, N., Reconstructing Solid State Nanopore Shape from Electrical Measurements. *Appl. Phys. Lett.* 2010, 97, 223105.
19. Ayub, M.; Ivanov, A.; Instuli, E.; Cecchini, M.; Chansin, G.; McGilvery, C.; Hong, J.; Baldwin, G.; McComb, D.; Edel, J. B.; Albrecht, T., Nanopore/Electrode Structures for Single-Molecule Biosensing. *Electrochim. Acta* 2010, 55, 8237-8243.
20. Stein, D.; Kruithof, M.; Dekker, C., Surface-Charge-Governed Ion Transport in Nanofluidic Channels. *Phys. Rev. Lett.* 2004, 93, 035901.
21. Frament, C. M.; Dwyer, J. R., Conductance-Based Determination of Solid-State Nanopore Size and Shape: An Exploration of Performance Limits. *J. Phys. Chem. C* 2012, 116, 23315-23321.
22. Kowalczyk, S. W.; Grosberg, A. Y.; Rabin, Y.; Dekker, C., Modeling the Conductance and DNA Blockade of Solid-State Nanopores. *Nanotechnology* 2011, 22, 315101.
23. Frament, C. M.; Bandara, N.; Dwyer, J. R., Nanopore Surface Coating Delivers Nanopore Size and Shape through Conductance-Based Sizing. *ACS Appl. Mater. Interfaces* 2013, 5, 9330-9337.
24. Makra, I.; Jágerszki, G.; Bitter, I.; Gyurcsányi, R. E., Nernst-Planck/Poisson Model for the Potential Response of Permselective Gold Nanopores. *Electrochim. Acta* 2012, 73, 70-77.
25. Yang, J.; Ferranti, D. C.; Stern, L. A.; Sanford, C. A.; Huang, J.; Ren, Z.; Qin, L.-C.; Hall, A. R., Rapid and Precise Scanning Helium Ion Microscope Milling of Solid-State Nanopores for Biomolecule Detection. *Nanotechnology* 2011, 22, 285310.
26. Li, J.; Stein, D.; McMullan, C.; Branton, D.; Aziz, M. J.; Golovchenko, J. A., Ion-Beam Sculpting at Nanometre Length Scales. *Nature* 2001, 412, 166-169.
27. Storm, A. J.; Chen, J. H.; Ling, X. S.; Zandbergen, H. W.; Dekker, C., Fabrication of Solid-State Nanopores with Single-Nanometre Precision. *Nature Materials* 2003, 2, 537-540.
28. Spinney, P. S.; Howitt, D. G.; Smith, R. L.; Collins, S. D., Nanopore Formation by Low-Energy Focused Electron Beam Machining. *Nanotechnology* 2010, 21, 375301.

29. Kim, M. J.; McNally, B.; Murata, K.; Meller, A., Characteristics of Solid-State Nanometre Pores Fabricated Using a Transmission Electron Microscope. *Nanotechnology* 2007, 18.
30. Kuan, A. T.; Golovchenko, J. A., Nanometer-Thin Solid-State Nanopores by Cold Ion Beam Sculpting. *Appl. Phys. Lett.* 2012, 100, 213104-213104.
31. Wu, M.-Y.; Smeets, R. M. M.; Zandbergen, M.; Ziese, U.; Krapf, D.; Batson, P. E.; Dekker, N. H.; Dekker, C.; Zandbergen, H. W., Control of Shape and Material Composition of Solid-State Nanopores. *Nano Lett.* 2009, 9, 479-484.
32. Vlassioug, I.; Apel, P. Y.; Dmitriev, S. N.; Healy, K.; Siwy, Z. S., Versatile Ultrathin Nanoporous Silicon Nitride Membranes. *Proceedings of the National Academy of Sciences of the United States of America* 2009, 106, 21039-21044.
33. Freedman, K. J.; Ahn, C. W.; Kim, M. J., Detection of Long and Short DNA Using Nanopores with Graphitic Polyhedral Edges. *ACS Nano* 2013, 7, 5008-5016.
34. Wei, R.; Pedone, D.; Zürner, A.; Döblinger, M.; Rant, U., Fabrication of Metallized Nanopores in Silicon Nitride Membranes for Single-Molecule Sensing. *Small* 2010, 6, 1406-1414.
35. Whelan, J. C.; Karawdeniya, B. I.; Bandara, Y. M. N. D. Y.; Velleco, B. D.; Masterson, C. M.; Dwyer, J. R., Electroless Plating of Thin Gold Films Directly onto Silicon Nitride Thin Films and into Micropores. *ACS Appl. Mater. Interfaces* 2014, 6, 10952-10957.
36. Kwok, H.; Briggs, K.; Tabard-Cossa, V., Nanopore Fabrication by Controlled Dielectric Breakdown. *PLoS ONE* 2014, 9, e92880.
37. Yusko, E. C.; Johnson, J. M.; Majd, S.; Prangkio, P.; Rollings, R. C.; Li, J.; Yang, J.; Mayer, M., Controlling Protein Translocation through Nanopores with Bio-Inspired Fluid Walls. *Nature Nanotechnology* 2011, 6, 253-260.
38. Wanunu, M.; Meller, A., Chemically Modified Solid-State Nanopores. *Nano Lett.* 2007, 7, 1580-1585.
39. Williams, K. R.; Muller, R. S., Etch Rates for Micromachining Processing. *J. Microelectromech. Syst.* 1996, 5, 256-269.
40. Møller, P.; Nielsen, L. P., *Advanced Surface Technology*. Møller & Nielsen APS: Denmark, 2013; Vol. 1, p 594.
41. de Groot, G. W.; Santonicola, M. G.; Sugihara, K.; Zambelli, T.; Reimhult, E.; Vörös, J.; Vancso, G. J., Switching Transport through Nanopores with Ph-Responsive Polymer Brushes for Controlled Ion Permeability. *ACS Appl. Mater. Interfaces* 2013, 5, 1400-1407.

CHAPTER 6: PREFACE

Published: *Electrophoresis*, 2018, 39, 626-634

CONDUCTANCE-BASED PROFILING OF NANOPORES: ACCOMMODATING FABRICATION IRREGULARITIES

Y.M. Nuwan D.Y. Bandara, Jonathan W. Nichols, Buddini Iroshika Karawdeniya,
and Jason R. Dwyer.

Department of Chemistry, University of Rhode Island, Kingston, RI, USA

Reprinted With Permission From:

Conductance-Based Profiling Of Nanopores: Accommodating Fabrication Irregularities. Y.M. Nuwan D.Y. Bandara, Jonathan W. Nichols, Buddini Iroshika Karawdeniya, and Jason R. Dwyer. *Electrophoresis* 2018 (39) 626-634.

CHAPTER 6

CONDUCTANCE-BASED PROFILING OF NANOPORES: ACCOMMODATING FABRICATION IRREGULARITIES

Y.M. Nuwan D.Y. Bandara, Jonathan W. Nichols, Buddini Iroshika Karawdeniya,
and Jason R. Dwyer.

Department of Chemistry, University of Rhode Island, 140 Flagg Road, Kingston,
RI, 02881, United States.

E-mail: jason_dwyer@uri.edu. Phone 1-401-874-4648. Fax 1-401-874-5072.

KEYWORDS: dielectric breakdown; nanopore; nanopore conductance; nanopore defect; pore density; silicon nitride nanopore.

ABBREVIATIONS: TEM-transmission electron microscopy; STEM-scanning transmission electron microscopy; EM-electron microscopy; MPVI-multilevel pulse-voltage injection

ABSTRACT

Solid-state nanopores are nanoscale channels through otherwise impermeable membranes. Single molecules or particles can be passed through electrolyte-filled nanopores by, e.g. electrophoresis, and then detected through the resulting physical displacement of ions within the nanopore. Nanopore size, shape, and surface chemistry must be carefully controlled, and on extremely challenging <10 nm-length scales. We previously developed a framework to characterize nanopores from the time-dependent changes in their conductance as they are being formed through solution-phase nanofabrication processes with the appeal of ease

and accessibility. We revisited this simulation work, confirmed the suitability of the basic conductance equation using the results of a time-dependent experimental conductance measurement during nanopore fabrication by Yanagi *et al.*, and then deliberately relaxed the model constraints to allow for (1) the presence of defects; and (2) the formation of two small pores instead of one larger one. Our simulations demonstrated that the time-dependent conductance formalism supports the detection and characterization of defects, as well as the determination of pore number, but with implementation performance depending on the measurement context and results. In some cases, the ability to discriminate numerically between the correct and incorrect nanopore profiles was slight, but with accompanying differences in candidate nanopore dimensions that could yield to post-fabrication conductance profiling, or be used as convenient uncertainty bounds. Time-dependent nanopore conductance thus offers insight into nanopore structure and function, even in the presence of fabrication defects.

INTRODUCTION

Nanopores are a rising tool for single-molecule science, featuring prominently in DNA sequencing efforts, but with broader reach into biophysics, and bioanalytical and materials chemistry.[1-12] The nanopore heart of these techniques is a nanofluidic channel generally less than 100 nm in all dimensions, formed through a membrane or support, with the particular dimensions dictated by the analyte and method. The essential determinants of nanopore performance include the elements of three general nanopore-specific parameter groupings: nanopore size, shape, and surface chemistry.[13-19] Even the most basic nanopore operating configuration illustrates the importance of these parameters, and also provides a means for assaying them. A nanopore is positioned as the sole fluid path

between two wells of electrolyte solution. Application of suitable voltages, typically ≤ 200 mV, across the impermeable support membrane drives ion passage through the nanopore. The resulting open-pore ionic conductance, G , is determined by the bulk solution conductivity, K , by the size and shape of the nanopore (here captured in volume and surface integrals, $A = \left(\int \frac{dz}{\pi(r(z))^2} \right)^{-1}$ and $B = \left(\int \frac{dz}{2\pi r(z)} \right)^{-1}$, respectively), and by properties of the nanopore-solution interface[13, 16, 18, 20-23]

$$G = K \cdot A(r, L) + \mu|\sigma| \cdot B(r, L) = G_{\text{bulk}} + G_{\text{surface}} \quad (1)$$

where σ is the nanopore surface charge density that attract counterions of mobility, μ . The pore has a radius, $r(z)$, that can vary along length, L , of the pore (aligned with the z -axis as shown in Figure S6.1). More complex theoretical approaches exist—a formulation including the access resistance term (neglected here for simplicity) is discussed in the supporting information (see Equation S6.1, Figure S6.2 and associated discussion)—but this straightforward conductance model provides a tractable and useful framework with good agreement with the measured conductance of nanopores across a range of experimentally determined sizes and shapes.[13, 16, 18, 20, 21, 24] As a species of interest passes through the nanopore, or is entrained therein, it perturbs the open-pore flow of ions, and frequently generates an analyte-specific current blockage (or enhancement)[4, 10, 13, 17, 23]. A simple analytical model for the conductance blockage wrought by the extension of an analyte such as DNA, of radius r_{analyte} , through the length of a uniformly cylindrical nanopore of radius r_0 , illustrates more directly the importance of nanopore dimensions:

$$\chi_B \equiv \frac{(\langle G \rangle - \langle G_b \rangle)}{\langle G \rangle} \cong \left(\frac{r_{\text{analyte}}}{r_0} \right)^2 \quad (2)$$

with $\langle G \rangle$ and $\langle G_b \rangle$ the time-averaged conductances of open, and analyte-filled, nanopore.[25] The more complex set of phenomena and parameters underpinning the current blockage explains the experimentally demonstrated ability to extract meaningful molecular information, such as detecting nucleotide sequence in such a strand of DNA.[2, 4, 8, 10, 17, 19, 26, 27] The details of nanopore surface charges are not only important in the context of conductance as in Equation 1, but extend to augmenting electrophoretic control over analyte motion through the nanopore with electroosmosis, and to allowing nanopores to analyte-select not only based on size, but also by charge.[9, 28-31] Conductance-based nanopore characterization is, in fact, uniquely positioned to provide geometric and chemical insights into nanopore properties. It is also exceedingly important in the context of solution-phase nanopore fabrication methods where post-fabrication microscopic characterizations are undesirable. The prevailing approach has been to assume formation of a single nanopore when one is intended, and to overlook possible structural defects. Inaccurate nanopore models will affect the quality of conductance characterizations, and other work has shown (and taken advantage of) the influence of internal nanopore structural irregularities on analyte current blockages.[32] While it is essential to control the size of isolated nanopores for single-molecule characterization and sensing applications; the use of arrays of nanopores as filters for physical and chemical separations multiplies the challenges and underscores the need to detail the formation of even single nanochannels.[11]

The extreme, ~10 nm feature size has historically been challenging to nanopore fabrication (and characterization) efforts. Methods have tended to be

instrumentation-intensive, using charged-particle microscopes such as scanning and (scanning) transmission electron microscopes (SEM and (S)TEM), and helium ion microscopes, or ion accelerator facilities to prepare membranes for subsequent chemical etching steps.[33-37] More recently, ~20 V potentials applied across thin membranes immersed in electrolytes conventionally used for nanopore experiments resulted in (controlled) dielectric breakdown of the films, and could produce size-tuned nanopores following voltage-assisted etching.[38] This truly low-overhead approach can yield <10 nm diameter nanopores, and produces them reliably wetted for use, without the risks of drying and surface contamination from steps such as TEM-based fabrication (or examination). A similarly all-solution-based approach uses deposition of largely conformal films to shrink suitable pores to the desired final dimension.[9, 39] By deliberately and beneficially removing high-magnification charged-particle microscopes from the fabrication workflow, however, the opportunity to immediately image the fabricated pores is lost. We therefore explored existing nanopore conductance formalisms[13, 18] and developed a framework to use conductance to characterize nanopore size, shape, and surface chemistry.[14-16] We most recently showed that the method could yield real-time insight into these nanopore properties during solution-phase fabrication processes such as those outlined above.[14] In all instances, however, the simulations assumed perfectly formed single nanopores. Here we (1) deliberately introduce defects into the pore models, and we moreover (2) allow for the possibility that a measured conductance arises from two separate nanopores forming in the same membrane (denoted a double pore). The latter allowance arises from TEM observations, post-pore fabrication, showing that dielectric breakdown formation of nanopores using unoptimized multilevel pulse-voltage

injection could yield more than one pore.[40] Conductance-based measurements should allow for these realities, at least through the setting of reasonable uncertainty levels. We focus here on nanopores formed in thin, free-standing silicon nitride membranes, so that our numerical simulations use parameter values from the most commonly used nanopore material platform. The films are amorphous and thus not inherently prone to anisotropic etching,[41] and silicon nitride is notably resistant to structural and chemical modification absent deliberate action.

METHODS

The form of Equation 1 means that a single measured conductance does not yield a single unique solution for the nanopore size and shape.[14-16] One can gain more degrees of freedom by measuring the conductances at two different solution conductivities, K , [15, 16] or after (or during) controlled structural modifications.[14, 15] A time-dependent framework was developed and examined conventionally in earlier work—without considering either defects or multiple pores.[14] During nanopore formation—by dissolution or deposition of material—the nanopore conductance is a function of time because the dimensions of the nanopore, $\{q_j(z, t)\}$, are changing in time, t :

$$\frac{dG}{dt} = K \sum_j \left(\frac{\partial A}{\partial q_j} \right) \frac{dq_j}{dt} + \mu |\sigma| \sum_j \left(\frac{\partial B}{\partial q_j} \right) \frac{dq_j}{dt}. \quad (3)$$

This particular implementation can determine geometries with two free parameters, and we chose the limiting (minimum) radius, $r_0(z, t)$, and the total nanopore length, $L(t)$. [14] The presence of a defect disrupts the usual cylindrical symmetry. For a membrane with more than one nanopore, the nanopores are

conductors in parallel (with identical surface chemistries and electrolyte contents) so that their conductances would be added directly, $G = \sum_n G_n$. Using a single measurement of the conductance at a single time t_i , it is not possible to distinguish between a single large pore and two smaller pores, or between a pore with or without a defect, when $G(t_i, \{q_j(t_i)\}) = G(t_i, \{q_j'(t_i)\})$. [14] The size- and geometry-dependence of the conductance change in time, however,

$$\frac{dG}{dt} = \sum_n \left(K \sum_j \left(\frac{\partial A_n}{\partial q_j} \right) \frac{dq_j}{dt} + \mu |\sigma| \sum_j \left(\frac{\partial B_n}{\partial q_j} \right) \frac{dq_j}{dt} \right) \quad (4)$$

provides a much-needed degree of freedom to possibly differentiate between such configurations. The characterization method then has a very simple implementation: measurements of several sequential experimental conductance values at times $\{t_i, \dots\}$, $\{G(t_i, \{q_j(t_i)\}), \dots\}$, are the inputs to the geometry optimization of candidate nanopore profiles. We simulated the experimental conductances using the experimentally supported Equation 1 in conjunction with experimentally supported nanopore profiles, and then fit the data using candidate nanopore profiles. [16, 18] The focus was whether including either defects or double pores would negatively affect the feasibility of the approach augured by the formalism. To allow this emphasis, the effect of measurement noise on the conductance was neglected. The change in nanopore radius in time, $\frac{dr}{dt} = v_{mt}$, occupies a privileged role as the material transfer rate (with opposite signs for etching and deposition). We used a constant $|v_{mt}| = 0.6 \text{ nm/h}$ to highlight the nonlinear dependence of conductance on geometry in Equations 1, 3, and 4, and in keeping with the linear etch rates common to micromachining, but the method does not depend on that particular magnitude or time-dependence. [14, 41] We chose four nanopore profiles finding widespread use: cylindrical, double-conical,

conical-cylindrical, and hyperbolic (Figure S6.1), but the method does not hinge on these particular choices.[13, 16, 18, 37, 42] The label r_0 is used here to denote the radius of the cylindrical pores, and the minimum radius (at any given time) of the pores with radii varying with z ; “pinch” and “outline” labels will be introduced for the r_0 of cylindrical nanopores with defects. All profiles were conventionally restricted to two free parameters, each, (r_0 and L) with the outer radius of the three tapered profiles fixed to be 10 nm greater than their corresponding r_0 , and the initial length of the inner cylinder of the conical-cylindrical pore restricted to 0.6 times its overall length, $L(t_0)$, where t_0 is the starting time. To model the double pore case, the two pores were set to be identical. Parameter values and calculations were consistent with previous work:[14-16, 22] 1 M potassium chloride electrolyte solution in water, $K=14.95 \text{ S}\cdot\text{m}^{-1}$, pH 7.0, and silicon nitride surface $\text{p}K_a=7.9$, with σ calculated in the usual way.[16, 22] The influence of solution pH is outlined in Figure S6.3 and the discussion immediately preceding it. For the defect-free pores, surface-deposited films were treated in a piecewise curved manner to maintain a uniform surface coating thickness (Figure S6.1) across the entire nanopore surface.[14] For the case of the pores with defects (Figure 6.1a) the half-cylinder protrusions running along the full length of the pore interior were centered on the pore outline, opposite each other. Simulations of $G(t_i)$ were performed using 0.01 nm step sizes in the nanopore radius (or 1 minute increments given v_{mt}), and fits to $r_0(t_0)$ versus t were plotted using 0.05 nm increments.

RESULTS AND DISCUSSION

Post-fabrication comparisons of electron microscopic and steady-state conductance measurements support the independent use of Equation 1 for nanopore characterization.[13, 16, 18, 20, 21, 24] Conductance measurements recorded during a fabrication process such as dielectric breakdown, however, occur in a different context than post-fabrication measurements.[38, 43] In Figure 6.2, we used experimental multilevel pulse-voltage injection (MPVI) nanopore formation measurements—both steady-state and time-dependent—by Yanagi *et al.*[43] to test whether a formalism such as Equation 1 would yield reasonable real-time size determinations using the time-dependent conductance of a forming nanopore. Yanagi *et al.*[43] measured the steady-state conductances, G , of post-fabrication pores and then used TEM imaging to determine their mean r_0 . With appropriate consideration of the usual caveats of EM nanopore characterization[14, 16], along with possible consequences of nanopore dewetting and handling, post-fabrication electron microscopy provides a valuable, albeit instrumentation- and expertise-intensive, measure of nanopore size. Unsurprisingly, we obtained good fits to post-fabrication data using Equation 1 (Figure 6.2a)—in particular with a conical-cylindrical profile with conventional constraints (see above)—and using Equation S1 (Equation 1 with an access resistance term—see discussion below) with cylindrical models with effective or adjustable fitting parameters. To correlate Yanagi *et al.*'s[43] measured G and mean r_0 without biasing the fit with an explicit choice of nanopore shape, we modified the cylindrical model of Equation S1 by replacing G_{bulk} with αG_{bulk} , and G_{surface} with βG_{surface} . We optimized the parameters α and β using the fit to the experimental data (with known r_0 , L , and G) in Figure 6.2a to correlate experimental post-fabrication nanopore conductances and mean

nanopore radii by TEM, $r_{0,TEM}^{\alpha,\beta}(G)$. We then used $r_{0,TEM}^{\alpha,\beta}(G)$ to convert Yanagi *et al.*'s[43] time-dependent measurements of the conductance into nanopore size as a function of time, $r_{0,TEM}^{\alpha,\beta}(t_i)$ (Figure 6.2b). In this context, the function $r_{0,TEM}^{\alpha,\beta}(G)$ is thus better thought of as simply a fit function relating nanopore conductance and TEM-based size, rather than representing a particular model choice for the nanopore conductance. Finally, for each $G(t_i)$ data point of Figure 6.2b, we calculated $r_{0,candidate}(t_i)$, with all other parameters fixed, for each of the candidate nanopore profiles, and compared the results with $r_{0,TEM}^{\alpha,\beta}(G)$ (Figure 6.2c). The experimental $G(t_i)$ of Yanagi *et al.*[43] was fit best, using Equation 6.1, by a conical-cylindrical model with overall length equal to the nominal membrane thickness. The cylindrical model using Equation S1 and with an effective length equal to a fraction of the nominal membrane thickness[43] did not fit as well as the conical-cylindrical model, but outperformed the remaining candidates. Overall, Equations 6.1 and S6.1 produce reasonable nanopore sizes when applied to conductance data recorded during nanopore fabrication. As discussed in earlier work[14], a time-dependent material-transfer rate, $v_{mt}(t)$, is no impediment to the time-dependent conductance profiling framework.[14]

As the first application of Equation 6.1 to more complex nanopore configurations, we investigated the effect of defects on our ability to extract reasonable geometric descriptions of nanopore sizes. Figure 6.1a shows a top-down view of defects in cylindrical nanopores ($L(t_0) = 10$ nm). Figure 6.1a also shows one of the key challenges of conductance-based nanopore characterizations: all of the different profiles shown have, by Equation 6.1, the same 200 nS conductance. With larger initial defect size, the initial radius of the cylindrical

outline of the nanopore (the “outline radius”, $r_0^{\text{outline}}(t_0)$) must also be larger to compensate for the internal volume lost for ionic transport. Defects distort the circular symmetry of the nanopore and introduce “pinch points” (as illustrated in Figure 6.3, characterized by the radius of a cylinder just fitting between the two protrusions—the “pinch radius”, $r_0^{\text{pinch}}(t_0)$) that could preclude analyte passage where a defect-free pore of equivalent conductance could allow passage. Such a failure, of course, is diagnostic, but would require the addition of gauging molecules or particles (compatible with the fabrication conditions) if it were to be used for real-time monitoring of the fabrication. Such adjuncts could naturally be used post-fabrication.[44, 45] Figure 6.1b shows the evolution of a cylindrical nanopore with 1 nm-radius defects: as more material is added to the surface with time, the nanopore interior becomes increasingly anisotropic. Depending on defect size, shape, and position, depositing material onto the surface of a pore with defects could readily lead to overlapping Debye layers followed by physical scission of a single pore into two distinct pores. The comparison of single and double pore systems thus also overlaps with the consideration of fabrication defects. Figure 6.1c illustrates the heart of the method motivated by the form of Equations 6.1 and 6.3: it shows the time evolution, with identical material transfer rates, of the nanopore profiles shown in Figure 6.1a. For small nanopore sizes where Debye layers overlap, more sophisticated treatments than Equation 6.1 are required, but as a guide to the eye we plotted the conductance until $r_0^{\text{pinch}} = 0$. [15, 46] From their identical initial value, the conductances of the different profiles differentiate in time, in spite of the constant material transfer rate changing all outline and pinch radii at the same rate.

When nanopore dimensions are changed during fabrication, the change in conductance with time is measured without knowledge of the presence or absence of defects. The question is whether the time-trace of the conductance can reveal the presence of defects or not—and if not, how serious the error in the resulting nanopore characterizations might be. To explore this, we chose to simulate (abbreviated to “sim” in labels) the time-dependent conductances, $G_{\text{case}}^{\text{sim}}(t_i)$ (case denotes defect size), for two cylindrical nanopores with $G_{\text{case}}^{\text{sim}}(t_0) = 200$ nS and $r_0^{\text{pinch}}(t_0) = 4$ nm: one with two 0.1 nm-radius defects, and the other with two 1.0 nm-radius defects (and lengths $L(t_0) \sim 4.1$ and ~ 5.9 nm, respectively, dictated by the conductance and radii). We attempted to fit these data by using the (known) material transfer rate and varying the dimensions of three candidate nanopore profiles: a defect-free cylindrical nanopore, and profiles with 0.1 and 1.0 nm-radii defects. The question was whether fitting to the $G_{\text{case}}^{\text{sim}}(t_i)$ would reveal the existence and size of defects. A step-by-step tutorial for this process is provided in earlier work,[14] which we abbreviate here to allow a suitable focus on fabrication irregularities. The initial conductance, $G_{\text{case}}^{\text{sim}}(t_0)$, was used to determine the (infinite) set of $\left\{ \left(r_{0,\text{candidate}}(t_0), L_{\text{candidate}}(t_0) \right) \right\}$ for which $G_{\text{candidate}}(t_0) = G_{\text{case}}^{\text{sim}}(t_0)$. After the dimension changes from depositing material at the known rate (outline and pinch radii diminish at v_{mt} , whereas the cylinder length increases at $2v_{\text{mt}}$), only one pairing $\left(r_{0,\text{candidate}}(t_0), L_{\text{candidate}}(t_0) \right)$ for each candidate also satisfied $G_{\text{candidate}}(t_1) = G_{\text{case}}^{\text{sim}}(t_1)$. This answer gave the unique initial nanopore size for each candidate with its specified defect size, but could not be used to identify the simulated defect size. That is, all three candidate profiles could exactly reproduce the two simulated conductances. After propagating the deposition one more time

from the three different $(r_{0,\text{candidate}}(t_0), L_{\text{candidate}}(t_0))$, only one pair of initial nanopore dimensions gave $G_{\text{candidate}}(t_3) = G_{\text{case}}^{\text{sim}}(t_3)$. Figure 6.3 summarizes this behavior: the ordinate is the initial nanopore radius, $r_{0,\text{candidate}}(t_0)$, that, after deposition until time t_i , would give $G_{\text{candidate}}(t_i) = G_{\text{case}}^{\text{sim}}(t_i)$ (the dimensions at time t_i are readily calculated from the initial dimensions and the known material transfer rate). When the candidate profile (here, defect size) matches the simulated profile, then all the $r_{0,\text{candidate}}(t_0)$ from each t_i are equal to each other, and equal to $r_{0,\text{case}}^{\text{sim}}(t_0)$, and the line connecting the data is horizontal. When the candidate profile is incorrect, then the plotted data is no longer horizontal. Thus, in Figure 6.3a, when the simulated data is generated using a cylindrical pore with a 0.1 nm-radius defect, only the fit data using the 0.1 nm-defect candidate pore is perfectly horizontal. The defect-free nanopore fit data is close to horizontal and overlaps substantially with the outline radius of the simulated pore, but the 1 nm-defect fit data has a larger nonzero slope and is therefore the incorrect candidate. While $r_0^{\text{outline}}(t_0)$ of the 1 nm-defect candidate was not substantially larger than the true $r_0^{\text{outline}}(t_0)$, its small $r_0^{\text{pinch}}(t_i)$ would suggest an incorrect threshold for analyte size-exclusion. Figure 6.3b shows that a 1 nm-defect simulated pore is successfully fit only with a 1 nm-defect candidate pore, and that radii for the remaining two candidates lie between limits set by the pore with the larger defect. In both fitting examples, the slopes of the fit data provide an indication of the correct defect magnitude, being positive when the candidate defect is too large, and negative when the candidate defect is too small. One might thus imagine a strategy in which a wider range of candidate defect sizes were used to more readily indicate the presence and provide bounds for the size of a defect. The feasibility of the method

thus extends from the formalism to successful numerical examples, but these model calculations portend limitations in experimental implementation: $\Delta r_{0,\text{candidate}}(t_0) \sim 0.1 \text{ nm}$ for incorrect candidates, compared to the full 2 nm deposition thickness. In the presence of measurement noise, or with an unfavorable combination of defect size, v_{mt} , fabrication time, and number of conductance measurements, for example, even detection of defects may elude real-time analysis.

We extended this exploration of the effect of defects by considering the effect of candidate nanopore shape on the conductance-based geometry optimization. Figure 6.4a illustrates the underlying premise. At t_0 , the six listed nanopore profiles have identical 200 nS conductances and $L(t_0) = 10 \text{ nm}$, generated by different $r_0(t_0)$. As material deposition narrows the nanopore constrictions at a constant linear rate (inset), all of the conductances diverge from each other in time. This occurs in spite of, for example, the r_0^{pinch} of the 1.0 nm-defect cylindrical pore and the r_0 of the conical-cylindrical pore having essentially identical values over time. Figures 6.4b and c use this behavior quantitatively. The same procedure used for Figure 6.3 was used to fit the simulated conductances of cylindrical nanopores with $r_0^{\text{pinch}}(t_0) = 5.0 \text{ nm}$, and two defects of either 0.1 or 1.0 nm radius, with defect-free pores representing typical nanopore shapes. Even the smaller, 0.1 nm defects caused the defect-free cylindrical nanopore to be unable to fit the simulated conductance. The correct candidate profile—0.1 nm defects inside a cylindrical profile—gave a perfectly horizontal line when fit to the simulated 0.1 nm-defect data. Fitting with the conical-cylindrical nanopore, however, generated nearly horizontal data, likely because the distinct narrow and wide sections of the profile (including constraints) were able to approximate the

defect-bearing cylinder's balance of pinch and outline radii. The radius of the opening through the inner cylinder ($r_{0,\text{conical-cylindrical}}(t)$), however, was smaller than for the simulated profile. For the simulated cylindrical pore with the larger, 1.0 nm defect, the fitting procedure again returned the correct profile and defect size. Once again, the conical-cylindrical profile fit data was almost horizontal with the wrong radius, although lying between the pinch and outline radii of the defect model. Depending on the size, distribution, number of defects, and current noise, it may be difficult to use this conductance model to distinguish, in real-time during formation, between an ideal pore of a given shape, and a pore of a different shape, but with defects. It may be necessary to then resort to more involved post-fabrication approaches.[15, 16, 44, 45] Indeed, one may be forced to adopt a strategy of repeated cycles of incomplete fabrication—with real-time profiling—followed by more in-depth characterization. In such a case it is important to understand the inherent uncertainties—such as the error in r_0 —of these real-time characterization procedures to ensure that the fabrication cycles do not pass by the desired final size.

A second complication for nanopore formation is the formation of more than one pore when only one is intended. Microscopy can be used to directly enumerate the pore number, but at the cost of instrumentation and user burdens, and possible nanopore surface contamination, among other drawbacks. We wanted to determine if conductance could provide any insight into this possible problem of multipore formation. We explored the case of double pores of matching size and shape. Figure S6.4 illustrates that the conductance change in time provides the prospect of differentiating between single and double pore systems, just as it did for single pores of different shapes.[14]

To explore whether the conductance time trace could reliably determine the size and number of the pores during their fabrication, we simulated conductances for single and double pore configurations of the four profiles in Figure S6.1, choosing 200 nS as a convenient initial conductance. Double pores for each shape were identical in size to each other. The conductance fitting in Figure 6.5 mirrors that of Figure 6.3 and 4b,c. For each column, a given profile with a single (a-d) or double (e-h) pore was chosen and used to calculate a minimum of three simulated conductance values in time: $G_{\text{case}}^{\text{sim}}(t_0)$, $G_{\text{case}}^{\text{sim}}(t_1)$, and $G_{\text{case}}^{\text{sim}}(t_2)$, with additional $G_{\text{case}}^{\text{sim}}(t_i)$ providing added robustness (case here denotes profile and pore number). The broad outlines of the results detailed in Fig. 5a-d and e-h are that one-pore simulated conductances were fit by the one-pore candidate profiles of the correct shape (as revealed by the constancy of the corresponding $r_0(t_0)$), and double pore conductances were fit by the matching double pore candidate profiles. Interestingly from these examples, double pore cylindrical and conical-cylindrical profiles did a reasonable job of fitting single pore hyperbolic and double-conical conductance data, and single hyperbolic and double-conical candidates did a reasonable job of fitting double pore cylindrical and conical-cylindrical conductance data. Exact agreement still only occurs for correct shape and pore number, but the wrong profile doesn't inherently produce a terribly inaccurate radius. While they returned the incorrect shapes, the nevertheless fairly accurate r_0 means the expectations of which sizes of molecules would fit through the candidate pores are unlikely to differ appreciably, although the double pore case would allow for twice the number of channels and have different analyte-induced current blockages. Sufficient attention should therefore be obtained to optimizing the nanopore fabrication conditions,[40] and more involved post-fabrication characterizations should be

considered if analyte-induced blockages do not fall within the range expected for the relative sizes of analyte and pore.[15, 16, 44, 45]

CONCLUDING REMARKS

The performance of a nanopore used for applications such as single-molecule sensing, separations, and manipulations is dictated in large part by its size, shape, and surface chemistry. These three parameter groupings underpin the nanopore conductance and allow a suitable analysis framework to use straightforward measurements of the conductance as a means to gain insight into these nanopore properties. Nanopore conductance is routinely used to coarsely gauge nanopore size during use, typically with at least the assumption of a cylindrical shape, and then often with deliberately incorrect parameter constraints to ensure that reasonable numerical estimates of the radius are nevertheless produced. More sophisticated conductance formalisms have been developed and validated for use with more complicated nanopore shapes and to account for additional considerations such as access resistance. Simple, analytical expressions allow for wider adoption of a characterization method that can easily accommodate a range of nanopore profiles, thereby providing both application flexibility and the possibility for using different model assumptions to explore the uncertainties in the extracted nanopore dimensions.[15, 16] New solution-based nanopore fabrication techniques have increased the importance of methods to characterize nanopores from their conductance. We tested the ability of a recently-developed method to characterize nanopores in real-time during fabrication by allowing for the possible formation of multiple pores or pores with defects. The simulations determined the correct nanopore number, size, and shape alongside the presence and size of any defects, but the numerical examples revealed challenges that await experimental

applications of the approach. While the basic equations showed good agreement with experimental time-dependent conductance measurements, example characterizations that explicitly considered the possibility of nanofabrication defects yielded only very slight differences in the key metrics designed to identify nanopore profiles and determine their dimensions. Inadequate measurement statistics may therefore impede the ability to uniquely or correctly determine the correct nanopore shape, number, and size. In challenging cases, a selection of analyses using different assumptions could produce a set of parameter values whose spread could offer a measure of the uncertainty of the characterization. Such real-time estimates could be followed by post-fabrication characterizations where larger conductance changes than those accompanying nanoscale changes of nanopore dimension would be wrought by changes of solution concentration, thereby easing the conductance analysis.[16] Thus, in spite of the limitations discussed here, the time-dependence of the nanopore conductance during fabrication remains a useful tool, given sufficient circumspection in application, for gaining insight into the evolving nanopore structure and for characterizing nanopores even without the usual assumptions of ideal formation.

ACKNOWLEDGEMENTS

This research has been supported by NSF CAREER award CBET-1150085, and by the University of Rhode Island, including URI graduate fellowships for Y. M. Nuwan D. Y. Bandara and Buddini Iroshika Karawdeniya. We thank Prof. Michael L. Greenfield for a considered reading of an earlier version of this manuscript, and the anonymous reviewer who proffered a scaling argument approach for the access resistance determination.

All authors declare no financial/commercial conflicts of interest.

REFERENCES

- [1] Haywood, D. G., Saha-Shah, A., Baker, L. A., Jacobson, S. C., *Anal. Chem.* 2015, 87, 172-187.
- [2] Taniguchi, M., *Anal. Chem.* 2015, 87, 188-199.
- [3] Reiner, J. E., Balijepalli, A., Robertson, J. W. F., Campbell, J., Suehle, J., Kasianowicz, J. J., *Chem. Rev.* 2012, 112, 6431-6451.
- [4] Howorka, S., Siwy, Z., *Chem. Soc. Rev.* 2009, 38, 2360-2384.
- [5] Miles, B. N., Ivanov, A. P., Wilson, K. A., Dogan, F., Japrun, D., Edel, J. B., *Chem. Soc. Rev.* 2013, 42, 15-28.
- [6] Kudr, J., Skalickova, S., Nejd, L., Moulick, A., Ruttkay-Nedecky, B., Adam, V., Kizek, R., *ELECTROPHORESIS* 2015, 36, 2367-2379.
- [7] Oukhaled, A., Bacri, L., Pastoriza-Gallego, M., Betton, J.-M., Pelta, J., *ACS Chemical Biology* 2012, 7, 1935-1949.
- [8] Branton, D., Deamer, D. W., Marziali, A., Bayley, H., Benner, S. A., Butler, T., Di Ventra, M., Garaj, S., Hibbs, A., Huang, X. H., Jovanovich, S. B., Krstic, P. S., Lindsay, S., Ling, X. S. S., Mastrangelo, C. H., Meller, A., Oliver, J. S., Pershin, Y. V., Ramsey, J. M., Riehn, R., Soni, G. V., Tabard-Cossa, V., Wanunu, M., Wiggin, M., Schloss, J. A., *Nat. Biotechnol.* 2008, 26, 1146-1153.
- [9] Sexton, L. T., Horne, L. P., Martin, C. R., *Molecular BioSystems* 2007, 3, 667-685.
- [10] Bayley, H., Martin, C. R., *Chem. Rev.* 2000, 100, 2575-2594.
- [11] Dwyer, J. R., Bandara, Y. M. N. D. Y., Whelan, J. C., Karawdeniya, B. I., Nichols, J. W., in: Edel, J., Ivanov, A., Kim, M. (Eds.), *Nanofluidics, 2nd Edition*, Royal Society for Chemistry 2016.
- [12] Guo, P., Martin, C. R., Zhao, Y., Ge, J., Zare, R. N., *Nano Lett.* 2010, 10, 2202-2206.
- [13] Kowalczyk, S. W., Grosberg, A. Y., Rabin, Y., Dekker, C., *Nanotechnology* 2011, 22, 315101.
- [14] Bandara, Y. M. N. D. Y., Karawdeniya, B. I., Dwyer, J. R., *ACS Appl. Mater. Interfaces* 2016, 8, 30583-30589.
- [15] Frament, C. M., Bandara, N., Dwyer, J. R., *ACS Appl. Mater. Interfaces* 2013, 5, 9330-9337.
- [16] Frament, C. M., Dwyer, J. R., *J. Phys. Chem. C* 2012, 116, 23315-23321.
- [17] Smeets, R. M. M., Keyser, U. F., Krapf, D., Wu, M.-Y., Dekker, N. H., Dekker, C., *Nano Lett.* 2006, 6, 89-95.
- [18] Liebes, Y., Drozdov, M., Avital, Y. Y., Kauffmann, Y., Rapaport, H., Kaplan, W. D., Ashkenasy, N., *Appl. Phys. Lett.* 2010, 97, 223105.

- [19] Harms, Z. D., Haywood, D. G., Kneller, A. R., Jacobson, S. C., *Analyst* 2015, *140*, 4779-4791.
- [20] Ayub, M., Ivanov, A., Instuli, E., Cecchini, M., Chansin, G., McGilvery, C., Hong, J., Baldwin, G., McComb, D., Edel, J. B., Albrecht, T., *Electrochim. Acta* 2010, *55*, 8237-8243.
- [21] Stein, D., Kruithof, M., Dekker, C., *Phys. Rev. Lett.* 2004, *93*, 035901.
- [22] Behrens, S. H., Grier, D. G., *J. Chem. Phys.* 2001, *115*, 6716-6721.
- [23] DeBlois, R. W., Bean, C. P., *Rev. Sci. Instrum.* 1970, *41*, 909-916.
- [24] Lee, C., Joly, L., Siria, A., Biance, A.-L., Fulcrand, R., Bocquet, L., *Nano Lett.* 2012, *12*, 4037-4044.
- [25] Wanunu, M., Sutin, J., McNally, B., Chow, A., Meller, A., *Biophys. J.* 2008, *95*, 4716-4725.
- [26] Aksimentiev, A., *Nanoscale* 2010, *2*, 468-483.
- [27] Schoch, R. B., Han, J., Renaud, P., *Reviews of Modern Physics* 2008, *80*, 839-883.
- [28] Vlassiouk, I., Smirnov, S., Siwy, Z., *Nano Lett.* 2008, *8*, 1978-1985.
- [29] Anmiv, S. P., Talukder Zaki, N. J., Kevin, J. F., Rafael, M., Prashanta, D., Min Jun, K., *J. Phys.: Condens. Matter* 2010, *22*, 454107.
- [30] Maglia, G., Restrepo, M. R., Mikhailova, E., Bayley, H., *Proceedings of the National Academy of Sciences* 2008, *105*, 19720-19725.
- [31] Wolfe, A. J., Mohammad, M. M., Cheley, S., Bayley, H., Movileanu, L., *J. Am. Chem. Soc.* 2007, *129*, 14034-14041.
- [32] Qiu, Y., Hinkle, P., Yang, C., Bakker, H. E., Schiel, M., Wang, H., Melnikov, D., Gracheva, M., Toimil-Molares, M. E., Imhof, A., Siwy, Z. S., *ACS Nano* 2015, *9*, 4390-4397.
- [33] Yang, J., Ferranti, D. C., Stern, L. A., Sanford, C. A., Huang, J., Ren, Z., Qin, L.-C., Hall, A. R., *Nanotechnology* 2011, *22*, 285310.
- [34] Li, J., Stein, D., McMullan, C., Branton, D., Aziz, M. J., Golovchenko, J. A., *Nature* 2001, *412*, 166-169.
- [35] Storm, A. J., Chen, J. H., Ling, X. S., Zandbergen, H. W., Dekker, C., *Nature Materials* 2003, *2*, 537-540.
- [36] Spinney, P. S., Howitt, D. G., Smith, R. L., Collins, S. D., *Nanotechnology* 2010, *21*, 375301.
- [37] Vlassiouk, I., Apel, P. Y., Dmitriev, S. N., Healy, K., Siwy, Z. S., *Proceedings of the National Academy of Sciences of the United States of America* 2009, *106*, 21039-21044.
- [38] Kwok, H., Briggs, K., Tabard-Cossa, V., *PLoS ONE* 2014, *9*, e92880.

- [39] Whelan, J. C., Karawdeniya, B. I., Bandara, Y. M. N. D. Y., Velleco, B. D., Masterson, C. M., Dwyer, J. R., *ACS Appl. Mater. Interfaces* 2014, 6, 10952-10957.
- [40] Goto, Y., Yanagi, I., Matsui, K., Yokoi, T., Takeda, K.-i., *Scientific Reports* 2016, 6, 31324.
- [41] Williams, K. R., Muller, R. S., *J. Microelectromech. Syst.* 1996, 5, 256-269.
- [42] Kim, M. J., McNally, B., Murata, K., Meller, A., *Nanotechnology* 2007, 18.
- [43] Yanagi, I., Akahori, R., Hatano, T., Takeda, K.-i., *Sci. Rep.* 2014, 4.
- [44] Vogel, R., Willmott, G., Kozak, D., Roberts, G. S., Anderson, W., Groenewegen, L., Glossop, B., Barnett, A., Turner, A., Trau, M., *Anal. Chem.* 2011, 83, 3499-3506.
- [45] Nablo, B. J., Halverson, K. M., Robertson, J. W. F., Nguyen, T. L., Panchal, R. G., Gussio, R., Bavari, S., Krasilnikov, O. V., Kasianowicz, J. J., *Biophys. J.* 2008, 95, 1157-1164.
- [46] Makra, I., Jágerszki, G., Bitter, I., Gyurcsányi, R. E., *Electrochim. Acta* 2012, 73, 70-77.

Figure Captions

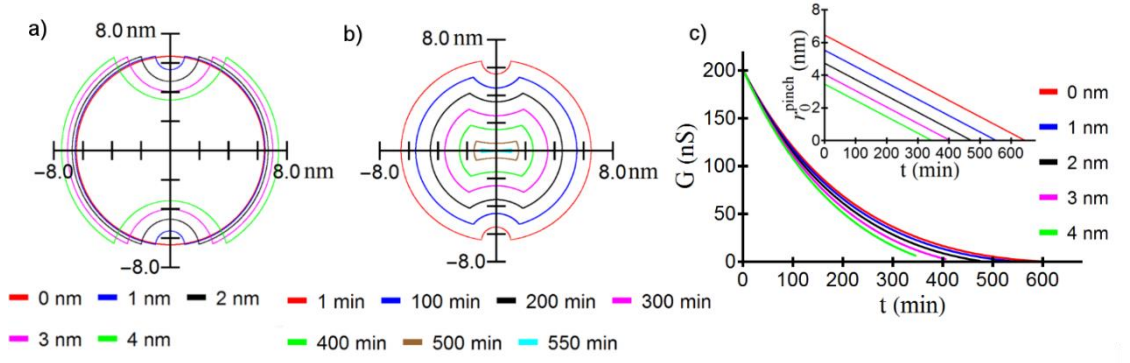


Figure 6.1. a) Top view of $L(t_0) = 10$ nm cylindrical nanopores that yield a 200 nS conductance with the radii of the two inward-pointing defects given in the legend. b) Top view of the initially 1 nm-radius defect nanopore from (a), closing at $v_{mt} = 0.6$ nm/h with deposition time indicated. c) Progression of conductance (and r_0^{pinch} in inset) with time for the cylindrical nanopores from (a).

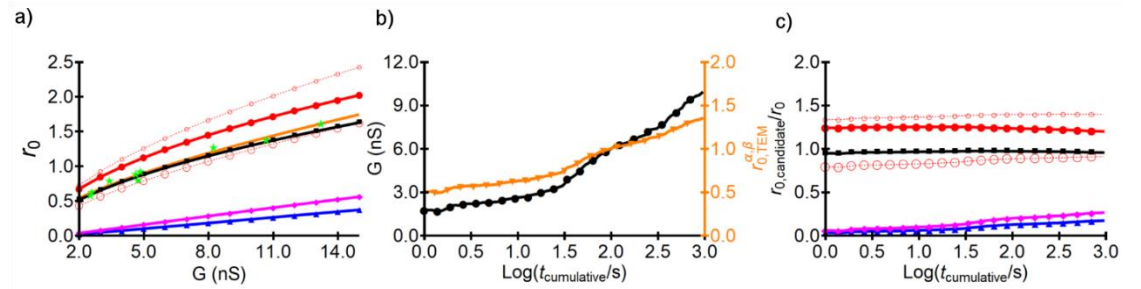
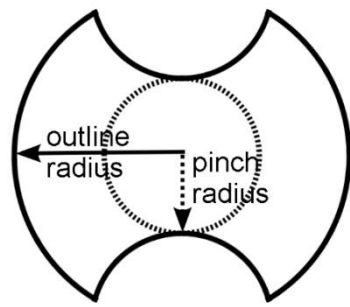


Figure 6.2 (a) Experimental post-fabrication measurements of nanopore conductance and their corresponding TEM-based mean $r_{0,\text{TEM}}^{\text{expt}}$ (green stars)[43] were plotted versus several models: Equation 1 (solid markers) – cylindrical (red circles), double-conical (blue triangles), conical-cylindrical with an inner cylinder length of $0.6L$ (black squares), and hyperbolic (magenta diamonds); and with an added access resistance term, by Equation S1 (hollow markers) – cylindrical with length L (small circles) and cylindrical with a $0.37L$ effective length [43] (large circles). To not bias further analysis with an explicit choice of nanopore profile, the $r_{0,\text{TEM}}^{\text{expt}}$ were fit to Equation S1 with G_{bulk} and G_{surface} from the cylindrical model weighted by fit parameters: αG_{bulk} and βG_{surface} (orange triangles— $r_{0,\text{TEM}}^{\alpha,\beta}(G)$). (b) Time-dependent conductance measurements were taken from the experimental work of Yanagi *et al.*[43] and were used with $r_{0,\text{TEM}}^{\alpha,\beta}(G)$ to determine $r_{0,\text{TEM}}^{\alpha,\beta}(t_i)$. (c) Candidate profiles matching those in (a) were used at each discrete value of $G(t_i)$ to calculate an $r_{0,\text{candidate}}(t_i)$. The figure compares the fit and experimentally-derived radii where the correct candidate size should result in a straight line at a ratio of 1. Selected data markers are shown for clarity.



outline radius	pinch radius	defect radius (nm)
		0
		0.1
		1.0

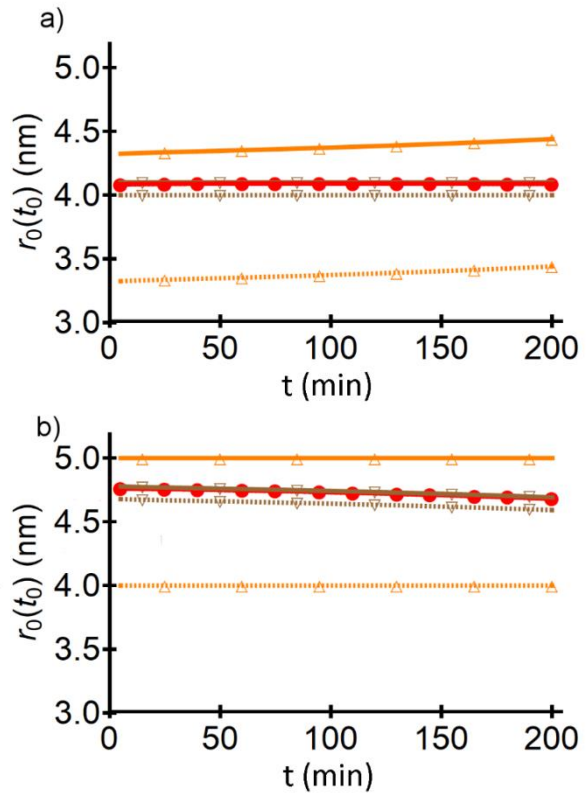


Figure 6.3. Conductances during simulated material deposition onto nanopores with initial conductances of 200 nS, and $r_0^{\text{pinch}}(t_0) = 4$ nm, were fit with candidate cylindrical nanopores: a defect-free pore, and pores with 0.1 and 1.0 nm-radius defects. Dotted and solid lines denote the pinch and outline radii, respectively. a) 0.1 nm defect pore and b) 1.0 nm defect pore profiles were used to furnish the simulated conductance data. The correct candidate profile in each case was indicated by the horizontal slope of the fit data; the defect-free $r_0(t_0)$ nearly completely overlaps with $r_0^{\text{pinch}}(t_0)$ for the 0.1 nm defect pores. Selected data markers are shown for clarity.

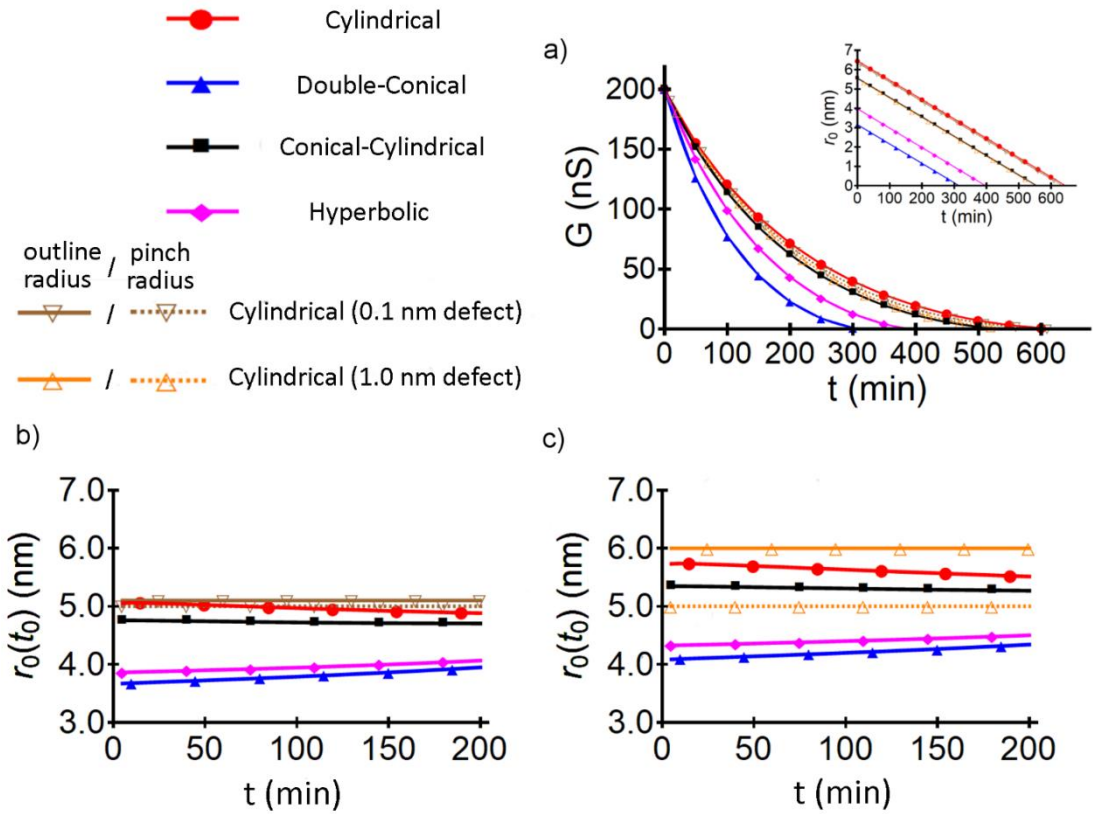


Figure 6.4: a) Conductances and (inset) radii as a function of profile and time when simulating deposition onto surfaces of initially 200 nS, $L(t_0) = 10$ nm nanopores. Dotted curves in the conductance plots belong to the cylindrical pores with defects, and denote the corresponding r_0^{pinch} in the inset (solid line- r_0^{outline}) and in (b)-(c). Conductance versus time for b) 0.1 nm-defect and c) 1.0 nm-defect cylindrical pores were fit with each candidate profile in the legend; horizontal fit lines for each case indicated the correct simulated profile. Selected data markers are shown for clarity.

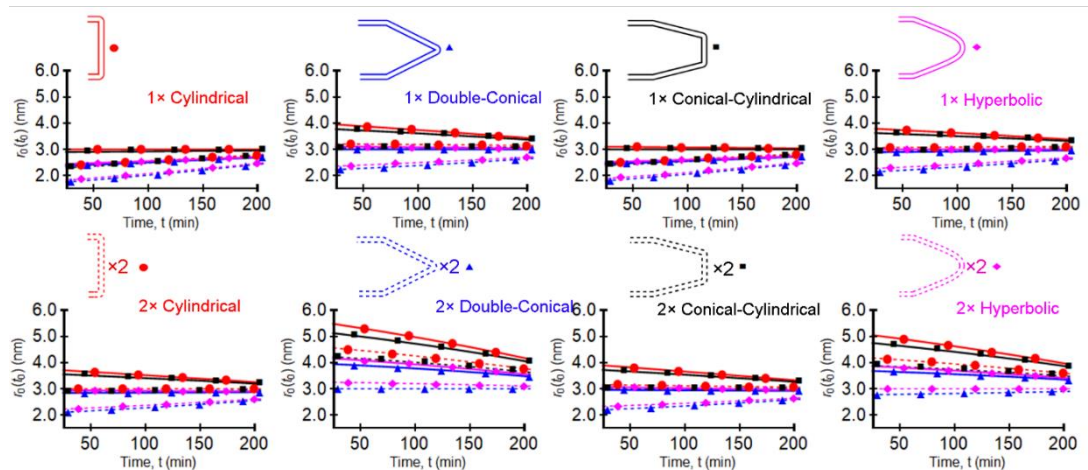


Figure 6.5: Single (solid lines) and double (dotted lines)—left to right matching the half-profile sketches—cylindrical (red circles), double-conical (blue triangles), conical-cylindrical (black squares), and hyperbolic (magenta diamonds) profiles were used to simulate nanopore conductance values versus time. Eight candidate

profiles (4 shapes, single and double) were used to fit (a-d) single pore simulated data and (e-h) double pore data from the 4 shapes. All experimental pores were initially 200 nS conductance. The correct nanopore shape was indicated by the constancy of the fit to $r_0(t_0)$ in time, and is labelled with the corresponding shape and number of pores. Selected data markers are shown for clarity.

CHAPTER 7: PREFACE

Published: ACS Appl. Nano Mater., 2018, 1 (2), pp 960–968.

GENERAL STRATEGY TO MAKE AN ON-DEMAND LIBRARY OF STRUCTURALLY AND FUNCTIONALLY DIVERSE SERS SUBSTRATES

Buddini Iroshika Karawdeniya, Y. M. Nuwan D. Y. Bandara, Julie C. Whelan, and
Jason R. Dwyer*.

Department of Chemistry, University of Rhode Island, 140 Flagg Road, Kingston,
RI, 02881, United States.

Reprinted with permission from:

General Strategy To Make An On-Demand Library Of Structurally And
Functionally Diverse Sers Substrates. Buddini Iroshika Karawdeniya, Y. M.
Nuwan D. Y. Bandara, Julie C. Whelan, and Jason R. Dwyer. ACS Appl. Nano
Mater., 2018, 1 (2), pp 960–968

Copyright 2018 American Chemical Society.

CHAPTER 7

A GENERAL STRATEGY TO MAKE AN ON-DEMAND LIBRARY OF STRUCTURALLY AND FUNCTIONALLY DIVERSE SERS SUBSTRATES

Buddini Iroshika Karawdeniya, Y. M. Nuwan D. Y. Bandara, Julie C. Whelan, and Jason R. Dwyer*.

Department of Chemistry, University of Rhode Island, 140 Flagg Road, Kingston, RI, 02881, United States.

KEYWORDS: Surface enhanced Raman spectroscopy; SERS; electroless plating; metallization.

ABSTRACT

Surface-enhanced Raman spectroscopy (SERS) is a powerful technique for sensing molecules proximal to suitable coinage metal surfaces. The physical structure of the SERS-active metal layer and its support is a key design parameter inspiring considerable, and frequently specialized, efforts in substrate fabrication. The necessary gold film structure can arise from both the metallization process and the underlying support structure, and the structure of the support can deliver additional functions including analytical capabilities such as physical filtering. We used electroless plating as a general approach to create a library of SERS substrates: SERS-active gold films on a range of supports made from a variety of materials, made with a mixture of simple and complex fabrication histories, and offering a selection of structurally-derived functions. The result was that supports with existing functions had their capabilities enhanced by the addition of SERS sensing. Electroless plating thus offers a host of beneficial characteristics for

nanofabricating multifunctional SERS substrates, including: tolerance to substrate composition and form factor; low equipment overhead requirements; process chemistry flexibility—including compatibility with conventional top-down nanofabrication; and a lengthy history of commercial application as a simple metallization technique. We gold-plated standard nanofabrication-compatible silicon nitride support surfaces with planar and porous architectures, and with native and polymer-grafted surface chemistries. We used the same plating chemistry to form SERS-active gold films on cellulose fibers arrayed in commercial filter paper and formed into nanocellulose paper. In a functional sense, we used electroless plating to augment nanoporous filters, chromatography platforms, and nanofabrication building blocks with SERS capability.

INTRODUCTION

Surface-enhanced Raman spectroscopy (SERS) is a tool at the forefront of chemical analysis for analytes ranging from single molecules to bacterial cells.¹⁻⁵ Raman enhancement is engineered by tuning SERS substrate design parameters such as elemental composition; the size and shape of nanoscale elements; close-range interparticle spacing responsible for hot spots; and patterning of solid substrates that can include ordered and random hierarchies across short, long, and multiple length scales.^{1, 3, 6-10} Physical structure of the SERS-active metal layer—either its inherent structure or the structure imposed upon it by an underlying support layer—is a critical and performance-determining factor. Considerable effort has been devoted to crafting a host of solid-supported SERS substrates, with results that inspire further efforts to improve and expand fabrication options, sensing capabilities, and sensing performance.^{1, 3, 7-26} Top-down nanofabrication using conventional and unorthodox approaches can produce exquisitely structured

substrates, but can require substantial practitioner expertise along with expensive, specialized, and complicated instrumentation, and can moreover substantially limit the palette of fabrication materials. SERS substrates developed outside the material and processing constraints of conventional micro- and nanofabrication have been compelling. Both approaches and material sets hold promise. We sought, therefore, to develop a general route for nanofabricating SERS substrates that would bridge both paradigms—to draw on the strengths of each, and to be useful for both. Conventional micro- and nanofabrication approaches offer well-established, highly optimized, large-scale manufacturing capabilities for reproducibly fabricating nanoscale structures. A less conventional fabrication material such as paper offers a myriad of advantages that have driven its adoption as a material of choice for low-cost diagnostics for use in resource-limited settings.^{23, 27-28} The genesis for the present work was the discovery that gold films we had electrolessly plated onto silicon nitride as part of a nanofabrication effort were also capable, easily and without optimization, of generating reproducible SER spectra.²⁹ We wanted to take a variety of interesting and functional support materials and structures, and determine if a simple electroless plating process could make them SERS-active—thereby augmenting their core functions by creating multifunctional SERS substrates. This goal of multifunction does not exclude the conventional quest for maximum signal enhancement, but does require that SERS substrate evaluation be application-context dependent. Paper, for example, can support a SERS-active metal component, offers obvious advantages such as low-cost and ubiquity, and has a pore structure that could improve sensing selectivity through separations by chromatography or by physical filtering.^{18-21, 23-26, 28, 30-42}

Electroless plating is a robust technique for surface metallization, well-established in commercial manufacturing applications for forming decorative, electrical, and optical elements, and with excellent substrate tolerance.^{17, 24, 29, 33, 41, 43-52} Objects are immersed in liquid baths, with solution access and homogeneity dictating the uniformity of the plating: rough and large-area surfaces can be coated without the geometric—including line-of-sight—constraints of physical vapor deposition. Equipment overhead is minimal, the surface being plated need not be conductive—allowing for support material tolerance—and the plating occurs without the need for external electrical power. Electroless plating is inherently different than the capture, by nonspecific or specific attachment protocols, of pre-formed, frequently ligand-coated solution-phase nanoparticles onto a surface.^{11-12, 15-16, 18, 30-32, 36-38, 40} the electrolessly plated metal film structure, properties, and composition can be controlled through surface pretreatment, plating bath formulation, and process conditions, and can occur on a timescale that can be measured in minutes. Vitrally important for our pursuit of a library of multifunctional SERS substrates, electroless plating is, in principle, compatible with coating sophisticated top-down nanofabricated, and low-cost bottom-up assembled structures and surfaces.

The term “electroless deposition” is used to describe a number of different plating mechanisms, including autocatalytic, substrate-catalyzed, and galvanic-displacement processes.⁵⁰ We adopted a single electroless plating process that had been optimized for coating nonconductive porous plastic membranes.⁴⁹ In brief, a Sn (II) solution is used to sensitize the surface which, when treated with an ammoniacal silver nitrate solution, undergoes a redox reaction to produce a nanoscopic metallic silver layer. Gold plating is then accomplished by immersing

this surface in a Au (I)-containing plating bath: the aurous ions galvanically displace silver, giving gold particles that catalyze the reduction of aurous ions by formaldehyde also present in the bath. Tin-based sensitizers provide fairly indiscriminate surface sensitization, which is beneficial since tolerance to surface composition is a desired goal of our SERS substrate fabrication explorations. There is also much flexibility in plating chemistry after sensitization, allowing full access to the metals typically used for SERS. While silver coatings can be produced through electroless plating, the chemical stability of gold motivates our testing of gold-coated substrates for SERS activity. The use of a conventional electroless plating protocol, with only minor material-specific modifications in washing steps, allowed us to focus on support material composition and physical structure—and thereby, function—in our exploration of whether electroless plating could be a general tool for incorporating SERS sensing capabilities into already functional and structured materials and platforms.

We selected a range of support structures and material compositions to explore the generality of using electroless plating to form a library of SERS substrates. Silicon-rich LPCVD silicon nitride (SiN_x) films on silicon were chosen for their ability to support a variety of nanofabricated structures and roles.⁵³⁻⁵⁵ Polished SiN_x films ensured the nanoscale gold grain structure would be the dominant substrate structural feature. Silicon nitride films with nanoscale through-channels introduced key structural features (the individual nanochannels and the nanochannel array) underpinning designer filters and multifunctional chemical analysis platforms using plasmonic nanopores.⁵⁶⁻⁵⁷ Surface-grafting of an acrylate-based polymer generated a more subtle structural modification of the planar SiN_x thin film, and was intended to increase the number of possible sensitizer interaction

sites on the film. Our next selection was standard filter paper, a frequent actor in paper-based low-cost diagnostics.^{23, 27} We explored the effect of fiber dimensions and spacing, by electrolessly plating and attempting to record SER spectra from standard filter paper and nanocellulose fiber paper—the fourth and fifth choices of material and structure. We characterized a commercial substrate (Silmeco) based on a gold-coated nanopillar array architecture⁹ and etched away its gold coating to expose the sixth surface for examining electroless plating for SERS: a nanopillar array. Given the vastly different SERS substrate configurations, and the often severe approximations necessary to calculate enhancement factors,⁴⁶ we used a comparison framework designed to compare SERS performance across disparate substrates. The method yields a SERS enhancement value (SEV), which is defined as the ratio of the analyte concentrations that produce the same instrument response by normal Raman and SER measurements.⁵⁸ While spectral acquisition was formalized to allow comparisons between substrates, it nevertheless cannot account for the performance benefits of matching substrate function to a particular application.

EXPERIMENTAL

A detailed listing of materials and exposition of methods is provided in the Supporting Information. All substrates were electrolessly gold-plated by sequential immersion in the same series of tin (II) chloride-, ammoniacal silver nitrate-, and sodium gold sulfite-containing solutions (Scheme S4.1), with appropriate rinsing steps in between immersions. The solutions were prepared as previously reported.^{29, 59} Immediately prior to direct plating of bare silicon or silicon nitride surfaces, they were oxygen-plasma-treated and then etched with dilute hydrofluoric acid. The severe chemical hazards presented by hydrofluoric acid

require special precautions such as those detailed in the Supporting Information. A subset of cleaned and etched planar silicon nitride supports was polymer-coated by formation of a covalently-linked sodium polyacrylate film before electroless plating, and once polymer-coated, was treated neither with plasma nor hydrofluoric acid. Silmeco gold-coated nanopillar SERS substrates were used, as-supplied, for comparison measurements. These silicon nanopillar substrates were also immersed in iodide-based gold etchant and then, after plasma treatment and HF etching, electrolessly gold-plated. Whatman 1 filter paper was plated without modification. Nanocellulose fibers were formed between two glass slides into a crude paper-like mat ~1 mm thick (referred to as “nanocellulose paper”) before plating. Surface characterization of the plated metal films was performed by field emission scanning electron microscopy (FE-SEM), x-ray photoelectron spectroscopy (XPS), and surface enhanced Raman spectroscopy (SERS).

SER spectra were acquired at an excitation wavelength of 785 nm, with a ~100 μm diameter (full-width-half-maximum) beam, and at an excitation power of ~57 mW for cellulose and as-provided Silmeco, and ~250 mW for all other substrates. Standard solutions of 4-nitrobenzenethiol (NBT) in ethanol were prepared, covering a concentration range from 5×10^{-9} to 1×10^{-4} M. All measurements (save for replated Silmeco) were performed with the substrates immersed in the standard solutions. Substrates were immersed in standard NBT solutions and SERS spectra were recorded every 2 minutes until saturation of the signal level. Following piecewise linear background subtraction (details provided in the SI), the data was analyzed according to a framework using receiver operating characteristic (ROC) curves and kinetic analysis to calculate the SEV.⁵⁸

RESULTS AND DISCUSSION

Figure 7.1a shows photographs of the complete set of materials before and after electroless gold plating: we use the term “support” to denote a material prior to gold plating, and the term “substrate” to denote a gold-plated support. All supports were successfully gold-plated by the series of baths of Scheme S7.1, as confirmed by visual inspection and XPS analysis (Figure S7.1). All plated substrates could be used to record SER spectra of 4-nitrobenzenethiol (NBT). The support composition, however, placed restrictions on the experimental parameters. Lower excitation power was required to avoid signal saturation using the as-supplied Silmeco substrates, and substrate damage using the cellulose-based substrates. The higher excitation power left a through-hole in the paper substrate, as shown in Figure 7.1b, and a hollow in the thicker nanocellulose substrate after 10 exposures (~60 s each) when both were irradiated when dry; fume evolution was observed when immersed in ethanol. No damage was apparent when unplated paper that had been soaked in NBT was irradiated, so that the damage mechanism is reasonably ascribed to photothermal transduction by the gold film. This susceptibility of paper to burning is a noted benefit of using paper diagnostics in resource-limited settings where safe disposal options for biocontaminated devices may be limited.^{23, 27}



Figure 7.1: a) Representative substrates before (supports, top row) and after (bottom row) electroless gold plating. Left to right: Silicon nitride, polymer-grafted

silicon nitride, paper, nanocellulose paper, nanopillar silicon (Silmeco etched of its as-supplied gold coating), silicon nanoporous substrates. b) Laser-induced damage at 250 mW sets an excitation power limit for paper (top, showing a through-hole) and nanocellulose paper (bottom, showing a hollow in the thicker substrate).

None of the (gold-free) supports produced detectable Raman spectra of NBT at a drop-cast $\sim 10^{-4}$ M test dose, and the (gold-plated) substrate analyte-free background spectra were, excepting a small ~ 1340 cm^{-1} peak in paper, flat and featureless in the key spectral regions used to benchmark the substrate performance (Figure S7.2). Figure 7.2 shows a representative background-subtracted SER spectrum from each substrate type using a 10^{-5} M NBT solution. The principal spectral features are consistent across substrate type, including the most intense signal from the NO_2 symmetric stretch, centered at ~ 1330 cm^{-1} in all spectra. The intensity ratio of this peak to the 880 cm^{-1} ethanol peak, $R_{\text{NBT}/\text{EtOH}}$, was used to construct the response versus concentration curve for each substrate type in Figure S7.3 in the Supporting Information. These response curves had profiles typical for this class of experiment.^{58, 60} The Raman spectral intensity at a given analyte concentration was strongly dependent upon the support material and preparation, with a substantial penalty in signal strength imposed by the excitation power limitations required by the cellulose substrates. The use of polymer-grafted silicon nitride substrates resulted in the highest signal at all concentrations compared to all other electrolessly plated substrates, most notably when compared at low analyte concentrations. To quantify the SERS performance, representative ROC curves were constructed to calculate the SEV for each substrate: 0.646×10^3 (paper), 0.694×10^4 (porous silicon nitride), 2.34×10^5 (nanocellulose), and 5.91×10^5 (silicon nitride), and at least 9.33×10^5 for both polymer and Silmeco substrates. Following low signal intensities in the test measurement for replated Silmeco substrates in Figure 7.2, we pursued structural characterization (*vide infra*)—instead of further

spectral characterization—in an effort to understand this lower response compared to as-supplied Silmeco substrates. For the Silmeco and polymer substrates, even the measurement at the lowest concentration demonstrated a better than 90% probability of detection for a 10% probability of false alarm and due to this, we can report only a minimum SEV.⁵⁸

These results emerged from proof-of-principle experiments of the general utility of electroless plating for SERS substrate creation rather than from longer-term substrate-specific optimizations. They are thus useful, when paired with the demands of a particular application, for indicating where efforts to gain additional enhancement might be warranted. The polymer-grafted silicon nitride is of note not simply for providing the largest SEV of our electrolessly plated substrates, but as an example of the benefits of nanoscale tailoring of SERS substrates, and for serving as a bridge between substrates based on traditional, silicon-containing nanofabrication materials, and those based on larger organic polymer fibers. More broadly, the design of a SERS substrate type should balance, in an application-specific way, the SEV and any special capabilities, such as filtering, offered by a given substrate. For example, gold films electrolessly plated onto and into these membrane filters can be used to physically optimize filter performance by tuning pore dimensions; to chemically optimize filter performance by serving as a first step in surface functionalization; and to augment filter performance by adding SERS-sensing capabilities in addition to separation.^{29, 61} Ultrathin, nanofabricated membrane filters, such as nanoporous silicon and silicon nitride, offer significant advantages over conventional polymer ultrafiltration membranes.^{54, 62-70} Mechanically robust, unsupported ultrathin filters allow for high hydraulic and diffusive permeabilities. The material properties and ultrathin dimensions allow for

the straightforward fabrication of smooth pores in controllable, well-defined sizes with narrow size distributions, and with high areal densities. The short, smooth walls do not suffer the drawbacks of flow resistance and sample losses due to the tortuosity and large surface area of conventional, thicker (polycarbonate) track-etched membranes. Such high-throughput, low-loss nanoporous membranes can be custom-fabricated with pore dimensions and characteristics optimized to filter micrometer-scale organisms such as bacteria, or even to separate macromolecules. Sensitivity might be enhanced by optimizing pore dimensions and distributions to form a nanoplasmonic array,⁵⁶ but at the cost of filtration performance (and selectivity).⁵⁷ A different example of the need to balance SEV and other application demands is illustrated in Figure S7.4: electrolessly gold-coated paper was used for the SERS readout of a crude paper-based assay that performed physical filtration and chromatographic separation. This multifunction capability augments the spectral selectivity of SERS for greater ease of analysis of multicomponent samples, but by no means circumscribes the utility of SERS-active paper. Indeed, the development of paper-based diagnostics has been characterized by the incorporation—by a variety of approaches, sophisticated and simple—of ever-greater function into paper-based supports.^{23, 27-28, 42}

One means to create useful multifunctional SERS substrates—or even highly optimized SERS-only substrates—is through the deliberate incorporation of carefully selected structural features in the supports. The presence of pores, or voids, in a support has a number of consequences for SERS substrates: the available surface area for sensing can be diminished; the likelihood of hot spot formation can be affected, depending on the spatial extent and distribution of the voids; signal collection can be affected by scattering, line-of-sight access, and focal

depth for three-dimensional and structured substrates; mismatches between the excitation volume and the surfaces bearing analyte can limit reproducibility or signal magnitude; plasmonic nanopores, especially in arrays, introduce new optical considerations; and if analyte is delivered by drop-casting, the open area can profoundly affect the spatial distribution of analyte during solvent evaporation. For SERS substrates fabricated using an electroless plating step, the pores can affect the electroless deposition nucleation and growth (by imposing boundaries, for example). These factors include effects that can be much stronger than simple geometric coverage, allowing for considerable parameter space for optimizing performance through the support geometry and through the electroless plating parameters. We recorded scanning electron micrographs, with representative examples shown in Figures 7.3, 7.4, and 7.5, to gain preliminary structural insights, particularly with respect to the diversity of support structures that could be electrolessly plated. The set of micrographs showed consistently high coverage across the different replicates and substrate types.

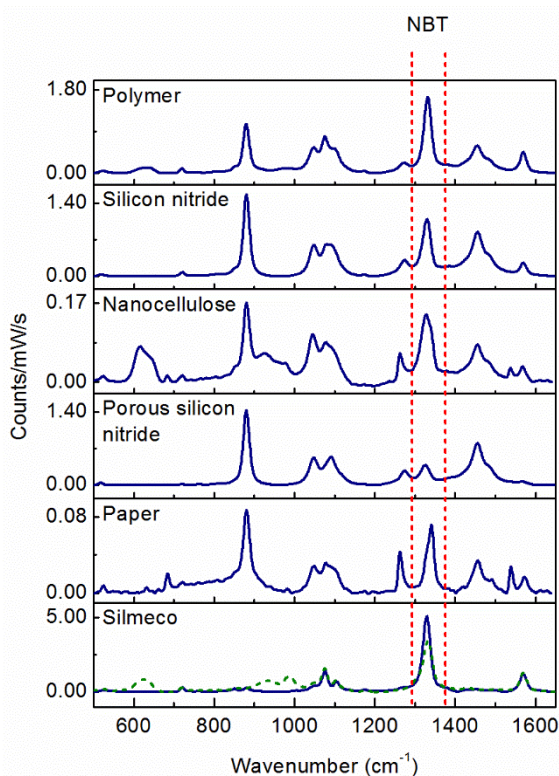


Figure 7.2: Representative baseline-corrected spectra of each substrate at 10^{-5} M NBT in ethanol (~ 57 mW for cellulose and as-supplied Silmeco; ~ 250 mW for all others). The dotted spectrum in the bottom panel shows the signal (scaled $20\times$) at 250 mW from $5\ \mu\text{L}$ of 1.6×10^{-5} M NBT in acetonitrile drop-cast onto the electrolessly-replated Silmeco. The vertical dotted lines denote the integration range for the NBT peak of interest.

Figure 7.3 provides a set of comparative micrographs of representative gold coatings on the silicon nitride-containing substrates. The uniform through-holes in the nanoporous membrane are a captivating structural feature compatible with compelling functions,⁵⁶⁻⁵⁷ and the nanoporous membrane was moreover free-standing between support bars (not shown) so that it was electrolessly gold-plated within the pores and on both sides of the membrane. We avoided any ultrasonic cleaning steps that might cause rupture of this thin porous membrane, and we were consistent in this purposeful omission across all substrates. The three substrates were composed of nanostructured gold films with low- and high-aspect ratio grains, but the preponderance and character of the high-aspect ratio structures

differed dramatically between the substrate types. The polymer-grafted silicon nitride gold film bore the greatest number of integral high-aspect ratio features, and with a unique grain structure characterized by the prevalence of larger, sharper, and more finely substructured gold flakes that projected from the surface. These flakes provide an increase in surface area for chemisorption of the NBT, and more significantly, are nanostructured on a length scale favorable for the existence of hot spots, and with an aspect ratio amenable to signal enhancement by the lightning rod effect.⁴ The nanoporous substrate imposed gaps between gold grains, although on length scales optimized, in this substrate, for filtering rather than hot spot formation.⁵⁷ The loss of planar substrate area might be compensated for by plating sufficiently long pores, but the nanochannel surface is normal to the conventional substrate surface, and longer pores would affect through-pore flow rates. Overall, detrimental decreases in sensitivity from surface area losses to pores may be quickly outpaced by beneficial gains to analytical performance through the selectivity and throughput that emerges from careful tuning of the pore geometry to support rapid and tuned sample filtering.

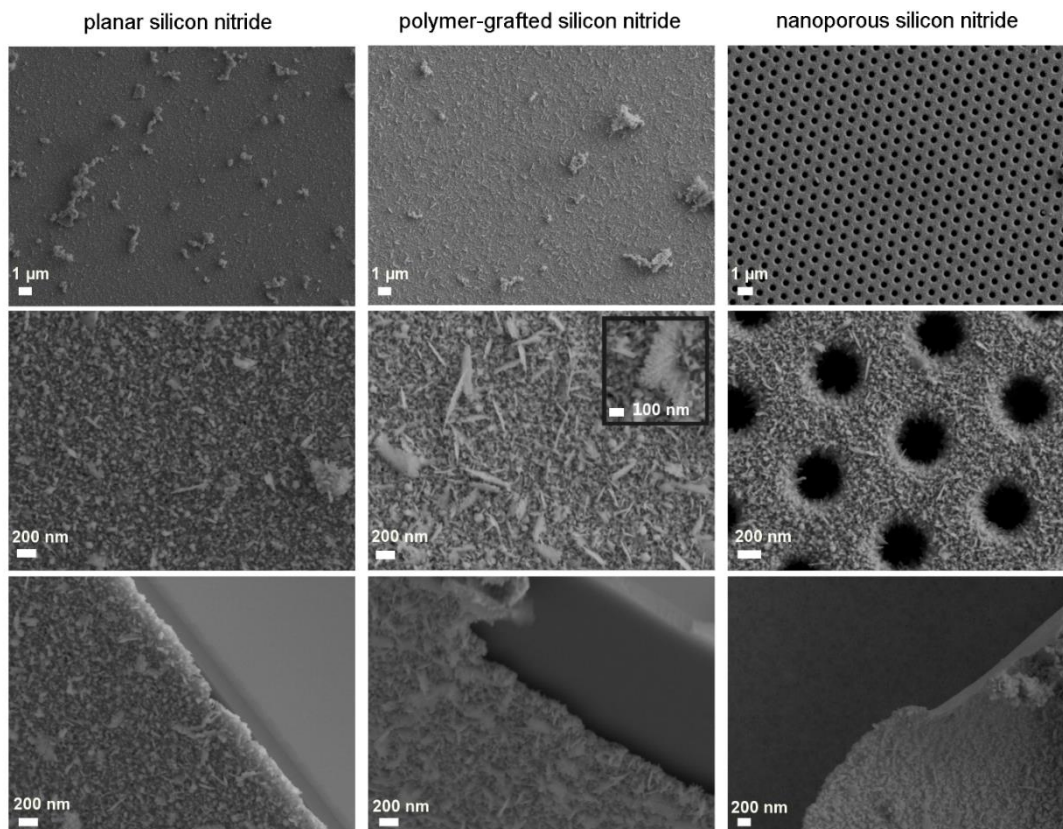


Figure 7.3: SEM images of, from left-to-right by column, gold-plated silicon nitride, polymer-grafted silicon nitride, and nanoporous silicon nitride. The top two rows show top-down images while the bottom row shows an angled view of gold film cross-sections. The inset in the center micrograph more clearly shows a representative highly-structured flake.

Figure 7.4 shows scanning electron micrographs from electrolessly-plated paper and nanocellulose samples. The paper substrate was distinguished by voids between large fibers constructed of bundled nanoscale fibers. The presence of void spaces in a given layer of the paper is partially compensated by overlap with fibers in underlying layers. The pore, or void space, size distribution in paper can be controlled during its manufacture, and is an important metric when selecting commercial filter paper, for example. The hand-fabricated nanocellulose substrate was highly textured and convoluted, without the fiber bundling, alignment, and low packing density that produced obvious microscale voids in the paper substrate. The ability of electroless plating to coat rough, nonplanar surfaces—beyond what was seen in the plating of the curved pore walls orthogonal to the planar upper

surface of the porous silicon nitride film—is dramatically illustrated by the impressive surface coverage. Thick, porous supports such as the nanocellulose paper have a large surface area for plating—distributed throughout their interior—and require a greater minimum plating solution volume than a planar support. Similarly, most of the plated gold surfaces will be able to bind analyte but will be optically inaccessible, and must be considered when aliquoting samples. Even after addressing these issues, the available signal strength using the cellulose-supported substrates was limited by the lower allowable excitation intensity. The fiber-based construction of the cellulose substrates, however, is an intriguing structural design feature that can provide additional analytical capabilities such as swab sampling and chromatographic separation.^{35, 44, 71} The cellulose substrates are evocative of other fiber-mat platforms used for SERS,^{11-12, 14-22} with paper supports being available at scale and at low cost using well-established manufacturing methods. When the ability to filter or chromatographically separate a sample using a SERS-active porous substrate is desired in addition to SERS sensing, one must consider the effect of the pore size on each capability—and on the interplay between each capability. Pore size is tunable through support fabrication or through the plating time-dependent thickness—within the limits of cost and available gold in the plating bath—of the plated gold layer. The flexibility, simplicity, and ease-of-handling of these nanofiber-based substrates stand in stark contrast to the more delicately engineered Silmeco nanopillar arrays, particularly for applications in resource-challenged settings.

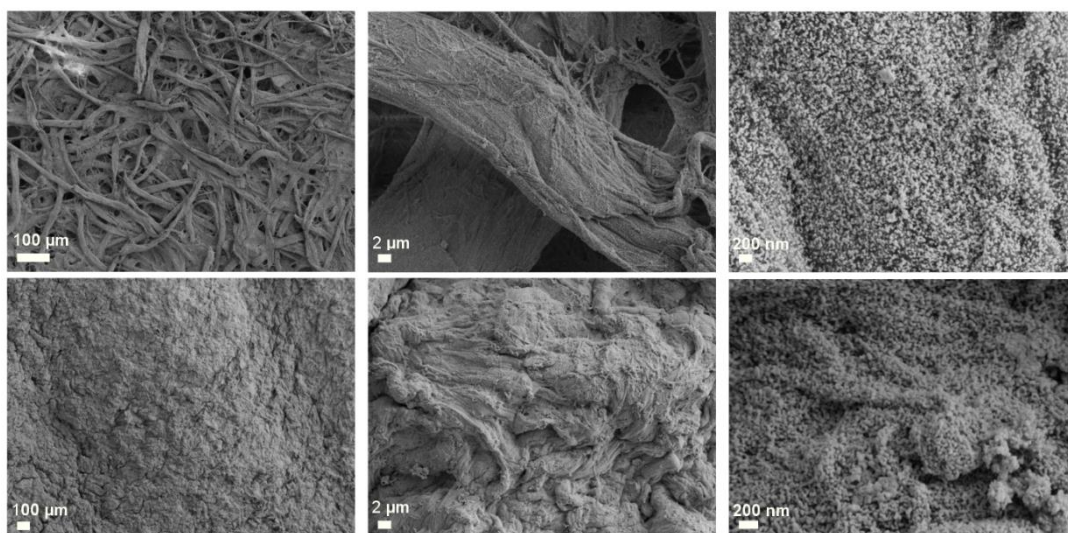


Figure 7.4: SEM images of gold-plated paper substrates (top row) and gold-plated nanocellulose paper substrates (bottom row).

The superb Raman enhancement that the nanopillar substrates provided when used as-supplied, without modification, reinforces the utility of rationally patterning traditional micro- and nanofabrication materials to create SERS substrates. One must, however, be careful during handling and solution processing to prevent unwanted damage or modification of such high-aspect ratio features:⁹ the gold-etched surface shows some broken nanopillars. SEM images in Figure 7.5 show that our general process chemistry was able to successfully electrolessly gold-plate a nanopillar array. The figure shows a section of electrolessly plated gold film that had peeled back from the nanopillar array surface: the surface of the gold film formerly in contact with the nanopillar array clearly shows dark areas that are consistent with electroless gold plating around extant nanopillars of the array. The dominant structural motifs of as-supplied Silmeco substrates—recognizable individual gold-encrusted nanopillars with limited numbers of contact points between nanopillars to yield likely hot spots—were not conspicuous in our top-down micrographs of the electrolessly plated substrates. This absence of a key SERS-associated (nano)structure is the most significant contributor to the dramatic loss of spectral intensity when using replated Silmeco. While several of the dark

areas of the underside of the gold film are evocative of plating around nanopillars likely already leaning together⁹, optimization of the electroless plating for this nanopillar support would be necessary to deliver the engineered hot spots of the as-supplied substrate. The most reasonable starting point for such an optimization would be to plate pristine gold-free nanoarrays so that the distance between the gold regions of adjacent nanopillars could be controlled by the plating kinetics and time, and any post-plating drying-induced pillar leaning. Producing a nanoarray surface by etching gold from the as-supplied Silmeco handicaps the subsequent replating with the initial structural modification of hot spot formation and the likely damage to the nanoarray of the gold etching step. Nevertheless, the robust gold film formed around nanopillars in this particular micrograph is a compelling reminder of the ability of electroless plating to plate nanoscale structures, and its ability to create, without substantial equipment overhead, SERS substrates from highly engineered supports.

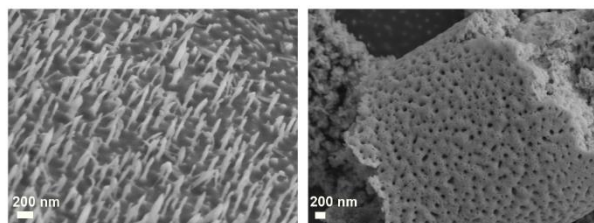


Figure 7.5: SEM image of a nanopillar substrate after gold etch (left), and with an electrolessly plated gold film peeled off from the underlying nanopillar support (right).

CONCLUSIONS

Electroless plating is a robust method for fashioning a variety of materials, exhibiting a range of structural features and capabilities, into SERS-active substrates. The general electroless plating procedure we employed was able to successfully plate gold onto planar, porous, nanopillar, and fibrous surfaces; into well-defined nanochannels and variably-sized void volumes; onto traditional nanofabrication-compatible materials; and onto less conventional device platform materials such as paper that are important in the domain of low-cost diagnostics. All resulting substrates in our library were capable of generating SER spectra. This electroless plating approach produced nanostructured films where the size, shape, and position of the gold grains could be tuned by the particular material and form factor of the support material being plated, and this tuneability was evident from both microscopic imaging and SERS intensities. The underlying support structure for the gold plating did more than imprint structure on the gold film, though. Electroless plating of already functional structured supports created multifunctional SERS substrates. The force of the work presented here is thus both foundational and prospective: there is much promise in exploring electroless plating—including extensions such as patterned electroless plating^{51, 55}—as a straightforward, robust, and low-overhead method to create custom SERS-active substrates that augment the compelling material properties, structures, and capabilities of their supports. Multifunctional SERS substrates require a rich, and application-specific, context and framework for design and performance evaluation. The substrate must, of course, generate a useful Raman spectrum, but the particular implementation—from design and fabrication to end-use—dictates the balance between Raman enhancement and other capabilities such as integral

sample processing. This balance dictates how to tune the electroless plating process chemistry, and the support structure, to optimize the SERS substrate. We believe that electroless plating has great potential in the creation of multifunctional SERS substrates useful for answering a host of design and sensing challenges.

ASSOCIATED CONTENT

SUPPORTING INFORMATION

The following files are available free of charge.

Experimental details, methods and sample characterizations (PDF)

AUTHOR INFORMATION

Corresponding Author:

*jason_dwyer@uri.edu

AUTHOR CONTRIBUTIONS

The manuscript was written through contributions of all authors. All authors have given approval to the final version of the manuscript.

FUNDING SOURCES

This research has been supported by NSF CAREER award CBET-1150085, by NSF EPSCoR Cooperative Agreement #IIA-1330406, and by the University of Rhode Island including URI graduate fellowships for Y. M. Nuwan D. Y. Bandara and Buddini Iroshika Karawdeniya.

ACKNOWLEDGMENT

B. L. Lucht research group at the University of Rhode Island for use of their XPS system, and for assistance in XPS data acquisition. This research has been

supported by NSF CAREER award CBET-1150085, by NSF EPSCoR Cooperative Agreement #IIA-1330406, and by the University of Rhode Island including URI graduate fellowships for YMNDYB and BIK.

ABBREVIATIONS

SERS, Surface enhanced Raman spectroscopy; LPCVD, low-pressure chemical vapor deposition; SiN_x, (silicon-rich) LPCVD silicon nitride; SEV, SERS enhancement value; FE-SEM, field emission scanning electron microscopy; XPS, x-ray photoelectron spectroscopy; ROC, receiver operating characteristic; NBT, 4-nitrobenzenethiol;

REFERENCES

1. Yang, L.; Yan, B.; Premasiri, W. R.; Ziegler, L. D.; Negro, L. D.; Reinhard, B. M., Engineering Nanoparticle Cluster Arrays for Bacterial Biosensing: The Role of the Building Block in Multiscale SERS Substrates. *Adv. Funct. Mater.* 2010, *20*, 2619-2628.
2. Patel, I. S.; Premasiri, W. R.; Moir, D. T.; Ziegler, L. D., Barcoding Bacterial Cells: A SERS-Based Methodology for Pathogen Identification. *Journal of Raman Spectroscopy* 2008, *39*, 1660-1672.
3. Stiles, P. L.; Dieringer, J. A.; Shah, N. C.; Van Duyne, R. P., Surface-Enhanced Raman Spectroscopy. *Annu. Rev. Anal. Chem.* 2008, *1*, 601-626.
4. Aroca, R., *Surface-Enhanced Vibrational Spectroscopy*. John Wiley & Sons Ltd: Chichester, West Sussex PO19 8SQ, England, 2006.
5. *Surface Enhanced Raman Spectroscopy: Analytical, Biophysical and Life Science Applications*. Wiley-VCH Verlag GmbH & Co. KGaA: 2010; p I-XXII, 1-331.
6. Murphy, C. J.; Sau, T. K.; Gole, A. M.; Orendorff, C. J.; Gao, J.; Gou, L.; Hunyadi, S. E.; Li, T., Anisotropic Metal Nanoparticles: Synthesis, Assembly, and Optical Applications. *J. Phys. Chem. B* 2005, *109*, 13857-13870.
7. Perney, N. M. B.; Baumberg, J. J.; Zoorob, M. E.; Charlton, M. D. B.; Mahnkopf, S.; Netti, C. M., Tuning Localized Plasmons in Nanostructured Substrates for Surface-Enhanced Raman Scattering. *Opt. Express* 2006, *14*, 847-857.
8. Tabatabaei, M.; Najiminaini, M.; Davieau, K.; Kaminska, B.; Singh, M. R.; Carson, J. J. L.; Lagugné-Labarhet, F., Tunable 3d Plasmonic Cavity Nanosensors for Surface-Enhanced Raman Spectroscopy with Sub-Femtomolar Limit of Detection. *ACS Photonics* 2015, *2*, 752-759.
9. Schmidt, M. S.; Hübner, J.; Boisen, A., Large Area Fabrication of Leaning Silicon Nanopillars for Surface Enhanced Raman Spectroscopy. *Adv. Mater.* 2012, *24*, OP11-OP18.
10. Gopinath, A.; Boriskina, S. V.; Reinhard, B. M.; Dal Negro, L., Deterministic Aperiodic Arrays of Metal Nanoparticles for Surface-Enhanced Raman Scattering (SERS). *Opt. Express* 2009, *17*, 3741-3753.
11. Aldeanueva-Potel, P.; Correa-Duarte, M. A.; Alvarez-Puebla, R. A.; Liz-Marzán, L. M., Free-Standing Carbon Nanotube Films as Optical Accumulators for Multiplex SERS Attomolar Detection. *ACS Appl. Mater. Interfaces* 2010, *2*, 19-22.
12. He, D.; Hu, B.; Yao, Q.-F.; Wang, K.; Yu, S.-H., Large-Scale Synthesis of Flexible Free-Standing SERS Substrates with High Sensitivity: Electrospun Pva Nanofibers Embedded with Controlled Alignment of Silver Nanoparticles. *ACS Nano* 2009, *3*, 3993-4002.
13. Manas, R. G.; Zhida, X.; Elaine, B.; Hoang, N.; Jerald, A. B.; Cindy, L.; Robin, M.; Mihail, B.; Allan, S. P. C.; Tiziana, C. B.; Liu, G. L., Rigorous Surface

Enhanced Raman Spectral Characterization of Large-Area High-Uniformity Silver-Coated Tapered Silica Nanopillar Arrays. *Nanotechnology* 2010, 21, 395701.

14. Dawson, P.; Duenas, J. A.; Boyle, M. G.; Doherty, M. D.; Bell, S. E. J.; Kern, A. M.; Martin, O. J. F.; Teh, A. S.; Teo, K. B. K.; Milne, W. I., Combined Antenna and Localized Plasmon Resonance in Raman Scattering from Random Arrays of Silver-Coated, Vertically Aligned Multiwalled Carbon Nanotubes. *Nano Lett.* 2011, 11, 365-371.

15. Zhang, C.-L.; Lv, K.-P.; Cong, H.-P.; Yu, S.-H., Controlled Assemblies of Gold Nanorods in Pva Nanofiber Matrix as Flexible Free-Standing SERS Substrates by Electrospinning. *Small* 2012, 8, 648-653.

16. Roskov, K. E.; Kozek, K. A.; Wu, W.-C.; Chhetri, R. K.; Oldenburg, A. L.; Spontak, R. J.; Tracy, J. B., Long-Range Alignment of Gold Nanorods in Electrospun Polymer Nano/Microfibers. *Langmuir* 2011, 27, 13965-13969.

17. Zhang, L.; Gong, X.; Bao, Y.; Zhao, Y.; Xi, M.; Jiang, C.; Fong, H., Electrospun Nanofibrous Membranes Surface-Decorated with Silver Nanoparticles as Flexible and Active/Sensitive Substrates for Surface-Enhanced Raman Scattering. *Langmuir* 2012, 28, 14433-14440.

18. Lee, C. H.; Hankus, M. E.; Tian, L.; Pellegrino, P. M.; Singamaneni, S., Highly Sensitive Surface Enhanced Raman Scattering Substrates Based on Filter Paper Loaded with Plasmonic Nanostructures. *Anal. Chem.* 2011, 83, 8953-8958.

19. Yu, W. W.; White, I. M., Inkjet Printed Surface Enhanced Raman Spectroscopy Array on Cellulose Paper. *Anal. Chem.* 2010, 82, 9626-9630.

20. Polavarapu, L.; Porta, A. L.; Novikov, S. M.; Coronado-Puchau, M.; Liz-Marzán, L. M., Pen-on-Paper Approach toward the Design of Universal Surface Enhanced Raman Scattering Substrates. *Small* 2014, 10, 3065-3071.

21. Berthod, A.; Laserna, J. J.; Winefordner, J. D., Analysis by Surface Enhanced Raman Spectroscopy on Silver Hydrosols and Silver Coated Filter Papers. *J. Pharm. Biomed. Anal.* 1988, 6, 599-608.

22. Qu, L.-L.; Li, D.-W.; Xue, J.-Q.; Zhai, W.-L.; Fossey, J. S.; Long, Y.-T., Batch Fabrication of Disposable Screen Printed SERS Arrays. *Lab on a Chip* 2012, 12, 876-881.

23. Then, W. L.; Garnier, G., Paper Diagnostics in Biomedicine. *Rev. Anal. Chem* 2013, 32, 269-294.

24. Penn, M. A.; Drake, D. M.; Driskell, J. D., Accelerated Surface-Enhanced Raman Spectroscopy (SERS)-Based Immunoassay on a Gold-Plated Membrane. *Anal. Chem.* 2013, 85, 8609-8617.

25. Polavarapu, L.; Liz-Marzán, L. M., Towards Low-Cost Flexible Substrates for Nanoplasmonic Sensing. *PCCP* 2013, 15, 5288-5300.

26. Fan, M.; Zhang, Z.; Hu, J.; Cheng, F.; Wang, C.; Tang, C.; Lin, J.; Brolo, A. G.; Zhan, H., Ag Decorated Sandpaper as Flexible SERS Substrate for Direct Swabbing Sampling. *Mater. Lett.* 2014, 133, 57-59.

27. Nery, E. W.; Kubota, L. T., Sensing Approaches on Paper-Based Devices: A Review. *Anal Bioanal Chem* 2013, 405, 7573-7595.
28. Yang, Y.; Noviana, E.; Nguyen, M. P.; Geiss, B. J.; Dandy, D. S.; Henry, C. S., Paper-Based Microfluidic Devices: Emerging Themes and Applications. *Anal. Chem.* 2017, 89, 71-91.
29. Whelan, J. C.; Karawdeniya, B. I.; Bandara, Y. M. N. D. Y.; Velleco, B. D.; Masterson, C. M.; Dwyer, J. R., Electroless Plating of Thin Gold Films Directly onto Silicon Nitride Thin Films and into Micropores. *ACS Appl. Mater. Interfaces* 2014, 6, 10952-10957.
30. Zheng, G.; Polavarapu, L.; Liz-Marzan, L. M.; Pastoriza-Santos, I.; Perez-Juste, J., Gold Nanoparticle-Loaded Filter Paper: A Recyclable Dip-Catalyst for Real-Time Reaction Monitoring by Surface Enhanced Raman Scattering. *Chem. Commun.* 2015, 51, 4572-4575.
31. Vo-Dinh, T.; Hiromoto, M. Y. K.; Begun, G. M.; Moody, R. L., Surface-Enhanced Raman Spectrometry for Trace Organic Analysis. *Anal. Chem.* 1984, 56, 1667-1670.
32. Tran, C. D., Subnanogram Detection of Dyes on Filter Paper by Surface-Enhanced Raman Scattering Spectrometry. *Anal. Chem.* 1984, 56, 824-826.
33. Laserna, J. J.; Campiglia, A. D.; Winefordner, J. D., Surface-Enhanced Raman Spectrometry on a Silver-Coated Filter Paper Substrate. *Anal. Chim. Acta* 1988, 208, 21-30.
34. Laserna, J. J.; Sutherland, W. S.; Winefordner, J. D., Microspectrometric Investigation of Active Substrates for Surface Enhanced Raman Scattering. *Anal. Chim. Acta* 1990, 237, 439-450.
35. Lee, C. H.; Tian, L.; Singamaneni, S., Paper-Based SERS Swab for Rapid Trace Detection on Real-World Surfaces. *ACS Appl. Mater. Interfaces* 2010, 2, 3429-3435.
36. Ngo, Y. H.; Li, D.; Simon, G. P.; Garnier, G., Gold Nanoparticle–Paper as a Three-Dimensional Surface Enhanced Raman Scattering Substrate. *Langmuir* 2012, 28, 8782-8790.
37. Ngo, Y. H.; Li, D.; Simon, G. P.; Garnier, G., Effect of Cationic Polyacrylamides on the Aggregation and SERS Performance of Gold Nanoparticles-Treated Paper. *J. Colloid Interface Sci.* 2013, 392, 237-246.
38. Zhang, L.; Li, X.; Ong, L.; Tabor, R. F.; Bowen, B. A.; Fernando, A. I.; Nilghaz, A.; Garnier, G.; Gras, S. L.; Wang, X.; Shen, W., Cellulose Nanofibre Textured SERS Substrate. *Colloids and Surfaces A: Physicochemical and Engineering Aspects* 2015, 468, 309-314.
39. Niu, Z.; Fang, Y., Surface-Enhanced Raman Scattering of Single-Walled Carbon Nanotubes on Silver-Coated and Gold-Coated Filter Paper. *J. Colloid Interface Sci.* 2006, 303, 224-228.
40. Ota, F.; Higuchi, S.; Gohshi, Y.; Furuya, K.; Ban, M.; Kyoto, M., Some Considerations of the SERS Effect of L-Phenylalanine in the near-Infrared Region Using Silver Colloid Solution. *Journal of Raman Spectroscopy* 1997, 28, 849-854.

41. Wigginton, K. R.; Vikesland, P. J., Gold-Coated Polycarbonate Membrane Filter for Pathogen Concentration and SERS-Based Detection. *Analyst* 2010, *135*, 1320-1326.
42. Zhang, K.; Zhao, J.; Xu, H.; Li, Y.; Ji, J.; Liu, B., Multifunctional Paper Strip Based on Self-Assembled Interfacial Plasmonic Nanoparticle Arrays for Sensitive SERS Detection. *ACS Appl. Mater. Interfaces* 2015, *7*, 16767-16774.
43. Møller, P.; Nielsen, L. P., *Advanced Surface Technology*. Møller & Nielsen APS: Denmark, 2013; Vol. 1, p 594.
44. Cabalín, L. M.; Laserna, J. J., Fast Spatially Resolved Surface-Enhanced Raman Spectrometry on a Silver Coated Filter Paper Using Charge-Coupled Device Detection. *Anal. Chim. Acta* 1995, *310*, 337-345.
45. Cheng, M.-L.; Tsai, B.-C.; Yang, J., Silver Nanoparticle-Treated Filter Paper as a Highly Sensitive Surface-Enhanced Raman Scattering (SERS) Substrate for Detection of Tyrosine in Aqueous Solution. *Anal. Chim. Acta* 2011, *708*, 89-96.
46. Norrod, K. L.; Sudnik, L. M.; Rousell, D.; Rowlen, K. L., Quantitative Comparison of Five SERS Substrates: Sensitivity and Limit of Detection. *Appl. Spectrosc.* 1997, *51*, 994-1001.
47. Saito, Y.; Wang, J. J.; Smith, D. A.; Batchelder, D. N., A Simple Chemical Method for the Preparation of Silver Surfaces for Efficient SERS. *Langmuir* 2002, *18*, 2959-2961.
48. Tabakman, S. M.; Chen, Z.; Casalongue, H. S.; Wang, H.; Dai, H., A New Approach to Solution-Phase Gold Seeding for SERS Substrates. *Small* 2011, *7*, 499-505.
49. Menon, V. P.; Martin, C. R., Fabrication and Evaluation of Nanoelectrode Ensembles. *Anal. Chem.* 1995, *67*, 1920-1928.
50. Porter, L. A.; Choi, H. C.; Ribbe, A. E.; Buriak, J. M., Controlled Electroless Deposition of Noble Metal Nanoparticle Films on Germanium Surfaces. *Nano Lett.* 2002, *2*, 1067-1071.
51. Zabetakis, D.; Dressick, W. J., Selective Electroless Metallization of Patterned Polymeric Films for Lithography Applications. *ACS Appl. Mater. Interfaces* 2009, *1*, 4-25.
52. Liu, F.-M.; Green, M., Efficient SERS Substrates Made by Electroless Silver Deposition into Patterned Silicon Structures. *J. Mater. Chem.* 2004, *14*, 1526-1532.
53. Dwyer, J. R.; Harb, M., Through a Window, Brightly: A Review of Selected Nanofabricated Thin-Film Platforms for Spectroscopy, Imaging, and Detection. *Appl. Spectrosc.* 2017, *71*, 2051-2075.
54. Dwyer, J. R.; Bandara, Y. M. N. D. Y.; Whelan, J. C.; Karawdeniya, B. I.; Nichols, J. W., Silicon Nitride Thin Films for Nanofluidic Device Fabrication. In *Nanofluidics, 2nd Edition*, 2 ed.; Edel, J.; Ivanov, A.; Kim, M., Eds. Royal Society for Chemistry: 2016; Chapter 7.

55. Bandara, Y. M. N. D. Y.; Karawdeniya, B. I.; Whelan, J. C.; Ginsberg, L. D. S.; Dwyer, J. R., Solution-Based Photo-Patterned Gold Film Formation on Silicon Nitride. *ACS Appl. Mater. Interfaces* 2016, 8, 34964-34969.
56. Dahlin, A. B., Sensing Applications Based on Plasmonic Nanopores: The Hole Story. *Analyst* 2015, 140, 4748-4759.
57. Kuiper, S.; van Rijn, C. J. M.; Nijdam, W.; Elwenspoek, M. C., Development and Applications of Very High Flux Microfiltration Membranes. *Journal of Membrane Science* 1998, 150, 1-8.
58. Guicheteau, J. A.; Farrell, M. E.; Christesen, S. D.; Fountain, A. W.; Pellegrino, P. M.; Emmons, E. D.; Tripathi, A.; Wilcox, P.; Emge, D., Surface-Enhanced Raman Scattering (SERS) Evaluation Protocol for Nanometallic Surfaces. *Appl. Spectrosc.* 2013, 67, 396-403.
59. Whelan, J. C.; Karawdeniya, B. I.; Bandara, Y. M. N. D. Y.; Velleco, B. D.; Masterson, C. M.; Dwyer, J. R., Correction to Electroless Plating of Thin Gold Films Directly onto Silicon Nitride Thin Films and into Micropores. *ACS Appl. Mater. Interfaces* 2015, 7, 26004-26004.
60. Massarini, E.; Wästerby, P.; Landström, L.; Lejon, C.; Beck, O.; Andersson, P. O., Methodologies for Assessment of Limit of Detection and Limit of Identification Using Surface-Enhanced Raman Spectroscopy. *Sensors and Actuators B: Chemical* 2015, 207, Part A, 437-446.
61. Wirtz, M.; Yu, S.; Martin, C. R., Template Synthesized Gold Nanotube Membranes for Chemical Separations and Sensing. *Analyst* 2002, 127, 871-879.
62. DesOrmeaux, J. P. S.; Winans, J. D.; Wayson, S. E.; Gaborski, T. R.; Khire, T. S.; Striemer, C. C.; McGrath, J. L., Nanoporous Silicon Nitride Membranes Fabricated from Porous Nanocrystalline Silicon Templates. *Nanoscale* 2014, 6, 10798-10805.
63. Striemer, C. C.; Gaborski, T. R.; McGrath, J. L.; Fauchet, P. M., Charge- and Size-Based Separation of Macromolecules Using Ultrathin Silicon Membranes. *Nature* 2007, 445, 749-753.
64. Joshua, J. M.; Robert, N. C.; Kelly, B. M.; Jon-Paul, S. D.; Christopher, C. S.; Joshua, D. W.; Thomas, R. G., Lift-Off of Large-Scale Ultrathin Nanomembranes. *Journal of Micromechanics and Microengineering* 2015, 25, 015011.
65. Gironès, M.; Borneman, Z.; Lammertink, R. G. H.; Wessling, M., The Role of Wetting on the Water Flux Performance of Microsieve Membranes. *Journal of Membrane Science* 2005, 259, 55-64.
66. Huang, H.; Song, Z.; Wei, N.; Shi, L.; Mao, Y.; Ying, Y.; Sun, L.; Xu, Z.; Peng, X., Ultrafast Viscous Water Flow through Nanostrand-Channelled Graphene Oxide Membranes. *Nat Commun* 2013, 4, 2979.
67. Liu, G.; Jin, W.; Xu, N., Graphene-Based Membranes. *Chem. Soc. Rev.* 2015, 44, 5016-5030.
68. Fine, D.; Grattoni, A.; Goodall, R.; Bansal, S. S.; Chiappini, C.; Hosali, S.; van de Ven, A. L.; Srinivasan, S.; Liu, X.; Godin, B.; Brousseau, L.; Yazdi, I. K.;

Fernandez-Moure, J.; Tasciotti, E.; Wu, H.-J.; Hu, Y.; Klemm, S.; Ferrari, M., Silicon Micro- and Nanofabrication for Medicine. *Adv. Healthcare Mater.* 2013, 2, 632-666.

69. Schoch, R. B.; Han, J.; Renaud, P., Transport Phenomena in Nanofluidics. *Reviews of Modern Physics* 2008, 80, 839-883.

70. Vlassioug, I.; Apel, P. Y.; Dmitriev, S. N.; Healy, K.; Siwy, Z. S., Versatile Ultrathin Nanoporous Silicon Nitride Membranes. *Proceedings of the National Academy of Sciences of the United States of America* 2009, 106, 21039-21044.

71. Yu, W. W.; White, I. M., Chromatographic Separation and Detection of Target Analytes from Complex Samples Using Inkjet Printed SERS Substrates. *Analyst* 2013, 138, 3679-3686.

APPENDIX 1: CHAPTER 2 SUPPORTING INFORMATION
**TASTY, THERAPEUTIC, OR TOXIC? GAUGING THIN-FILM SOLID-
STATE NANOPORES FOR POLYSACCHARIDE SENSING**

Buddini Iroshika Karawdeniya, Y.M. Nuwan D.Y. Bandara, Jonathan W. Nichols,
Robert B. Chevalier, and Jason R. Dwyer

**Department of Chemistry, University of Rhode Island, 140 Flagg Road,
Kingston, 02881, USA.**
REAGENTS AND MATERIALS

The following materials, identified by their product number and specification, were obtained from Sigma-Aldrich Corporation (St. Louis, MO, USA): potassium chloride (60130, puriss. p.a., $\geq 99.5\%$ (AT)); sodium chloride (S7653, BioXtra, $\geq 99.5\%$ (AT)); HEPES potassium salt (H0527, $\geq 99.5\%$ (titration)); sulphuric acid (339741, 99.999%); alginate lyase (A1603, $\geq 10,000$ units/g); and hydrochloric acid (320331, ACS reagent, 37%). Polysaccharides were commercially obtained: sodium alginate A1-B25266 (~75-120 kDa, 40-90 centipoise (1% solution); Alfa Aesar [Ward Hill, MA, USA]) and A2-PROTANAL® LFR5/60 (120kDa, 300-700 centipoise (10% solution); FMC Corporation Health and Nutrition, PA, USA); heparin sodium salt (USP, 1304038, Rockville, MD; mol. wt. ~16 kDa by lot certificate) and over sulfated chondroitin sulfate (OSCS) (USP, 1133580; est. mol. wt. ~17 kDa by porcine origin¹; from Sigma Aldrich Corporation (St. Louis, MO, USA)). The potency of the USP heparin samples was 180 USP heparin units according to Pharmacopeial Forum Vol. 35(5) [Sept.–Oct. 2009].

Silicon-rich LPCVD silicon nitride (nominally) 10 nm-thick membranes on 200 μm -thick silicon frame (NT001Z and NT005Z; with reported membrane thicknesses for Lot # L8 10.5 \pm 0.3 nm, L15 16 \pm 2 nm, L31 14 \pm 2 nm, L68 12 \pm 2 nm) were purchased from Norcada, Inc. (Alberta, Canada). All aqueous solutions were prepared using Type I water (~18 M Ω -cm resistivity from either a Millipore Synergy UV [Billerica, MA], or American Aqua

Maxicab system [Narragansett, RI, USA]); all dilutions and washes also used this water. Stericup-VP vacuum filtration systems were used to filter electrolyte solutions after preparation, and water to prepare alginate solutions (SCVPU11RE 0.10 μm pore size in polyethersulfone membrane; EMD Millipore Corporation [MA, USA]).

Ag/AgCl electrodes were made from 1.0 mm-diameter silver wire (Alfa Aesar 11434, annealed, 99.9% (metals basis)) by soaking overnight in sodium hypochlorite (Alfa Aesar 33369, 11-15% available chlorine). Electrodes were insulated using shrink-wrap PTFE tubing (McMaster-Carr, 7960K21, high-temperature harsh environment tubing, moisture seal, heat-shrink, 0.07" ID before; and 7564K67, high-temperature harsh environment tubing, heat-shrink, 0.08" ID before, 0.05" ID after) and connected to electronics using pins (Connectivity TE Connectivity / AMP 205090-1 D sub circular connector contact, AMPLIMITE 109 Series, Socket, Crimp, 20-24 AWG). Nanopore chips were compressed between silicone gaskets (McMaster-Carr, 86435K43, high-temperature silicone rubber sheet, ultra-thin, 12" x 12", 0.015" thick, 35A durometer) in custom-machined PTFE holders with ~ 500 μL sample wells.² Silicone tubing with ID 1.0 mm x OD 3.0 mm was obtained from Nanion Technologies GmbH, Munich, Germany.

INSTRUMENTAL DETAILS

Measurements of solution pH and conductivity were with an Orion Star™ pH meter and Orion™ ROSS Ultra™ Refillable pH/ATC Triode™ Combination Electrodes and Orion™ DuraProbe™ 4-Electrode Conductivity Cells (Thermo Fisher Scientific Inc, MA, USA). Nanopore formation by dielectric breakdown was performed using programmable DC power supplies (Model 9121A, B&K Precision Corporation, CA, USA) interfaced to a home-built circuit;³ real-time current measurements were by a 428-Programmable Current Amplifier (Keithley Instruments, Cleveland, OH, USA) interfaced to NI USB 6351 DAQ card using custom LabView-based (National Instruments Corp., TX, USA) software to control the applied voltage. All nanopore measurements were performed using an

Axopatch 200B amplifier (Axon Instruments, Foster City, CA, USA) in voltage clamp mode. The amplifier was interfaced to a computer system using a data acquisition card (779512-01 NI PCIE-6251 M Series with 777960-01 NI BNC-2120 shielded connector block) and control software written in LabView. Current-versus-time measurements were typically acquired for 1 h (3×20 min) at 100 kHz acquisition rates with the 4-pole low pass Bessel filter built-in to the Axopatch 200B set to 10 kHz. Measurements of nanopore conductance were acquired at a rate of 10 kHz, with the filter set to 1 kHz.

Infrared spectra of the powder were acquired by FTIR-ATR (Bruker Tensor 27 equipped with a Ge crystal) averaged over 256 scans with 4 cm^{-1} spectral resolution. All measurements done inside a nitrogen filled glovebox.

UV/Vis spectra were collected using a Varian Cary 50 Bio UV/Visible Spectrophotometer with a quartz cuvette with a 1 cm pathlength. Single run measurements were taken from 200 to 400 nm at a scan rate of 300 nm/min and 0.50 nm intervals.

All 3D printed components were designed in Solid Works 2014 Professional Edition (Dassault Systems SolidWorks Corporation, Waltham, MA) and printed by Makerbot Replicator (MakerBot Industries, Brooklyn, NY) using PLA plastic (MP06103, MakerBot Industries, Brooklyn, NY).

GENERAL NANOPORE SENSING PROCEDURE

Nanopores in the ~ 10 nm-thick silicon nitride membranes were fabricated by controlled dielectric breakdown using 11-15.5 V DC applied potentials.³ The nanopore formation was carried out in 1 M KCl electrolyte, HEPES-buffered to pH ~ 7 , and the membranes and pores were secured in custom-machined PTFE holders with $\sim 500 \mu\text{L}$ sample wells. Nanopore conductances, G , were the slope of the linear fit to the experimental Ohmic current-voltage data, measured in 1 M KCl electrolyte buffered with HEPES at pH ~ 7 . The corresponding nominal nanopore diameters were calculated using a conductance model (including bulk, surface, and access resistance terms) and cylindrical nanopore shape

suitable for this salt concentration and fabrication method, $G = \left(\frac{1}{G_{\text{bulk}} + G_{\text{surface}}} + \frac{1}{G_{\text{access}}} \right)^{-1}$.³⁻⁶

Nanopores used for measurements produced stable open-pore (analyte-free) currents at the salt concentrations used.

All electrolyte solutions were HEPES-buffered (10 mM) to pH ~7 unless otherwise noted (adjusted with dropwise addition of concentrated hydrochloric acid), and measurements were carried out using filtered solutions with 0.1, 1.0, and 4.0 M KCl concentrations. Solutions of 0.2% (w/v) sodium alginate, 0.2% (w/v) heparin, and 0.2% (w/v) OSCS were made by dissolving the solids in filtered Type I water. For routine measurements and unless otherwise specified, 4 μL aliquots were added to the headstage side (Figure 2.1), leaving the ground side free of initially added analyte. Calibration curves for each nanopore were constructed by repeated cycles of measurement followed by the addition of another analyte aliquot. Current blockages were extracted using a current-threshold analysis. Any current blockages exceeding 100 s ($\approx 0.1\%$) were not included in analyses.

POLYSACCHARIDE VISCOSITY MEASUREMENTS

Apparent viscosity measurements were carried out on aqueous sodium alginate solutions (0.15-1.0 g/dL) in 0.1 M sodium chloride solutions using a capillary viscometer (SI Analytics Ubbelohde Viscometer, Thermo Fisher Scientific, Inc., MA, USA) immersed in a water bath at $\sim 23^\circ\text{C}$. Triplicate measurements of the apparent viscosity were made at each solution concentration to yield the intrinsic viscosity, $[\eta]$, from a plot of⁷

$$\frac{\eta_{\text{sp}}}{C} = [\eta] + k[\eta]^2 C$$

where C is the macromolecule's concentration in g/dL, k is a constant characteristic of the solute-solvent system, $\eta_{\text{sp}} = \frac{\eta_{\text{solution}}}{\eta_{\text{solvent}}} - 1$ is the specific viscosity calculated from the apparent viscosities. The weight- and number-average molecular masses, M_w and M_n , and the of the polymers in kDa were calculated according to⁸

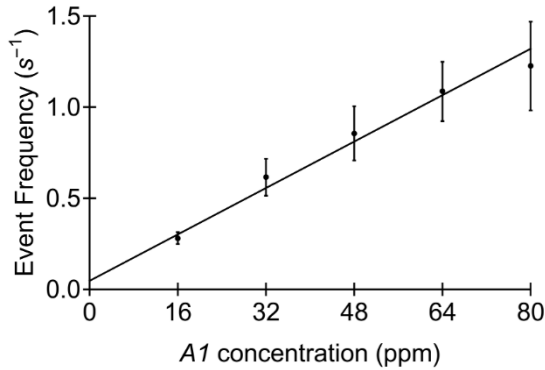
$$[\eta] = 0.023(M_w)^{0.984}$$

$$[\eta] = 0.095(M_n)^{0.963}$$

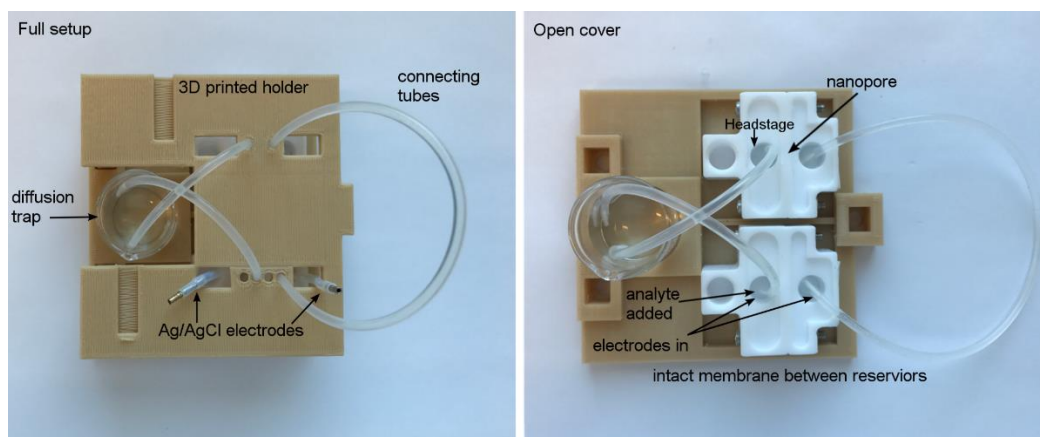
The respective molecular masses of the two alginate samples were determined by this method to be ~286 kDa and ~74 kDa for *A1*, and ~71 kDa and ~18 kDa for *A2*. Using a polymer's molecular weight, M , we can calculate the hydrodynamic radius (N_A is Avogadro's number)⁹

$$R_h = \left(\frac{3[\eta]M}{10\pi N_A} \right)^{1/3}$$

to be ~19 nm for *A1* and ~8 nm for *A2* (on an M_n -basis). The corresponding root-mean-squared end-to-end distance, $\langle r^2 \rangle^{1/2}$ for each sample is equal to $3.1R_h$.



Supplementary Figure 2.1: Calibration curve of sodium alginate event frequency versus concentration of *A1*. Three trials were performed, with each data point including at least 1000 events extracted from at least 1 h long measurements at 200 mV applied voltage after consecutive additions of 4 μ L aliquots to the headstage side of the same nanopore. Error bars represent the standard deviation across the trials.



Supplementary Figure 2.2: A special nanopore configuration in which the electrolyte wells proximal to the electrodes and to the nanopore were physically separated. The purpose of this configuration was to determine if the current blockages arose from analyte interaction with the electrodes, or with the nanopore, itself. The electrolyte wells in the lower PTFE cell held the electrodes and were separated by an intact SiN_x membrane that did not allow ionic flow. These wells were connected through electrolyte-filled silicone tubing and an electrolyte-filled beaker (acting as a diffusion trap), to a second electrolyte-filled PTFE cell in which the wells were separated by a SiN_x nanopore. With analyte injected into the bottom cell, the only possible mechanism of current blockage was either by direct interaction with the electrodes, or by the passage of analyte through the tubing and beaker of solution until it could interact with the nanopore. When a $4 \mu\text{L}$ aliquot of the alginate was added to the head stage side of the lower cell, only 18 appreciable current transients were detected in a 1 hour measuring period, contrasted with 561 events in 1 hour when the alginate was directly injected adjacent to the head stage side of the nanopore. The additional electrolyte between electrodes and nanopore reduces the cross-pore applied potential compared to the usual single-cell sensing configuration

ACID AND ENZYMATIC DIGESTION PROCEDURES

ACID DIGESTION POST-NANOPORE MEASUREMENT

A $\sim 9 \text{ nm}$ nanopore was mounted in the PTFE sample holder. A $200 \mu\text{L}$ amount of 0.2% (w/v) *AI* was added to the head stage side in $5 \mu\text{L}$ aliquots per hour throughout the work day during 4 days of application of a $+200 \text{ mV}$ cross-membrane voltage. For overnight voltage applications, the electrode polarity was maintained, but the electrodes were placed in the opposite wells. The head-stage and initially analyte-free ground side solutions were extracted, individually mixed with 1 mL of 75% sulphuric acid and heated overnight (16 h) at 80°C . Samples were diluted with 3 mL of water before spectral

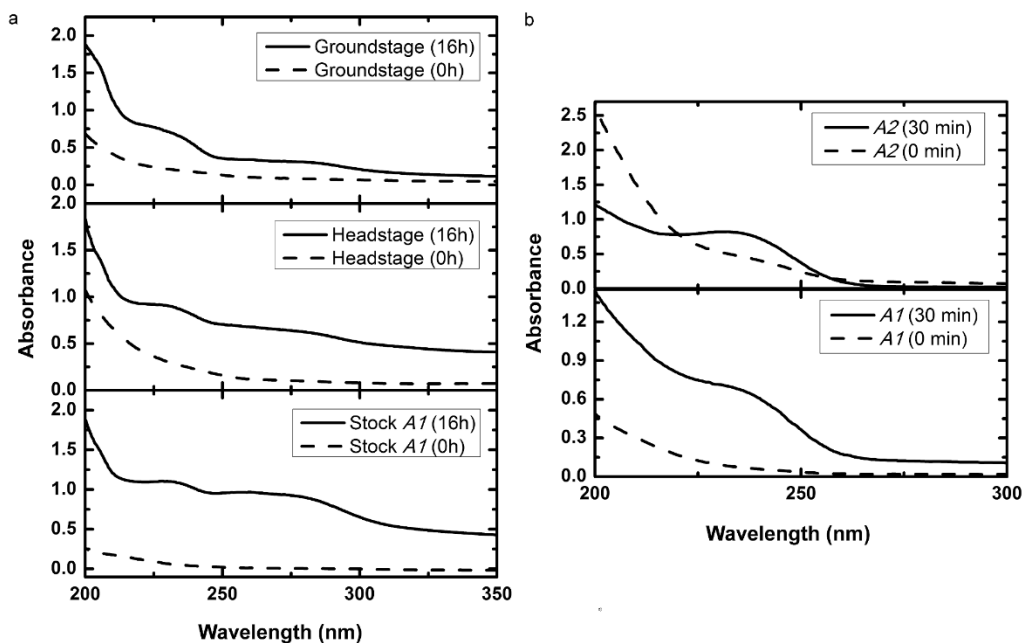
acquisition. For comparison, 500 μL aliquots of 0.2% (w/v) *A1* and *A2* were each subjected to the same acid digestion and dilution before spectral acquisition.

ENZYMATIC DIGESTION FOR SPECTROSCOPIC MEASUREMENTS

A 2250 μL aliquot of 0.2% (w/v) *A1* was added to a 150 μL aliquot of 1 unit/mL alginate lyase and heated in a water bath at 37°C for 30 minutes. The procedure was repeated for sample *A2*, but the sample was diluted with 10 mL H_2O before spectral acquisition.

ENZYMATIC SAMPLE PREPARATION FOR NANOPORE SENSING

For enzymatic digestion, samples of 3% (w/v) *A2* were mixed with alginate lyase (1:1 (v/v) mixture with 1 unit/mL enzyme) for 10 minutes at 37°C. 20 μL of this mixture was added to the headstage side and events were detected with the application of +200 mV on the head stage side. Measurements in the presence of 20 μL of 1 unit/mL of alginate lyase, alone, in the headstage side support that the detected events in the presence of analyte originated from enzymatic digestion products.



Supplementary Figure 2.3: UV/Vis spectra of acid and enzymatic digestion products. a) Stock *A1* subjected to 16 h of sulphuric acid digestion generated a ~ 270 nm absorption band characteristic of the digested polysaccharide^{10, 11} that was replicated in the samples taken from the headstage and from the groundstage sample wells after 4 days of a translocation experiment (200 μL aliquot). The dashed lines denote the UV/Vis spectra of the sample before digestion, and the

solid lines denote the spectra after digestion. b) Alginate lyase digestion of alginate is expected to introduce chromophores with a peak absorption at ~232 nm, consistent with observations here.¹²

PREPARATION OF HEAT MAPS BY HISTOGRAMMING INDIVIDUAL EVENTS

Heat maps were prepared in Origin (Originlab Corporation, MA) from event data sorted into bins by paired f_b and τ . The bin width along the f_b axis was set equal to $W_{\text{bin}} = 3.49\sigma(f_b)N^{\frac{1}{3}}$, where $\sigma(f_b)$ is the standard deviation across all events, and N is the total number of events.¹³ Bin size along the τ axis was set to $\sqrt{10}$. Heat maps are plotted using \log_{10} of the number of events in each bin.

The distributions of event counts by f_b in Supplementary Figure 2.4 were fit using the function

$$\Phi_{f_b} = \frac{1}{2}(1 + \theta) \sum_{i=1}^M A_i \cdot \exp\left(-\frac{(f_b - \mu_i)^2}{2\sigma_i^2}\right)$$

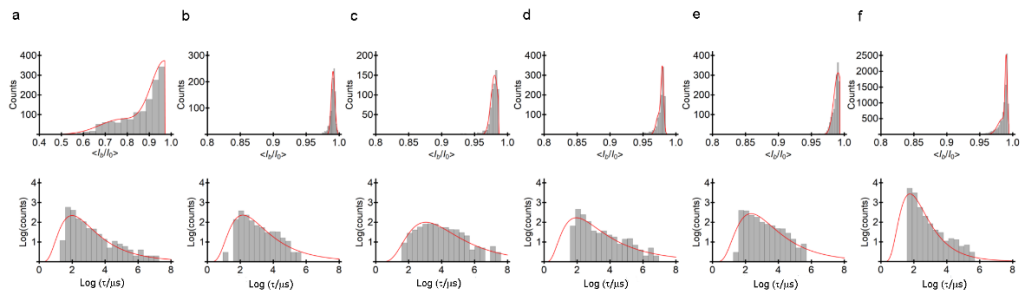
where the parameters of the unmodified Gaussian function are as conventional - A_i , μ_i , and σ_i are the magnitude scaling, expected value, and standard deviation. The step function, $(1 + \theta)$, was set to 1 for $f_b < f_b^{\text{cutoff}} + W_{\text{bin}}$, and 0 otherwise, so that the fit function covers only the accessible experimental data (f_b^{cutoff} was the threshold for event extraction). The fit parameters were

Panel	A_1	μ_1	σ_1
a	364	0.971	0.0624
	$A_2 = 76$	$\mu_2 = 0.773$	$\sigma_2 = 0.0992$
b	240	0.991	0.00274
c	150	0.98	0.00558
d	100	0.974	0.0041
	$A_2 = 304$	$\mu_2 = 0.979$	$\sigma_2 = 0.002$

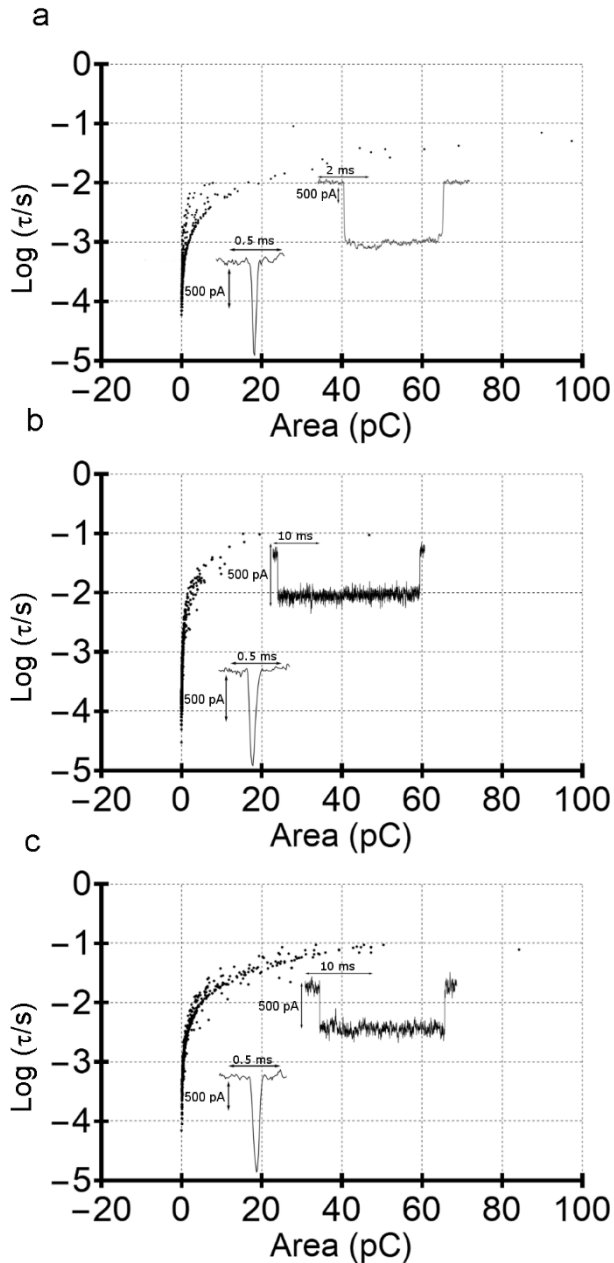
e	312	0.991	0.00635
f	500	0.985	0.0077
	$A_2=2120$	$\mu_2 = 0.989$	$\sigma_2 =0.0016$

The distributions of the log of event counts by duration were fit to a log-normal distribution, $\phi_\tau = \frac{A}{\tau} e^{-(\ln \tau - M)^2 / (2S^2)}$, where the parameters had conventional meanings, and the event duration was expressed in μs . The event duration corresponding to the peak of the event count distribution, τ_p , was found by taking the first derivative of the curve.

Panel	A	M	S	τ_p (μs)
a	5.49	1.01	0.57	98.91
b	5.93	1.07	0.55	143.98
c	6.95	1.38	0.51	1102.32
d	5.43	1.11	0.67	89.31
e	6.62	1.15	0.55	218.69
f	6.85	0.81	0.50	57.27

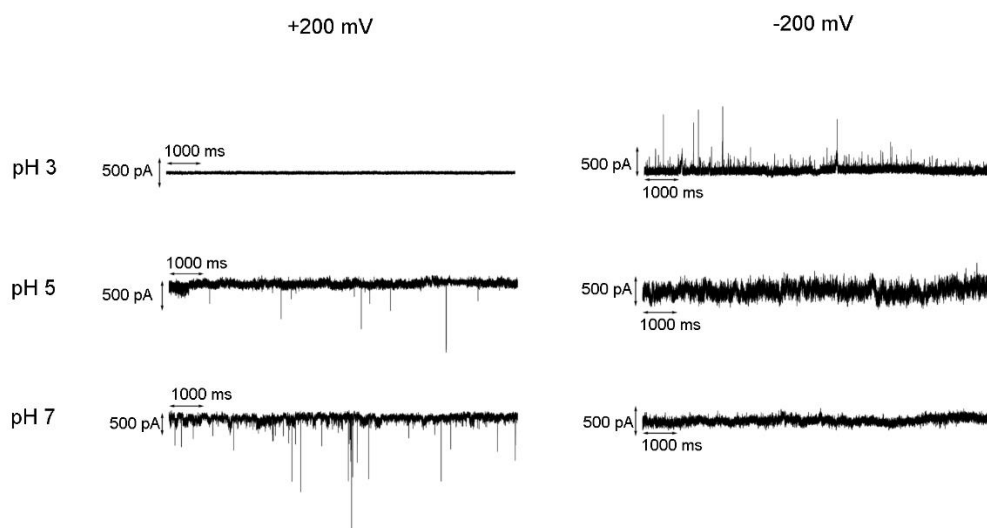


Supplementary Figure 2.4: Histograms of (top row) $\langle i_b \rangle / \langle i_0 \rangle$ (bottom row) duration in \log_{10} of $A1$ alginate in (a) ~ 5 nm and (b) ~ 19 nm pore, $A2$ in (c) ~ 22 nm, (d) 10-min enzyme digested $A2$ in ~ 23 nm pore, (e) heparin and (f) OSCS in the same ~ 14 nm pore with the bin size set automatically by the measurement statistics as described above.

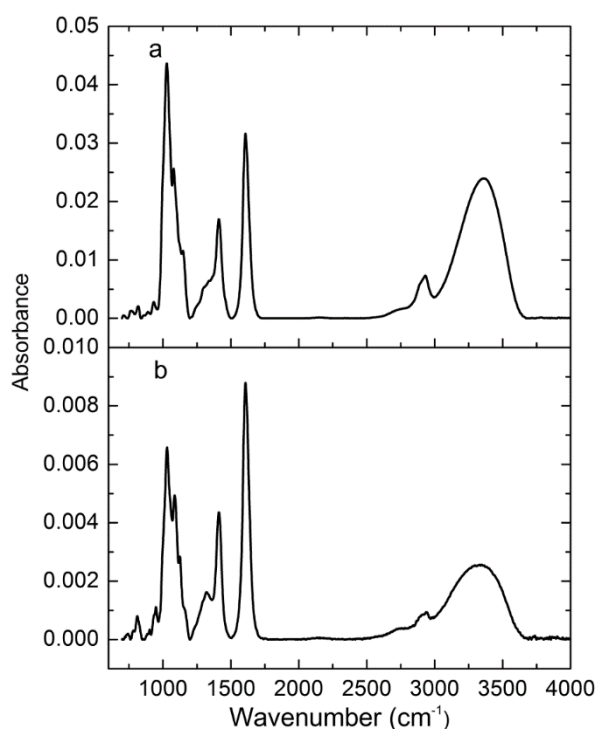


Supplementary Figure 2.5: Plots of \log_{10} of event duration (τ) versus area under each event for alginate A1 in a) ~5 nm and b) ~19 nm diameter pores and c) for alginate A2 in a ~22 nm diameter pore recorded for 1 hour in 1 M KCl at pH ~7. Two distinct event distribution tails are visible corresponding to short-lived spike-like pulses and longer-lived rectangular blockages. The longer-lived tail for A2 is more prominent as a percentage of total events than for A1, consistent with the appearance of the combined heat and scatter plots in Figure 2.3. The shorter events could be attributed to either “bumps” or fast translocations, and longer-lived events could be attributed to slower translocations or longer-lived interactions with the pore (in both cases, complementary measurements independently confirmed alginate translocation). The low molecular weight and high M/G ratio (more G is attributed to stiffness) of A2 meant, it has a greater probability of translocating through a given pore hence tails seen in the figure above are not surprising. Area

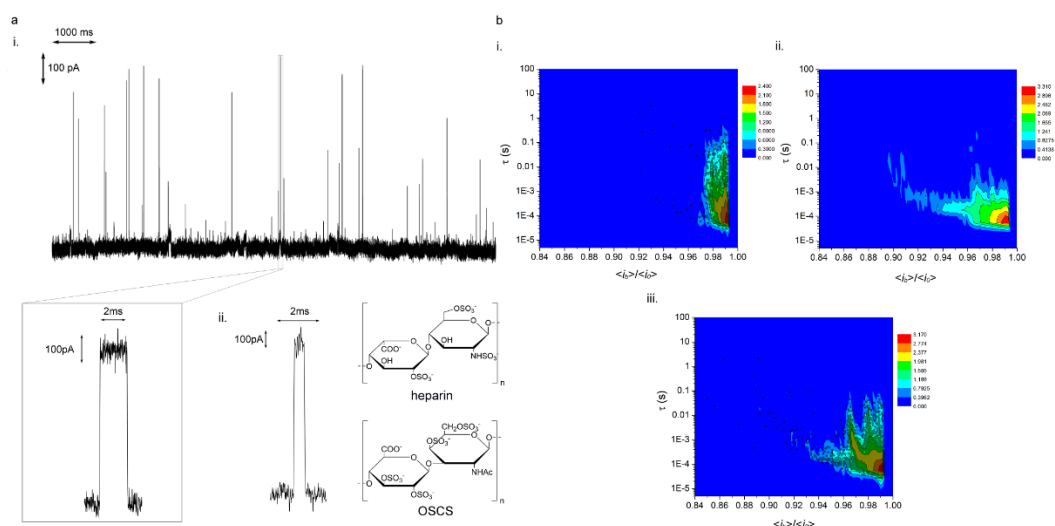
under each event was calculated by integrating the interpolation function (interpolation order of 1) of each event in Mathematica.



Supplementary Figure 2.6: Representative current events of *AI* alginate at pH 3,5 and 7 at negative and positive 200 mV applied on the head stage side for 1-hour each in the same ~8 nm diameter pore at 1M KCl.



Supplementary Figure 2.7: Infrared spectra of alginate samples. The intensity of the peaks near 1400 and 1600 cm^{-1} , relative to the remainder of the spectrum, are consistent with a lesser proportion of carboxylic acid salt residues in (a) *A1* than in (b) *A2*. Comparison of the intensity of the guluronic (G) unit absorption at $\sim 1025 \text{ cm}^{-1}$ to the mannuronic (M) unit absorption at $\sim 1100 \text{ cm}^{-1}$ allows calculation of the M/G ratio that varies with particular alginate source.¹⁴ Using this approach, alginate *A1* was determined to be $\sim 63\% \text{G}/37\% \text{M}$, and alginate *A2* was $\sim 57\% \text{G}/43\% \text{M}$. These relative proportions were supported by additional analysis: in Supplementary Figure 3b, the particular alginate lyase was a mannuronic lyase, so that the greater absorption from the digestion of *A2* than *A1* was consistent with a greater proportion of *M* in *A2*.



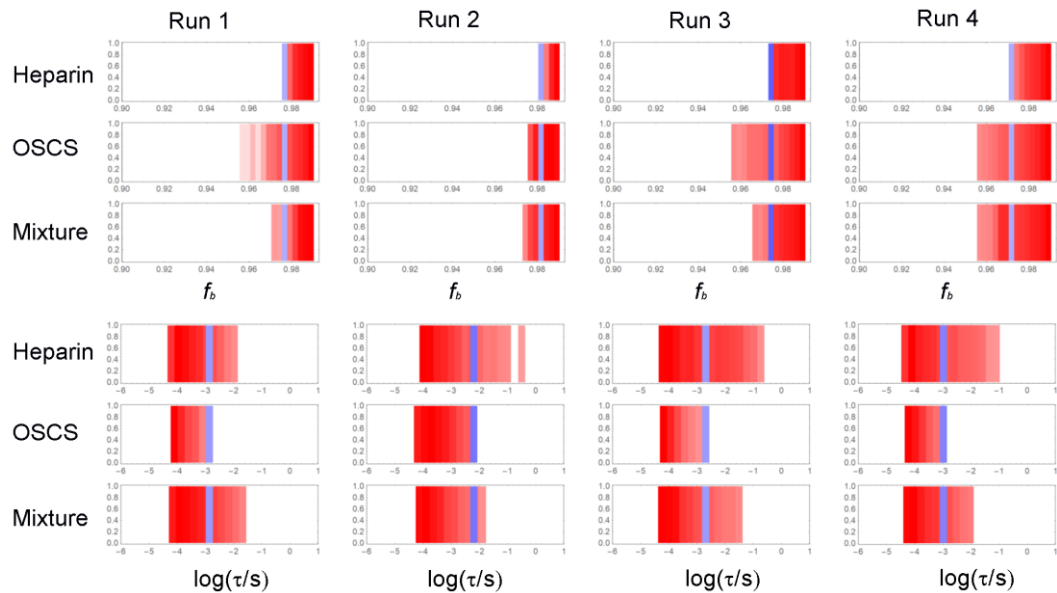
Supplementary Figure 2.8: Heparin and OSCS events. A representative a) i) segment of a heparin induced-current trace using a ~ 10 nm-diameter pore with a magnified current event from the same trace, and from ii) OSCS through the same pore in response to a -200 mV applied voltage in 4 M KCl at pH ~ 7 . b) Contour+scatter plots of i) heparin, ii) OSCS and iii) heparin contaminated with OSCS through a ~ 14 nm diameter pore.

RECOGNITION FLAG GENERATION

Recognition flag generation was done using custom codes written in Mathematica 11.0.1.0 (Wolfram, Champaign, IL). (1) All individual events were histogrammed with respect to f_b using a bin width of 0.0025 (using nanopores with diameters from ~ 8 -14 nm, and determined using the USP heparin data). (2) Any bin with counts below 0.5% of the maximum bin count were removed, and all counts were then normalized. (3) The OSCS identification threshold was taken to be at the nearest bin at the distance of three standard deviations (after the 0.5% filter) from the bin with the maximum number of counts. (4) When events had been detected at f_b below this threshold, the recognition flag was set to red to signal the presence of OSCS; it was otherwise left white. (5) All individual events were then histogrammed with respect to the logarithm (\log_{10}) of the event duration (τ) using a bin width of 0.25 (here, determined using the USP OSCS data). (6) The same 0.5% filter was applied to these histograms, which then had their counts normalized. (7) The event duration threshold was taken to be the nearest bin at the distance of three standard

deviations (after the 0.5% filter) from the bin with the maximum number of counts. (8)

When events had been detected at $\log_{10} \tau$ above this threshold, the recognition flag was set to red to signal the presence of heparin; it was otherwise left white.



Supplementary Figure 2.9: Hue plots of show the outcomes of recognition flag generation (and measurement statistics—see procedure detailed above) after steps 3 (top) and 7 (bottom), based on $f_b = \langle i_b \rangle / \langle i_0 \rangle$ and $\log_{10} \tau$ of the individual events. The identification threshold, determined by the measurement statistics of each run, is given by the blue line. The corresponding final recognition flags, showing successful detection of the toxic OSCS impurity across four independent trials in $\sim 8.6, 9.8, 9.9,$ and 13.6 nm (left to right), are shown in Figure 2.5.

REFERENCES

1. Viskov, C. et al. Isolation and Characterization of Contaminants in Recalled Unfractionated Heparin and Low-Molecular-Weight Heparin. *Clinical and Applied Thrombosis/Hemostasis* **15**, 395-401 (2009).
2. Trivedi, D.M. in *Electrical and Computer Engineering*, Vol. Master of Applied Science 91 (The University of British Columbia, Vancouver; 2009).
3. Kwok, H., Briggs, K. & Tabard-Cossa, V. Nanopore Fabrication by Controlled Dielectric Breakdown. *PLoS ONE* **9**, e92880 (2014).
4. Frament, C.M. & Dwyer, J.R. Conductance-Based Determination of Solid-State Nanopore Size and Shape: An Exploration of Performance Limits. *J. Phys. Chem. C* **116**, 23315-23321 (2012).
5. Kowalczyk, S.W., Grosberg, A.Y., Rabin, Y. & Dekker, C. Modeling the conductance and DNA blockade of solid-state nanopores. *Nanotechnology* **22**, 315101 (2011).
6. Lee, C. et al. Large Apparent Electric Size of Solid-State Nanopores Due to Spatially Extended Surface Conduction. *Nano Lett.* **12**, 4037-4044 (2012).
7. Huggins, M.L. The Viscosity of Dilute Solutions of Long-Chain Molecules. IV. Dependence on Concentration. *J. Am. Chem. Soc.* **64**, 2716-2718 (1942).
8. Clementi, F., Mancini, M. & Moresi, M. Rheology of alginate from *Azotobacter vinelandii* in aqueous dispersions. *J. Food Eng.* **36**, 51-62 (1998).
9. Armstrong, J.K., Wenby, R.B., Meiselman, H.J. & Fisher, T.C. The Hydrodynamic Radii of Macromolecules and Their Effect on Red Blood Cell Aggregation. *Biophys. J.* **87**, 4259-4270 (2004).
10. Foulger, J.H. THE USE OF THE MOLISCH (α -NAPHTHOL) REACTIONS IN THE STUDY OF SUGARS IN BIOLOGICAL FLUIDS. *J. Biol. Chem* **92**, 345-353 (1931).
11. Hallal, J.L.J., Lucho, A.M.S. & Gonçalves, R.S. Electrochemical polymerization of furfural on a platinum electrode in aqueous solutions of potassium biphthalate. *Materials Research* **8**, 23-29 (2005).
12. Skidmore, M.A., Guimond, S.E., Dumax-Vorzet, A.F., Yates, E.A. & Turnbull, J.E. Disaccharide compositional analysis of heparan sulfate and heparin polysaccharides using UV or high-sensitivity fluorescence (BODIPY) detection. *Nat. Protocols* **5**, 1983-1992 (2010).
13. Draréni, J. & Roy, S. in *Image Analysis and Recognition*, Edn. 1. (eds. M. Kamel & A. Campilho) 558-568 (Springer-Verlag Berlin Heidelberg, 2007).
14. Pereira, L., Sousa, A., Coelho, H., Amado, A.M. & Ribeiro-Claro, P.J.A. Use of FTIR, FT-Raman and ^{13}C -NMR spectroscopy for identification of some seaweed phycocolloids. *Biomol. Eng* **20**, 223-228 (2003).

APPENDIX 2: CHAPTER 3 SUPPORTING INFORMATION
ELECTROLESS PLATING OF THIN GOLD FILMS DIRECTLY ONTO
SILICON NITRIDE THIN FILMS AND INTO MICROPORES

*Julie C. Whelan, Buddini Iroshika Karawdeniya[†], Y.M. Nuwan D.Y. Bandara[†],
Brian D. Velleco, Caitlin M. Masterson and Jason R. Dwyer*.*

Department of Chemistry, University of Rhode Island, 51 Lower College Road,
Kingston, RI, 02881, United States. * E-mail: jdwyer@chm.uri.edu.

MATERIALS

The following chemicals were purchased from Sigma-Aldrich Corp. (St. Louis, MO, USA), identified by (product number, specifications), and used as-supplied: methanol (34860, CHROMASOLV[®] for HPLC $\geq 99.9\%$), tin(II) chloride (208256, Reagent Grade 98%), trifluoroacetic acid (6508, ReagentPlus[®] 99%), silver nitrate (S6506, ReagentPlus[®] $\geq 99.0\%$), ammonium hydroxide solution (320145, ACS Reagent 28.0-30.0% NH₃ basis), sodium tetrachloroaurate(III) dihydrate (298174, 99%), barium hydroxide octahydrate (B2507, $\geq 98\%$), sodium hydroxide (S5881, reagent grade $\geq 98\%$), sodium sulfite (S0505, $\geq 98\%$), and formaldehyde (252549, ACS reagent, 37 wt% in water, methanol-stabilized). A 5% solution of hydrofluoric acid (C4354) was purchased from Science Lab Supplies (St. Augustine, FL) and diluted prior to use. All aqueous dilutions and washes were performed using 18M Ω -cm ultrapure water (Millipore Synergy UV, Billerica, MA). Silicon nitride-coated wafers were purchased from Rogue Valley Microdevices, Inc. (Medford, OR), and consisted of 200nm-thick, low-stress (<250 MPa Tensile; silicon-rich), LPCVD silicon nitride films deposited on 3" diameter,

<100> polished silicon wafers. A diamond scribe was used to create $\sim 1\text{cm}^2$ sample chips. The silicon nitride micropore arrays had $2\mu\text{m}$ diameter pores in 200nm-thick membranes and were purchased from Protochips (DTM-25231, Raleigh, NC). The efficacy of Scheme 3.1 for electrolessly plating gold onto silicon was examined using polished <111> silicon wafers (University Wafer, product number 1080).

ELECTROLESS PLATING

Each chip was plasma-cleaned prior to use in a Glow Research (Phoenix, AZ) Autoglow plasma cleaner with 10 minutes of 50W air plasma (0.8-1.2Torr pressure) followed by 5 minutes of 50W O_2 plasma (0.8-1.2Torr pressure). Each chip was then etched for 10 minutes in 2mL of a 2.5% aqueous HF solution to remove unwanted silicon oxide from the silicon nitride surface¹⁻², followed by 3 immersion rinses in water and then drying under an argon stream. The prepared chips were immersed for 45 minutes in 2mL of a 50/50 methanol/water solution that was 0.025M tin(II) chloride and 0.07M trifluoroacetic acid, followed by a methanol rinse and 5 minute methanol soak, a 5 minute soak in 2mL of ammoniacal silver nitrate solution³, 5 minutes in methanol and finally 5 minutes in water³. Electroless gold plating involved submersing the chips in aqueous plating baths comprised of $7.9 \times 10^{-3}\text{M}$ sodium gold sulfite⁴, 0.127M sodium sulfite and 0.625M formaldehyde⁵. The chips were plated in 1.5-3mL of plating solution in small plastic beakers with gentle rocking in a refrigerator (3°C plating) or thermoelectric cooler (10°C plating). After plating for the desired time at the desired temperature, the chips were thrice rinsed in alternating methanol and water, and dried in an argon stream (Airgas PP300). For comparison, we additionally sputter-coated (Denton Vacuum Desk II, Moorestown, NJ) a plasma-cleaned silicon nitride-coated wafer with gold.

Even dilute hydrofluoric acid presents significant chemical hazards upon operator exposure, requiring special working precautions. All beakers for HF containment were polypropylene, instead of glass which can be etched and rendered permeable. Dilute (5%) stock solutions were purchased to avoid handling concentrated solutions and Calgonate (Port St. Lucie, FL) 2.5% calcium gluconate gel was kept at hand in case of accidental skin exposure. To minimize exposure risk, all personnel wore a full faceshield, a disposable polypropylene apron and thick neoprene long-sleeved gloves over standard chemical safety glasses, laboratory coat and long-sleeved nitrile gloves, respectively. Finally, we employed a “buddy system” so that one researcher monitored the other’s work with HF. All labware and gloves were thoroughly rinsed with water after use.

PREPARATION OF AMMONIACAL SILVER NITRATE³

This solution was prepared by adding 4 drops of 1M sodium hydroxide solution to 0.010g of silver nitrate. Ammonium hydroxide was slowly added, dropwise, until all traces of dark precipitate had dissolved. The solution was then diluted to a final volume of 10mL using ultrapure water.

Ammoniacal silver nitrate solution can form explosives if allowed to dry. This solution should be prepared on only a scale sufficient for immediate use, and should preferably be deactivated by precipitation by the addition of dilute hydrochloric acid or sodium chloride prior to disposal⁶.

PREPARATION OF SODIUM GOLD SULFITE^{4,7}

The synthesis of the gold plating solution was in accordance with the Alys *et al.* patent⁴ modified by the addition of a drying step⁷, as described here. 0.275g

sodium tetrachloroaurate dihydrate was added to approximately 15 mL ultrapure water at 80°C with stirring. To this solution were added 1.500g barium hydroxide octahydrate and 54µL of 50% w/w sodium hydroxide to yield an orange-yellow precipitate. The solution was boiled until all visible water had evaporated, and then allowed to cool to room temperature. The precipitate was slurried with approximately 10mL of ultrapure water and filtered through a medium porosity Buchner funnel. The precipitate was slurried with approximately 10mL of ultrapure water, heated to 60-65°C with stirring, cooled, and then filtered (*bis*). The precipitate was then slurried with approximately 20mL of ultrapure water, and 0.500g sodium sulfite was added to the solution. The solution was heated to 60-65°C with stirring until the precipitate turned blue-purple. This solution was filtered while still warm, and the resulting filtrate was diluted to a final volume of 25mL. The pH was adjusted with 1M sodium hydroxide to a final pH above 10.

CHARACTERIZATION

Gold film depositions were carried out in triplicate at each temperature and time point, and the 3°C trial was repeated so that each film thickness was based on deposition and measurements from between 3-6 different silicon nitride chips (allowing for occasional chip breakage). A step edge from gold film to exposed silicon nitride substrate was created by selectively removing gold film with adhesive tape (Scotch® 810 Magic™ tape) or, when film adhesion to the substrate was stronger, with a gentle pass of plastic tweezers across the substrate. AFM measurements of gold film thickness were performed in tapping mode at 0.1Hz across 10µm × 10µm segments of the step edge with an AFM Workshop (Signal Hill, CA) TT-AFM (equipped with SensaProbes™190-A-15, 190kHz, aluminum-coated probes with tip radius <10 nm). Line profiles at several points across the

step edge were analyzed, using the planar silicon nitride surface as a reference for quadratic background subtractions. For each background-subtracted profile, the means of the coated and uncoated sides were calculated (omitting large particle outliers from the statistics), and averaged for each chip over several profiles. These mean step heights were then averaged over each deposition time and temperature point, propagating the standard deviation as an uncertainty to yield the final reported step heights (Figure 3.1).

Gold film morphology was examined using a Zeiss Sigma VP FE-SEM at an electron energy of 8keV (Oberkochen, Germany), and elemental analysis by EDS was performed on the same instrument equipped with an Oxford Instruments X-MaxN 50mm² silicon drift detector (Concord, MA). Custom code was written in Mathematica 9 (Wolfram Research, Champaign, IL) to yield gold film grain size estimates via watershed analysis. X-ray photoelectron spectroscopy was used for the majority of the elemental analysis. XPS spectra were acquired using a PHI 5500 system (Physical Electronics, Inc., Chanhassen, MN) using unmonochromatized Al K α radiation (1486.6 eV) and an aperture size of 600 \times 600 μ m². Survey scans were performed with 0.8eV step sizes and 20ms per step, with a pass energy of 187.85eV and 10 scans per spectrum. High resolution spectra were recorded with 50 scans per spectrum, 0.1eV step sizes, 40ms per step and a pass energy of 23.50eV. Spectra were analyzed initially with Multipak 6.1 (Physical Electronics). All curve fitting was performed using XPSPeak 4.1⁸ using linear baselines and the minimum meaningful number of fixed 90% Gaussian-10% Lorentzian peak profiles per peak, with all other peak parameters free. To compensate for substrate charging, we aligned the N1s peak from silicon nitride substrates to 398.00eV, and the lower binding energy Si2p peak from silicon

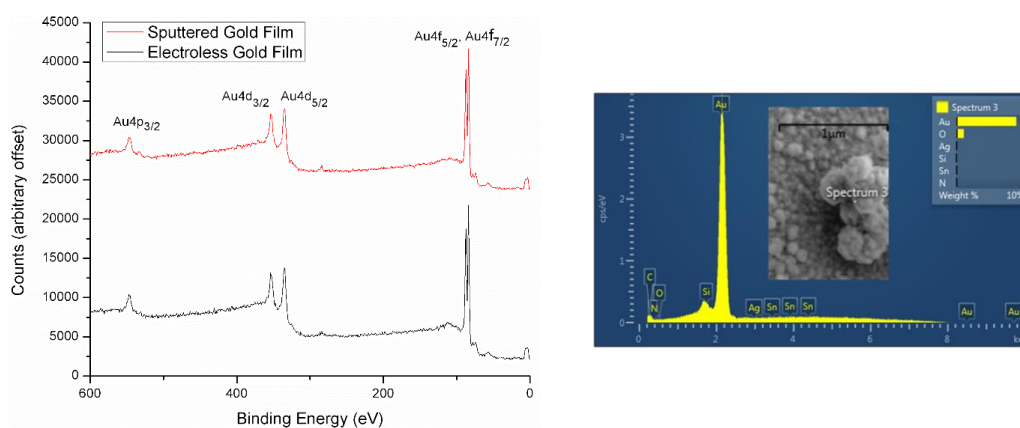
substrates to 99.25eV⁹, shifting spectra by up to 0.49eV. The particular choice of reference precludes analysis based on the binding energy, alone, of that component of the XPS spectrum. We chose these peaks, rather than the commonly used C1s peak¹⁰, because they had better signal-to-noise ratios; the peak fitting reliability would be less frequently compromised by the presence of multiple contributing features; and the C1s binding energy, itself, has been shown to be variable, notably in response to the particular surface treatment of silicon^{9, 11}. To gain a measure of the binding energy uncertainties useful for guiding the interpretation of binding energy shifts, and of the consistency of the reference alignment, we fit the main, shifted, C1s peak centers, yielding a range of values between 284.61 and 285.49eV that arises from a combination of the shortcomings of multicomponent peak fitting and any real shifts in binding energy. As an additional check on the silicon nitride alignment, we also aligned the spectra using the Si2p region by fixing its principal component at 102.5eV. For silicon-rich silicon nitride, the Si2p peaks include overlapping contributions from hydrogen-, oxygen-, silicon- and nitrogen-bound silicon, with magnitudes weighted by the substrate processing conditions; the N1s binding energies, referenced to the 102.5eV components of fits of the Si2p peaks, were 398.35, 398.48, 398.53 and 398.43eV after plasma, HF, tin and silver treatments, respectively. These results of these referencing sensitivity studies helped to guide the interpretation of Si2p-referenced silicon XPS spectra and N1s-referenced silicon nitride XPS spectra.

Gold film conductivity was measured using an Alessi 4-point probe head with spring-loaded contacts, mounted on a translation stage. Voltages of ~3-6mV were applied with an HP 6115a precision power supply and measured with a

Keithley 196 DMM (Cleveland, OH); the current was measured using a Hewlett-Packard 973a multimeter.

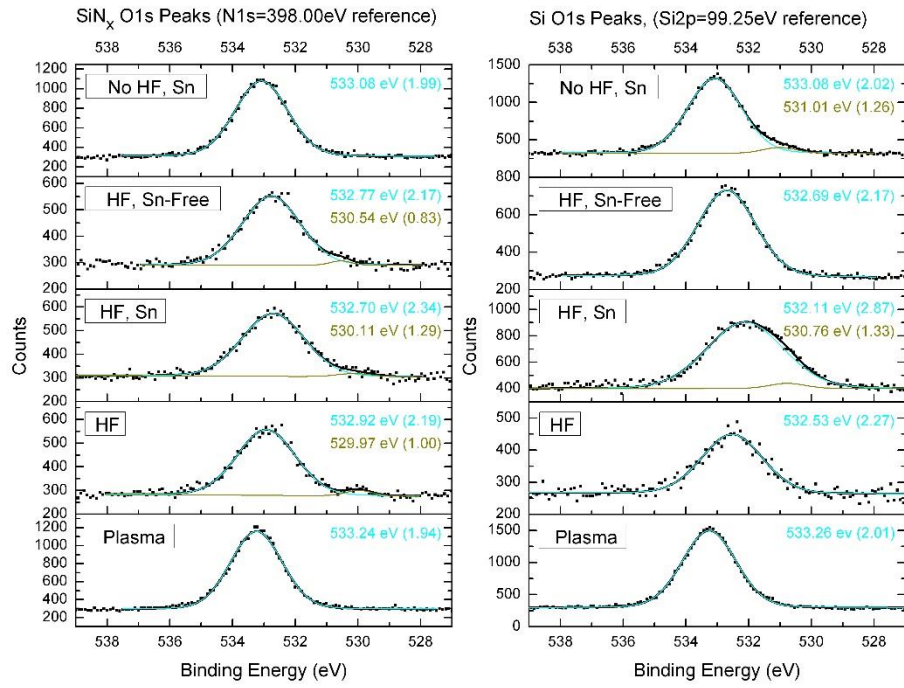
SERS measurements were performed on an R3000QE Raman Systems spectrometer using 290mW laser excitation at 785 nm. Substrates were submerged in a 0.01M solution of NBT for 5 minutes before 3× rinsing in acetonitrile and argon drying. Spectra were collected at three random locations for each substrate and averaged together after correcting to a zero baseline at $\sim 494\text{cm}^{-1}$.

Supporting Information Figure S3.1: Elemental analysis of gold films. At left, XPS scans comparing a sputtered gold film with an electrolessly plated gold film. The curves are vertically offset for clarity. At right, EDS profiling confirms the gold composition of one of the larger surface particles.

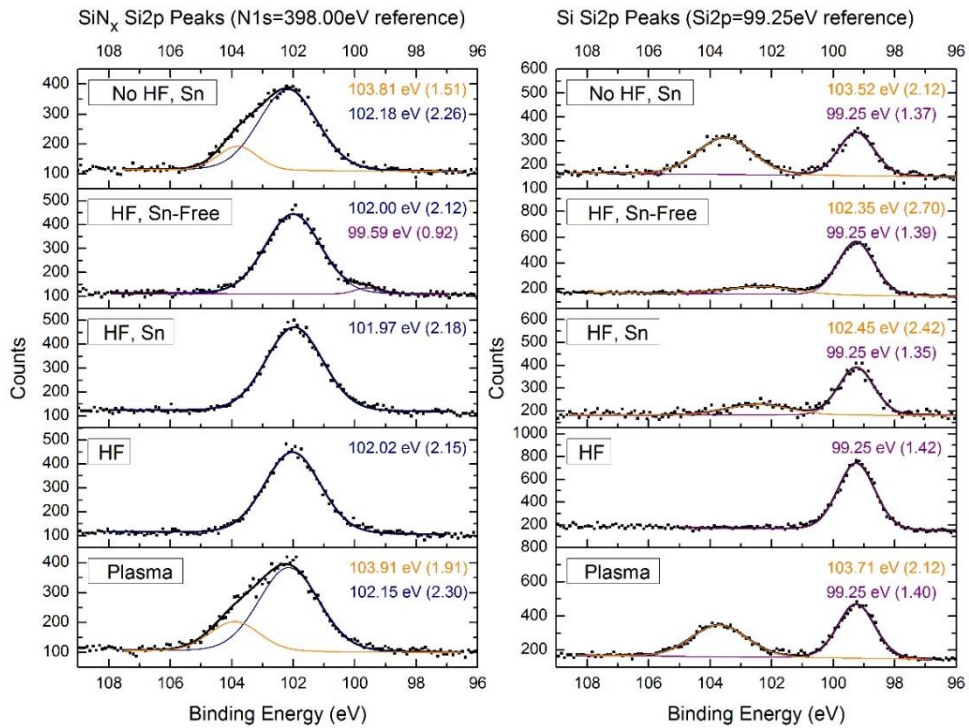


Supporting Information Figure S3.2: XPS spectra at key steps in the application of Scheme 1, and after selected control experiments. The label given to each spectrum indicates the terminal steps of Scheme 1 (or control experiment variation) that were performed on the substrate. The control data center on the effect of HF etching (performed or omitted) and tin sensitization (with standard solution or tin-free control). The scattered points are experimental data, and solid lines are used for the fit to the data (individual components and their sum). Each plot includes the center value and (width) of each component used to fit the experimental spectrum.

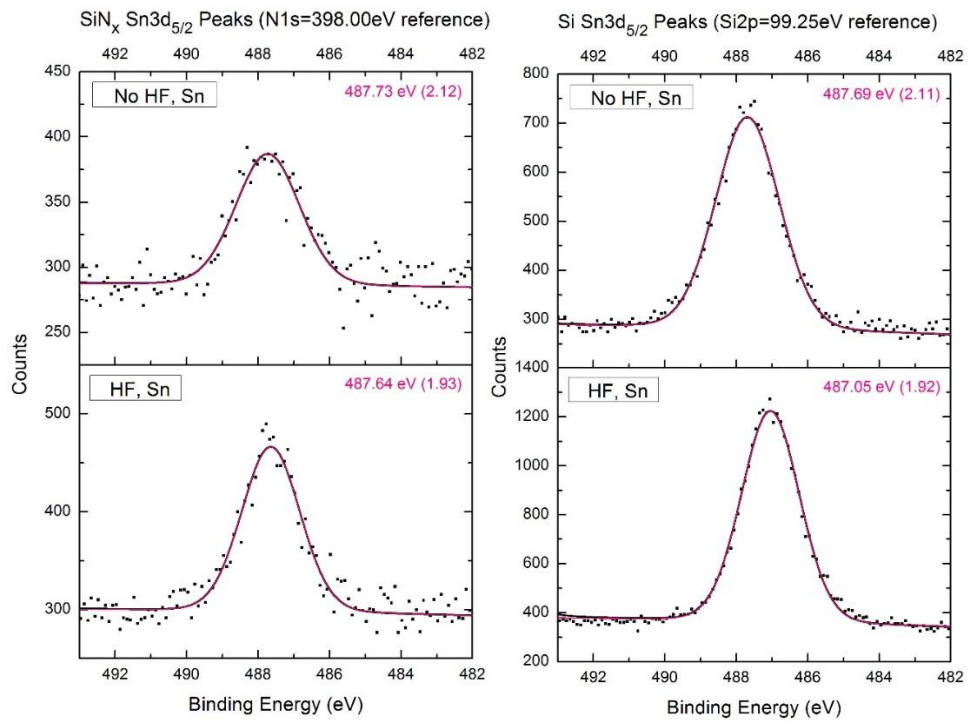
(a)



(b)



(c)



REFERENCES

1. Rosso, M.; Giesbers, M.; Arafat, A.; Schroën, K.; Zuilhof, H., Covalently Attached Organic Monolayers on SiC and Si_xN₄ Surfaces: Formation Using UV Light at Room Temperature. *Langmuir* **2009**, *25*, 2172-2180.
2. Williams, K. R.; Muller, R. S., Etch rates for micromachining processing. *J. Microelectromech. Syst.* **1996**, *5*, 256-269.
3. Menon, V. P.; Martin, C. R., Fabrication and Evaluation of Nanoelectrode Ensembles. *Anal. Chem.* **1995**, *67*, 1920-1928.
4. Abys, J. A.; Maisano, J. J. Process for Making Sodium Gold Sulfite Solution. 6,126,807, **2000**.
5. Ko, J. W.; Koo, H. C.; Kim, D. W.; Seo, S. M.; Kang, T. J.; Kwon, Y.; Yoon, J. L.; Cheon, J. H.; Kim, Y. H.; Kim, J. J.; Park, Y. J., Electroless Gold Plating on Aluminum Patterned Chips for CMOS-Based Sensor Applications. *J. Electrochem. Soc.* **2010**, *157*, D46-D49.
6. Sigma-Aldrich ACCUSTAIN® RETICULUM STAIN (Procedure No. HT102). http://www.sigmaaldrich.com/content/dam/sigma-aldrich/docs/Sigma/General_Information/1/ht102.pdf (accessed 3/5/2014).
7. Ahn, W.; Taylor, B.; Dall'Asén, A. G.; Roper, D. K., Electroless Gold Island Thin Films: Photoluminescence and Thermal Transformation to Nanoparticle Ensembles. *Langmuir* **2008**, *24*, 4174-4184.
8. Kwok, R. W. M. *XPSPeak*, 4.1; **2009**.
9. Zazzera, L. A.; Moulder, J. F., XPS and SIMS Study of Anhydrous HF and UV/Ozone- Modified Silicon (100) Surfaces. *J. Electrochem. Soc.* **1989**, *136*, 484-491.
10. Arafat, A.; Giesbers, M.; Rosso, M.; Sudhölter, E. J. R.; Schroën, K.; White, R. G.; Yang, L.; Linford, M. R.; Zuilhof, H., Covalent Biofunctionalization of Silicon Nitride Surfaces. *Langmuir* **2007**, *23*, 6233-6244.
11. Cros, A., Charging Effects in X-Ray Photoelectron Spectroscopy. *J. Electron. Spectrosc. Relat. Phenom.* **1992**, *59*, 1-14.

APPENDIX 3: CHAPTER 4 SUPPORTING INFORMATION
SOLUTION-BASED PHOTO-PATTERNED GOLD FILM FORMATION
ON SILICON NITRID

*Y.M. Nuwan D.Y. Bandara, Buddini Iroshika Karawdeniya, Julie C. Whelan,
Lucas D.S. Ginsberg, and Jason R. Dwyer*.*

Department of Chemistry, University of Rhode Island, 140 Flagg Road, Kingston,
RI, 02881, United States.

SUPPORTING INFORMATION

MATERIALS AND EQUIPMENT

To photoprotect the LPCVD SiN_x films, we purchased 1-octene (O4806, 98%) and 11-bromo-1-undecene (467642, 95%) from Sigma-Aldrich (St. Louis, MO, USA), and the following 3.05 mm diameter, 0.8 mil thick copper Veco Specimen Grids from Electron Microscopy Sciences (Hatfield, PA, USA):

Type	Catalog #	Pitch (μm)	Hole (μm)	Bar (μm)
50 mesh	0050-Cu	500	450	50
100 mesh	0100-Cu	250	200	50

The general framework for metallization follows that of earlier electroless plating work,¹⁻² and is fully detailed here, for completeness, alongside the new procedures necessary to achieve spatial selectivity. The following chemicals were purchased from Sigma-Aldrich Corp. (St. Louis, MO, USA), identified by (product number, specifications), and used as-supplied: methanol (34860, CHROMASOLV® for HPLC ≥99.9%), tin (II) chloride (208256, Reagent Grade

98%), palladium (II) chloride (205885, ReagentPlus®, 99%), trifluoroacetic acid (6508, ReagentPlus® 99%), silver nitrate (S6506, ReagentPlus® ≥99.0%), ammonium hydroxide solution (320145, ACS Reagent 28.0–30.0% NH₃ basis), sodium tetrachloroaurate (III) dihydrate (298174, 99%), barium hydroxide octahydrate (B2507, ≥98%), sodium hydroxide (S5881, reagent grade ≥98%), sodium sulfite (S0505, ≥98%), dichloromethane (270997, anhydrous, ≥99.8%, contains 50–150 ppm amylene as stabilizer), isopropanol (W292907, ≥99.7%, FCC, FG), 3,4,5-trihydroxy benzoate (274194, 98%), polyethylene glycol (81227, BioUltra, 3,000; M_r 2700–3300), phosphoric acid (695017, ACS reagent, ≥85 wt % in H₂O), hydrochloric acid (320331, ACS reagent, 37%), and formaldehyde (252549, ACS reagent, methanol-stabilized). A 5% solution of hydrofluoric acid (C4354) was purchased from Science Lab Supplies (St. Augustine, FL) and was diluted with water by 50% prior to use. All aqueous dilutions and washes were performed using 18 MΩ·cm ultrapure water (Millipore Synergy UV, Billerica, MA). Silicon nitride-coated wafers were purchased from Rogue Valley Microdevices, Inc. (Medford, OR), and consisted of 200 nm-thick, low-stress (<250 MPa Tensile; silicon-rich), LPCVD SiN_x films deposited on 3” diameter, <100> polished silicon wafers. A diamond scribe was used to create ~ (1 cm)² sample chips.

PRECAUTIONS FOR WORKING WITH HYDROFLUORIC ACID

Even dilute hydrofluoric acid (HF) presents significant chemical hazards upon operator exposure, requiring special working precautions. All beakers for HF containment were polypropylene, instead of glass which can be etched and rendered leaky. Dilute (5%) stock solutions were purchased to avoid handling concentrated solutions and Calgonate (Port St. Lucie, FL)—2.5% calcium

gluconate gel—was kept at hand in case of accidental skin exposure. To minimize exposure risk, all personnel wore a full faceshield over standard chemical safety glasses, a disposable polypropylene apron, thick neoprene long-sleeved gloves over extended cuff nitrile gloves, and a laboratory coat. Finally, we employed a “buddy system” so that one researcher actively monitored the other’s work with HF. All labware and gloves were thoroughly rinsed with water after use.

PREPARATION OF REAGENTS

PALLADIUM SOLUTIONS³

0.014 M PALLADIUM (II) STOCK SOLUTION

0.050 g of palladium (II) chloride was added to a solution consisting of 1.50 mL of 0.9 M hydrochloric acid and 18.50 mL of water. The solution was shaken well, and, to prevent possible degradation, was covered with aluminum foil and stored overnight at 3°C so that all solids dissolved.

PALLADIUM SURFACE TREATMENT SOLUTION

To 1120 µL of water were added: 80 µL of 0.014 M palladium (II) stock solution, 600 µL of 0.014 M 3,4,5-trimethylbenzoate, 100 µL of phosphoric acid and 100 µL of 43 wt % polyethylene glycol.

0.014 M 3,4,5-TRIMETHYLBENZOATE STOCK SOLUTION

To 0.10 g of 3,4,5-trimethylbenzoate, 40.00 mL of water was added and shaken well for about 10–15 minutes until all solids dissolved. The vial containing the solution was covered with aluminum foil and stored in a dark and cool place.

43 WEIGHT % POLYETHYLENE GLYCOL STOCK SOLUTION

To 15.00 g of polyethylene glycol, 20.00 ml of water was added and stirred vigorously until all solids dissolved. The solution vial was covered with aluminum foil and stored at 3°C.

AMMONIACAL SILVER NITRATE⁴

This solution was prepared by adding 4 drops of 1 M sodium hydroxide solution to 0.010 g of silver nitrate. Ammonium hydroxide was slowly added, dropwise, until all traces of dark brown precipitate had dissolved. The solution was then diluted to a final volume of 10 mL with water.

HAZARD NOTIFICATION

Ammoniacal silver nitrate solution can form explosives if allowed to dry. This solution should be prepared only on a scale sufficient for immediate use, and should preferably be deactivated by precipitation by the addition of dilute hydrochloric acid or sodium chloride prior to disposal⁵.

SODIUM GOLD (I) SULFITE⁶⁻⁷

The synthesis of the gold plating solution was in accordance with the Abys et al. patent⁷ modified by the addition of a drying step⁶, as described here. 0.275 g sodium tetrachloroaurate (III) dihydrate was added to approximately 15 mL water at 80°C with stirring. To this solution, 0.15 g barium hydroxide octahydrate and 54 µL of 50% w/w sodium hydroxide were added to yield an orange-yellow precipitate. The solution was boiled until all visible water had evaporated, and then allowed to cool to room temperature. The precipitate was slurried with approximately 10 mL of water and filtered through a medium porosity Büchner funnel. The precipitate was slurried with approximately 10 mL of water, heated to

60–65°C with stirring, cooled, and then filtered. The precipitate was then slurried with approximately 20 mL of water, and 0.500 g sodium sulfite was added to the solution. The solution was heated to 60–65°C with stirring until the precipitate turned blue-purple. This solution was filtered while still warm, and the resulting filtrate was diluted to a final volume of 25 mL. If necessary, the pH was adjusted with 1 M sodium hydroxide to a final pH above 10.

METALLIZATION

Each chip was plasma-cleaned at least one day prior to the subsequent hydrosilylation and metallization steps using a Glow Research (Phoenix, AZ) Autoglow plasma cleaner with 10 minutes of 50 W N₂ plasma (0.8–1.2 Torr pressure) followed by 5 minutes of 50 W O₂ plasma (0.8–1.2 Torr pressure). Each chip was then etched for 10 minutes in 2.5% aqueous HF solution, followed by 3 immersion rinses in water and then drying under an argon stream. The chips were placed in a custom holder under <2 mm of 1-octene, sealed under a quartz plate (Fisher, CGQ-0620-09), and irradiated for 24 hours by a 15 W UV lamp operating at 254 nm (Model XX-15S, Part # 95-0042-05; UVP, LLC, Upland, CA, USA). The chips were rinsed with dichloromethane, allowed to dry, rinsed by isopropanol, and then processed in the metal-ion-containing solutions.

SN (II) / AG (I) / AU (I): ELECTROLESS GOLD PLATING PROCESS FLOW FOR LPCVD SiN_x¹⁻²

The patterned (HF-etched, then patterned) chips were immersed in a series of custom electroless plating bath solutions⁴ that had been successfully used to gold-plate suitably prepared SiN_x.¹⁻² The first immersion was for 45 minutes in 2 mL of a 50/50 methanol/water solution that was 0.025 M tin (II) chloride and 0.07 M trifluoroacetic acid, followed by a methanol rinse and 5 minute methanol

soak. The next step was a 5 minute soak in 2 mL of ammoniacal silver nitrate solution, with a methanol rinse, and 5 minute soak in methanol and then 5 minutes in water. The chips were then submerged in aqueous plating baths comprised of 7.9×10^{-3} M sodium gold (I) sulfite,⁷ 0.127 M sodium sulfite and 0.625 M formaldehyde.²⁻³ The chips were plated in 1.5 mL of plating solution in small plastic beakers with gentle rocking in a refrigerator (3°C plating) for 30 minutes. The chips were then thrice-rinsed in alternating methanol and water, and dried in an argon stream.

PD (II) / AG (I) / AU (I)

Similar to the previous procedure, but with the Sn (II) step replaced with a Pd (II)-based treatment. The patterned chips were immersed in 1 M hydrochloric acid for 5 minutes, washed with isopropanol, and then immersed for 1 hour in 2 mL of the palladium surface treatment solution, followed by 3 rinses, each, of 1 M hydrochloric and water, a 5 minute soak in 2 mL of ammoniacal silver nitrate solution, one rinse with methanol and three rinses with water. The chips were then submerged in the Au (I) bath as described in the previous section.

AG (I) / AU (I)

The patterned SiN_x chips were immersed in 1 M hydrochloric acid for 5 minutes, washed with isopropanol, and then immersed for 5 minutes in 2 mL of ammoniacal silver nitrate solution followed by one rinse with methanol and three rinses with water. The chips were then submerged in the Au (I) bath as described in the two previous sections.

CHARACTERIZATION

Optical micrographs of SiN_x patterning were taken with a Digiscope DS-300 (Motic, Hong Kong; controlled with Motic Educator, 2004 ed. software). Gold film morphology was examined using a Zeiss Sigma VP FE-SEM at an electron energy of 8 keV (Oberkochen, Germany), elemental analysis by EDS was performed on the same instrument equipped with an Oxford Instruments X-MaxN 50 mm² silicon drift detector (Concord MA). XPS (Phi 5500 Al K α) was used for additional elemental analyses. A DHM-R 2200 (Lyncée Tec SA, Lausanne, Switzerland) operating at 666 nm, 680 nm, and 794 nm, was used to extract gold film thicknesses; all DHM measurements were courtesy of Lyncée Tec SA staff. Custom codes were written in Mathematica 10.3.1 (Wolfram Research, Champaign, IL) to analyze gold film properties.

GRID RECOGNITION

To distinguish between grid and grid-free zones of an FE-SEM or DHM contour image, each image was first filtered using a median filter with an appropriate pixel value threshold (usually 5), followed by image binarization (with automatic thresholding) and color-negation.

THICKNESS OF DEPOSITED GOLD

ImageJ⁸ was used to extract raw gold film thickness data from a DHM image at 5 \times magnification, provided by Lyncée Tec, of a gold replica of a 100 mesh grid. The grid recognition algorithm was used to distinguish between grid and grid-free zones of a given contour plot. The mean film thickness with standard deviation ($\sim 23 \pm 1.5$ nm) was calculated by averaging across 10 such grid images each with metal-plated grid lines containing at least 35,000 pixels.

WIDTH OF GOLD AND COPPER (TEM) GRID LINES

Regions of interest of grid-recognized FE-SEM micrographs were chosen so that the grid lines we analyzed were distant from the curved sections (from the as-supplied Cu mesh) at grid line intersections. At least 300 line profiles were sampled from each micrograph, and used to calculate a mean grid line width and standard deviation ($54.4 \pm 1.3 \mu\text{m}$ for copper grids provided by the supplier and $44.8 \pm 3.3 \mu\text{m}$ for the gold plated mesh grids on SiN_x).

SURFACE AREA COVERAGE

FE-SEM micrographs of grid lines were taken at $25,000\times$ magnification and the grid recognition algorithm was used to subdivide the image into regions with and without metal particle coverage. This delineated image was then binarized using the “Automatic” thresholding setting in Mathematica. The surface area coverage was calculated using the following equation,

$$\text{Surface area coverage} = \frac{(\# \text{ of total pixels}) - (\# \text{ of zero valued pixels})}{\# \text{ of total pixels}} 100\%$$

and the mean surface area coverage across micrographs of 15 gold replica grids, with standard deviation, was $\sim 83 \pm 13\%$.

BOLTZMANN FIT TO EDS LINE PROFILES

EDS line profiles of the gold thin-film grid replicas were made by acquiring data for ~ 7.5 minutes per line with readings taken every 59 nm, and 15 lines from each of 5 chips were used in the analysis. Each line profile was then fit to a Boltzmann function to quantify the transition from open-area to gold-filled lines

$$f(x) = \frac{A_{\min} - A_{\max}}{1 + e^{(x-x_0)/dx}} + A_{\max}$$

where A_{\min} and A_{\max} are the initial and final values, and x_0 and dx are the center and slope (spatial resolution) of the edge transition. These were set as free parameters for fitting the EDS line profiles using the “Automatic” setting of the nonlinear-model-fit in Mathematica. The mean spatial resolution (as the mean dx , with standard deviation) from the EDS line profiles was $0.92 \pm 0.24 \mu\text{m}$.

SELECTIVITY

Pixel values corresponding to grid and grid-free regions of grid-recognized FE-SEM images were used to build histograms for each region. A single Gaussian fit was made to each of the histograms using the following equation,

$$g(x) = A^2 \cdot e^{\left(\frac{x-\mu}{\sqrt{2}\sigma}\right)^2}$$

where A^2 , μ , σ , and x are the amplitude coefficient, mean, standard deviation, and pixel intensity, respectively. All parameters were left free during the fit to the histogram, using Mathematica’s nonlinear-model-fit method with “Automatic” setting. The selectivity was then defined, in a classical signal-to-noise sense, as

$$\text{selectivity} = \frac{\mu_{\text{grid region}} - \mu_{\text{grid-free region}}}{\sigma_{\text{grid-free region}}}$$

so that 0 is the lower bound and larger values represent superior selectivity. Figure S-4.1 shows photographs of the results of various spatially selective metallization approaches. The selectivity using photopatterned 1-octene masking was ~ 2.7 using Sn (II) (single chip), and ~ 10.1 (8 chips) when begun with Pd (II). With air-based

photopatterning followed by Pd (II) as the first metallization step, the selectivity was ~3.2 (2 chips).

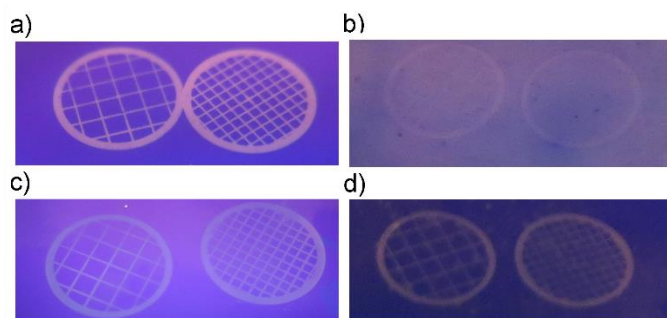


Figure S-4. 1: (a) Use of the standard Pd (II) surface treatment solution produced excellent spatial selectivity and pattern quality for the process flow Pd (II)/Ag (I)/Au (I). The pattern quality was sensitive to the solution preparation, as shown by the example in (b) for which we omitted phosphoric acid from the Pd (II) solution. (c) Metallization begun with the Ag (I) solution, as a Ag (I)/Au (I) process flow, produced marginal pattern quality, (d) as did replacing 1-octene with an air layer during the patterning step.

INSTALLATION AND REMOVAL OF 1-ALKENE-DERIVED MONOLAYER

A bromine-terminated 1-alkene, 11-bromo-1-undecene, was photolinked to an HF-etched SiN_x surface. The bromine label allowed straightforward examination of XPS spectra (Figure S-4.2) to confirm (a) surface attachment (black spectrum), and (b) successful intentional removal after 18 hours of UV irradiation in air (red spectrum).

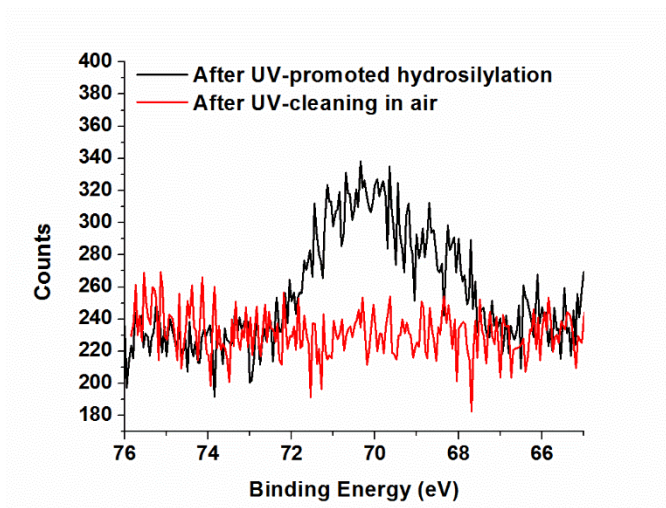


Figure S-4.2: XPS peaks corresponding to Br 3d region. (a) Photo-attachment of 11-bromo-1-undecene to the surface (black spectra) was followed by (b) removal of the alkane monolayer through prolonged exposure (18 hours) to UV in air (red spectra).

REFERENCES

1. Whelan, J. C.; Karawdeniya, B. I.; Bandara, Y. M. N. D. Y.; Velleco, B. D.; Masterson, C. M.; Dwyer, J. R., Correction to Electroless Plating of Thin Gold Films Directly onto Silicon Nitride Thin Films and into Micropores. *ACS Appl. Mater. Interfaces* **2015**, *7*, 26004-26004.
2. Whelan, J. C.; Karawdeniya, B. I.; Bandara, Y. M. N. D. Y.; Velleco, B. D.; Masterson, C. M.; Dwyer, J. R., Electroless Plating of Thin Gold Films Directly onto Silicon Nitride Thin Films and into Micropores. *ACS Appl. Mater. Interfaces* **2014**, *6*, 10952-10957.
3. Ko, J. W.; Koo, H. C.; Kim, D. W.; Seo, S. M.; Kang, T. J.; Kwon, Y.; Yoon, J. L.; Cheon, J. H.; Kim, Y. H.; Kim, J. J.; Park, Y. J., Electroless Gold Plating on Aluminum Patterned Chips for Cmos-Based Sensor Applications. *J. Electrochem. Soc.* **2010**, *157*, D46-D49.
4. Menon, V. P.; Martin, C. R., Fabrication and Evaluation of Nanoelectrode Ensembles. *Anal. Chem.* **1995**, *67*, 1920-1928.
5. Sigma-Aldrich Accustain® Reticulum Stain (Procedure No. Ht102). http://www.sigmaaldrich.com/content/dam/sigma-aldrich/docs/Sigma/General_Information/1/ht102.pdf (accessed 3/5/2014).
6. Ahn, W.; Taylor, B.; Dall'Asén, A. G.; Roper, D. K., Electroless Gold Island Thin Films: Photoluminescence and Thermal Transformation to Nanoparticle Ensembles. *Langmuir* **2008**, *24*, 4174-4184.
7. Abys, J. A.; Maisano, J. J. Process for Making Sodium Gold Sulfite Solution. *6,126,807*, **2000**.
8. Schneider, C. A.; Rasband, W. S.; Eliceiri, K. W., Nih Image to Imagej: 25 Years of Image Analysis. *Nat Meth* **2012**, *9*, 671-675.

APPENDIX 4: CHAPTER 5 SUPPORTING INFORMATION

REAL-TIME PROFILING OF SOLID-STATE NANOPORES DURING SOLUTION-PHASE NANOFABRICATION

Y.M. Nuwan D.Y. Bandara, Buddini Iroshika Karawdeniya, and Jason R. Dwyer*.

Department of Chemistry, University of Rhode Island, 140 Flagg Road, Kingston, RI, 02881, United States.

Notation	Definition
r_0	limiting nanopore radius
R	pore opening radius ($R = r_0 + 10$ nm, except for the cylindrical
z -axis	principal rotation axis of the nanopore along its length
$r(z)$	radius of the pore at a given location along the z axis of the
$L_{a-b}, L_{b-c} \dots$	length of a region of the nanopore surface along the z -axis of the nanopore between the subscripted points
L	total nanopore length
l	inner nanopore length of conical-cylindrical profile
α and β	angles defining the curved sections of the coating deposited onto
Δr_i	thickness of the deposited nanopore coating

Table S-5.1: Definitions of notation used in describing the nanopore profiles.

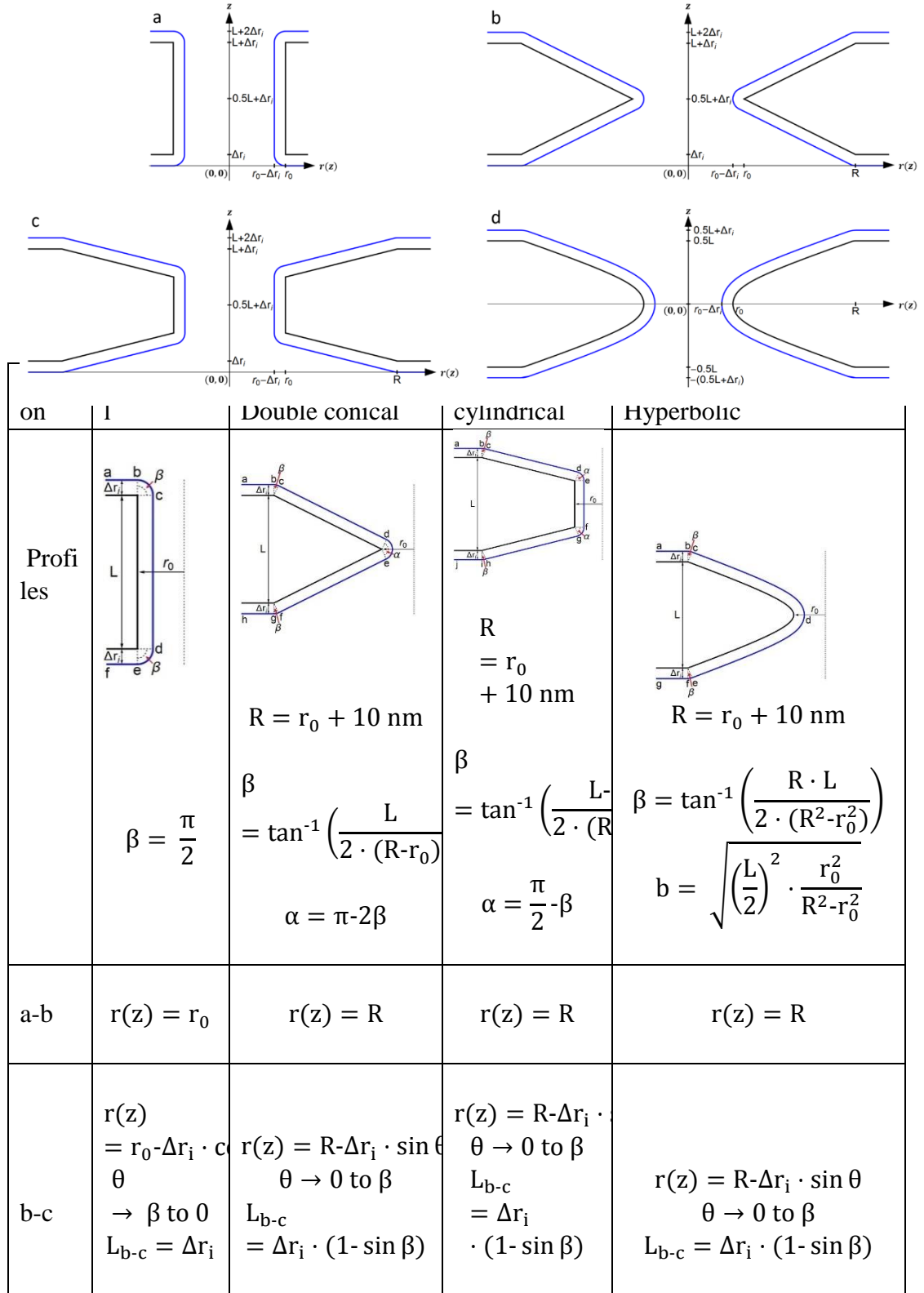


Figure S-5.1: 2D cross-sections of pristine (black lines) (a) cylindrical, (b) double conical, (c) conical-cylindrical and (d) hyperbolic nanopore profiles modified uniformly across their surfaces by a thickness of Δr_i (blue lines).

c-d	$r(z) = r_0 - \Delta r_i$ $L_{c-d} = L$	$r(z) = (R - \Delta r_i \cdot \sin \beta) - y \cdot \tan \beta$ $y \rightarrow 0 \text{ to } \frac{L}{2}$ $L_{c-d} = \frac{L}{2}$	$r(z) = (R - \Delta r_i \cdot \sin \beta) \cdot \tan \beta$ $y \rightarrow 0 \text{ to } \frac{(L-l)}{2}$ $L_{c-d} = \frac{(L-l)}{2}$	$r(z) = r_0 \cdot \sqrt{\left(1 + \frac{y^2}{b^2}\right)} + \Delta r_i$ $\cdot \sin \left(\tan^{-1} \left(\frac{r_0 \cdot \sqrt{\left(1 + \frac{y^2}{b^2}\right)}}{y \cdot r_0^2} \right) \right)$ $y \rightarrow -\frac{L}{2} \text{ to } 0$ $L_{c-d} = \frac{L}{2}$
d-e	$r(z) = r_0 - \Delta r_i \cdot \cos \theta$ $\theta \rightarrow 0 \text{ to } \beta$ $L_{d-e} = \Delta r_i$	$r(z) = r_0 - \Delta r_i \cdot \cos \left(\frac{\alpha}{2} - \epsilon \right)$ $\epsilon \rightarrow 0 \text{ to } \alpha$ $L_{d-e} = 2 \cdot \Delta r_i \cdot \sin \frac{\alpha}{2}$	$r(z) = r_0 - \cos \theta$ $\theta \rightarrow \alpha \text{ to } 0$ $L_{d-e} = \Delta r_i (1 - \sin \alpha)$	$r(z) = r_0 \cdot \sqrt{\left(1 + \frac{y^2}{b^2}\right)} - \Delta r_i$ $\cdot \sin \left(\tan^{-1} \left(\frac{r_0 \cdot \sqrt{\left(1 + \frac{y^2}{b^2}\right)}}{y \cdot r_0^2} \right) \right)$ $y \rightarrow 0 \text{ to } \frac{L}{2}$ $L_{d-e} = \frac{L}{2}$
e-f	$r(z) = r_0$	$r(z) = (R - \Delta r_i \cdot \sin \beta) \cdot \tan \beta$ $y \rightarrow \frac{L}{2} \text{ to } 0$ $L_{e-f} = \frac{L}{2}$	$r(z) = r_0 - \Delta r_i$ $L_{e-f} = l$	$r(z) = R - \Delta r_i \cdot \sin \theta$ $\theta \rightarrow \gamma \text{ to } 0$ $L_{e-f} = \Delta r_i (1 - \sin \beta)$
f-g	-	$r(z) = R - \Delta r_i \cdot \sin \theta$ $\theta \rightarrow \beta \text{ to } 0$ $L_{f-g} = \Delta r_i \cdot (1 - \sin \beta)$	$r(z) = r_0 - \cos \theta$ $\theta \rightarrow 0 \text{ to } \alpha$ $L_{f-g} = \Delta r_i \cdot (1 - \sin \alpha)$	$r(z) = R$
g-h	-	$r(z) = R$	-	-

			$r(z)$ $= (R - \Delta r_i \cdot \sin \theta)$ $\cdot \tan \beta$ y $\rightarrow 0 \text{ to } \frac{(L-l)}{2}$ $L_{g-h} = \frac{(L-l)}{2}$	
h-i	-	-	$r(z) = R - \Delta r_i \cdot$ $\theta \rightarrow \beta \text{ to } 0$ L_{h-i} $= \Delta r_i (1 - \sin \beta)$	-
i-j	-	-	$r(z) = R$	-

Table S-5.2: Geometric profiles and equations describing nanopore shapes before (black line) and after (blue line) a uniform surface modification of thickness of Δr_i over the entire pore surface. We provide the equations that determine the nanopore profile, $r(z)$, for the piecewise integration, between points labelled with undercase letters, of volume (A) and surface (B) integrals.

METHOD OF CALCULATING VOLUME (A) AND SURFACE (B) INTEGRALS

Integrals were calculated using Mathematica 10.3.1 (Wolfram Research, Champaign, IL) in the following manner,

$$A = \left(\int_{z_{\text{initial}}}^{z_{\text{final}}} \frac{dz}{\pi(r(z))^2} \right)^{-1} \cong \left(\int_{z_{\text{initial}}}^{z_{\text{final}}} \frac{dz}{\pi(r_{\text{int}}(z))^2} dz \right)^{-1}$$

$$B = \left(\int_{z_{\text{initial}}}^{z_{\text{final}}} \frac{dz}{2\pi \cdot r(z)} \right)^{-1} \cong \left(\int_{z_{\text{initial}}}^{z_{\text{final}}} \frac{dz}{2\pi \cdot r_{\text{int}}(z)} dz \right)^{-1}$$

where $r_{\text{int}}(z)$ is a 3rd-order polynomial interpolation of $r(z)$ sampled with a step height, $\Delta z = 0.0001$ nm, along the z -axis from z_{initial} to z_{final} . Here, z_{initial} and z_{final} are 0 and L for all profiles except the hyperbolic profile for which they are set to $-L/2$ and $L/2$, respectively.

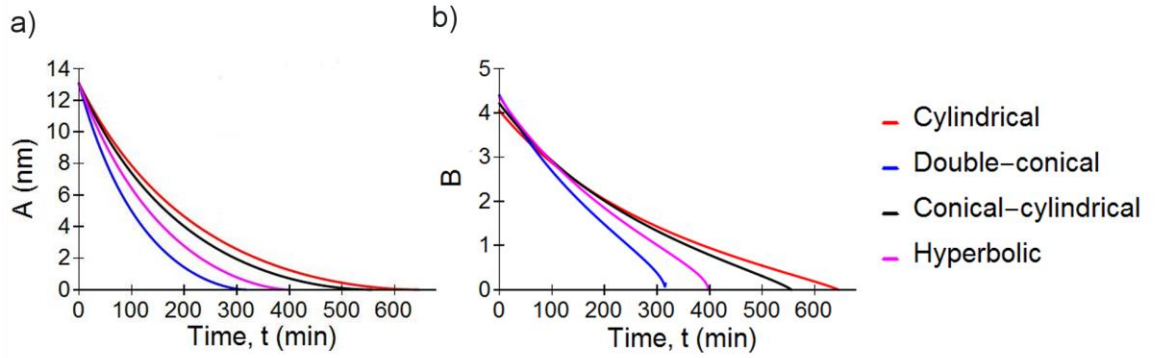


Figure S-5.2: As 10 nm-long nanopores of different shapes, all with initial conductances of 200 nS are progressively reduced in size due to material deposition, the profile-dependent decreases in the conductances are caused by profile-dependent changes in the underlying geometry integrals, A and B .

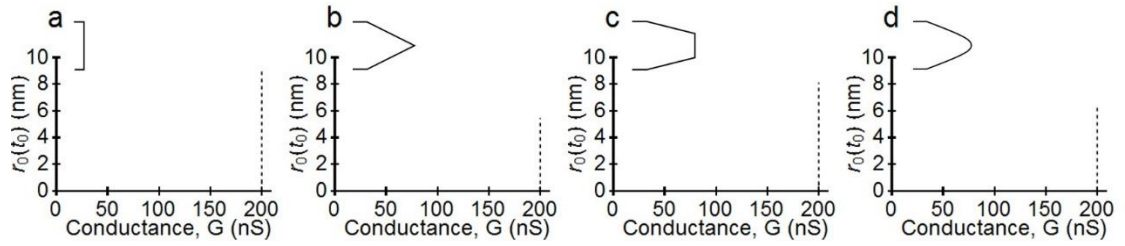
TUTORIAL: Stepwise Construction of Figure 5.4

Generating the experimental data for a cylindrical experimental nanopore.

An experimental first conductance, $G_{\text{cylindrical}}^{\text{expt}}(t_0) = 200 \text{ nS}$ is simulated using a cylindrical model with $(r_{0,\text{cylindrical}}^{\text{expt}}(t_0), L_{\text{cylindrical}}^{\text{expt}}(t_0)) = (3.5 \text{ nm}, 3.8 \text{ nm})$. We calculate $G_{\text{cylindrical}}^{\text{expt}}(t_1) = \sim 114.5 \text{ nS}$ after a $\Delta r_1 = 0.5 \text{ nm}$ decrease in the pore radius. Similarly, $G_{\text{cylindrical}}^{\text{expt}}(t_2) = \sim 67.3 \text{ nS}$ is calculated after a $\Delta r_2 = 1.0 \text{ nm}$ change in the pore radius.

Step 1: First conductance value, $G_{\text{cylindrical}}^{\text{expt}}(t_0) = 200 \text{ nS}$

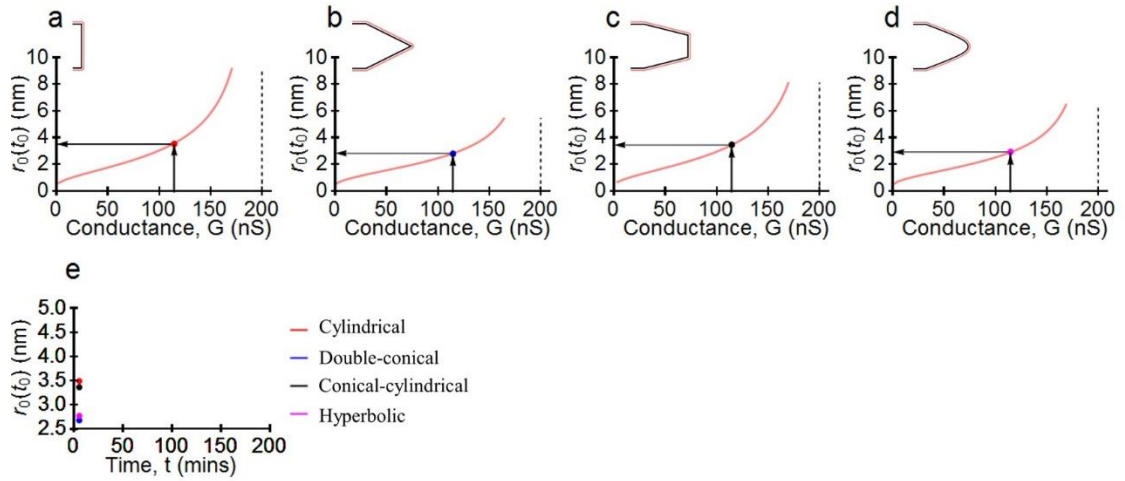
This conductance could be generated equally well by any appropriate combination of nanopore shape and geometric parameters, $(r_{0,\text{shape}}(t_0), L_{\text{shape}}(t_0))$, plotted in Figure 5.2. The dotted lines in Panels a-d below show the range of possible $r_{0,\text{shape}}(t_0)$ for each shape given the 200 nS initial conductance.



Step 1 in construction of Figure 5.4: Plots of $r_0(t_0)$ versus conductance for (a) cylindrical, (b) double-conical, (c) conical-cylindrical, and (d) hyperbolic nanopore shapes for an initial conductance of 200 nS.

Step 2: Second conductance value, $G_{\text{cylindrical}}^{\text{expt}}(t_1) = \sim 114.5$ nS

Knowing the change in radius, $\Delta r_1 = 0.5$ nm, we take each possible $(r_{0,\text{shape}}(t_0), L_{\text{shape}}(t_0))$ from Step 1 and calculate the conductance for each profile given $(r_{0,\text{shape}}(t_0) - \Delta r_1, L_{\text{shape}}(t_0) + 2\Delta r_1)$. The ordinate of the $G_{\text{shape}}(t_1)$ point shows that the initially (but now smaller) 200 nS conductance pore must have had an *initial* limiting radius, $r_{0,\text{shape}}(t_0)$, of 3.5 nm (if cylindrical); ~ 2.7 nm (if double-conical); ~ 3.3 nm (if conical-cylindrical); and ~ 2.7 nm (if hyperbolic), plotted in panel e, below. Figure 2 gives us the corresponding $L_{\text{shape}}(t_0)$: ~ 3.8 nm (if cylindrical); ~ 8.3 nm (if double-conical); ~ 3.8 nm (if conical-cylindrical); and ~ 6 nm (if hyperbolic).



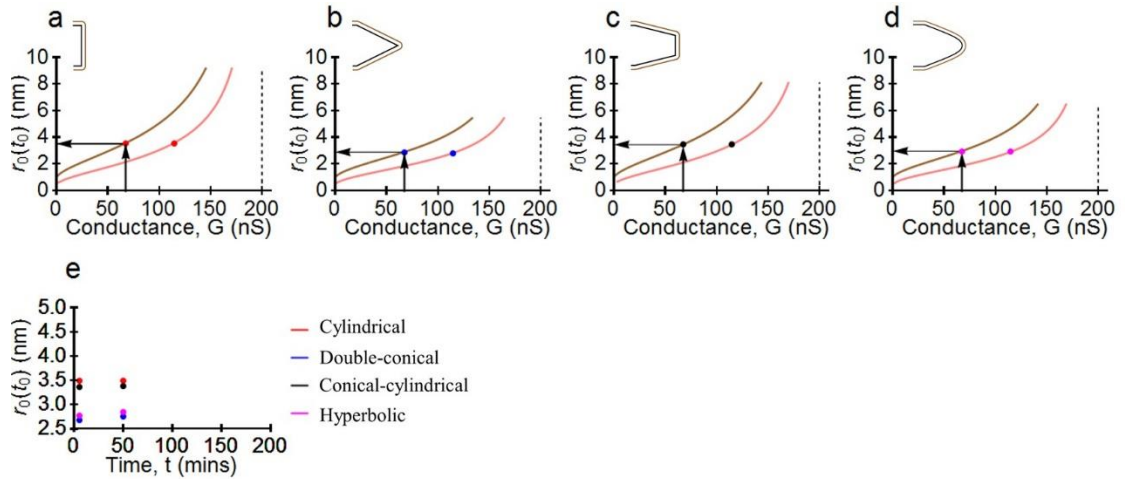
Step 2 in construction of Figure 5.4: Plots of $r_0(t_0)$ with conductance for (a) cylindrical, (b) double-conical, (c) conical-cylindrical and (d) hyperbolic nanopore profiles with $\Delta r_1 = 0.5$ nm, and (e) the corresponding $r_0(t_0)$ for each candidate profile.

Step 3: Third conductance value, $G_{\text{cylindrical}}^{\text{expt}}(t_2) = \sim 67.3$ nS

Knowing the change in radius, $\Delta r_2 = 1.0$ nm, we take each possible $(r_{0,\text{shape}}(t_0), L_{\text{shape}}(t_0))$ from Step 1 and calculate the conductance for each profile given $(r_{0,\text{shape}}(t_0) - \Delta r_2, L_{\text{shape}}(t_0) + 2\Delta r_2)$. The ordinate of the $G_{\text{shape}}(t_2)$ point shows that the pore must have had an *initial* limiting radius, $r_0(t_0)$, of 3.5 nm (if cylindrical); ~ 2.8 nm (if double-conical), ~ 3.4 nm (if conical-cylindrical), and ~ 2.8 nm (if hyperbolic), plotted in panel e below. Figure 2 gives us the corresponding $L(t_0)$: ~ 3.8 nm (if cylindrical); ~ 8.6 nm (if double-conical); ~ 4 nm (if conical-cylindrical); and ~ 6.3 nm (if hyperbolic).

The consistent value of $r_0(t_0)$ in panel e (and of the $L(t_0)$ that we don't show) for the cylindrical trial profile tells us that the simulated pore was cylindrical, and that

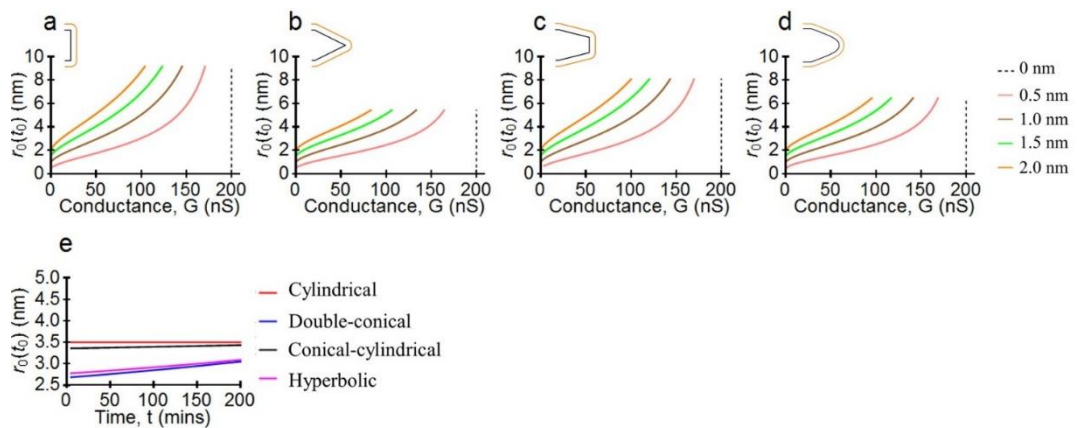
its initial size was $(r_{0,\text{cylindrical}}^{\text{expt}}(t_0), L_{\text{cylindrical}}^{\text{expt}}(t_0)) = (3.5 \text{ nm}, 3.8 \text{ nm})$.



Step 3 in construction of Figure 5.4: Plots of $r_0(t_0)$ with conductance for (a) cylindrical, (b) double-conical, (c) conical-cylindrical and (d) hyperbolic nanopore profiles with $\Delta r_2 = 1.0$ nm, and (e) the corresponding $r_0(t_0)$ for each candidate profile.

Step 4: Additional conductance values, $G_{\text{cylindrical}}^{\text{expt}}(t_i)$

Additional conductance values can be collected and used to, for example, improve the robustness of the $r_0(t_0)$ determinations.



Step 4 in construction of Figure 5.4: $r_0(t_0)$ with time for a large pool of Δr_1 (only 4 shown for clarity) for (a) cylindrical, (b) double-conical, (c) conical-cylindrical and (d) hyperbolic nanopore profiles. Only for the experimental model (cylindrical

profile), is $r_0(t_0)$ constant for all time-dependent conductance values, as plotted in (e).

To generate Fig. 5.4f-h, we repeated this process by respectively simulating the experimental conductances as double-conical, conical-cylindrical, and hyperbolic profiles.

REFERENCES

1. Frament, C. M.; Dwyer, J. R., Conductance-Based Determination of Solid-State Nanopore Size and Shape: An Exploration of Performance Limits. *J. Phys. Chem. C* 2012, *116*, 23315-23321.
2. Kowalczyk, S. W.; Grosberg, A. Y.; Rabin, Y.; Dekker, C., Modeling the Conductance and DNA Blockade of Solid-State Nanopores. *Nanotechnology* 2011, *22*, 315101.

APPENDIX 5: CHAPTER 6 SUPPORTING INFORMATION

CONDUCTANCE-BASED PROFILING OF NANOPORES: ACCOMMODATING FABRICATION IRREGULARITIES

ACCOMMODATING FABRICATION IRREGULARITIES

*Y.M. Nuwan D.Y. Bandara, Jonathan W. Nichols, Buddini Iroshika Karawdeniya,
and Jason R. Dwyer.*

Department of Chemistry, University of Rhode Island, 140 Flagg Road, Kingston,
RI, 02881, United States.

E-mail: jason_dwyer@uri.edu. Phone 1-401-874-4648. Fax 1-401-874-5072.

SUPPORTING INFORMATION.

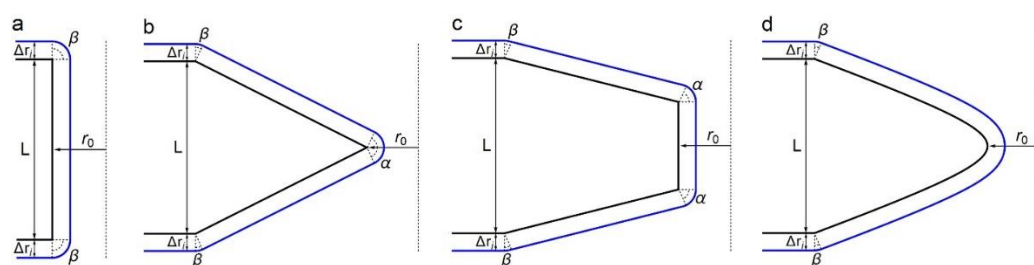


Figure S6.1: (a) Cylindrical, (b) double-conical, (c) conical-cylindrical, and (d) hyperbolic nanopore half-profile cross-sections cylindrically symmetric about the vertical z -axis (dotted vertical line) of the pore. Profiles are shown before (black line) and after (blue line) material deposition to decrease the limiting nanopore radius, r_0 , by an amount Δr_i determined by the deposition time and material transfer rate. Reprinted with permission from [1]. Copyright 2016 American Chemical Society.

Nanopore Access Resistance. Departures from the cylindrical profile, or from bulk-only access resistance formulations, can make arriving at closed-form solutions for the access resistance of a nanopore difficult or intractable.[2-6] A conventional formulation for the access resistance of a cylindrical nanopore, here with a surface conductance term included in parallel with the bulk conductance, gives

$$G = K \left(\frac{1}{\frac{\pi r_0^2}{L} + \frac{\mu|\sigma|}{K} \frac{2\pi r_0}{L}} + \frac{1}{2r_0} \right)^{-1} \quad (\text{S1})$$

where the second fraction arises from a common formulation of the nanopore access resistance, $2/G_{\text{access}}$ (where there is a $1/G_{\text{access}}$ contribution from each open side of the nanopore).[2-6] More complex treatments exist that also include a surface term in the access resistance, and others have noted the difficulty of treating the access resistance of other nanopore shapes.[2, 3] To investigate the effect of including the access resistance into the conductance modelling, we used equation (S1) to calculate the conductances of nanopores with selected aspect ratios, $L(t_0)/r_0(t_0)$, and then fit the results to the cylindrical conductance model of equations (1) and (S1), where access resistance is neglected in equation (1). Simulation results are shown in Figure S6.2.

If one rewrites equation (S1) more generally, $G = \left(\frac{1}{G_{\text{bulk}} + G_{\text{surface}}} + \frac{1}{G_{\text{access}}^{\text{total}}} \right)^{-1}$, it can then be rearranged to

$$G = (G_{\text{bulk}} + G_{\text{surface}}) \left(1 + \frac{G_{\text{bulk}} + G_{\text{surface}}}{G_{\text{access}}^{\text{total}}} \right)^{-1} \quad (\text{S2})$$

that is, to equation (1) multiplied by a term containing the total contribution (*i.e.* from both openings of the pore) to the nanopore conductance provided by the

access resistance: $G = G_{\text{eqn1}} G_{\text{access}}^{\text{scaled}}$. In the limit of low access resistance when

$\frac{G_{\text{bulk}} + G_{\text{surface}}}{G_{\text{access}}^{\text{total}}} \ll 1$, a first-order expansion gives

$G \cong (G_{\text{bulk}} + G_{\text{surface}}) \left(1 - \frac{G_{\text{bulk}} + G_{\text{surface}}}{G_{\text{access}}^{\text{total}}}\right)$, so that for sufficiently low access resistance,

equation (1) is recovered from equation (S2). Constructing a more general analytic formulation of $\frac{2}{G_{\text{access}}}$, beyond that shown in equation (S1) for a cylindrical

nanopore, remains challenging, especially if nanopore surface contributions are to

be included.[2, 6] Scaling arguments and earlier work,[2] however, offer a possible

approach in which setting $G_{\text{access}} = \alpha K r_0$ is followed by numerical calculations of

α , a parameter dependent on nanopore shape.

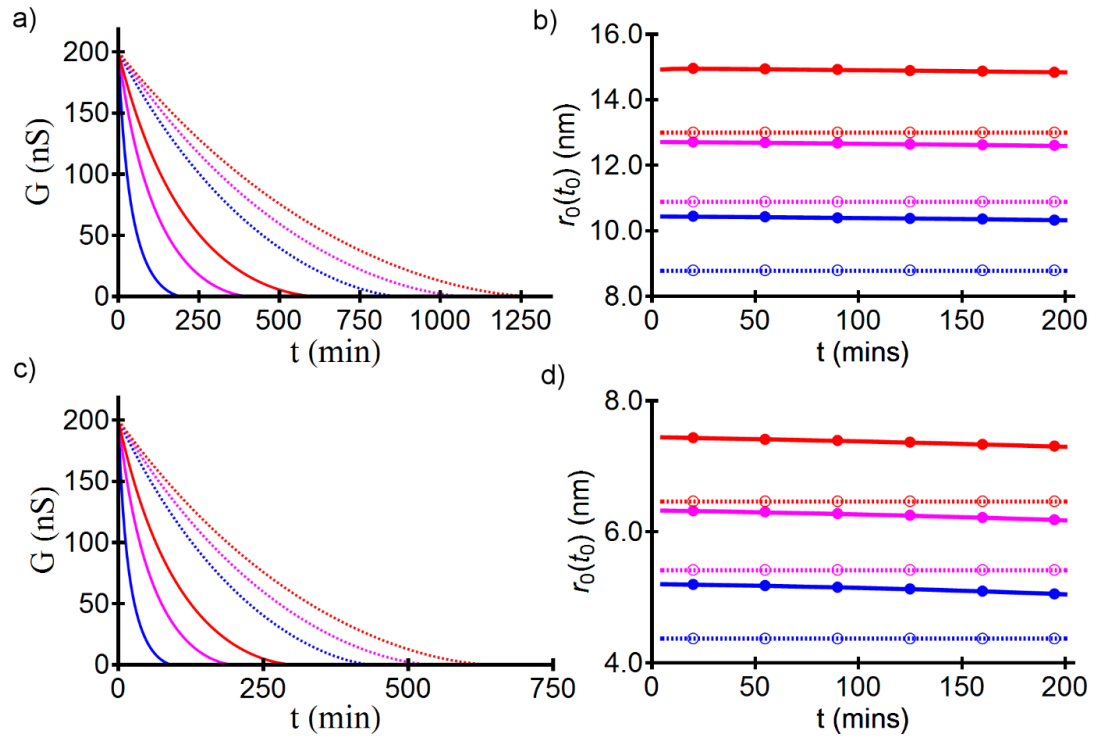


Figure S6.2: Simulations of conductance versus time for initially 200 nS pores with $L(t_0)/r_0(t_0)$ ratios of 0.5 (blue), 1.0 (magenta), and 1.5 (red) for (a) single and (c) double pores, with (dotted lines) and without (solid-lines) the access resistance term in Equation S1. In (b) and (d), we fit candidate pore models with and without access resistance using the conductance data in (a) and (c) that included the access resistance. There are three correct fits in (b) and (d)—one for each $L(t_0)/r_0(t_0)$ —that are indicated by the horizontal slope of the fit $r_0(t_0)$ versus t data. Neglecting the access resistance when fitting the conductance-versus-

time simulations results in a ~2 nm overestimate of the nanopore dimensions and a nonzero slope that indicates the incorrect fit. The simulations used step sizes in the nanopore radius of 0.01 nm to calculate G versus t , and 0.05 nm to determine $r_0(t_0)$.

The dependence of nanopore conductance show in Equation (1) is explicitly on solution conductivity, K , and implicitly on solution pH through its effect on the surface charge density, σ (and, where a surface can carry a solution-pH-dependent charge of either polarity, through the mobility of the counterion, μ). Here we take the reasonable step of treating the case where the solution conductivity is not itself dependent on pH. Thus, without change of either nanopore dimension or solution conductivity, a change of solution pH can change the nanopore conductance—especially at lower solution conductivities.[7, 8] This behavior is shown in Figure S6.3, and can be expressed by rewriting Equation (1) as

$$G(\text{pH}) = K \cdot A(r, L) + \mu|\sigma(\text{pH})| \cdot B(r, L) = K \cdot A(r, L) + \chi(\text{pH}) \cdot \mu|\sigma(\text{pH}_{\text{ref}})| \cdot B(r, L) \quad (\text{S3})$$

where the parameter $\chi(\text{pH})$ is used to explicitly carry the pH-dependence of the nanopore conductance (calculated relative to a particular chosen reference pH). In this form, with $\mu|\sigma(\text{pH}_{\text{ref}})|$ and $\chi(\text{pH})$ constant in time for a given fixed solution composition as for Equation (1), the consequence of solution pH is simply a reweighting of the surface contribution to the conductance, relative to the behavior at the reference pH. Figure S6.3 shows the time-dependence of the conductance of the nanopore conductance at several pH values, and their successful use to correctly recover the nanopore size.

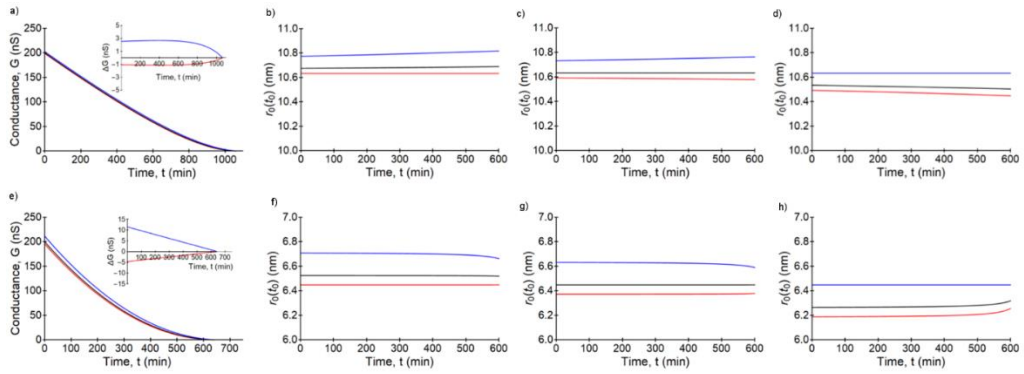


Figure S6.3: Plots of nanopore ($L=10$ nm, $r_0=6.45$ nm) conductance in time at pH 4 (red), 7 (black), and 10 (blue), showing the effect of pH on initial conductance (200 nS at pH 7) and on the time-evolution of the nanopore conductance, (a) with and (e) without access resistance. The inset shows the difference between the curves at all pH values, relative to the curve at pH 7. Geometry determinations (b-d) with and (f-h) without access resistance included in the candidate cylindrical profile were performed using the data in (a) and (e), using values of 4, 7, and 10 for the solution pH, respectively.

Figure S6.4a reinforces that for a given experimental conductance value and even a given candidate nanopore profile, unless the nanopore length is known, then one must contend with an infinite set of $\{(r_{0,\text{candidate}}, L_{\text{candidate}})\}$ that deliver that single conductance value through Equation 1. This figure furthermore illustrates that the presence of multiple pores further expands the combinations of the possible nanopore dimensions delivering that single conductance value. Figure S6.4a gives single vs. double pore values of r_0 for a 200 nS pore. Choosing a 10 nm-long nanopore for each profile gives the corresponding r_0 : cylindrical—6.4 vs. 4.5 nm; double-conical—3.1 vs. 1.7 nm; conical-cylindrical—5.5 vs. 3.8 nm; and hyperbolic—4.0 vs. 2.3 nm. For translocation-based experiments, this physical pore size is vital: the 200 nS single pore double-conical profile could allow intact passage of a species too large to fit through the smaller pores of its 200 nS double pore equivalent. Figure S6.4b shows that, as established for single pores,[1] the conductance change in time provides the prospect of differentiating between single

and double pore systems. As an example of the complexity introduced by more than one nanopore, the double pore conductance of the cylindrical pore here lies close to the single pore conductance of the hyperbolic profile. Such time traces thus reveal insights into the type and number of pores, but also suggest practical challenges.

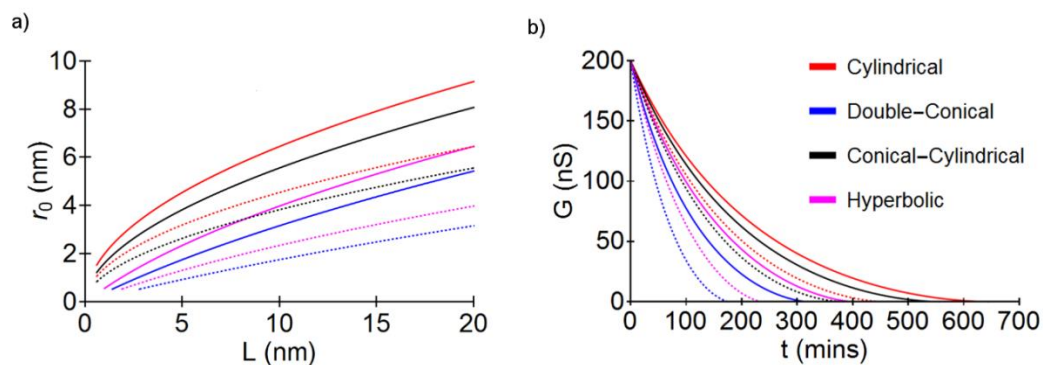


Figure S6.4: a) Pairings of r_0 and L for a given nanopore shape and number (solid line-single pore; dotted line-double pore) giving a nanopore with 200 nS conductance. b) Change in conductance with time for 10 nm-long profiles with single and double pore configurations. The simulations used step sizes in the nanopore radius of 0.01 nm to calculate G versus t .

REFERENCES

- [1] Bandara, Y. M. N. D. Y., Karawdeniya, B. I., Dwyer, J. R., *ACS Appl. Mater. Interfaces* 2016, 8, 30583-30589.
- [2] Kowalczyk, S. W., Grosberg, A. Y., Rabin, Y., Dekker, C., *Nanotechnology* 2011, 22, 315101.
- [3] Lee, C., Joly, L., Siria, A., Biance, A.-L., Fulcrand, R., Bocquet, L., *Nano Lett.* 2012, 12, 4037-4044.
- [4] Vodyanoy, I., Bezrukov, S. M., *Biophys. J.* 1992, 62, 10-11.
- [5] Hall, J. E., *The Journal of General Physiology* 1975, 66, 531-532.
- [6] Wang, J., Ma, J., Ni, Z., Zhang, L., Hu, G., *RSC Advances* 2014, 4, 7601-7610.
- [7] Frament, C. M., Dwyer, J. R., *J. Phys. Chem. C* 2012, 116, 23315-23321.
- [8] Liebes, Y., Drozdov, M., Avital, Y. Y., Kauffmann, Y., Rapaport, H., Kaplan, W. D., Ashkenasy, N., *Appl. Phys. Lett.* 2010, 97, 223105.

APPENDIX 6: CHAPTEd 7 SUPPORTING INFORMATION

A GENERAL STRATEGY TO MAKE AN ON-DEMAND LIBRARY OF STRUCTURALLY AND FUNCTIONALLY DIVERSE SERS SUBSTRATES

*Buddini Iroshika Karawdeniya, Y. M. Nuwan D. Y. Bandara, Julie C. Whelan, and
Jason R. Dwyer**

Department of Chemistry, University of Rhode Island, 140 Flagg Road, Kingston,
RI, 02881, United States.

*E-mail: jason_dwyer@uri.edu

MATERIALS

The following materials, identified by their product number and specification, were obtained from Sigma-Aldrich Corporation (St. Louis, MO, USA): allyl 2-bromo-2-methylpropionate (381756, 98%); sodium acrylate (408220, 97%); copper (I) bromide (254185, 99.999% trace metals basis); copper (II) bromide (221775, 99%); 2,2'-bipyridyl (D216305, ReagentPlus[®], ≥99%); methanol (34860, CHROMASOLV[®], for HPLC, ≥99.9%); ethanol (34852, CHROMASOLV[®], for HPLC, absolute, ≥99.8%); gold etchant (651818, “standard gold etchant”: iodine and potassium iodide basis); 4-nitrobenzenethiol (NBT; N27209, technical grade, 80 %); acetonitrile (34998, CHROMASOLV[®] Plus, for HPLC, ≥99.9%). Ethanol (200CSPTP, 200 proof ACS/USP grade) was purchased from Ultra-Pure LLC (CT, USA). A 5% solution of hydrofluoric acid (C4354) was purchased from Science Lab Supplies (St. Augustine, FL) and diluted to 2.5% with

water. Dichloromethane (390700010, 99.5%); chloroform (326820010, 99.9%, Extra Dry, stabilized, AcroSeal®); and 4-aminothiophenol (ATP; 104680, 96%) were purchased from Acros Organics (NJ, USA). Planar, 200 nm-thick, low-stress (<250 MPa tensile) LPCVD silicon nitride thin films on 356 ± 25 μm -thick polished <100> silicon wafers (P/Boron doped, 1-20 $\Omega \cdot \text{cm}$ resistivity) were purchased from Rogue Valley Microdevices, Inc. (Medford, OR). The following materials, identified by their product number and specification, were purchased from Fisher Scientific (Pittsburgh, PA, USA): $2 \times 2 \times \frac{1}{4}$ "-thick quartz plate (CGQ062009); acetone (A16P, histological grade, $\geq 99.5\%$); hexane (H303, Optima™); ethyl acetate (E145, certified ACS, $\geq 99.5\%$); Whatman Grade 1 qualitative filter paper (1001-055 and 1001-110, GE Healthcare Bio-Sciences, Pittsburgh, PA); Whatman™ Grade 1 Chr Cellulose Chromatography Paper (3001-672); vacuum filtration system (SCVPU11RE, Stericup-VP, 0.10 μm pore size in polyethersulfone membrane) from EMD Millipore Corporation (MA, USA). Nitrogen (NI HP200), oxygen (OX UHP300), and argon (AR PP300) were purchased from Airgas Inc. (PA, USA). A UV lamp (Model XX-15S, Part # 95-0042-05) was acquired from UVP, LLC (CA, USA). Nanoporous silicon nitride substrates with 450 nm-diameter pores in 100 nm-thick membranes were purchased from Innosieve Diagnostics (custom-provided, reference number ID12200; Wageningen, Netherland). Commercial silicon nanopillar substrates (item ID 15G, gold on nanostructured Si with a SERS active area of $5 \times 5 \text{ mm}^2$) were purchased from Silmeco ApS (Copenhagen, Denmark). For easier handling for the drop-casting spectral acquisition, nanopillar substrates were mounted at the center of a 1 cm \times 1 cm plain silicon nitride chip with carbon tape (16084-6; Ted Pella, Inc., Redding, CA) after electroless plating. Nanocellulose fibers of

(declared) nominal 50 nm diameter and hundreds of micrometers length, were obtained as a slurry (University of Maine: The Process Development Center Nanocellulose Facility, Orono, Maine). No special precautions were taken during processing to avoid potentially breaking nanocellulose fibers. All aqueous dilutions and washes were performed using 18 M Ω ·cm ultrapure water (Millipore Synergy UV, Billerica, MA). For the laser power measurements, an 842-R-USB power meter with 919P-040-50 thermopile sensor was used (Newport Corporation, CA, USA).

ELECTROLESS PLATING

Electroless plating baths were prepared as previously reported¹ (note: a mass of 0.1500 g of barium hydroxide octahydrate was incorrectly reported previously² as 1.500 g). Material-specific preliminary processing steps preceding the electroless plating method are detailed below, before a more general discussion of the electroless plating steps outlined in Scheme S1.

MATERIAL-SPECIFIC SURFACE PREPARATION

Hydrofluoric acid presents significant chemical hazards, so that we adopted special operating procedures when working with it. All containers used were polypropylene because HF can etch glass containers and render them porous and at risk of leaking. To reduce the risk of handling concentrated HF, dilute (5%) stock solutions were purchased and Calgonate (Port St. Lucie, FL) 2.5% calcium gluconate gel was kept at hand in case of accidental skin exposure. To minimize the risk of exposure, all personnel wore a full face shield over chemical safety glasses, a disposable polypropylene apron over a standard laboratory coat, and thick neoprene long gloves over extended-cuff nitrile gloves. We also used a

“buddy system” so that one researcher supervised the other’s work with HF. All labware, gloves, and working areas were thoroughly rinsed with water after use.

POLYMER-GRAFTED SILICON NITRIDE

A subset of purchased planar silicon nitride films (with films on silicon supports cut to 1 cm×1 cm) was polymer-grafted, as described briefly here, before electroless plating. The as-supplied silicon nitride-coated substrates were exposed first to 10 minutes of a nitrogen plasma, and then to 5 minutes of an oxygen plasma, using a Glow Research Autoglow plasma cleaner (Phoenix, AZ) set to 50 W and with operating pressures held between 0.8-1.2 Torr during the flow of each process gas. The chips were then etched in 2.5% hydrofluoric acid for 10 minutes, rinsed 3 times in water, argon-dried, and submerged in 50 μ L of allyl 2-bromo-2-methylpropionate to a depth of \sim 100 μ m in a custom holder, and therein irradiated with UV light through a ¼"-thick quartz plate, for 5 hours using a 15 W, 254 nm UV lamp.³ Post-irradiation, they were rinsed at least three times with alternating washes of dichloromethane and acetone before being dried under an argon stream. In a glass vial, 1.88 g of sodium acrylate; 57.4 mg of copper (I) bromide; 9.0 mg of copper (II) bromide; and 137.4 mg of 2,2'-bipyridyl were dissolved in 4 mL of argon-purged methanol and stirred (1000 rpm) under argon for 10 minutes at 30°C, followed by filtering into a Schlenk flask containing four of the silicon nitride substrates that had been pretreated with allyl 2-bromo-2-methylpropionate. The wafers were gently stirred (300 rpm) in this solution at 30°C, under argon, for 2 hours.⁴ After this polymerization step, the substrates were alternately washed with water and ethanol at least three times, then dried under an argon stream.

SILICON NANOPILLAR ARRAY (GOLD-ETCHED SILMECO)

A number of the commercial gold-coated silicon nanopillar SERS substrates were immersed in gold etchant under vacuum (to remove any initial air layer and any generated bubbles preventing full etching solution access between the pillars) for 30 minutes and then washed with copious amounts of water. A gold coating was no longer visible, and while x-ray photoelectron spectroscopy (XPS) analysis showed low residual amounts of gold, there was no measurable SERS response from the gold-etched Silmeco substrates before they were electrolessly plated according to Scheme S1.

CELLULOSE

Whatman 1 filter paper substrates were used without modification. Nanocellulose fibers were formed into a crude paper-like mat by filtering the as-supplied slurry of nanocellulose in water with a polyethersulfone membrane with 0.1 μm pores. When most of the water had filtered through, the resulting paper-like mat (hereafter referred to as “nanocellulose paper”) was compressed to ~ 1 mm thickness (thickness chosen for fabrication convenience) between two glass slides in a custom-designed, 3D printed holder and left to dry under vacuum in a desiccator for two days before plating.

SILICON- AND SILICON NITRIDE SURFACES

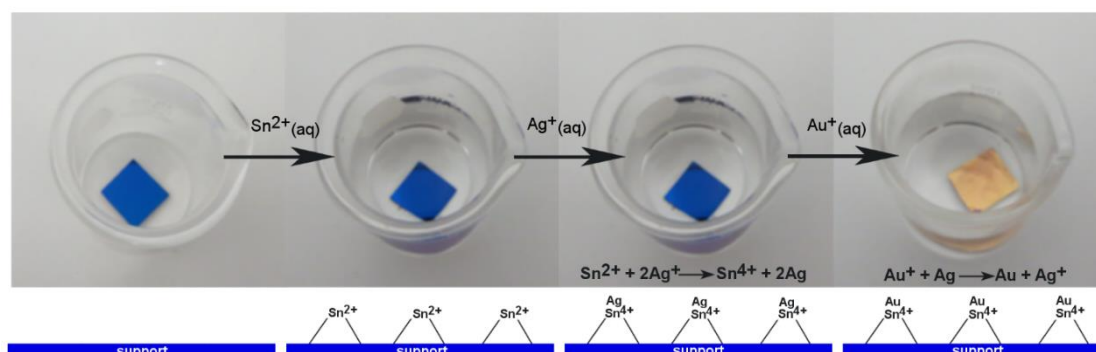
Prior to plating, the planar and nanoporous silicon nitride chips, and the gold-etched silicon nanopillar array, were subjected to cleaning and etch steps. Nitrogen and oxygen plasma treatment were used to remove organic contaminants and hydrofluoric acid etching was used to remove surface oxide layers, as

described above and also in reference 1. Plasma-based surface pretreatments were not performed for the surfaces bearing organic moieties.

ELECTROLESS PLATING SCHEME

Scheme S1 illustrates the general electroless plating process which followed the previous material-specific surface preparation steps, and consisted of sequential plating bath immersions interleaved with rinsing steps. Electroless plating of planar and porous silicon nitride, polymer-grafted silicon nitride, and gold-etched Silmeco was carried out for 2 hours at $\sim 3^{\circ}\text{C}$ with gentle rocking of the plating baths. Whatman 1 filter paper substrates and nanocellulose paper were electrolessly plated at room temperature for 2 hours with gentle rocking using a BenchRocker 3D (Benchmark Scientific, Edison, NJ, USA), and then vacuum dried (~ 15 minutes) as the final step. Plating bath volumes were 2 mL, 2 mL, and 1.5 mL for tin-, silver-, and gold-containing solutions for all substrates except for nanocellulose paper for which the volumes were tripled. Solvent washes between metal ion baths were identical for all plated materials: after tin, rinsing and 5 minutes of soaking in methanol followed by drying; after silver, soaking in methanol for 5 minutes and in water for 5 minutes; and after gold, alternate rinses with methanol and then water at least three times.

Scheme S1. Process flow for the electroless plating steps common to the plating of each support type.



SURFACE CHARACTERIZATION OF ELECTROLESSLY PLATED FILMS

Gold film morphology was examined using a Zeiss Sigma VP FE-SEM at an electron energy of 3-8 keV (Oberkochen, Germany). Elemental analysis was performed using a Thermo Scientific K-Alpha-X-ray Photoelectron Spectrometer System used with monochromator micro-focused Al K α x-rays with a spot size of 400 μm and source energy of 486.6 eV. The energy step was 0.050 eV, dwell time was 50 ms, and pass energy was 20.000 eV, with a charge-neutralizing flood gun used during each acquisition. The number of scans varied from 5-30 depending on the sensitivity factor for each element.

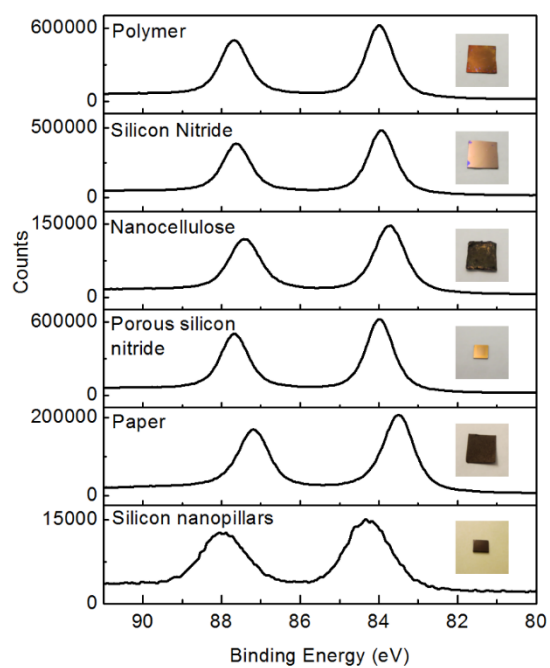


Figure S7.1: Au4f peaks of X-ray photoelectron spectroscopy data confirm gold deposition on the surface of each substrate. Photographs of gold-coated substrates are shown as insets.

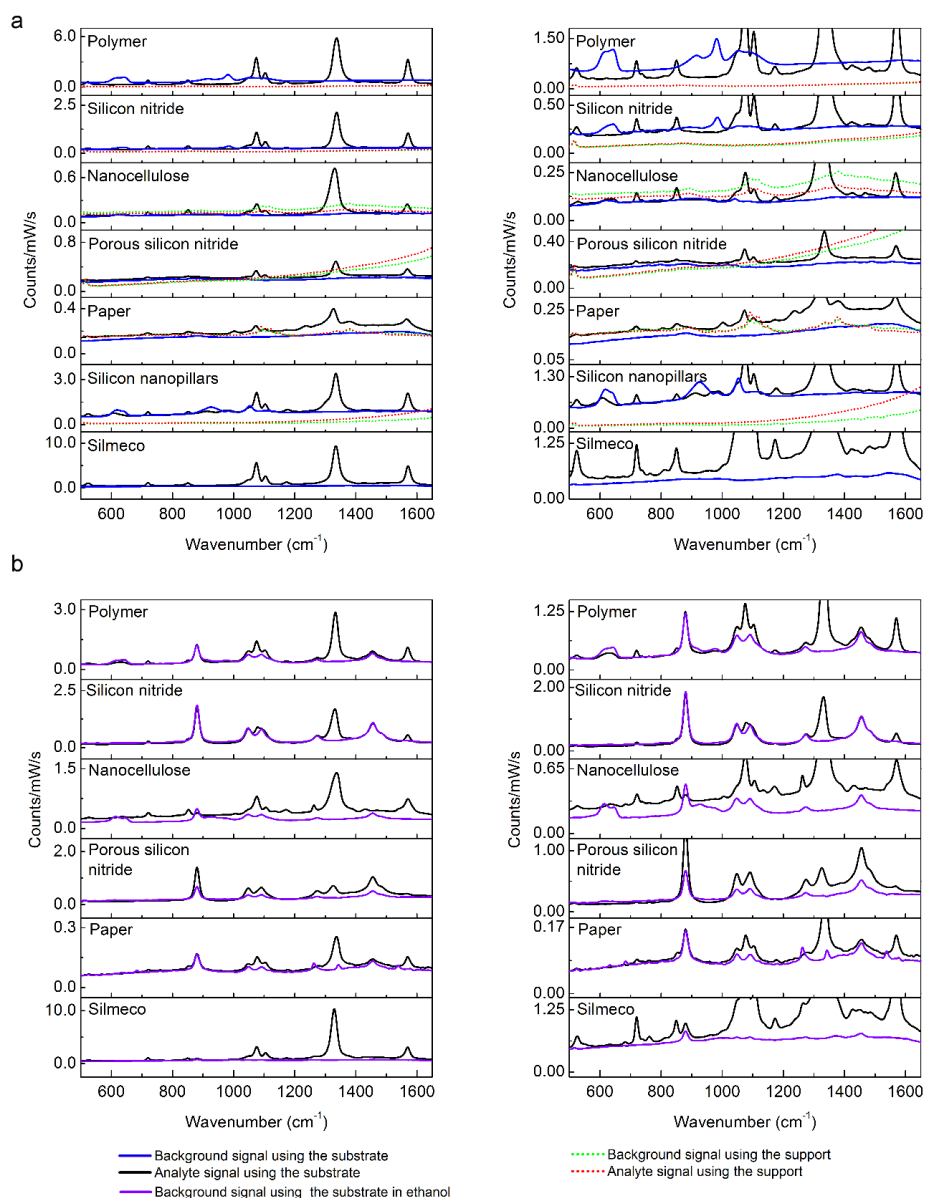


Figure S7.2: As-acquired spectra of support materials, substrates, and analyte. Spectra are displayed at full vertical range at left, and scaled at right to more clearly reveal the details of the baseline. (a) 1.67×10^{-4} M NBT in acetonitrile was added to each element (drop-casting followed by 5 minutes of air-drying: 20 μ L aliquots for silicon- and silicon-nitride-containing elements; 5 μ L aliquots for commercial silicon nanopillar and nanoporous silicon nitride; and by soaking for 5 minutes followed by 5 minutes of vacuum drying: 1 mL for paper and 10 mL for nanocellulose paper), with the solvent allowed to dry before spectral acquisition. (b) Elements were immersed in 10^{-4} M solutions of NBT in ethanol and spectra were recorded after signal level saturation in time.

SURFACE ENHANCED RAMAN SPECTROSCOPY

SPECTRAL ACQUISITION

Standard solutions of 4-nitrobenzenethiol (NBT) in ethanol were prepared by serial dilution, covering a concentration range from 5×10^{-9} - 1×10^{-4} M. Solutions were covered in aluminum foil to minimize any photodamage and stored around 3°C in the refrigerator when not in use. Solutions were allowed to reach room temperature before use. An R3000QE Raman Systems spectrometer was used for all SERS measurements, with an excitation laser wavelength of 785 nm set to a power of 57 mW on cellulose and as-provided Silmeco substrates, and 250 mW power on all other substrates. The full-width-half-maximum excitation spot size was ~ 100 μm , measured at the substrate surface with the reader head placed at a slight stand-off of ~ 2.0 mm from the substrate. Each substrate was placed in a glass beaker and a spectrum was acquired at this point to ensure that the substrate was not contaminated. The substrate was then immersed in ethanol and spectra were collected every 2 minutes for about 20 minutes. Once this ethanol-only blank experiment was done, the substrate was removed from solution and dried under nitrogen before being immersed in the standard NBT solution. A spectrum was recorded every 2 minutes until equilibrium was reached, and then the rinsing, drying, immersion, and signal acquisition were repeated for all NBT standard solution from lowest to highest concentration. To provide (unenhanced) Raman spectra for the SEV analysis,⁵ the same procedure was repeated using a gold-free silicon nitride substrate, using NBT concentrations in the range of 2×10^{-4} M to 2.5×10^{-3} M.

SPECTRAL ACQUISITION FOR DRIED SAMPLES

A 1.67×10^{-5} M solution of NBT in acetonitrile was prepared and a 5 μ L aliquot was pipetted onto the Silmeco substrate. The substrate was allowed to air-dry for about 5 minutes before spectral acquisition, and the Raman spectrometer read head was aligned with the center where the pipette tip had been for drop-casting. There was a slight ~ 1.2 mm stand-off between the SERS substrate and the pipette tip and read head to prevent mechanical damage to the SERS substrate (the nanopillar substrates were especially susceptible to scratches). Excitation power was 250 mW. This alignment of pipette tip and read head was repeated for the other drop-cast spectra in Figure S7.2a, and additional details specific to each substrate are provided in the figure caption.

SPECTRAL ANALYSIS

All spectra were analyzed by custom programs written in Mathematica 11.2 (Wolfram Research, Champaign, IL). Acquired spectra were background-subtracted using piecewise linear fitting between local minima that were selected using a relative thresholding approach to bracket known spectral peaks. To obtain the SEV for all substrates, the remainder of the analysis was performed according to Guicheteau *et al.*⁵ For each spectrum we calculated the ratio of the area of the ~ 1330 cm^{-1} peak of NBT to the area of the ~ 880 cm^{-1} peak of ethanol, $R_{\text{NBT/EtOH}}$. For a given substrate and concentration, the plot of $R_{\text{NBT/EtOH}}$ versus time, t , was fit to the equation $R_{\text{NBT/EtOH}} = R_{\text{NBT/EtOH}}^{\text{max}} At / (1 + At)$, with A and $R_{\text{NBT/EtOH}}^{\text{max}}$ as free parameters, using the Levenberg-Marquardt method implemented in Mathematica. The standard error of the fit, $\sigma([\text{NBT}])$, used for subsequent calculation of the SEV for each substrate, was determined in this step. The best-fit

value for $R_{\text{NBT}/\text{EtOH}}^{\text{max}}$ (here, representing the surface adsorption equilibrium value) for each concentration was then plotted against [NBT] for each substrate, as shown in Figure S7.3. For each substrate and analyte concentration, we used $R_{\text{NBT}/\text{EtOH}}^{\text{max}}([\text{NBT}])$ and $\sigma([\text{NBT}])$ as the mean and standard deviation of a Gaussian distribution, $\rho(r, [\text{NBT}]) = \exp\left(-\left(r - R_{\text{NBT}/\text{EtOH}}^{\text{max}}\right)^2 / (2\sigma^2)\right)$, to calculate detection thresholds. Using the ethanol-only (NBT-free) samples, we calculated $r_{90\%,\text{blank}}$, the limit of integration capturing 90% of the distribution's area, $\int_{-\infty}^{r_{90\%,\text{blank}}} \rho(r, \theta) dr = 0.9 \int_{-\infty}^{\infty} \rho(r, \theta) dr$, for each substrate. For each analyte-containing sample for each substrate, we then calculated $\text{PD}([\text{NBT}]) = \int_{r_{90\%,\text{blank}}}^{\infty} \rho(r, [\text{NBT}]) dr / \int_{-\infty}^{\infty} \rho(r, [\text{NBT}]) dr$, where PD is the probability of detection with a 10% probability of false alarm (PFA). Subsequently, receiver-operator characteristic (ROC) curves were constructed for each substrate by plotting PD versus [NBT]. The concentration, C_{SER} , at which $\text{PD}=0.9$ was found for each substrate by linearly extrapolating between the two experimental concentration values bracketing the PD threshold: $C_{\text{SER}}=7.89 \times 10^{-9}$ M for SiN_x , 6.72×10^{-7} M for porous silicon nitride, 7.23×10^{-6} M for paper, and 2×10^{-8} M for nanocellulose. For the commercial Silmeco and custom polymer-coated SiN_x substrates, even the lowest concentration measured better than 90% PD for a 10% PFA, and so the lowest concentration we used provides an upper bound for C_{SER} (and a lower bound for the SEV, below). The same procedure was repeated for Raman spectra (in the absence of substrate) to get $C_{\text{RS}}=0.00467$ M, the concentration at which the PD became 0.9. The SERS enhancement value, $\text{SEV} = C_{\text{RS}}/C_{\text{SER}}$, was developed by Guicheteau *et al.*,⁵ to provide a representative

metric for comparing Raman enhancement between often widely different SERS substrate types.

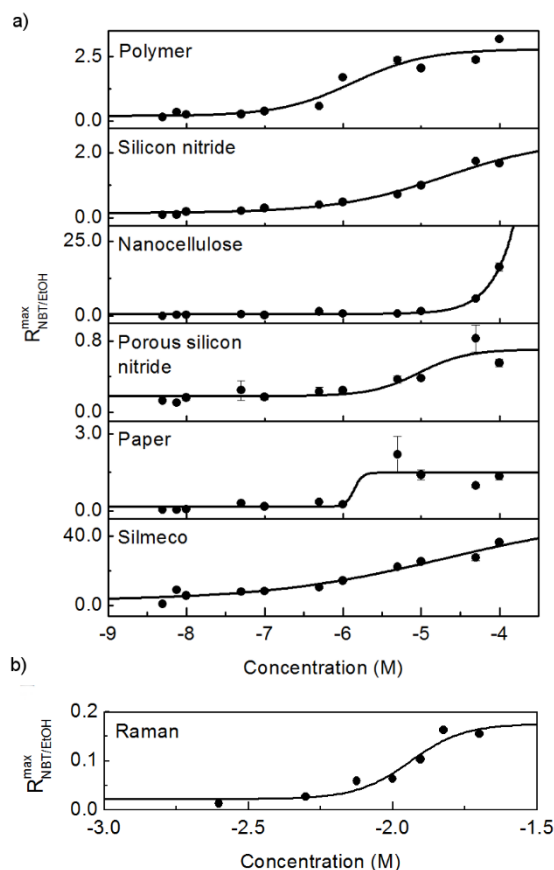


Figure S7.3: Peak area ratio as a function of concentration for a) SERS and b) normal Raman measurements, with solid lines to aid the eye. Spectra were acquired using 250 mW excitation, except as noted: for cellulose substrates and commercial substrate, excitation was limited to 57 mW. Limits of detection ($LOD = 3s_{\text{blank}}/\text{sensitivity}$) were estimated by fitting the first 3–4 data points of each response curve to a straight line. The sensitivity was equated to the linear slope and the standard deviation of the blank, s_{blank} , was calculated from experimental measurements. The LOD, in matching order to the substrates, were 2.58×10^{-10} , 2.7×10^{-10} , 2.13×10^{-10} , 1.08×10^{-9} , 1.16×10^{-8} and 3.62×10^{-11} M, but these should be understood, along with the data below, as providing a benchmark for optimizing the *application-specific* substrate preparation.

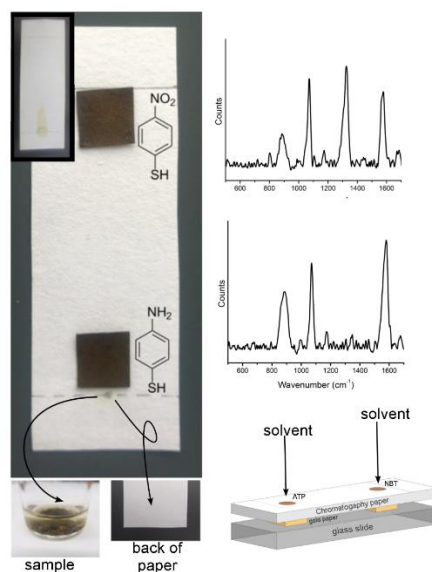


Figure S7.4: We constructed a crude paper-based assembly to demonstrate the prospects of using electrolessly gold-plated supports as multifunction SERS substrates. This assembly incorporated physical filtration of a heterogeneous sample, chromatographic separation of a multicomponent mixture, and SERS readout. The sample was constructed from NBT in acetonitrile and 4-aminothiophenol (ATP) in ethanol, with dirt added to the mixture. The mixture was spotted onto chromatography paper (7.5 cm×2.5 cm), which physically filtered the dirt (a view of the back shows the dirt did not fully penetrate through the paper). A separation was run in 4% (v/v) ethyl acetate in hexane. Iodine staining allowed visual determination of the ATP retention time (photograph shown as an inset), but SERS was needed to localize the NBT spot. After sampling then separation, squares of electrolessly gold-coated paper were placed on a glass slide underneath the two individual analyte spots. Transfer of the separated analytes was achieved using 10–40 μ L drops of ethanol and SER spectra were then recorded from each piece of electrolessly gold-plated readout paper.

REFERENCES

1. Whelan, J. C.; Karawdeniya, B. I.; Bandara, Y. M. N. D. Y.; Velleco, B. D.; Masterson, C. M.; Dwyer, J. R., Electroless Plating of Thin Gold Films Directly onto Silicon Nitride Thin Films and into Micropores. *ACS Appl. Mater. Interfaces* **2014**, *6*, 10952-10957.
2. Whelan, J. C.; Karawdeniya, B. I.; Bandara, Y. M. N. D. Y.; Velleco, B. D.; Masterson, C. M.; Dwyer, J. R., Correction to Electroless Plating of Thin Gold Films Directly onto Silicon Nitride Thin Films and into Micropores. *ACS Appl. Mater. Interfaces* **2015**, *7*, 26004-26004.
3. Arafat, A.; Schroën, K.; de Smet, L. C. P. M.; Sudhölter, E. J. R.; Zuilhof, H., Tailor-Made Functionalization of Silicon Nitride Surfaces. *J. Am. Chem. Soc.* **2004**, *126*, 8600-8601.
4. Dong, R.; Krishnan, S.; Baird, B. A.; Lindau, M.; Ober, C. K., Patterned Biofunctional Poly(Acrylic Acid) Brushes on Silicon Surfaces. *Biomacromolecules* **2007**, *8*, 3082-3092.
5. Guicheteau, J. A.; Farrell, M. E.; Christesen, S. D.; Fountain, A. W.; Pellegrino, P. M.; Emmons, E. D.; Tripathi, A.; Wilcox, P.; Emge, D., Surface-Enhanced Raman Scattering (SERS) Evaluation Protocol for Nanometallic Surfaces. *Appl. Spectrosc.* **2013**, *67*, 396-403.